## UNIVERSITY OF GENOA

PHD'S PROGRAM IN SCIENCE AND TECHNOLOGIES OF CHEMISTRY AND MATERIALS

# PRODUCTION OF GRAPHENE AND TWO DIMENSIONAL CRYSTALS BASED FUNCTIONAL ELECTRODE FOR LITHIUM ION BATTERIES

Duc Anh Dinh

**Supervisor:**

Dr. Francesco Bonaccorso

**Co-supervisors:**

Dr. Vittorio Pellegrini

Prof. Paolo Piccardo

# LIST OF PUBLICATIONS AND CONTRIBUTIONS

## Journal articles

1. H. Sun, A. E. Del Rio Castillo, S. Monaco, A. Capasso, **D. A. Dinh**, A. Ansaldo, M. Prato, V. Pellegrini, B. Scrosati, L. Manna and F. Bonaccorso, *Binder-free graphene-based anode for Li ion battery*, Journal of Materials Chemistry A, 4, 6886-6895 (2016).

2. H. Sun, A. Varzi, V. Pellegrini, **D. A. Dinh**, R. Raccichini, A. E. Del Rio-Castillo, M. Prato, M. Colombo, R. Cingolani, B. Scrosati, S. Passerini, and F. Bonaccorso, *How much does size really matter? Exploring the limits of graphene as Li ion battery anode material*, Solid State Communication, 251, 88-93 (2017).

3. H. Sun, D. Hanlon, **D. A. Dinh**, J. B. Boland, A. E. Del Rio Castillo, C. D. Giovanni, A. Ansaldo, V. Pellegrini, J. N. Coleman and F. Bonaccorso, *Carbon nanotubes-bridged molybdenum trioxide nanosheets as high performance anode for lithium ion batteries*, 2D Materials, 5, 015024 (2018).

4. A. E. Del Rio Castillo, V. Pellegrini, H. Sun, J. Buha, **D. A. Dinh**, E. Lago, A. Ansaldo A. Capasso, L. Manna, and F. Bonaccorso, *Exfoliation of Few-Layer Black Phosphorus in Low Boiling Point Solvents and its Application in Li-ion Batteries*, Chemistry of Materials, DOI: 10.1021/acs.chemmater.7b04628 (2017).

5. **D. A. Dinh**, H. Sun, L. Najafi, A. E. Del Rio Castillo, A. Ansaldo, Z. Dang, C. D. Giovanni, V. Pellegrini, and F. Bonaccorso, *Synthesis of $MoS_2$-flakes/amorphous-carbon hybrid as anode for lithium-ion batteries*, **submitted**.

## Conferences

### Invited talks

1. H. Sun, A. E. Del Rio-Castillo, **D. A. Dinh**, V. Pellegrini, and F. Bonaccorso "*Graphene and two-dimensional crystals based Li-ion batteries"* Solid State Ionics 2017, 18-23 June 2017 Padova, Italy.

### Oral presentations

1. H. Sun, A. E. Del Rio Castillo, **D. A. Dinh**, V. Pellegrini, and F. Bonaccorso, *Binder-free graphene-based anode for Li ion battery*, GrapChina, October 28-30, 2015, Qingdao, China.

2. H. Sun, A. Varzi, V. Pellegrini, **D. A. Dinh**, R. Raccichini, A. E. Del Rio-Castillo, M. Prato, M. Colombo, R. Cingolani, B. Scrosati, S. Passerini, and F. Bonaccorso, *How much does size really matter? Exploring the limits of graphene as Li ion battery anode material*, EMRS Spring Meeting, May 22- 26, 2017, Strasbourg, France.

3. **D. A. Dinh**, H. Sun, L. Najafi, C. Di Giovanni, A. Esau Del Rio Castillo, A. Ansaldo, Z. Dang, V. Pellegrini and F. Bonaccorso, *Carbon coated $MoS_2$ flakes as anode for lithium-ion batteries*, International Nanotech & Nanoscience Conference, June 28-30, 2017, Paris, France.

4. H. Sun, **D. A. Dinh**, A. E. Del Rio-Castillo, V. Pellegrini, and F. Bonaccorso, "*Graphene and two-dimensional crystals based Li-ion batteries*" GrapChina 2017, 24-26 Sept. 2017, Nanjing, China.

5. **D. A. Dinh**, H. Sun, L. Najafi, C. Di Giovanni, A. Esau Del Rio Castillo, A. Ansaldo, Z. Dang, V. Pellegrini and F. Bonaccorso, *Facile synthesis of $MoS_2$-flakes/amorphous-carbon composite as anode for lithium-ion batteries*, Applied Nanotechnology and Nanoscience International Conference 2017, October 18-20, 2017, Italy

**Posters**

1. **D. A. Dinh**, H. Sun, A. E. Del Rio-Castillo, S. Monaco, A. Capasso, A. Ansaldo, M. Prato, V. Pellegrini, B. Scrosati, L. Manna and F. Bonaccorso, *Binder-free graphene film via solvent exchange process as anode in Li-ion battery*, Graphene 2016, April 19-22, 2016, Genova, Italy.

2. H. Sun, A. Varzi, **D. A. Dinh**, R. Raccichini, A. E. Del Rio Castillo, R. Cingolani, V. Pellegrini, B. Scrosati, S. Passerini, and F. Bonaccorso, *Influence of graphene flakes morphology on the lithium ion storage capability*, Graphene 2016, April 19-22, 2016, Genova, Italy.

3. **D. A. Dinh**, H. Sun, L. Najafi, C. Di Giovanni, A. Esau Del Rio Castillo, A. Ansaldo, V. Pellegrini and F. Bonaccorso, *Binder-free anode based on carbon-coated $MoS_2$*, the Italian national conference on materials Science and Technology, December 12-16, 2016, Catania, Italy.

4. H. Sun, A. Varzi, **D. A. Dinh**, R. Raccichini, A. E. Del Rio Castillo, R. Cingolani, V. Pellegrini, B. Scrosati, S. Passerini, and F. Bonaccorso, *How much does size really matter? Exploring the limits of graphene as Li ion battery anode material*, Graphene 2017, March 28-31, 2017, Barcelona, Spain.

# ACKNOWLEDGMENTS

First of all, I would like to express my gratitude and respect to my thesis supervisor Dr. Francesco Bonaccorso for his inspiration and incredible passion to guide me during my PhD program. I would also like to thank my co-supervisor, Dr. Vittorio Pellegrini, Director of Graphene Labs, and Prof. Paolo Piccardo, University of Genoa, who gave me the opportunity to perform my research projects in Istituto Italiano di Tecnologia (IIT).

Moreover, I sincerely thank Dr. Haiyan Sun for her valuable guidance and constant encouragement. Dr. Haiyan Sun devoted a lot of efforts in every stage of my research, from laboratory to paper work, during three years of my PhD program. The support of Dr. Haiyan Sun is a big part of my achievement, I really appreciate it. Besides, I would like to extend my great appreciation to Dr. Antonio Esaú Del Rio Castillo who was always willing to discuss with me and give me helpful suggestions in the field of material science.

I further would like to express my thanks to other senior researcher and postdocs in Graphene Lab, Alberto Ansaldo, Sebastiano Bellani, Gianluca Longoni, Michele Serri, Reinier Oropesa, Sanjay Thorat, and Andrea Gamucci for spending their time to discuss with me not only science but also life. Especially, I am thankful for Dr. Alberto Ansaldo for his support in lab work and scientific suggestions.

I wish to thank other students in Graphene Lab, Leyla Najafi, Nikhil Santh, Emanuele Lago, Nicola Curreli, Silvia Gentiluomo, Elisa Petroni, and Valentino Romano for being a large source of encouragement, motivation in working and studying.

I would like to acknowledge the great support from technician team of Graphene Lab, Elisa Mantero, Manuel Crugliano, Luca Gagliani and Luigi Marasco. My lab work would not be fluent without your help.

An extra thanks to the formers of Graphene Lab, Filiberto Ricciardella, Davide Maria Di Paola, Carlo Di Giovanni and Eugenio Greco and Huy Nam Tran for their support in my work and my life.

It is also my great pleasure to work with my friends in IIT, Andrea Castelli, Zhiya Dang, Lin Chen, Thanh Binh Mai, Thi Nga Tran, Umair Gulzar, Guilherme Almeida, Javad Shamsi and Anatolii Polovitsyn for their support and experience in research. A special thanks to Andrea Castelli (my flatmate) who always extended his time to help me to overcome any trouble in Italy life. Moreover, I appreciate the support of Dr. Zhiya Dang (bunny), who has always been with me and given me the academic and emotional support during my last year of PhD.

Last but not least, I am extremely grateful to my parents and sister for their love, support and continuous encouragement throughout my study in Italy.

# LIST OF ABBREVIATIONS

| | |
|---|---|
| 0D | zero dimensional |
| 1D | one dimensional |
| 2D | two dimensional |
| 3D | three dimensional |
| γ | surface tension |
| AFM | atomic force microscopy |
| BET | Brunauer – Emmett – Teller measurement |
| BM | ball-milling |
| b.p. | boiling point |
| CB | carbon black super-P |
| CMGs | chemically modified graphene |
| CNTs | carbon nanotubes |
| CPE | constant phase element |
| CV | cyclic voltammetry |
| CVD | chemical vapor deposition |
| CHP | N-cyclohexyl-2-pyrrolidone |
| DMC | dimethyl carbonate |
| DMF | dimethylformamide |
| DOD | depth of discharge |
| EC | ethylene carbonate |
| EFTEM | energy filtered elemental mapping |
| (HAADF)-STEM | high angular annular dark field - scanning TEM |
| EDS | energy dispersive X-ray spectroscopy |
| EIS | electrochemical impedance spectroscopy |
| EELS | electron energy loss spectroscopy |
| ESSs | energy storage systems |
| EtOH | ethanol |
| EVs | electric vehicles |
| FCs | fuel cells |
| FL-BP | few-layer black phosphorous |
| FLG | few layer graphene |
| FWHM | full width at half maximum |
| GNPs | graphene nanoplatelets |
| GO | graphene oxide |
| HAADF-STEM | high angular annular dark field-Scaning TEM |
| HEVs | hybrid electric vehicles |
| HMWPs | high molecular-weight polymers |
| HRTEM | high resolution-TEM |
| IPA | 2-propanol |
| LCO | $LiCoO_2$ |
| LFP | $LiFePO_4$ |
| LIBs | lithium ion batteries |
| LNMO | $LiNi_{0.5}Mn_{1.5}O_4$ |
| LO | longitudinal |
| LPE | liquid phase exfoliation |
| MC | micromechanical cleavage |

| | |
|---|---|
| MLG | multi-layer graphene |
| $MoO_3$/SWNTs | hybrid structure of SWNT-bridged $MoO_3$ |
| $MoS_2$/C | $MoS_2$/amorphous carbon composites |
| m-SWNTs | metallic SWNTs |
| OES | optical extinction spectroscopy |
| OAS | optical absorption spectroscopy |
| PAA | poly(acrylic acid) |
| PVdF | polyvinylidene fluoride |
| RBMs | radial breathing modes |
| $R_{CT}$ | charge transfer resistance |
| $R_E$ | electrolyte resistance |
| RGO | reduced graphene oxide |
| SA | surface area |
| SBS | separation based sedimentation |
| SCs | supercapacitors |
| SEI | solid electrolyte interface |
| SEM | scanning electron microscopy |
| HRSEM | high resolution-SEM |
| SLG | single-layer graphene |
| SOC | state of charge |
| s-SWNTs | semiconducting SWNTs |
| SWNTs | single wall carbon nanotubes |
| TEM | transmission electron microscopy |
| TGA | thermogravimetric analysis |
| TMOs | transition metal oxides |
| TMSs | transition metal sulfides |
| TO | tangential |
| XPS | X-ray Photoelectron Spectroscopy |
| XRD | powder X-ray diffraction |

# CONTENTS

# Abstract

The rapid development of electronic portable devices, electric cars, etc. has boosted the requirement of portable and efficient energy storage systems. In this context, lithium ion batteries (LIBs) technology has emerged as one of the most promising for the aforementioned applications. In the last years, strong efforts have focused on LIBs research and technology. As a result, substantial achievements in LIB technology have been harvested, such as the introduction of new electrode materials with high capacity, and the invention of new electrolytes with high electrochemical stability in different environmental conditions. Although the present LIBs exhibit more than twice the energy density with respect to the first commercial one introduce by Sony in 1991, several challenges still need to be solved in order to further apply LIBs for high energy and power applications, *e.g.*, electrical vehicles. These challenges include safety, cost, improvement in life-time, and increase in energy and power densities of LIBs. It should be noted that most of these concerns are related to the use of electrode active materials; therefore, the development of high-performance anode and cathode is one of the critical requirements in current LIBs technology. The on-going research exhibits that the current cathode with particular specific capacity values leaves small room for further improvement in energy density, but the anode can be tuned to obtain higher specific capacity and energy efficiency, as well as longer cycle life. Thus, tremendous efforts have been devoted to the development of high-performance LIB anodes, which can provide high energy, power density for the LIBs and can adapt to the environmental constraints and ultimately suit the needs of industrial-scale production at low-cost. Up to date, conventional LIB anodes commonly use graphite as active material due to its high coulombic efficiency (~99%), low potential profile versus lithium (~ 0.2 V) and structural stability during charge/discharge cycling. However, the main limiting factor of graphite relies on its theoretical maximum specific capacity that is limited to 372 mA h $g^{-1}$ since every six carbon atom can host only one $Li^+$ determined by the $LiC_6$ stoichiometry, which is not suitable for the development of high energy density LIBs. For this reason, there is a significant scientific interest in replacing graphite with higher specific capacity anode materials. For example, metal and metal oxides, such as Sn (933 mAh $g^{-1}$), Si (3579 mAh $g^{-1}$), Ge (1623 mAh $g^{-1}$), $SnO_2$ (782 mAh $g^{-1}$), and $Co_3O_4$ (890 mAh $g^{-1}$), have higher lithium storage capacities than graphite via the formation of alloys with lithium or through the reversible reactions with $Li^+$. However, these electrodes are still facing with the severe issue associated with the large volume change during the charging/discharging cycles, resulting in the pulverization of the electrode, and consequently poor electrochemical reversibility. The exploitation of anode materials with long lasting life cycles and high specific capacity for LIBs is still a challenge for the scientific community.

Thus, seeking new anode materials for the next-generation of LIBs is a mandatory task for both academia and industry. The aim of my PhD work was to investigate nanomaterials, *e.g.*, carbon nanotubes (CNTs), graphene and other two-dimensional (2D) crystals as potential materials for future LIB electrodes. In particular, I studied the electrochemical properties of four promising materials for LIB anodes, *e.g.*, graphene, molybdenum trioxide ($MoO_3$), molybdenum disulfide ($MoS_2$) and black phosphorous (BP). For what concerns graphene, I focused on the production and processing to optimize the fabrication of binder-free graphene anode. Furthermore, I carried out the study of the effect of graphene flakes dimension (lateral size and thickness) on the $Li^+$ storage capability. In particular, I sorted graphene flakes by layer numbers and lateral size, investigating the influence of the flakes morphology on the electrochemical performance upon lithiation/de-lithiation. This strategy provides useful guidelines for the practical exploitation of few- (FLG) and multi- (MLG) layer graphene as stand-alone anode materials in LIBs. To achieve this target, I have produced graphene flakes by liquid phase exfoliation (LPE) of graphite and then tuned the morphology of graphene flakes by means of *sedimentation-based separation* (SBS).

After the study on graphene, I shifted my interest to other layered materials such as $MoO_3$ and $MoS_2$. Similar to the production of graphene, I started carrying out the production of few-layer $MoO_3$ and $MoS_2$ flakes via LPE of their bulk counterparts, then studied the electrochemical behaviors of $MoO_3$ and $MoS_2$ flakes based anodes in order to find the strategies to improve $Li^+$ storage ability of these anodes. This approach utilizes the LPE to produce nano-sized flakes, which are able to resist the mechanical degradation caused by volume changes of these materials upon cycling of LIB. Although the nano-sized $MoO_3$ and $MoS_2$ flakes can exhibit the advantage in structural preservation of anodes, they are still facing with the issues of low intrinsic electrical conductivity which cause poor rate performance. Thus, it is necessary to integrate the high electrical conductive materials, *e.g.*, carbon based materials, with $MoO_3$ and $MoS_2$ to improve their electrical conductivity when integrated in LIB anodes.

To realize this strategy, I firstly synthesized the hybrid structure of single wall carbon nanotubes-bridged $MoO_3$ ($MoO_3$/SWNTs) via a low-cost, non-toxic and simple solution mixing method. Afterward, the binder-free $MoO_3$/SWNT anodes were fabricated to study the effects of SWNTs content (wt%) on the electrochemical behaviors of $MoO_3$. The SWNTs network in this electrode is demonstrated to play the role of conducting channels for electronic transport, and a buffered network for volume change of $MoO_3$. This study sets the basis for the exploitation of exfoliated $MoO_3$ flakes as anode materials in high performance

LIB. Moreover, the binder-free $MoO_3$/SWNTs hybrid anode prepared by the simple aforementioned method can boost the development of high performance anodes for LIBs.

As for $MoS_2$, I designed a fabrication method of $MoS_2$ flakes/amorphous carbon hybrid ($MoS_2$/C) anodes based on a thermal composition of a carbon source, *e.g.*, poly(acrylic acid) (PAA) in the mixtures of $MoS_2$/PAA. The $MoS_2$/C based anodes are built to investigate the effects of different carbon contents on electrochemical performance of the hybrid and optimize the proper carbon content. This work clarified that a proper content of carbon not only improves the electrical conductivity of electrode by facilitating the electron transport, but also acting as a buffer layer for active materials to avoid its pulverization upon cycling. Hence, the study of $MoS_2$/C electrodes gives the research community a protocol for large-scale production of $MoS_2$/carbon hybrid and also can be easily extended to the construction of other 2D nano-crystals, such as transition metal sulfide (TMSs), transition metal oxides (TMOs), dispersed in amorphous carbon networks for $Li^+$ storage application.

The last activity in this thesis focuses on the study of production and LIB application of few-layer BP (FL-BP) flakes. Similar to the production of graphene, $MoO_3$ and $MoS_2$, LPE was used as strategic route for the large-scale production of FL-BP. The exploitation of FL-BP flakes in cutting-edge technologies, *e.g*, in flexible electronics and energy storage, is however limited by the fact that the LPE of BP is usually carried out at a high boiling point (b.p.) and in toxic solvents. In fact, the solvent residual is detrimental to device performance in real applications, thus complete solvent removal is critical. To overcome these issues, I carried out the LPE of BP in different low-b.p. solvents. Among these solvents, the LPE of BP in acetone exhibited a high concentration of FL-BP ($FL\text{-}BP_{acetone}$) flakes. Taking the advantage of low-b.p. solvent, *e.g.*, acetone, I further fabricated the FL-BP based anode to study the electrochemical properties of this material for LIB anode. The electrochemical study of $FL\text{-}BP_{acetone}$-based anode indicates a promising design of fast charge/discharge devices.

In summary, the Thesis is organized as follow.

**Chapter 1** shows the global view and the fundamental understanding of current LIB technology, a brief review of challenges and opportunities for future LIB, together with the introduction of several promising candidates for LIB anodes such as graphene and other 2D materials ($MoO_3$, $MoS_2$ and BP).

**Chapter 2** reviews LPE for layered materials. The production and processing of graphene, $MoO_3$, $MoS_2$ and BP by LPE as well as the synthesis of $MoO_3$/SWNTs and $MoS_2$/C hybrids for LIB are reported. The electrode fabrication, cell-assembling are introduced, together with full material and electrochemical characterization techniques.

**Chapter 3** dedicates to the characterizations of each type of materials, e.g., graphene, $MoO_3$, $MoS_2$, $MoO_3$/SWNTs, $MoS_2$/C hybrids and BP. This chapter lays a solid foundation for the understanding of electrochemical performances of each material which will be discussed in Chapter **4, 5 and 6**.

**Chapter 4** concerns the study of graphene for LIB application. The first part of this chapter focuses on the processing of LPE graphene via a solvent exchange process and electrochemical performance of binder-free graphene anode in both half-cell and full-cell configurations. The second part provides a fundamental understanding of the role of graphene flakes dimension (lateral size and thickness) on the $Li^+$ storage ability of graphene anodes.

**Chapter 5** covers the activities of $MoO_3$ and $MoS_2$ based LIB anodes. The study on electrochemical properties of $MoO_3$ and $MoO_3$/SWNTs hybrid demonstrates the role of SWNTs in $Li^+$ storage ability of $MoO_3$. While the study on electrochemical properties of $MoS_2$ and $MoS_2$/C hybrid provides the understanding of the effects of carbon content on $Li^+$ storage ability of $MoS_2$ based anodes.

**Chapter 6** describes the study on electrochemical properties of FL-BP-based anodes for LIBs. The study on electrochemical properties of FL-BP exfoliated in acetone indicates that it is promising with regards to the fast charge/discharge LIBs. Overall, the presented process is a step towards the fabrication of phosphorene-based devices.

**Chapter 7** summarizes the most important insights achieved in the research topics of graphene, $MoO_3$ and $MoS_2$, from material to electrochemical characterizations. Moreover, the future plans for exploring these materials for LIBs are discussed.

# Chapter 1:

# Introduction

## 1.1. Global overview of lithium ion batteries

The changing global landscape, such as industrial development and growing human population, has led to a range of problems, such as environmental pollution, fossil fuel exhaustion and climate change. In this context, energy has been recognized as a primary factor to resolve the aforementioned problems. [1] Therefore, the exploitation of various sustainable and renewable energy resources, such as solar and wind energy, have been continually progressed. [2] However, those energy resources are highly intermittent being dependent on time, climate, or region. Hence, there is urgent need for the development of efficient energy storage systems (ESSs) in order to make use of those energy resources globally and in full. Moreover, the extreme progress of portable electronic devices (cell phones, laptops, cameras, etc.) and electric- (EVs) or hybrid- electric vehicles (HEVs) have created an ever-increasing demand for ESSs. In this regard, one of the greatest challenges is to construct highly efficient, convenient, low-cost, and environmentally friendly ESS devices. Many effective and practical technologies for portable ESSs, such as rechargeable batteries, [3-5] fuel cells (FCs), [6-8] and supercapacitors (SCs), [9-11] have been developed in the past decade. The recent researches have shown that FCs and SCs can provide high energy density which can meet the requirement of EVs/HEVs. [12-14] However, on the one hand, the operation problems related to electro-catalysis in FCs and hydrogen storage will need more research & development effort. [14, 15] On the other hand, the absences of chemical reactions in SCs enable them to deliver energy quickly, with charging time in the order of minutes or even seconds. [16] Therefore, SCs are primarily used to provide peak power and store regenerative braking energy. [17, 18] Owing to the issues of FCs and SCs, rechargeable batteries have been recognized to be the most practically viable power source for both portable electronic and EV/HEV applications for the near future. [2, 19] In particular, in order to meet the requirement of ever-growing portable electronic market, battery technology need to be improved in term of high power, large capacity and light weight. [20] For this reason, many investigations have been dedicated to different battery types such as lead-acid (Pb-acid) batteries, [21] Nickel-Cadmium (Ni-Cd) batteries, [22] Nickel-metal-hydride batteries [23] and LIBs. [2] Among these, LIBs have been recognized as promising candidate for portable electronic and EV/ HEV applications because of its remarkable advantages: (*i*) the low reduction potential of Li (-3.04 V vs. standard hydrogen electrode) allows LIBs to have higher working voltage than the Pb-acid, Ni-Cd, Ni-metal-hydride batteries; [24] (*ii*) the light weight of Li element (6.94 g $mol^{-1}$) [2] allows LIBs to have high energy and power densities (Figure 1.1a). [20, 25] As a result, LIBs became the most advanced mobile power sources [15] and currently dominates the market for portable electronic devices (Figure 1.1b). [25] However, despite LIBs are currently the first choice for portable energy storage, the improvement of their performances can greatly expand their applications and enable new technologies. [24] In this perspective, researchers worldwide continue to work on many different aspects of this technology such as enhancing the energy and power densities, improving the cycling life and stability, as well as reducing the cost. [26] For instance, the ever-growing markets of EVs and larger stationary storage systems require the significant improvement of current LIB technology, such as the increase in energy density, the reduction in cost and the enhancement of safety. [15, 24, 27]

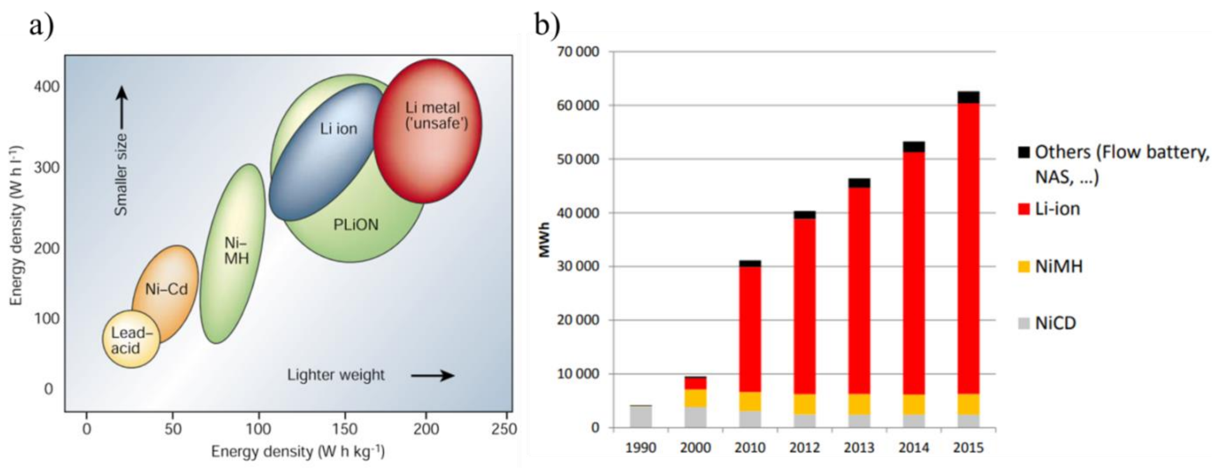


Figure 1.1. *(a) Comparison of the different battery technologies in terms of volumetric and gravimetric energy density [2] and (b) Worldwide battery market. [28]*

## 1.2. Fundamental of lithium ion batteries

### 1.2.1. History of lithium ion batteries

The first rechargeable LIB with metallic Li based anode and $TiS_2$ based cathode was proposed by Whittingham (Exxon Mobil Corporation) in 1976. [29] However, Exxon unsuccessfully commercialized these LIBs due to the problems of Li dendrite formation and short circuit upon extensive cycling and safety concern. [30] In 1981, Goodenough firstly proposed to use layered $LiCoO_2$ (LCO) as high energy (1.11 kWh $kg^{-1}$) and high voltage (~ 4.0 V vs. Li/$Li^+$) cathode materials. [31] Nevertheless, the lack of safety in anode materials, *e.g.*, Li metal, limited the application of layered LCO cathode in LIBs. In late 1970s and early 1980s, graphite, having a layered structure was recognized as a good candidate to reversibly store Li by intercalation/de-intercalation by Besenhard, [32] Yazami, [33] and Basu. [34] In 1987, Yohsino *et al.* had filed a patent and built a prototype cell using carbonaceous anode and LCO as cathode. [35] The high stability of carbon and LCO in air is highly beneficial from the engineering and manufacturing point of view. In 1991, Sony Corporation successfully commercialized LIBs for the first time. Since then, LIBs have been attracting increasing attention and Japan became the leader of global LIB market with 57% market share in 2010. [24] The global production of LIBs continuously increases in the past two decades, especially with the growing popularity of portable electronics devices. Besides, to satisfy the ever-increasing demand of energy market, the research activity in LIBs has also been progressively increased year after year. In fact, the number of scientific publications also keep increasing each year (see Figure 1.2), [36] achieving impressive progresses in term of electrode materials, safety and cell-design, etc.

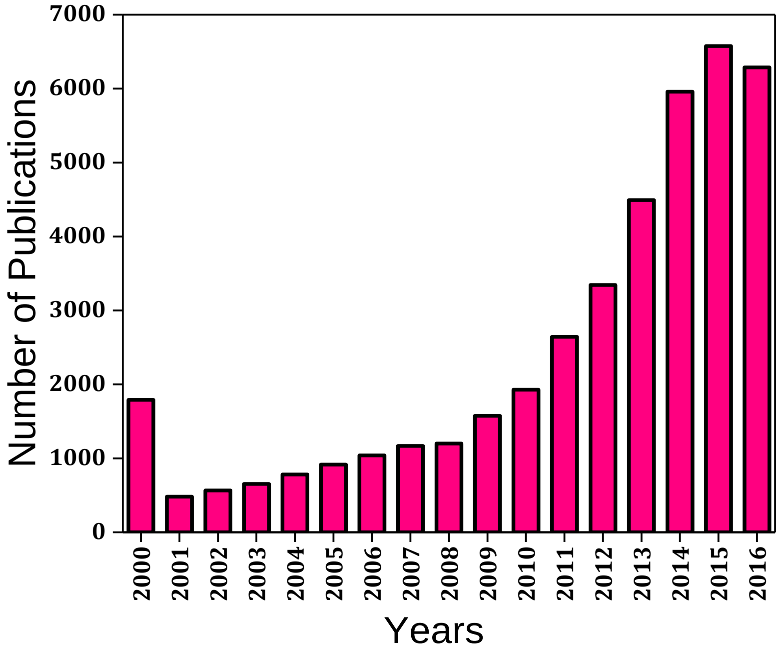


Figure 1.2. *The increase in number of publications related to lithium ion batteries since 2000 to 2016. [37]*

To date, there are four well-known different types of LIB geometries according to the current manufacturing market, namely the prismatic, cylindrical, coin, and the pouch cell configurations (Figure 1.3a). [2] Both the cylindrical and prismatic cells are commonly made of "laser-welded" aluminum can with cylindrical or rectangular shape, which contains a jelly-rolled cathode, anode and separator immersed in a liquid electrolyte. [38, 39] Typical applications for the cylindrical and prismatic cells are medium-scale electronic devices, such as power tools, laptops, electrical bikes, mobile phones, and tablets. [40] The pouch cell with aluminized plastic bag contains a flexible cathode, anode and polymer/gel electrolyte. The pouch cell offers a flexible and light-weight solution to battery design with respect to cylindrical and prismatic cells, resulting in its wide range of applications in consumer, military, as well as automotive industries. [2] The coin cell exhibits a compact design, consisting of a round cathode, anode, separator, spacer and spring (O-ring) immersed in a liquid electrolyte (Figure 1.3b). [41] Thanks to the simplest design, coupling with the advantage of lightness and versatile assembling with respect to other LIB geometries, coin cells have been popularly used for small-scale electronic devices, *e.g.*, watches, hearing aids, car keys and memory backup, [40] as well as research samples in laboratories.

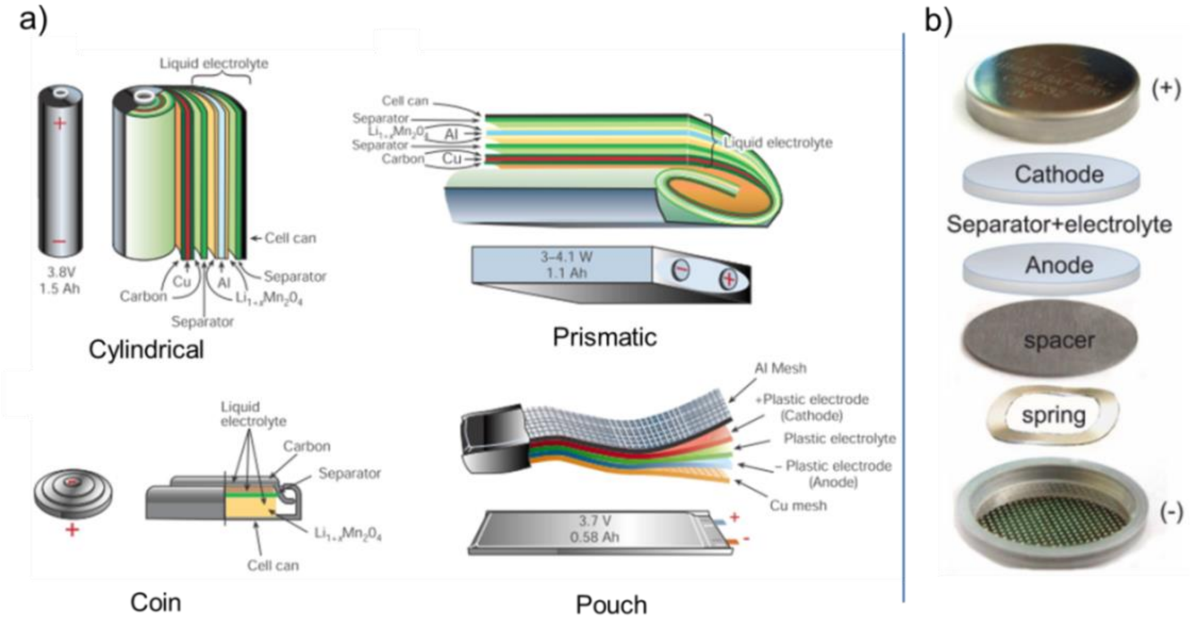


Figure 1.3. *(a) Schematic drawing showing the shape and components of various Li-ion battery geometries, [2] and (b) Detailed configuration of coin cell. [41]*

### 1.2.2. Working principles of lithium ion batteries

In general, LIB is a simple electrochemical system that is able to convert chemical energy into electrical energy during discharging process and then re-convert the electrical energy to chemical energy during charging process. [42] As shown in Figure 1.4, a conventional LIB consists of two major components: anode (negative electrode) and cathode (positive electrode), immersed in an electrolyte which acts as an environment for $Li^+$ transfer between two electrodes. [25] The anode and cathode are separated by a porous permeable membrane, namely separator, which not only allows $Li^+$ to pass through but also prevents a short circuit due to direct contact of electrodes. [36] Both anode and cathode are deposited onto copper (Cu) and aluminum (Al) current collectors, respectively which are connected by an external electrical circuit. The working mechanism of LIBs, taking LCO and graphite as typical cathode and anode materials, respectively, can be described as following. During charging process, $Li^+$ de-intercalates from cathode, travels through the electrolyte and intercalates to the anode. Meanwhile, the electrons travel through the external electrical circuit in order to couple with the intercalated $Li^+$ in anode. The reverse mechanism occurs in the discharging process. The electrode reactions can be expressed by the following equations: [42]

$$\text{Cathode: } LiCoO_2 \leftrightarrow Li_{1-x}CoO_2 + xLi^+ + xe^- \quad (1.1)$$

$$\text{Anode: } 6C + xLi^+ + xe^- \leftrightarrow Li_xC_6 \quad (1.2)$$

$$\text{Total reaction: } 6C + LiCoO_2 \leftrightarrow Li_xC_6 + Li_{1-x}CoO_2 \quad (1.3)$$

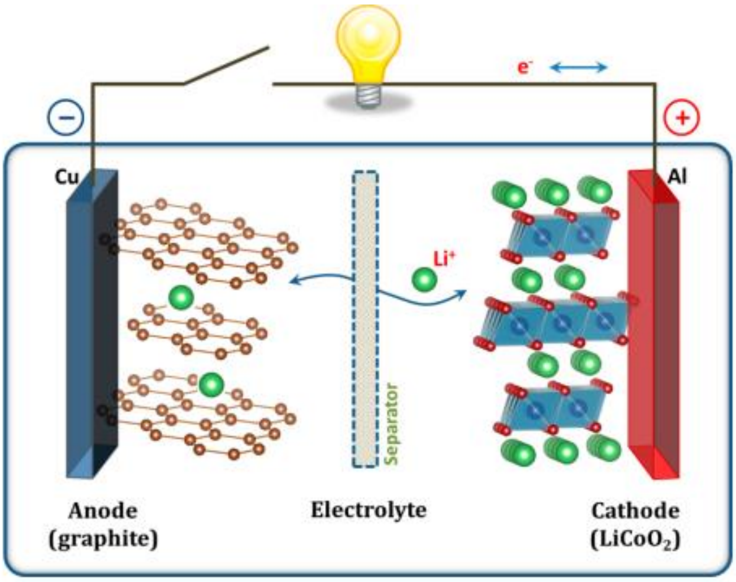


Figure 1.4. *Schematic illustration of the first lithium-ion battery ($LiCoO_2$/$Li^+$ electrolyte/graphite). [25]*

The performance of LIBs can be evaluated by several parameters, such as open circuit voltage, operating voltage, theoretical specific capacity, specific capacity, coulombic efficiency, energy density, power density, and the charge/discharge rate. [43]

The *open circuit voltage* ($V_{ocv}$) is the voltage between anode and cathode when there is no current load on the battery (equation 1.4). [43] The *operating voltage* ($V_{ov}$) is determined by the potential difference between anode and cathode when there is a current load (equation 1.5). [43]

$$V_{ocv} = (\mu_A - \mu_C) \quad (1.4)$$

$$V_{ov} = \frac{1}{nF(\mu_A - \mu_C)} \quad (1.5)$$

in which $\mu_A$ and $\mu_C$ is the chemical potential of anode and cathode, respectively; $n$ is the number of electrons involved in the chemical reaction of the cell and $F$ is the Faraday constant (96485 C $mol^{-1}$).

The *theoretical specific capacity* ($Q_{th}$) of active electrode material is the maximum charges that can be stored per unit mass of active electrode material. The value of $Q_{th}$ can be obtained by Faraday law, see equation 1.6. [43]

$$Q_{th} = \frac{nF}{3.6 \times M_w} \tag{1.6}$$

in which $n$ is the number of electrons involved in the chemical reactions of the electrode and $M_w$ (g $mol^{-1}$) is the molecular mass of the active electrode material.

The *specific capacity* ($Q$) (mAh $g^{-1}$) of active electrode material measures the amount of charge that can be reversibly stored per unit mass of active electrode material at a certain current load during the charging/discharging process, see equation 1.7 [41]

$$Q = \frac{It}{m} \tag{1.7}$$

in which $I$ (mA) is the current load during charging/discharging process, $t$ (h) is the total charging/discharging time and $m$ (g) is the weight of electrode active material.

In case of the full-battery, *e.g.*, graphite as anode and LCO as cathode, the specific capacity of the full battery ($Q_{cell}$) is determined by both specific capacity of anode $Q_A$ and cathode $Q_C$, see equation 1.8 [43]

$$Q_{cell} = \frac{Q_A \times Q_C}{Q_A + Q_C} \tag{1.8}$$

*The coulombic efficiency* ($CE$), is the ratio between *discharge specific capacity* ($Q_{discharge}$) and the *charge specific capacity* ($Q_{charge}$) for each cycle: [36]

$$CE = \frac{Q_{discharge}}{Q_{charge}} \times 100\% \tag{1.9}$$

The *energy density (E)* (Wh $g^{-1}$) [43] defines the amount of energy that can be stored and released per unit mass of the electrode. It can be obtained by multiplying the $Q$ with $V_{ov}$, see equation 1.10. The *energy density* is an important parameter for practical application as it determines the ultimate useful work from a battery. [24]

$$E = V_{ov} \times Q \tag{1.10}$$

The *power density* (*P*) (W $g^{-1}$) is the output energy per unit mass of the electrode, see equation 1.11. The *P* is a characteristic of the battery chemistry and packaging. It determines the battery size required to achieve a given performance target.

$$P = \frac{I \times V_{ov}}{m} \tag{1.11}$$

The *charge/discharge rate* (*C-rate*) is the current (mA) used to charge/discharge the battery relative to its maximum capacity. A charge at *x*C rate means a full charge in a time of 1/*x* hours. For instance, a 2C rate means that the current will charge/discharge the entire battery in 1/2 h. [43]

### 1.2.3. Anodes of lithium ion batteries

Various anode materials have been extensively investigated for the development of LIBs. Depending on their electrochemical reaction mechanisms, the anode materials are categorized into three groups: intercalation-, alloy- and conversion reaction-based anode materials. [44]

#### *1.2.3.1. Intercalation-based anode materials*

The electrochemical reaction occurring at this type of anode is based on the intercalation of $Li^+$ into the structure of active materials, *e.g.*, layered, cylindrical and spinel structures. [45-47] These materials enable fast $Li^+$ diffusion by providing the effective ionic transport channels during lithiation/de-lithiation, which are either one dimensional (1D) path or two dimensional (2D) planes. [36] However, they offer low specific capacities because the intercalation of $Li^+$ is mostly limited by the intrinsic redox reactions of materials, *e.g.*, number of exchanged electrons. [48, 49] Presently, graphite is the primary choice and has been commercialized as the most successful intercalation-based anode material. [2] Graphite has a layered structure of carbon hexagon network in an orderly arrangement, as shown in Figure 1.5. In fact, when the layers are stacked, the different graphitic structures occur. The ABAB stacking results in the more common hexagonal graphite, whereas a stacking order of ABCABC gives the rhombohedral graphite. [50] The structure of graphite allows $Li^+$ transport between its inter-spacing layers without the considerable volume change (the expansion and contraction in volume of material during lithiation which cause structural degradation), resulting in high coulombic efficiency, reaching 99.9 %. [51] Moreover, graphite has advantages of low-cost, high electrical conductivity (~ $3\times10^5$ S $m^{-1}$), [52] high $Li^+$ diffusivity ($10^{-11}$ – $10^{-7}$ $cm^2$ $s^{-1}$), [20] compared to other intercalation-based anode materials, *e.g.*, $TiO_2$, $Li_4Ti_5O_{12}$ and $Li_{1.03}V_{0.97}O_2$. [20, 53] However, the most Li-enriched intercalation of graphite has a stoichiometry of $LiC_6$, meaning one $Li^+$ per 6 carbon atoms, resulting in a theoretical specific capacity of 372 mAh $g^{-1}$ (see equation 1.2). [2] This is a major drawback associated with commercial graphite-based LIBs, especially for applications, such as EVs and HEVs, which require high energy and power density, see equation 1.10. Hence, the use of graphite as anode is still limited to low-power devices like smart watches, mobile phones and laptops. [20]

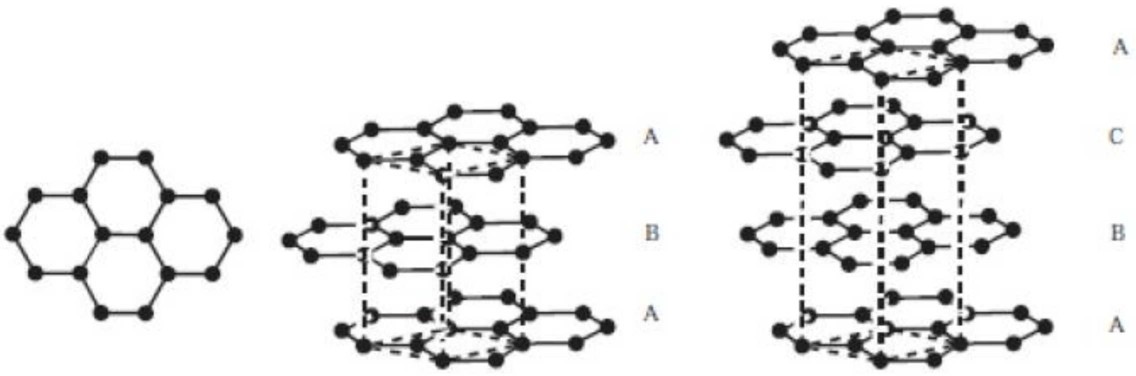


Figure 1.5. *The structure of a carbon layer, hexagonal and rhombohedral graphite. [50]*

#### *1.2.3.2. Alloy-based anode materials*

This type of materials is associated with elements which are able to electrochemically alloy and form compound phases with lithium. [44] Alloy forming compounds have higher theoretical specific capacity compared to that of commercial graphite (372 mAh $g^{-1}$), *e.g.*, Si, Ge, Sn, etc. with capacity values of 4200, 1600, 999 mAh $g^{-1}$, respectively through an alloying product of $Li_{4.4}N$ (N = Si, Ge and Sn). [54, 55] The role of N is to provide the matrix of the alloy electrode to support the strain generated during the lithiation and de-lithiation process, as well as to improve the electrical conductivity. [56] Beside their high theoretical specific capacities, the alloy-based materials gained tremendous attention thanks to their abundance and low-cost. [57] Thus, it is believed that these materials will result in high enhancement in the overall energy density of LIBs, making them eligible for EVs and HEVs. However, the alloy-based anode materials suffer from slow lithium reaction kinetics and poor intrinsic conductivities which cause low rate capability of the LIBs. [36] Moreover, the critical challenge of this kind of anode materials relies on their large volume changes due to the reaction with $Li^+$. For example, the alloy of lithium with Si results in 440% increase in number of atoms in the alloyed Li-Si particle with respect to the initial Si particle, inducing a large volume change of ~ 300%, see Figure 1.6. [58] This dramatically introduces a mechanical stress in the material during cycling of LIBs, leading to the pulverization of the electrode. [59] Consequently, this cause the electrical contact loss between Si particles and the current collector, [20, 60] resulting in severe capacity fading of the electrodes. [59, 61] Various strategies, such as carbon coating on the surface active materials and the size reduction of the active materials, have been adopted to alleviate volume change without significantly compromise the specific capacity. [62, 63] Very recently, Sn and Si have been allowed to be used as anode in commercial LIBs with improved capacity up to 30%, along with better rate performance, compared to that of traditional graphitic anode.

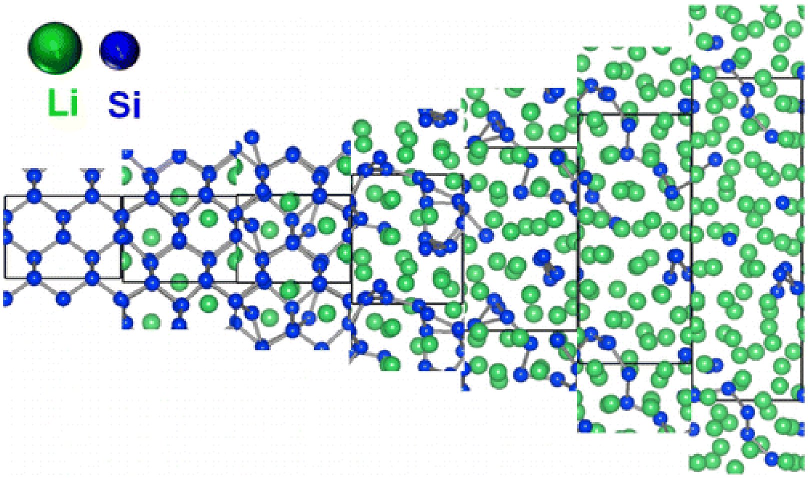


Figure 1.6. *The volume change of silicon during lithiation. [58]*

#### *1.2.3.3. Conversion reaction-based anode materials*

This type of material is mainly transition metal compounds ($M_aX_b$, M = transition metal, X = O, S, F, P, N etc.), [64] which store the $Li^+$ through a conversion reaction. In this reaction, $Li^+$ reacts with metal ions to form $Li_nX$ and reduces metal ions to their zero oxidation state, as shown in Figure 1.7. [65] During the conversion reaction, the structure and composition of electrode materials have completely changed. Therefore, an ideal conversion-based electrode material is expected to have the ability to regenerate their initial structure and composition during charging/discharging processes. [65] Anodes based on these compounds exhibit high reversible capacities (500 – 1000 mAh $g^{-1}$) owing to the participation of a high number of electrons in the conversion reactions. [66] One of the most typical conversion-based anode materials is TMOs, *e.g.*, CoO, FeO, NiO and $Cu_2O$, which were firstly introduced in LIBs by Poizot *et al.* [67] and then intensively studied, thanks to their high specific capacities and capacity retentions.

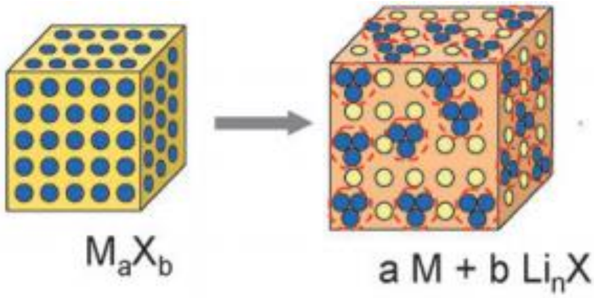


Figure 1.7. *Conversion reaction-based anode material. [68]*

During lithiation process, the TMOs react with $Li^+$ and yield metal nanoparticles in the matrix of $Li_2O$ via a conversion reaction, as shown in equation 1.12. During de-lithiation process a reverse reaction occurs. [69]

$$M_xO_y + 2yLi^+ + 2ye^- \leftrightarrow xM^0 + yLi_2O \qquad (1.12)$$

in which M is Co, Ni, Fe, Cu, Mn, etc.

However, there are also drawbacks that limited the application of such materials in LIBs. Firstly, the hysteresis in voltage (a difference between lithiation and de-lithiation voltage) increases with ongoing conversion reactions, leading to a decrease in operating voltage of LIBs and consequently to a poor energy efficiency. Secondly, the $Li^+$ stored per formula unit of TMOs through a conversion reaction, causing a volume change of active materials. Most conversion-based TMOs have much higher theoretical capacities than graphite (372 mAh $g^{-1}$), such as iron oxides (1007 mAh $g^{-1}$), [64] manganese dioxide (1223 mAh $g^{-1}$) [64] and cobalt oxide (890 mAh $g^{-1}$). [64] Despite the high theoretical specific capacity, conversion reaction-based TMOs should be further optimized to overcome other unsatisfactory electrochemical properties including volume change and voltage hysteresis. [67, 70]

TMSs, another important class of conversion reaction-based anode materials, follow similar mechanism for $Li^+$ storage as that of TMOs. In general, the chemical reaction of metal sulfides with $Li^+$ can be represented by equation 1.13. [71]

$$M^{n+}S + ne^- + nLi^+ \leftrightarrow M^0 + nLi_2S \qquad (1.13)$$

in which, M is Mo, W, Zr, V, Sn, Mn, etc.

During lithiation process, TMSs react with $Li^+$ and yield metal nanoparticles in the matrix of $Li_2S$ *via* a conversion reaction, whereas the reverse reaction occurs during de-lithiation process.

TMSs are considered as promising candidate for anode of LIBs thanks to their good thermal stability and conductivity along with high theoretical specific capacities, *e.g.*, $MoS_2$ (670 mA h $g^{-1}$). [72] However, capacity fading is one of the critical issues for TMSs and it arises from two reasons. One is related to the voltage hysteresis that causes poor energy efficiency of LIBs. [65] The other is related to the $Li^+$ transport in electrolyte hindered by the polysulfide anions, *e.g.,* $Li_2S_x$ ($6 < x \leq 8$), which are produced from the conversion reaction (equation 1.13). These polysulfide anions tend to breakdown to smaller $Li_2S_x$ ($2 < x \leq 6$) with continuous charging/discharging processes, [65] and then develop a barrier for $Li^+$ diffusion and charge transport by depositing an insulating sulfur layer on electrode surface. [73, 74]

The blockage of $Li^+$ diffusion can not only causes capacity fading, but also creates an increase in the internal temperature of battery and results in the thermal explosion. [75]

### 1.2.4. Cathodes of lithium ion batteries

Plenty of promising materials have been explored as cathode materials for LIBs. The cathode materials can be categorized based on their operating voltage versus lithium (from 2.5 to 5V). Typically, 3-Volt cathode materials are $MnO_2$ and $V_2O_5$; [24] 4-Volt cathode materials are LCO, $LiNiO_2$ with layered structure, three dimensional (3D) spinel $LiMn_2O_4$, and olivine $LiFePO_4$ (LFP), tavorite $LiVPO_4F$; [24] 5-Volt cathode materials are olivine $LiMnPO_4$, $LiCoO_4$ and 3D spinel $Li_2Fe_xMn_4O_8$ structure. [24] Generally, high operating voltage cathode is desirable because the operating voltage of cathode is proportional to the cell operating voltage, which could help to increase the energy density.

In order to optimize the performance of cathode, we also need to consider the structure of materials which is one the most important factors for the cyclability of the cathode. For examples, the 3D spinel structures exhibit high operating voltage (4-5 V), but they are still facing the issue of fast capacity fading due to the phase transition during cycling, which is related to mechanical stress in material. [76-78] Currently, layered LCO and olivine LFP are most widely used in commercial LIBs because of their good cycle life (> 500 cycles). [24]

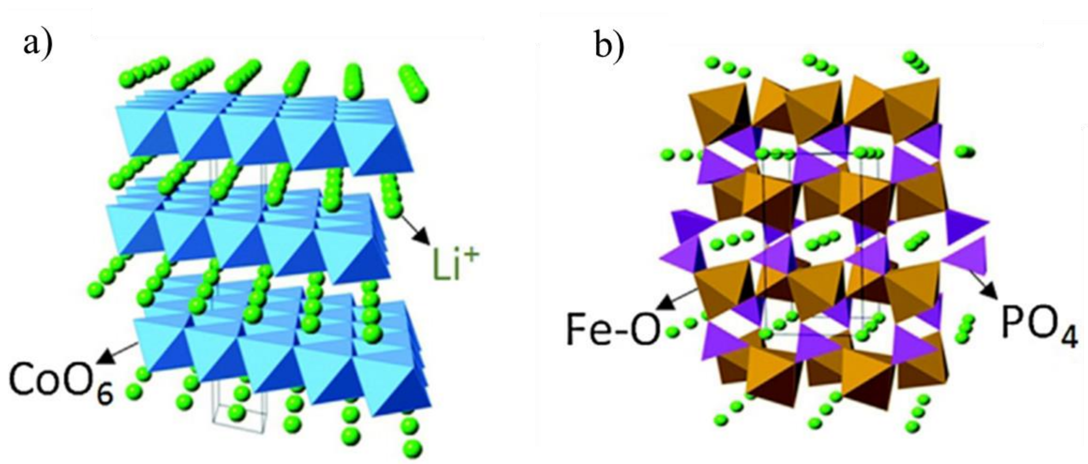


Figure 1.8. *Cyrstal structure of typical cathode materials: (a) layered $LiCoO_2$, (b) olivine $LiFePO_4$. [20]*

LCO exhibits the layered structure with Co and Li located in octahedral sites, as shown in Figure 1.8a, occupying alternating layers and forming a hexagonal symmetry. LCO is attractive for industrial production because it has high theoretical specific capacity (274 mAh $g^{-1}$) and can be easily manufactured in large scale, being also stable in air. [79] However, the major limitation of LCO relies on its high cost and toxicity of Co. Also, low thermal stability is a major concern of this material. LCO typically experience thermal runaway past ~ 200 ℃ due to an exothermic reaction between the released oxygen and organic materials in electrolyte. [24] Moreover, LCO can suffer from the lattice distortion from hexagonal to monoclinic symmetry at the de-lithiation voltage ~ 4.2V (approximately > 50% if $Li^+$ extract from LCO lattice), inducing capacity fading. [80] For these reasons, various types of metals, *e.g.*, Ni, Mn, Al, Fe and Cr, were studied with the aim to substitute Co. [81-83] Among the aforementioned materials, spinel $LiNi_{0.5}Mn_{1.5}O_4$ (LNMO) was found to be attractive material because it can exhibit the similar electrochemical performance as LCO, while reducing cost and toxicity. Also, the presence of Ni allows higher de-lithiation capacity to be achieved with respect to original LCO due to the continuous reaction of $Ni^{2+/3+/4+}$ with lithium, resulting in high operating voltage (4.6 to 4.8V vs. $Li/Li^+$). This makes LNMO as a potential candidate of cathode for LIBs to power EVs and HEVs. Moreover, the presence of $Mn^{3+}$ exhibit better rate performance in LNMO with respect to the $Co^{3+}$ in LCO due to a higher electronic and ionic conductivity. However, $Mn^{3+}$ is unstable and may be turned into: $Mn^{2+}$ and $Mn^{4+}$. The produced $Mn^{2+}$ then dissolves into the electrolyte, leading to a capacity fading during charging/discharging process [84, 85]. In the LNMO products, $Li_xNi_{1-x}O$ usually appears as impurity phase, lowering the capacity and hindering $Li^+$ transport in the material. Therefore, it is crucial to investigate the reaction mechanism of $Mn^{3+}$ and control their content of impurity in the spinel product. [86, 87]

Another type of commercial cathode, olivine structure LFP, is attracting much attention in the past decade due to its low-cost and low-toxicity. In LFP, Li and Fe atoms are located in octahedral sites, whereas P occupies tetrahedral sites in a hexagonal close-packed oxygen array, see Figure 1.8b. Compared to LCO, LFP also offers a number of advantages, such as stability, excellent cycle life, and temperature tolerance (−20 to 70°C). However, LPF has issues of poor electronic and ionic conductivity of $10^{-10}$ S $cm^{-1}$ and $10^{-8}$ $cm^2$ $sec^{-1}$, respectively, as well as relatively low theoretical capacity (170 mAh $g^{-1}$). [88] The other issue is that $Li^+$ diffusion can easily be blocked by defects and impurities in the material. [89] In order to overcome this issue, synthesizing nano-sized LFP has been considered as a promising strategy by reducing $Li^+$ diffusion paths during lithiation and de-lithiation in LIBs. [90]

### 1.2.5. Electrolyte, separator and current collectors

The *electrolytes* in LIBs act as an ionic media for $Li^+$ transport back and forth between anode and cathode as the battery are charged and discharged. [42] Currently, the *liquid electrolyte*, solution containing lithium salts and organic solvents, is common used in commercial LIBs. [24] These organic solvents in liquid electrolytes are required to have high ionic mobility in a wide temperature range and good chemical/thermal stability. [91] In order to meet these requirements, the content of solvents are typically formulated and mixed to effectively dissolve the lithium salts selected for practical application in LIBs. Over the past two decades, alkyl carbonates have been found to be the most suitable solvents for LIBs, thanks to their electrochemical stability, non-toxicity and low-cost. [15] However, the electrolytes are not only determined by the solvents, but also highly dependent on the properties of lithium salts. [24] Therefore, various lithium salts have been explored, including lithium hexafluorophosphate ($LiPF_6$), lithium tetrafluoroborate ($LiBF_4$), lithium hexafluoroarsenate(V) ($LiAsF_6$) and lithium perchlorate ($LiClO_4$). [24] Among these, $LiPF_6$ is the most suitable lithium salt to make electrolyte (using alkyl carbonates as solvent), from the perspective of safety, high ionic conductivity and high solubility in organic solvents. [24] So far, the widely used commercial liquid electrolyte, as shown in Figure 1.9, is 1M $LiPF_6$ in a 50:50 w/w mixture of ethylene carbonate (EC) and dimethyl carbonate (DMC). [91, 92] The mixture of EC/DMC allows high solubility of $LiPF_6$ to form an electrolyte with high ionic conductivity with respect to the electrolytes formed by other alkyl carbonates. [93] Besides the liquid electrolyte, other types of electrolytes have also been developed and proposed for LIBs, such as *polymer, gel and ceramic electrolyte*. [42] *Polymer electrolyte* is solvent-free because it is formed by the mixing of high molecular-weight polymers (HMWPs) with lithium salts. [94] The advantage of polymer electrolyte with respect to liquid electrolyte is the low volatility, flexible design thanks to the high flexibility of HMWPs. [95] Moreover, the polymer electrolyte can also function as a potential to eliminate separators in LIB configuration, due to high ion permeability and electrochemical inert of HMWPs. [96] *Gel electrolyte* is formed by absorbing a solution of lithium salt and polar solvents into a network of HMWP. [97] Because the solvent containing lithium salt is fully absorbed within the polymers, the solvent leakage issue, which happened in LIB using liquid electrolyte and causes safety problems, can be avoided. *Ceramic electrolytes* have long been explored for fuel cells, and recently attracting increasing interest for the application in LIBs. [98, 99] The most obvious property of ceramic electrolyte is the robust mechanical strength of ceramic materials which make them more suitable for rigid battery designs as in, for example, thin-film-based devices. [98] The ionic conduction in ceramic compounds occurs by movement of ionic point defects, which requires energy, so the conductivity of ceramic electrolyte increases with increasing temperature. Therefore, the batteries with ceramic electrolyte can find applications in high temperature environment, including handheld orthopedictools and powered medical devices  that need to be sterilized in autoclaves under high temperature conditions.

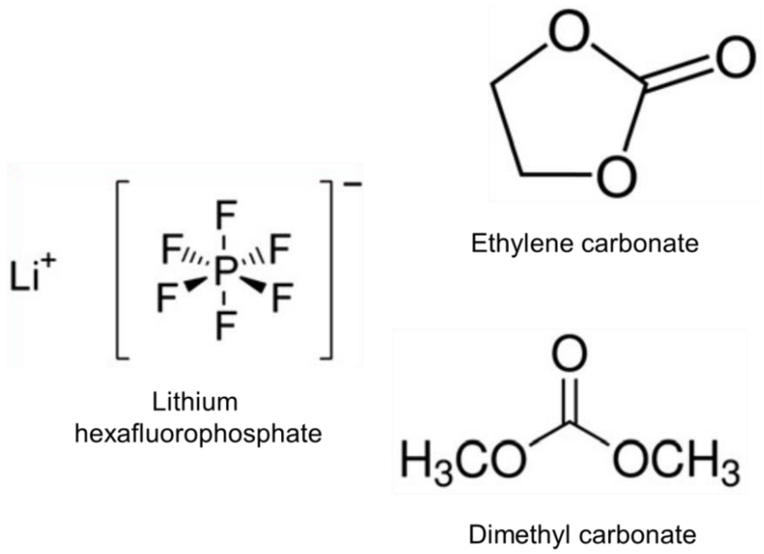


Figure 1.9. *Chemical structures of common components in commercial electrolyte: lithium hexafluorophosphate as the lithium salt and the solvent composed of ethylene carbonate and dimethyl carbonate [24]*

The *separator* is a porous membrane placed between electrodes, which is permeable to ionic flow, but prevents electric contact between the two sides of electrodes. [100] The separator must be chemically and electrochemically stable towards the electrolyte and electrode materials. In term of structure, the separator should have sufficient porosity with pore size < 1 μm to absorb sufficient liquid electrolyte for the high ionic conductivity. [24] However, the presence of separator increases the electrical resistance and takes space inside the battery, negatively affecting the battery performance. [101] Up to date, battery separators can be categorized into three types: *microporous polymer membranes*, *non-woven fabric mats* and *inorganic composite membranes*. [102] Among them, the microporous polymer membranes have been most widely used in batteries with liquid electrolyte due to their low-cost, light weight and facile manufacturing. Nevertheless, the main issues of these separators are poor mechanical strength and low melting point (~100 ℃). [103, 104] Thus, for the development of future LIBs for high temperature applications inorganic composite membranes, *e.g*., $Al_2O_3$, as separators are highly attractive, thanks to their excellent thermal stability and mechanical property. [105]

The *current collector* works as an electrical conductor between the electrode and external circuits and a support for the deposition of the electrode materials. [106] To completely form the electrode, the electrode materials are coated onto current collectors. The main requirements for current collector material are light weight, electrochemical stable at battery operation voltage and high electrical conductivity. For most commercial LIBs, Cu is the choice for anode because it is electrochemically stable in the range below 3 V vs. $Li/Li^+$, while aluminum is extensively used for cathode due to its electrochemical stability for higher voltages between 3-5 V vs. $Li/Li^+$. [107] However, with extensive cycling, the adhesion of active materials to the current collector is reduced due to the structural degradation of active materials upon lithiation/de-lithiation. [108, 109] Especially for the alloying- and conversion-based anode materials, the contact between active material and current collector is easily lost upon cycling due to volume change. Recent research has focused on the use of a 3D micro-porous current collector to improve the mechanical stability of the electrodes.[110] Such current collectors offer a high porosity, which can accommodate the volume change of the active materials. [111]

## 1.3. Current challenges and opportunities of anodes in lithium ion batteries

Although LIBs have been commercialized for about two decades and are dominating the portable electronic device market, the increasing demand for energy storage requires further improvements in the existing LIBs. Next generation LIBs with lower-cost, higher power and energy density is highly expected to power HEVs and EVs, without compromising vehicle performances, such as driving distances, speed, and safety. The main challenge of current LIBs is their low energy density which highly depends on specific capacity and operating voltage of electrode materials. Hence, the choice of electrode material is one of the crucial factors determining the performance of LIBs. Present commercial LIBs utilize graphite anode and LCO cathode, which only have power density of ~ 387 W $kg^{-1}$ and energy densities of ∼120−150 Wh $kg^{-1}$ due to the following reasons: (*i*) the theoretical capacity of graphite anode (is low 372 mAh $g^{-1}$), (*ii*) the practical capacity of LCO cathode (~140 mAh $g^{-1}$) only reached 50% of its theoretical value (274 mAh $g^{-1}$) and (*iii*) the operating voltage of LCO is limited at 4.2 V vs $Li/Li^+$. [112, 113] In order to increase energy and power density of LIBs, it is desirable to find anodes with high specific capacities (Figure 1.10), *e.g.*, TMOs (600-1200 mAh $g^{-1}$), TMSs (1000-1200 mAh $g^{-1}$) [44] and cathodes with high operating voltage, *e.g.*, LNMO, $LiMnPO_4$ (> 4.5 V). [24] There are a large numbers of anode candidates that could increase the specific capacities with respect to graphite, as shown in Figure 1.10. It should be noticed that the groups of conversion materials and alloying materials are highly attractive due to their large specific capacities, see section **1.2.3.3**. Although the alloying materials can provide extremely large capacities, *e.g.*, Si (3579 mAh $g^{-1}$), their alloying process involves large volume expansion which results in substantial capacity loss upon cycling. The conversion materials, such as TMOs, TMSs are still under development due to volume changes (~ 100%) and large voltage hysteresis, resulting in capacity fading and low energy density. Hence, tremendous efforts on the production and design of anode materials have been carried out to enable the application of anode materials.

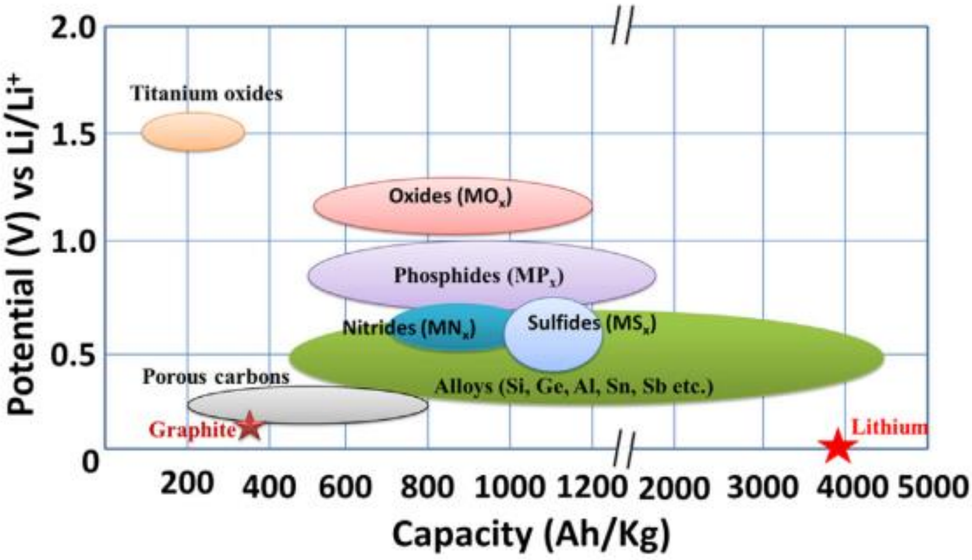


Figure 1.10. *Schematic illustration of active anode materials for the next generation of LIBs. Potential vs. Li/Li$^+$ and the corresponding specific capacity are shown. [44]*

To date, there are two promising strategies for the development of anode materials: (*i*) *nanostructured anode materials* and (*ii*) *composite anode materials*. [44]

On one hand, nanostructured anode material, respect to the bulk one, can dramatically reduce the length of the paths for Li$^+$ and electron transport, mitigating the volume change during charging/discharging process. [114] The alloying anode materials, *e.g*., Sn, Si, and Ge, have shown evidence for the existence of a critical size below ~150 nm which the fracture of a particle may not occur. [115] Using nanomaterials for LIB electrode, it can decrease the Li$^+$ diffusion length and the Li$^+$ diffusion time constant (see equation 1.14), consequently resulting in the improvement of rate capability. [116, 117] Furthermore, small particle size allows efficient mixing of the active material with other components such as the conductive carbon additive. However, the high specific surface area of nanomaterials leads to a large irreversible capacity in the first cycle due to the formation of *solid electrolyte interface (SEI)*, formed by the decomposition of the electrolyte. [24]

$$\tau = \frac{L^2}{D} \qquad (1.14)$$

in which $\tau$ the diffusion time constant, $L$ is diffusion length and $D$ is the diffusion coefficient.

Additionally, the shape of the nanomaterials plays a very important role in the electron and ion transport within electrode. Therefore, recent developments in nanostructured anode materials for LIBs have been based on zero dimensional (0D) (nanoparticles), 1D (nanowires, nanotubes), 2D (nanosheets, nanoplates) materials, as well as 3D porous framework, see

Figure 1.11. [118] Although 0D nanoparticles, *e.g.*, nanoparticles of Si and Sn, have been expected as the promising active materials in LIBs, their performances are limited by various factors. Firstly, 0D materials create the random pathways that can restrict the electron and $Li^+$ transport. [36] Secondly, the grain boundaries and voids in between the nanoparticles hinder electron transport, limiting the LIB performance. [119, 120] Thirdly, the extremely high surface area of the 0D nanoparticles and access of the electrolytes trigger side reactions of electrolyte decomposition, forming SEI film. [120] The formation of SEI film consumes excessive charge supplied by the cathode, exhibiting low coulombic efficiency and capacity loss. [44, 119] In the case of 1D material, it is considered to be superior to 0D nanoparticles because its directional channels facilitate efficient electronic and ionic transport. [121] Moreover, 1D structure also provides mechanical stability during lithiation/de-lithiation. [61] For the 3D structured materials, *e.g.*, 3D graphene aerogels with porous frameworks, it can provide excellent properties of large specific surface area, rapid $Li^+$ diffusion, excellent mechanical strength as well as multidimensional continuous electron-transport. However, the complexity in designing such nano-architecture is still a challenge that requires great efforts to reach practical LIB anode applications. [122, 123]

On the other hand, the synthesis of composite materials, combining active materials with inactive materials which can compensate for the limited properties of active material, *e.g.*, buffering the volume change and enhancing the conductivity of electrode. For instance, the composite of alloying materials and carbon-based materials (CNTs, graphene, etc.) can increase the ionic and electronic transport of the electrode. [124] Furthermore, carbon can form network to buffer the volume change of active material during charging/discharging processes. [125-127] Besides, developing a layer of inactive materials between electrolyte and active materials can prevent the direct contact between electrolyte and active material, hindering the side reactions between electrolyte and active materials, and then limiting the irreversible capacity. [128, 129] However, thickness of the inactive layer highly influences the electrochemical performance. In fact, if this layer is too thin, it might be collapsed with volume changes and bring electrode surface in contact with electrolyte. In contrast, if the inactive layer is too thick, the diffusion of $Li^+$ will be hindered, resulting in a low performance of composite with respect to that of pristine active material. Thus, the thickness of inactive materials in the composites should be properly controlled to provide the ultimate performance of anodes. [130]

Furthermore, nanomaterials enable the facile synthesis of composite materials [131-133] Therefore, the nanostructured composite anode materials have been developed by the growth of various nanostructures of active materials along with inactive materials to build hybrid/composite structures. This is a good strategy of exploiting the novel properties of inactive materials, *e.g.*, high conductivity, robust mechanical strength to support the limited properties of active materials, *e.g.*, low conductivity, volume change (see Figure 1.11). [134, 135] For instance, multiple nanostructures, *e.g.*, core-shell ($SnO_2$/carbon) and hollow sphere ($SnO_2$, $Fe_2O_3$) structures have been designed/produced with the aim to improve the conductivity, protect the surface and limit volume changes of active materials. [134]

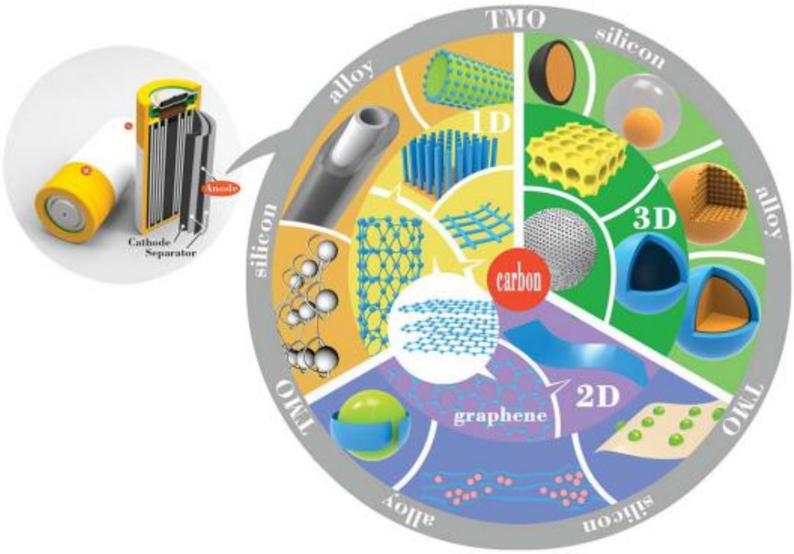


Figure 1.11. *Schematic diagram of the recent anode materials for lithium ion batteries. [118]*

## 1.4. Graphene and other two dimensional materials: the promising anode materials for lithium ion batteries

Since the success in the exfoliation of graphite in 2004, [136] new classes of 2D materials, such as TMOs, [137] TMSs, [138] transition metal carbides/nitrides (Mxenes) [139], BP and elemental analogues of graphene (silicene, phosphorene, and borophene), [140] (Figure 1.12), have been successfully exfoliated or synthesized for many applications. In recent years, significant advances have been made in 2D materials, having the potential to bring unprecedented functionality to next-generation LIBs. [141] In general, 2D materials are defined as the free-standing atomic crystals that are strictly 2D and can be viewed as individual atomic planes exfoliated from bulk layered crystals or as unrolled single-wall nanotubes. [142] This structure provides the efficient ion transport channels between the layers, facilitating the diffusion of $Li^+$. Moreover, the large surface areas provide a large number of active site for $Li^+$ storage. [143-146] It has been clearly shown in section **1.3** (see Figure 1.10) that graphene, layered TMOs and TMSs are the most promising materials which can replace graphite to become the future anode materials for LIBs. Additionally, BP has recently stimulated research interests to develop the extremely high specific capacity anode due to its high theoretical capacity of 2596 mAh $g^{-1}$ [147-149] with respect to that of graphene, layered TMOs and TMSs.

Up to date, there are plenty of production techniques, including bottom-up and top-down approaches, [150] to produce graphene, 2D TMOs, TMSs and BP for LIBs applications. [150] However, most of the productions methods are still facing with the issues of high-cost, [151, 152] toxicity, [153, 154] time-consuming synthesis and low-yield of mass production [155, 156] which are the current challenges towards practical industrial application. For example, the chemical vapor deposition (CVD) method can be used to grow graphene, [157] TMOs [151] and TMSs. [158] However, this method is still facing with the issue of high-cost and low-yield in term of mass production,  hindering the large-scale application for commercial LIBs. Hence, the low-cost processes via chemical solution methods have been proposed to overcome the issues of CVD. Large efforts have been devoted to the exploitation of chemically modified graphene (CMGs) such as graphene oxide (GO) and reduced GO (RGO). [159, 160] However, the chemical solution process is time-consuming and the CMGs suffer from limited conductivity and slow diffusion of $Li^+$ due to the defects on the basal planes. [5, 161] Concerning the growth of TMOs and TMSs, *e.g.*, $MoO_3$ and $MoS_2$, the most frequently used approach for their producing is hydrothermal, [162, 163], solvothermal [164, 165] and template assisted techniques. [166, 167] However, these approaches involves toxic precursors, *e.g.*, $(NH_4)_2MoS_4$ or $Na_2MoO_4$, [168-171] and time-consuming synthesis, [172, 173] resulting in unresolved issues, *e.g.*, safety and scalability. [174-176] Furthermore, the TMSs and TMOs produced by these methods usually have an amorphous structure and contains defects,[177] which requires annealing at high temperature (700-800 ℃) to obtain the layered structure of TMOs and TMSs, severely impacting on the production cost. [168, 178-182] Apart from the production of graphene, TMOs and TMSs, the production of 2D BP flakes can be performed using micromechanical cleavage (MC), [183, 184] which consists of consecutively peeling off crystal layers by using adhesive tape. [142] However, this technique is only suitable for research activities due to both the scalability limitation and morphological heterogeneity of the exfoliated flakes. [142] The other exfoliation technique, *e.g.*, ball-milling (BM), [185, 186] has been applied to synthesis BP flakes because it can meet the requirement of scalable production. However, ball milling usually introduces impurities in the obtained products. [145, 187]

In this context, LPE has been recognized as a potential method to produce graphene, TMO and TMS flakes thanks to its low-cost, simplicity and scalability, which can reach the industrial-scale production. [188-190] Therefore, the scope of this thesis is to provide the insight-into study on production of graphene, $MoO_3$ and $MoS_2$ via LPE, as the representatives for 2D carbon, TMO and TMS materials, respectively, for LIB anodes.

### 1.4.1. Graphene

Graphene, a defect-free carbon monolayer, is considered the mother material of a family of 2D carbon forms. [191] The novel properties of graphene, such as large surface to mass ratio (2600 $m^2$ $g^{-1}$), [192] high electrical conductivity [193] and high mechanical strength [194], make it a promising material as electrodes in LIBs. Differently from graphite, in which $Li^+$ are intercalated between the stacked layers, [195] single-layer graphene (SLG) can theoretically store $Li^+$ on both surfaces, reaching the theoretical capacity of 744 mAh $g^{-1}$. [196, 197] Also, the edges in graphene nanoflakes (< 100 nm) are able to offer the considered active sites for $Li^+$ storage. [198] However, both theoretical and experimental studies have evidenced that $Li^+$ storage is not thermodynamically favored in SLG, where only low $Li^+$ occupancy levels can be achieved. [160, 199, 200] Meanwhile, graphene nanoplatelets (GNPs) have demonstrated some appealing features for niche applications, *e.g.*, low temperature and high power), but no considerable gain in maximum specific capacity with respect to graphite. [201] This raises a natural question. What about what lies in between? Is there a critical flakes size where both beneficial properties of graphite, *e.g.*, low operating voltage and graphene, *e.g.*, high conductivity and short diffusion length, are found? Is few-layer graphene a good active material for next-generation LIBs? Despite the fact that it is well accepted that dimension (lateral size and thickness) of the flakes, [202] as well as their edges, [198] are expected to play key roles on the $Li^+$ storage mechanisms, [198, 202] the link between these morphological properties, and electrochemical performances has not been established yet. The answer for these questions will be unveiled in **chapter 4**.

### 1.4.2. Molybdenum trioxide

$MoO_3$, especially $\alpha$-$MoO_3$ with the stable orthorhombic phase, exhibits a very high theoretical capacity of 1117 mAh $g^{-1}$ as LIB anodes. [203, 204] Additionally, the interlayer spacing as large as 0.69nm of $\alpha$-$MoO_3$ compared to 0.34 nm of graphite, guarantees its $Li^+$ host capability. [205] Moreover, its higher intercalation voltages (1.5-2.3V Vs $Li/Li^+$), with respect to that of graphite (< 0.4V Vs $Li/Li^+$), could reduce the safety problems caused by the decomposition of electrolyte, especially for the utilization in HEVs. [64] However, the main drawbacks of bulk $MoO_3$ for LIB application is its low ionic [206] and electrical conductivity ($10^{-5}$ S $m^{-1}$) [155] as well as volume change during charging/discharging processes. [64] In this regard, to enable $MoO_3$ for LIB application, the nanostructured design and synthesizing composite, including nano-sized $MoO_3$ and carbon-based materials, *e.g.*, amorphous carbon

[207, 208], CNTs [209, 210] and graphene [211, 212] are the highly promising strategies to overcome the aforementioned drawbacks of $MoO_3$. In this thesis, the $MoO_3$ nanoflakes are firstly produced by LPE of bulk $MoO_3$. A simple solution mixing process of SWNTs and $MoO_3$ flakes allows forming a hybrid structure of $MoO_3$/SWNTs for LIB anode. The nano-sized $MoO_3$ reduces the $Li^+$ diffusion length, promoting fast $Li^+$ transport, whereas the SWNTs play a role of conductive agent to improve the conductivity of electrode and a buffer layer to accommodate the volume change. The synthesis of $MoO_3$/SWNTs hybrid and its electrochemical properties as anode material for LIBs will be reported in **chapter 3 and 5**.

### 1.4.3. Molybdenum disulfide

Molybdenum disulfide ($MoS_2$) with the 2H phase possesses sandwich-like layered structure in which the S and Mo atoms are covalently bonded forming 2D layers, and the layers are held together through weak van der Waals interactions. [213] The inter-layer spacing of $MoS_2$ (0.62 nm) [72] is more favourable for $Li^+$ intercalation [214, 215] with respect to that of graphite (0.34 nm). Notably, $MoS_2$ is able to deliver the theoretical capacity of 670 mAh $g^{-1}$. [72] Moreover, the high insertion voltage of $MoS_2$ anode (~ 0.5-1.1 V vs. $Li/Li^+$) can make itself as a safer anode than graphite (< 0.4 V vs. $Li/Li^+$), because the Li dendrite formation, a layer progressively formed during the cycling process on the surface of electrode, is less likely to occur at higher insertion voltage. [216] Nevertheless, there are following issues that need to be solved: (*i*) the fast capacity fading of the bulk $MoS_2$ because of the volume change during lithiation/de-lithiation; [72, 217, 218] (*ii*) the low rate performance due to the low electrical conductivity of 2H phase $MoS_2$ (200 $cm^2\ V^{-1}\ s^{-1}$). [214, 219-221] Therefore, many efforts have been devoted to develop nanostructure of $MoS_2$, and to the synthesis of hybrid of $MoS_2$ and carbon-based materials. In particular, the composites of $MoS_2$/GO, [222] $MoS_2$/rGO [223, 224] and $MoS_2$/CNTs [225] have been synthesized and demonstrated the significant improvement in LIB performance with respect to the individual components.

This thesis presents the hybrid structure of $MoS_2$ flakes (produced via LPE of bulk $MoS_2$) and amorphous carbon, prepared by a thermal decomposition of a carbon source, *e.g.*, PAA. The presence of carbon network in the hybrid structure is expected as a conducting agent to improve the electrical conductivity of electrode and a buffer layer for active materials to hinder its pulverization during lithiation and de-lithiation. The synthesis of $MoS_2$/C hybrid and its electrochemical properties for LIB anode will be introduce in **chapter 3 and 5**.

### 1.4.4. Black phosphorous

Black phosphorus (BP), a layered crystal, having an orthorhombic phase, with puckered layers [186] held together by interlayer van der Waals interactions. [186] This structure allows BP to uptake three $Li^+$ to reach a composition of $Li_3P$, [149] leading to a very high theoretical specific capacity of 2596 mA h $g^{-1}$ [147-149]. Also, the puckered structure is able to promote fast $Li^+$ diffusion ($10^4$ times faster than that in graphite), [226] resulting in its outstanding rate-capability. Moreover, when exfoliated into single layer (phosphorene) or FL-BP flakes, the increased available surface area can further enhance the electrochemical activity, [186] which is beneficial for energy storage applications. [147, 202] Therefore, exfoliated BP is a promising candidate for the next generation of LIB anodes. The exfoliation of bulk BP into FL-BP flakes can be performance by many methods, e.g., MC, BM and LPE. [186] However, the MC has the issues of scalability limitation [142] and morphological heterogeneity of the BP flakes, [150] whereas the drawback of BM is the presence of impurities in the BP flakes. [145, 187] In this regard, LPE has been recognized as a strategic route for the large-scale production of less defective phosphorene and FL-BP flakes. [226] However, current approaches for the LPE of BP present several issues especially in aqueous environment, where the chemical integrity of the exfoliated flakes is compromised due to the oxidation promoted by the presence of $O_2/H_2O$. [227-229] The formation of phosphorus-oxide species, *i.e.* $P_2O_5$ and $P_2O_4$, [230] has been reported when the BP is exposed to air. These processes accelerate the degradation of BP. [231] Performing the LPE in pure organic solvents can solve this issue, since the presence of water and $O_2$ is avoided. The organic solvents that commonly used to exfoliate BP are generally toxic (Health code ≥ 2 NFPA704), [232] and have a b.p. usually above 100 °C, *e.g.* N-methyl-2-pyrrolidone (NMP, b.p. = 202°C), [233] N,N-dimethylformamide (DMF, b.p. = 153°C) [234] N-cyclohexyl-2-pyrrolidone (CHP, b.p. = 284°C) [235] or formamide (b.p. 210 °C). [236] The solvent b.p. is critical for LIB technology because the solvent removal is of paramount importance for the realization of high performance electrodes of batteries.

In this thesis, the bulk BP is exfoliated by LPE using 14 different solvents, which were selected after having considered the different values of surface tension (γ), b.p. and/or Hansen and Hildebrand solubility parameters of each solvent. A stability analysis of BP on the diverse solvents provides information about the solubility parameters of BP, *e.g.*, γ, Hansen and Hildebrand solubility parameters. These BP solubility parameters give me a clue on the adequate solvent selected to exfoliate and/or store exfoliated BF flakes. Ideally, the solvent should have a low-b.p., which would allow a fast deposition, especially useful for the aim of designing LIB anodes. This thesis firstly presents the analysis of dispersability and stability of exfoliated BP flakes in various solvents to determine the ideal solvent, *e.g.,* acetone, for the

LPE of BP. Then the feasibility and up-scalability of this approach is demonstrated by designing homogeneous films of FL-BP flakes exfoliated in acetone and used as anodes for LIBs. The details of solvent selection for LPE of BP and the study of electrochemical properties FL-BP based anode will be described in **chapter 3 and 6**.

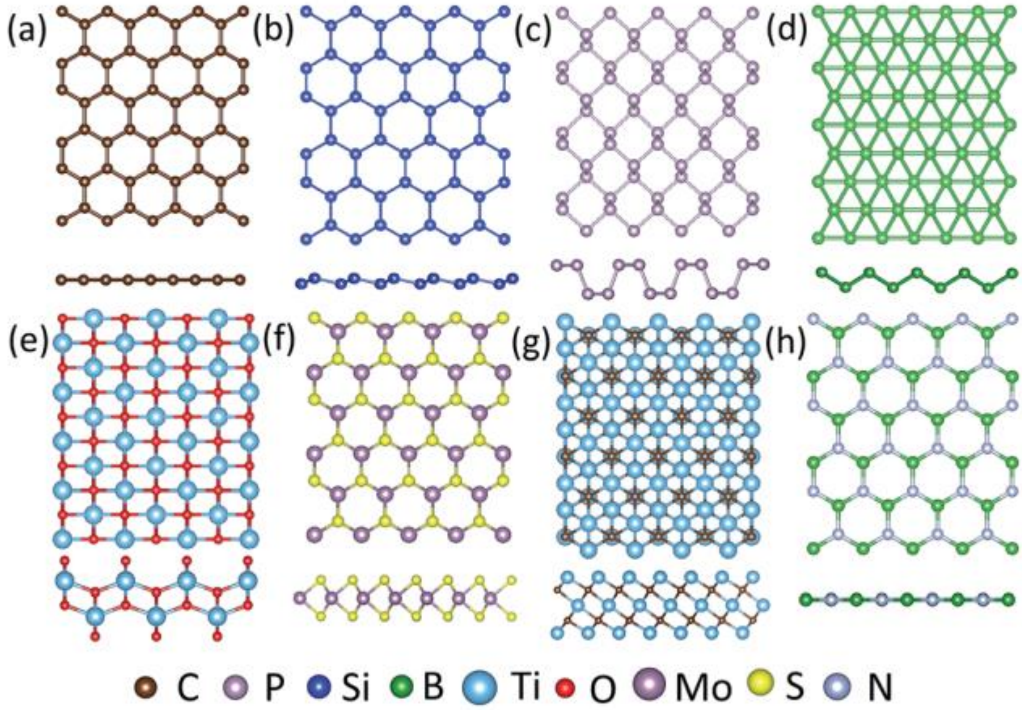


Figure 1.12. *Top and side view of the atomic structure of 2D single layered: (a) graphene, (b) silicene, (c) phosphorene, (d) borophene, (e) $TiO_2$, (f) $MoS_2$, (1H) (g) $Ti_3C_2$ and (f) h-BN. [145]*

# Chapter 2:

# Experimental procedure

### 2.1. Production and processing of graphene and other two dimensional materials

In this thesis, LPE [237, 238] is exploited to produce graphene and other 2D materials, e.g., $MoO_3$ and $MoS_2$ owing to its low-cost, simplicity and high throughput, which can scalable at the industrial level. [188-190] In particular, the LPE graphene exhibits a low level of basal plane defects and high crystallinity, [188, 189, 202, 239] which is, an important feature for the electron transport within electrode in LIB application. [129]

#### 2.1.1. Liquid phase exfoliation of graphite and other layered materials

The LPE (Figure 2.1) [240] process typically involves three steps: (*1*) dispersion of bulk materials in solvents, (*2*) exfoliation and (*3*) purification. [150]

In the first step, bulk material is dispersed in a solvent. Then the exfoliation of bulk materials in the solvent is realized by ultra-sonication in the second step. During the ultra-sonication process, propagation of cavitons, [202] *e.g.*, the growth and subsequent collapse of bubbles or voids in solvents due to pressure fluctuations, [150] creates hydrodynamic shear-force which acts on bulk materials, inducing exfoliation. [241] After exfoliation, the solvent–2D flakes interaction needs to balance the inter-sheet attractive forces. [150] Solvents ideal to stably disperse 2D flakes are those that minimize the interfacial tension between the liquid and graphene flakes, *e.g.,* the force that minimizes the area of the surfaces in contact). [242] Therefore, the good dispersions of 2D flakes require the solvents having $\gamma$ as close as the surface energy of 2D flakes. [243] For instance, NMP has a $\gamma$ of 41.2 mN $m^{-1}$ [244] close the value of surface energy of graphene (46.7 mN $m^{-1}$). [241] Thus, NMP is the good solvent to disperse graphene. However, the exfoliation process produces a heterogeneous dispersion of thin/thick and small/large 2D flakes. Therefore, the purification step is necessary to separate exfoliated from un-exfoliated flakes, and is usually carried out via ultracentrifugation. [240] In this step, thick flakes can be removed by ultracentrifugation in a uniform medium, so called SBS. [245] The SBS is the most common separation strategy and, to date, flakes ranging from few nanometers to a few microns have been produced, with concentrations up to a few mg $ml^{-1}$. [246]

The SBS is applied generally to particles (in this case flakes) dispersed in a medium (solvent) under a force field. [247] The forces acting on particles dispersed in a solvent during centrifugation are ($i$) the centrifugal force $F_c = m_p\omega^2 r$, proportional to the mass of the particle itself ($m_p$), the distance from the rotational axes (r), and to the square of the angular velocity ($\omega$); ($ii$) the buoyant force $F_b = -m_s\omega^2 r$, *e*.g., the force deriving from the Archimedes' principle that is proportional to the mass of the displaced solvent ($m_s$) times the centrifugal acceleration; and ($iii$) the frictional force $F_f = -fv$, *e.g.*, the force acting on the particles while moving with a sedimentation velocity ($v$) in a fluid. This force is proportional to the friction coefficient ($f$) between the solvent and the particle itself. The sum of the forces acting on the dispersed flakes is represented as: [247]

$$F_c - F_b - F_f = F_{tot} \qquad (2.1)$$

The ratio of sedimentation or sedimentation coefficient ($S$) can be defined as the ratio between the sedimentation velocity and the particle acceleration, *e.g*, the centrifugal acceleration ($\omega^2 r$) in this case:

$$S = \frac{v}{\omega^2 r} = \frac{m_p - (1 - \frac{\rho_s}{\rho_p})}{f} \qquad (2.2)$$

in which $\rho_s$ and $\rho_p$ are the density of the solvent and the particle, respectively. Following equation 2.2, the $S$ increases according to the mass of the 2D flakes, while decreases with their physical dimensions (lateral size and thickness). The un-exfoliated bulk flakes, as well as large and thick ones, have a larger mass than the thin and small flakes, thus $S$ of the un-exfoliated flakes is higher than that of thin and small flakes. By tuning centrifugal force, it is possible to obtain dispersions with flakes of different lateral size and thickness.

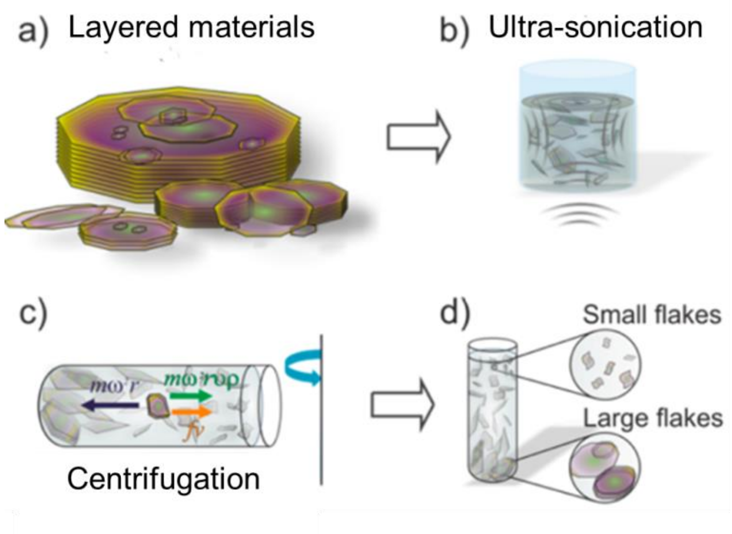


Figure 2.1. *Liquid phase exfoliation of bulk layered materials [240]*

### 2.1.2. Solvent exchange processes

It has been reported that liquids with γ of ~ 40 mN $m^{-1}$, such as NMP, DMF, benzyl benzoate, etc., are the proper solvents for the dispersion of graphene and other 2D flakes, *e.g.*, $MoS_2$, $WS_2$. [150] Among these, NMP has been found to be one of the most effective solvents for the exfoliation of graphene and other 2D materials [150, 248]. However, NMP is not an environmentally friendly solvent, which is a considerable issue in development of 2D layered materials-based LIB technology. [3, 249, 250] Besides, due to the high b.p. ($202^o$ C), [3] the evaporation of NMP after electrode fabrication requires high temperature (> $150^o$ C) [3, 249] and vacuum to avoid the oxidation of active materials. [251] To address these limitations, a solvent exchange process [252] is exploited to eliminated NMP. Moreover, the solvent exchange process allows recycling over 90% of NMP, decreasing production costs, waste disposal and pollution. Besides, the direct exfoliation of bulk 2D materials in an environmental friendly solvent is considered as a promising strategy to produce exfoliated 2D flakes.

### 2.1.3. Experimental

In this thesis, the LPE of graphite in NMP is exploited to firstly produce graphene. A solvent exchange process from NMP to a low b.p. and environmentally friendly solvent such as ethanol (EtOH), is deployed to obtain graphene flakes dispersion. Also, graphene flakes with different lateral size and thickness are sorted by means of SBS.

Concerning $MoO_3$ and $MoS_2$, the exfoliation of bulk $MoO_3$ and $MoS_2$ is directly carried out in 2-propanol (IPA) in order to avoid the use of NMP. Then the SBS process is carried out to eliminate the bulk counter parts from the exfoliated $MoO_3$ and $MoS_2$. More importantly, the LPE of BP is carried out in 14 different solvents in order to serve for the study on the effects of solvent properties on the exfoliation of BP. The productions of four materials are as following:

#### *2.1.3.1. Liquid phase exfoliation of graphite*

1 g of graphite flakes (Sigma-Aldrich) is dispersed in 100 mL of NMP (Sigma-Aldrich) and exfoliated by ultra-sonication in a sonic bath (Branson®5800) for 6 hours. The resulting dispersion is then ultra-centrifuged at 10000 rpm (17100 *g*) (in a Beckman Coulter Optima ™ XE-90 with a SW32Ti rotor) for 30 min at 15 ℃, to remove thick flakes and un-exfoliated graphite. After the ultracentrifugation process, 80% of the supernatant is collected by pipetting, thus delivering a graphene dispersion in NMP. This dispersion is filtered through a Millipore® filter with 0.2 mm pore size by vacuum filtration to obtain the graphitic flakes.

Meanwhile 1 L of EtOH (Sigma-Aldrich, $ 99.8%) is added in batches of 100 mL each to the filtration flask in order to remove the residual NMP in graphitic flakes. Finally, 5 mL of EtOH are used to recover the graphitic flakes from the filter and 10 mins of sonication is then applied to re-disperse the graphitic flakes in EtOH.

#### *2.1.3.2. The sorting of graphene flakes by size and thickness via sedimentation-based separation*

Four batches of 10 g of graphite flakes (Sigma Aldrich) are dispersed in 1 L of NMP (Sigma Aldrich, biotech grade) by ultra-sonication (USC-2600 THD, VWR®) for 6 hours at a frequency of 40 kHz and power of 300W (10 g of graphite are distributed in 20 vials with 0.5 g graphite and 50 ml NMP in each vial). The obtained dispersions are settled for 12 hours, and then 80% of their supernatants are collected by pipetting, followed by an ultracentrifugation step at 2000 rpm (769 *g*) for 30 min using a Sigma 3-16P centrifuge with an 11180 rotor (S3-16P). Afterwards, the precipitate is collected and named as Sample #1. The supernatant is then collected and used for a second round of centrifugation at 4000 rpm (3076 *g*) for 30 mins; the precipitate is collected and named as Sample #2. Next, the supernatant is ultra-centrifuged at 10000 rpm (17100 *g*) for 50 mins using a Beckman Coulter Optima™ XE-90 ultracentrifuge with a SW32Ti rotor for the third round of ultracentrifugation to collect the precipitate and named as Sample #3. With the same rotor, a fourth round of ultracentrifugation is performed at 30000 rpm (153700 *g*), and the precipitated part is named Sample #4. To eliminate the presence of NMP in the 4 samples, we carried out the solvent exchange process, as outlined in the following procedure. Each sample in NMP is dispersed in 100 ml of EtOH (99.8%, Sigma Aldrich), namely in an environmentally friendly solvent having a much lower b.p. than NMP (78 ℃ vs 204.3 ℃), ultra-sonicated for 15 min, and then left to sediment for 72 h. Afterward, the sediments of 4 samples are collected (the supernatant discarded) and stored in EtOH.

#### *2.1.3.3. Liquid phase exfoliation of molybdenum trioxide*

$MoO_3$ powder (240 mg) is added to IPA (80 mL) in a 100 mL open top, flat bottomed beaker. The dispersion is ultra-sonicated using a horn probe sonic tip (VibraCell CVX, 750W, 25% amplitude) for 5 h. The sonic tip is pulsed for 9 sec on and 2 sec off to avoid damage to the processor and reduce any solvent heating. To minimize heating effects, an external cooling system circulated cooled water at 5 ℃ around the beaker during ultra-sonication. To remove any un-exfoliated material the ultra-sonicated dispersion is filled in glass vails (~30 ml) and centrifuged at 1000 rpm (~100 *g*) for 30 mins. The supernatant is decanted (~20 ml) and further centrifuged at 1000 rpm for 105 mins to remove small flakes. The supernatant is decanted (containing small flakes) and discarded while the sediment is re-dispersed in IPA.

#### *2.1.3.4. Liquid phase exfoliation of molybdenum disulfide*

100 mg of $MoS_2$ are dispersed in 10 mL of IPA and ultra-sonicated (USC-2600 THD, VWR®) for 6 h at a frequency of 40 kHz and power of 300W. The obtained dispersion is centrifuged at 4000 rpm (3076 *g*) for 30 mins using a Sigma 3-16P centrifuge with an 11180 rotor (S3-16P), to remove thick and un-exfoliated $MoS_2$ flakes. After the centrifugation process, the upper 80% of the supernatant is collected by pipetting.

#### *2.1.3.4. Liquid phase exfoliation of black phosphorous*

Black Phosphorus (500 mg, from Smart Elements) is pulverized with a mortar and pestle. The selected solvents (*i.e.* acetone, toluene, chloroform, IPA, trichloroethylene, methanol, ethylene glycol, acetonitrile, EtOH, n-hexane, NMP, CHP, DMF and diethyl carbonate) have different $\gamma$, b. p. and/or Hansen solubility parameters (see Table 3.3). All the solvents are of anhydrous grade and were purchased from Sigma Aldrich.

For the analysis of the dispersability and stability of exfoliated BP, 20 mg of pulverised BP and 20 mL of solvents are mixed using a sonic bath (VWR®, USC2600THD) for 6 hours, followed by centrifugation at 900 g for 60 min in order to promote the precipitation of the thicker and un-exfoliated flakes. The precipitation of thick or un-exfoliated flakes promotes the enrichment of BP flakes in dispersion with a specific lateral size and thickness. The centrifugation is carried out in a Sigma 2-16K centrifuge (11170-bucket 2x13299 rotor). After the centrifugation, the supernatant is collected and subjected to another centrifugation run at 900 g for 30 min to further purify the BP dispersions. The pulverization and weighting of the BP crystals and the balancing and sealing of the centrifuge tubes are carried out in a nitrogen-filled glovebox.

For the aging analysis, the samples are stored for three months at room temperature in a closed transparent glass vial. Note that after the LPE process, all the other experimental processes for the material production are conducted outside the glove box.

## 2.2. Preparation of single wall carbon nanotube-bridged molybdenum trioxide and molybdenum disulfide/amorphous carbon hybrids

### 2.2.1. Preparation of single wall carbon nanotube-bridged molybdenum trioxide hybrid

Single wall carbon nanotubes have displayed great potential as anode materials for lithium ion batteries due to their unique 1D structural, high electrical conductivity ($10^6$ S $m^{-1}$). [167, 253] Thus, the combination of SWNTs into the hybrid structure with 2D materials, *e.g.*, $MoO_3$, can improve the electrochemical performance of electrodes. SWNTs play a role as (*i*) a conducting agent, promoting electronic charge transport, [254] (*ii*) an active anode material, offering extra capacity thanks to its $Li^+$ storage capability by surface and/or inside individual nanotubes. [254]

In this thesis, the P3 SWNTs (carbon solution) are dispersed in IPA at a concentration of 0.1 g $L^{-1}$ and sonicated in both a horn sonic probe and a sonic bath to achieve a homogeneous dispersion. The procedure involves horn probe ultra-sonication (30 mins) followed by 1h in a sonic bath and an additional 30 min in the horn probe tip. After that, The as-produced $MoO_3$ (as reported in section **2.1.3.3**), SWNTs and carbon black super-P (CB) dispersions are mixed, without centrifugation, to form hybrid structures of known wt% ($MoO_3$ : SWNTs = 9:1, 8:2 and 7:3, respectively). Accurate weighing of an alumina membrane (pore size 25nm) before and after filtration of $MoO_3$ dispersion allowed determining the concentration.

### 2.2.2. Preparation of molybdenum disulfide/amorphous carbon hybrid

The aim of synthesizing $MoS_2$/C hybrid is to overcome drawbacks of $MoS_2$ for LIB anode, *e.g.,* low conductivity and volume change. The carbon network is expected to improve the electrical conductivity of electrode [168, 169] and buffer the volume change of active materials upon cycling. [168, 169]

In the present work, PAA is used as a carbon source to form carbon network. The exfoliated $MoS_2$ flakes (as reported in section **2.1.3.4**) are mixed with PAA in IPA with various weight ratios of $MoS_2$ : PAA, *e.g.*, 1:1, 1:2 and 1:4 wt%, followed by magnetic stirring for 60 min. Then the mixtures of $MoS_2$ and PAA ($MoS_2$/PAA) are dried at 40° C under vacuum overnight in order to remove the IPA, obtaining the $MoS_2$/PAA powders. These powders are annealed at 500 °C for 30 minutes under argon atmosphere in order to carbonize the PAA. The pyrolysis forms a $MoS_2$/C hybrid. The $MoS_2$/C powders are named as $MoS_2$/C-1, $MoS_2$/C-2, and $MoS_2$/C-3 corresponding to the different weight ratios of $MoS_2$/PAA as 1:1, 1:2 and 1:4 wt%, respectively. These powders are used as active material in the LIB anodes.

## 2.3. Material characterization techniques

### 2.3.1. Optical absorption spectroscopy

The Optical absorption spectroscopy (OAS) is carried out in a Cary Varian 5000UV-vis spectrophotometer. For the OAS measurements, the graphene samples are diluted 1:10 (v/v) in NMP and the $MoO_3$ and $MoS_2$ samples are diluted 1:100 (v/v) in IPA and the SWNTs sample is diluted 1:10 in IPA. The absorption spectra are acquired using a 1 mL quartz glass cuvette. The absorption spectra of the solvents used are subtracted to each spectrum.

### 2.3.2. Thermogravimetric analysis

Thermogravimetric analysis (TGA) (TG-Q500) is carried out in air. The temperature ramp started from room temperature (RT) to 900°C at a heating rate of 10°C $min^{-1}$. 5 mg of each $MoS_2$ and $MoS_2$/carbon composite samples are used for TGA.

### 2.3.3. Powder X-ray diffraction

Powder X-ray diffraction (XRD) measurement is performed on a PANalytical X-ray powder diffractometer with monochromatic $CuK_\alpha$ radiation ($\lambda$ = 1.5418 Å). The 2θ range used in the measurements is from 10 ° to 65 °. Samples ($MoS_2$ and $MoS_2$/carbon $MoS_2$/C hybrid powders) are prepared on quartz substrate.

### 2.3.4. Raman spectroscopy

Raman spectroscopy (Renishaw inVia confocal Raman microscope) is performed with laser excitation wavelength of 514.5, 532, 633 and 785 nm (incident power of ~1 mW on the samples) and a 100 × objective. The graphene samples are dispersed in NMP and EtOH, whereas the SWNTs, $MoO_3$ and $MoS_2$ samples are dispersed IPA and the BP sample are dispersed in CHP and acetone by sonication. All samples are drop-casted on a Si/$SiO_2$ (300 nm $SiO_2$) (Si-Mat Silicon Materials) substrate and dried under vacuum overnight.

### 2.3.5. Transmission electron microscopy

Transmission electron microscopy (TEM) images of samples are acquired with a JOEL JEM-1011 microscope, operated at 100 kV. The high-resolution TEM (HRTEM) and high angular annular dark field - scanning TEM ((HAADF)-STEM)) images are obtained on a JEOL JEM-2200FS microscope, operating at 200 kV, which is equipped with a CEOS objective corrector, and an in-column filter (Ω-type). The energy dispersive X-ray spectroscopy (EDS) and energy filtered (EFTEM) elemental mapping were acquired by a Bruker Quantax 400 system with a 60 $mm^2$ XFlash 6T silicon drift detector (SDD) on the same microscope. The electron energy loss spectroscopy (EELS) data are collected in TEM mode using a FEI Tecnai F20 TEM operating at 200 kV and equipped with Gatan Enfinum SE spectrometer. The EEL spectra are acquired with a collection semi-angle of 100 mrad. The SWNTs, $MoS_2$ and $MoO_3$ samples are dispersed in IPA, graphene samples are dispersed of NMP and EtOH and BP are dispersed of CHP and acetone by sonication. 100 μL of the resulting inks are drop-casted at RT onto carbon coated Cu TEM grids (300 mesh), and subsequently dried under vacuum overnight.

### 2.3.6. Scanning electron microscopy

Scanning electron microscopy (SEM) images of all electrodes are taken using a field-emission scanning electron microscope FE-SEM (Jeol JSM-7500 FA) at the operating voltage of 10 kV without any metal coating, for all samples.

### 2.3.7. Atomic Force Microscopy

Atomic Force Microscopy (AFM) images are acquired with Bruker Innova AFM in tapping mode using silicon probes (f = 300 kHz, k = 40 N/m). Intermittent contact mode AFM images of $5 \times 5$ $\mu m^2$ were collected with 512 data points per line and the working set point was kept above 70% of free oscillation amplitude and measurements were taken at scan rate of 0.7 Hz. Thickness statistic is performed measuring ∼ 100 flakes from AFM images. Statistical analyses are fitted with log-normal distributions. The graphene, $MoS_2$ and BP samples are diluted 1:100 (v/v) in EtOH. 100 μL of the dilutions are drop-cast onto $Si/SiO_2$ wafers.

### 2.3.8. X-ray Photoelectron Spectroscopy

X-ray Photoelectron Spectroscopy (XPS) analysis is carried out for all samples, using a Kratos Axis Ultra spectrometer. The samples are drop-casted onto silicon (Si-Mat Silicon Materials) wafers. The XPS spectra are acquired using a monochromatic Al $K_\alpha$ source operated at 20 mA and 15 kV. The analyses are carried out on a 300 μm × 700 μm area. High-resolution spectra are acquired at pass energy of 10 eV and energy step of 0.1 eV. The photoelectrons are detected at a take-off angle (i.e., the angle defined by the sample surface normal and the position of the detector) $\varphi = 0$ with respect to the surface normal. The pressure in the analysis chamber is maintained below $10^{-6}$ Pa for data acquisition.

### 2.3.9. Specific surface-area measurements

Specific surface-area measurements are carried out by nitrogen physisorption at 77 K in a Quantachrome equipment, model autosorb iQ. The graphene-based anodes deposited onto the Cu support substrates (~1.0 mg) are cut into pieces fitting into the **BET** (Brunauer – Emmett – Teller) measurement chamber. The specific surface area is calculated using the multi-point BET model, considering 11 equally spaced points in the P/P 0 range from 0.05 to 0.30. Prior to measurements, the sample is degassed for 2 hours at 200 ℃ under vacuum to eliminate adsorbates.

### 2.3.10. Optical extinction spectroscopy

The optical extinction spectroscopy (OES) is carried out by a Cary Varian 5000UV-Vis. In order to measure the extinction spectra, FL-BP dispersions in the different solvents are diluted 1:25 with the respective pure solvents. The dispersions in acetone are diluted at different ratios in order to determine the extinction coefficient of FL-BP. The dilutions prepared are: 1:1, 1:2, 1:5, 1:10; 1:20, 1:50 and 1:100. For each sample, the extinction spectra (absorbed plus scattered light) of their corresponding pure solvents are subtracted from the sample spectrum. After the extinction measurement, the samples that are dispersed in acetone are dried and the residue powder is weighted. The initial volume of the solvent and the mass of the dried powder gave the exact concentration for each dilution. The optical extinction coefficient is determined by using the Beer-Lambert law ($E = \alpha C_{Ph} l$, in which E is the optical extinction at 600 nm, $\alpha$ is the extinction coefficient, $C_{Ph}$ is the concentration of the exfoliated BP and $l$ is the path length, 0.01 m).

## 2.4. Electrode fabrication and battery assembling

### 2.4.1. Electrode fabrication

#### *2.4.1.1. Graphene electrodes*

The Cu foil with (Sigma-Aldrich) is cut into round shaped disks with a diameter of 1.5 cm and cleaned with acetone (Sigma-Aldrich) in an ultrasonic bath for 10 minutes. Then, the Cu foils are dried at 80 ℃ and $10^{-3}$ bar for 2 hours in a glass oven (BÜCHI, B-585) and weighted (Mettler Toledo XSE104); the preparation of Cu foils is applied for all electrodes in this thesis. Subsequently, 250 mL of graphene ink in EtOH is drop-cast on Cu foil under air atmosphere at RT and then dried at 120 ℃ and $10^{-3}$ bar for 30 min in an oven (BUCHI, B-585). The graphene mass loading (1 mg) for each anode is calculated by subtracting the weight of bare Cu foil from the total weight of the electrodes**.**

#### *2.4.1.2. $MoO_3$ and $MoO_3$/SWNTs hybrid electrodes*

50 mg of $MoO_3$ flakes (section **2.1.3.3**) and $MoO_3$/SWNTs hybrid (section **2.2.1)** samples are dried and re-dispersed in 5ml EtOH via ultra-sonication for 15 min. Subsequently, the aforementioned samples are drop-cast on the Cu foils as supporting substrates in a circular shape with a diameter of 1.5 cm at 40˚C in air. Then, the as deposited films are dried at 120˚C and $10^{-3}$ bar pressure for 12 hours in oven (BÜCHI, B-585). The mass loading of the active materials are calculated by subtracting the average weight (obtained with balance of Mettler Toledo XSE104) of bare Cu foil with the same area, from the total weight of the electrodes.

### *2.4.1.3. $MoS_2$ and $MoS_2$/amorphous carbon hybrid electrodes*

The $MoS_2$ flakes (see section **2.1.3.4**) or $MoS_2$/C powders (see section **2.2.2**) are mixed with CB and PAA with a weight ratio of 8:1:1 in IPA to form the slurries. The slurries are pasted onto Cu disks with diameter of 1.5 cm. The disks are then dried in an oven (BÜCHI, B-585) at 60 °C and $10^{-3}$ bar pressure for 12 hours. The mass loading of active materials (~1.0 mg) for each anode is calculated by subtracting the weight of bare Cu disks (using an analytical balance of Mettler Toledo XSE104) from the total weight of the electrode. The mass loading of the active materials are calculated by subtracting the average weight (obtained with balance of Mettler Toledo XSE104) of bare Cu foil with the same area, from the total weight of the electrodes.

### *2.4.1.4. Few-layer black phosphorous electrodes*

The round copper disks (99.98% trace metals basis, Sigma-Aldrich) with a diameter of 1.5 cm cleaned with acetone and then dried for 2 hours in a glass vacuum oven (BÜCHI, B-585) at 80˚ C with a $10^{-3}$ bar pressure. The FL-BP dispersions in CHP and acetone are mixed with carbon black (CB, super-P) and Polyvinylidene fluoride (PVdF, Sigma-Aldrich), with a mass ratio of 3:1:1, then drop-cast onto the cleaned copper substrates inside the glove box at room temperature. The resulting FL-BP coated electrodes are subsequently dried in a vacuum oven at 120 ˚C for acetone, and to 180 ˚C for CHP dispersed sample, at a $10^{-3}$ bar pressure for 30 mins. The average mass loading of FL-BP (not including CB or PVdF) that is obtained from both the CHP and acetone dispersions is 0.6 mg $cm^{-2}$ for both samples.

### 2.4.2. Assembling of half- and full-cells

All electrodes are assembled in half-cell configuration to characterize the electrochemical properties of each material. Half-cells are assembled in coin cells (2032, MTI) in an argon filled glove box ($O_2$ and $H_2O$ < 0.1 ppm) at 25 °C, using 1M $LiPF_6$ in a mixed solvent of ethylene carbonate/dimethylcarbonate (EC/DMC, 1:1 volume ratio) (Sigma Aldrich, CAS 21324-40-3) as electrolyte (LP30, BASF), and a glass-fibre as separator (Whatman GF/D). For the half-cell con figuration, the anodes are tested against Li foil) as the counter and reference electrodes (two electrodes system).

In case of binder-free graphene electrode, the full-cell configurations are assembled with the commercial LNMO powder as active material for cathode (NEI Corporation). The cathode composition is 80 wt% of LNMO, 15 wt% of CB (TIMCAL) and 5 wt% Polyvinylidene fluoride (PVdF) (Sigma-Aldrich). The three components, in the form of powders, are mixed with NMP using a ball mill at 250 rpm for 2 hours. To promote a better adhesion between the cathode slurry and the current collector, the roughness of Al foils is increased by an etching procedure in KOH. For this propose, the Al foils are immersed for 1 min in 5 wt% KOH aqueous solution, and afterward washed with distilled water and dried at 60 ℃ for 4 hours. The PVdF/LNMO/CB slurry is deposited, by using a doctor-blade, on KOH-etched Al foils. After the drying process, the electrodes are shaped in a circular form by a cutting procedure followed by a pressing process at ~ 2 MPa for 1 min. Before full-cell assembling, the anode is pre-lithiated by placing the graphitic film in direct contact with a Li foil wet by using the electrolyte solution (LP30) for 30 minutes.

## 2.5. Electrochemical characterizations

### 2.5.1. Cyclic Voltammetry

Cyclic voltammetry (CV) is a useful technique for acquiring qualitative information about electrochemical process occurring within electrode. A typical electrode reaction involves the transfer of charge between an electrode and a species in solution. [255] The CV technique can detect the charge transfer process of electrode reaction through recording the current response in a certain potential range when the fixed voltage scan rate is applied. In CV measurements the current response is plotted as a function of voltage.

The electrochemical reaction of electrode in the case of LIB can be described by CV, as shown in Figure. 2.2. As the voltage is initially swept from $V_1$, the equilibrium at the electrode surface begins to alter and the current begins to flow. The current rises as the voltage is swept further toward to $V_2$ from its initial value equilibrium position ($V_1$) due to the continuous reduction of $Li^+$ in to Li, see equation 1.2, on the electrode surface (lithiation process). [256] Thus more active material is lithiated by the reduction of $Li^+$, resulting in the increase in the flux of $Li^+$ to electrode surface. [255] This leads to the increase in Li concentration at electrode surface. The peak ($i_c$) occurs once the concentration of Li is sufficient on the electrode surface. At this moment the flux of $Li^+$ reduces, reaching the subsequent depletion of $Li^+$ on electrode surface, therefore, the current begins to drop. When the scan is reversed, voltage is swept back from $V_2$ to $V_1$, the reversible electrochemical reactions, *e.g.*, the oxidation of Li into $Li^+$ (de-lithiation), is observed which is evidenced by the peak $i_a$.

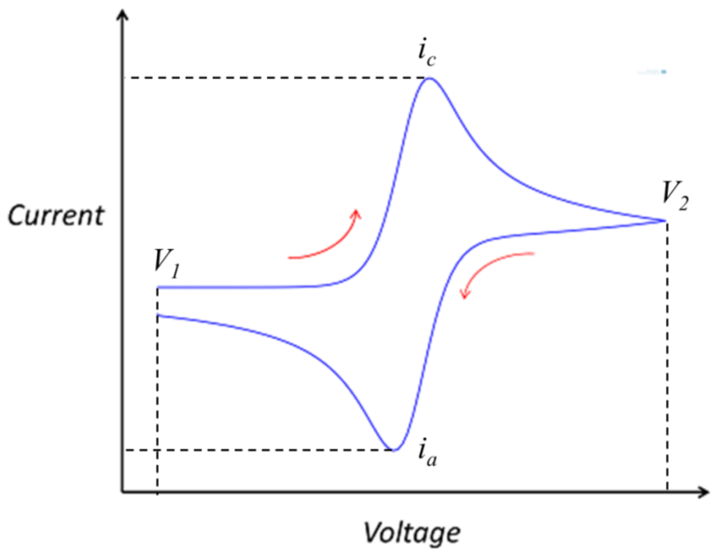


Figure 2.2. *Schematic of cyclic voltammetry of lithium ion battery electrode [257]*

In this thesis, the CV measurement is performed at a scan rate of 50 μVs$^{-1}$ between 3 V and 5 mV vs Li/Li$^{+}$ with a Biologic MPG2 potentiostat/galvanostat for all electrodes in half-cell configurations against Li foils (Sigma-Aldrich) as the counter and reference electrodes (two electrodes system). All electrochemical measurements are performed at room temperature.

### 2.5.2. Galvanostatic charge/discharge cycling measurement

Galvanostatic charge/discharge cycling measurement, so called the constant current method, is considered to be a very useful method to characterize the electrochemical performance of an electrode. It measures the amount of charge stored within an electrode (capacity) under a constant current load over increasing cycle numbers. In order to characterize an electrode of LIB, a current pulse is applied to the electrode and its resulting potential is measured against a reference electrode (Li foil) as a function of time, see Figure 2.3a. In order to calculate the capacity, the duration of a single charge or discharge step has been multiplied by the current applied during that step, see Figure 2.3b. The plot of potential vs. capacity is called *voltage profile*.

In the galvanostatic charge/discharge cycling measurement, the constant current applied to the electrode causes the active materials, *e.g.*, graphite, to be oxidized/ reduced at a constant rate. [255] The electrode potential accordingly varies with time as the concentration ratio of active material, to lithiated-active material, *e.g.*, ratio of C/$LiC_6$) changes at the electrode surface. After the concentration of active material drops to zero at the electrode surface (fully charged), the active material might be insufficiently supplied to the surface to accept all of the electrons being forced by the application of a constant current. The electrode potential will then sharply change to more negative/positive values. The fixed potential range with the cut-off potentials, *e.g.*, $E_1$ and $E_2$, is always set according to the working voltage of electrode to avoid side reactions, see Figure 2.3. When the voltage reaches the $E_2$, the electrode process, *e.g.*, charging/discharging, will stops. Then the new electrode process will start and the voltage will change back to the $E_1$.

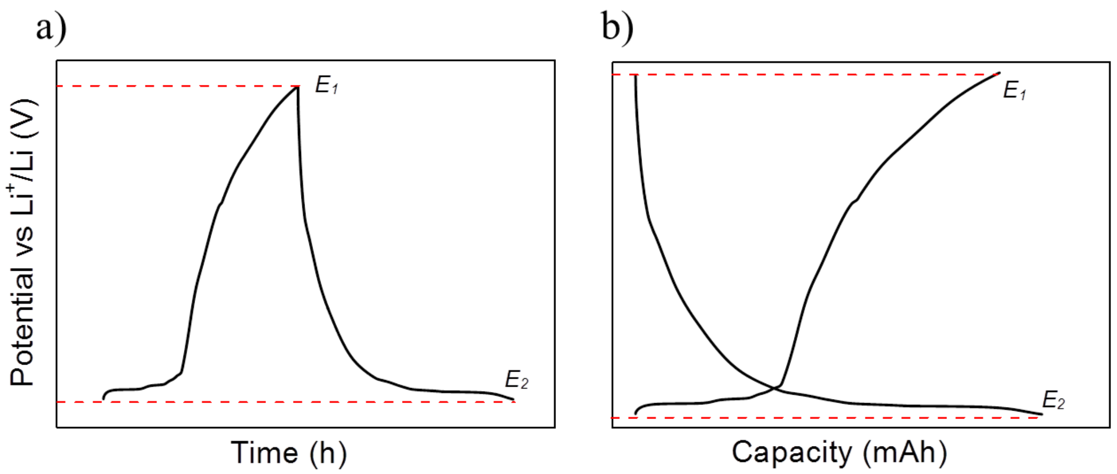


Figure 2.3. *Schematics of galvanostatic charge/discharge curves of lithium ion battery electrode: (a) potential versus time and (b) potential versus capacity plots.*

In this thesis, the galvanostatic charge/discharge cycling tests of all electrodes are performed at a constant current density, using a battery analyser BCS-805 (BioLogic). The charge/discharge cycling tests are performed at different rates (C-rate) by battery analyser BCS-805 (BioLogic). All electrochemical measurements are performed at room temperature.

### 2.5.3. Electrochemical impedance spectroscopy

In electrochemical impedance spectroscopy (EIS), the system under investigation is excited by a small amplitude AC sinusoidal signal of potential or current in a wide range of frequencies and the response of the current or voltage is measured. Since the amplitude of the excitation signal is small enough for the system to be in the (quasi-) equilibrium state, the EIS measurements can be used to effectively evaluate the system properties without significantly disturbing them. Frequency sweeping in a wide range from high-to low-frequency enables the reaction steps with different rate constants, such as mass transport, charge transfer, and chemical reaction, to be separated.

In the EIS measurement, a sinusoidal potential applied to the system leads to a sinusoidal current output at the same frequency which cause the exponential increase in output current with the applied potential. [255] In case an excitation signal with large amplitude is applied, the system is deviated from linearity; the current output to the sinusoidal potential input contains the harmonics of the input frequency. Because the system excitation caused by the time-dependent, the impedance is expressed as [255]

$$Z(t) = \frac{E(t)}{I(t)} = \frac{Z_0 cos(\omega t)}{cos(\omega t - \emptyset)} \qquad (2.3)$$

in which $Z(t)$ is the impedance of the system, $E(t)$ is the applied potential at time t, $Z_0$ is the impedance amplitude, and $\omega$ is the angular frequency that is defined as the number of vibrations per unit time (frequency, Hz) multiplied by $2\pi$. The output current signals $I(t)$ has is shifted in phase by $\emptyset$. By using Euler's relationship, [255] the system impedance is expressed as a complex function of

$$Z(\omega) = Z_0 cos\emptyset + Z_0 jsin\emptyset = Z_{Re} + jZ_{im} \qquad (2.4)$$

When the real part of the impedance ($Z_{Re}$) is plotted on the axis of the abscissa and the imaginary ($Z_{im}$) part is plotted on the axis of the ordinate, a "Nyquist plot" is obtained, [258] see Figure 2.4.

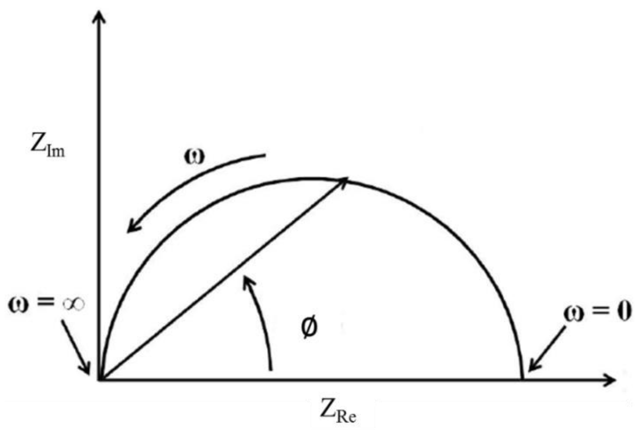


Figure 2.4. *Nyquist plot, representing phase angle (Ø), and angular frequency (ω) dependence of the impedance. [258]*

In the case of LIBs, it can be seen that the electrode composition changes during lithiation/de-lithiation processes due to electrode reactions which is related to $Li^+$ transport process, the electron transport process, and the charge transfer process. [259] Because the time constants of each process are different, the EIS is a suitable technique to investigate these reactions and can allow us to separate most of these processes. Therefore, using EIS to analyze the kinetic parameters related to lithiation/de-lithiation materials such as the SEI film resistance, charge transfer resistance ($R_{CT}$), is essential to understand the reaction mechanism of $Li^+$ with active material, to study degradation effects, to facilitate further electrode optimization, and to improve the charge/discharge cycle performance of LIBs. At present, the common electrode processes, especially for intercalation electrode, in LIBs are represented by several steps, [258] as shown in Figure 2.5: (*i*) $Li^+$ transport in an electrolyte; (*ii*) $Li^+$ migration through the SEI film; (*iii*) electrochemical reaction on the interface of active material particles including electron transfer; (*iv*) $Li^+$ diffusion in the solid phase and (*v*) phase-transfer in cases where several phases are presented in active material and a capacitive behavior that is related to the occupation of $Li^+$, which give a semicircle and straight line perpendicular to $Z_{Re}$ axis in the Nyquist plot (commonly below $10^{-2}$ Hz), respectively.

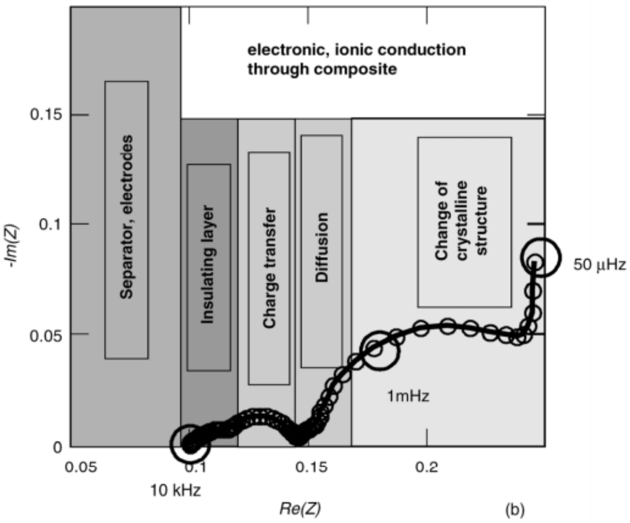


Figure 2.5. *Typical electrochemical impedance spectra of intercalation electrode. [258]*

In this thesis, the EIS of the half-cells (two electrode system) is performed at a bias voltage of 5 mV at room temperature with a VMP3 (BioLogic) in the frequency range of 10 kHz-10 mHz. Galvanostatic charge/discharge cycling tests are performed at a constant current density, using a battery analyser BCS-805 (BioLogic). The charge/discharge cycling tests are performed at different rates (C-rate) by battery analyser BCS-805 (BioLogic). All electrochemical measurements are performed at room temperature.

# Chapter 3:

# Characterizations of graphene and other two-dimensional materials

This chapter provides the detailed characterization of graphene, $MoO_3$, $MoS_2$ flakes, SWNTs, $MoO_3$/SWNTs, $MoS_2$/C hybrids and BP. Different techniques are used in order to probe the physical and chemical properties of the samples. Optical absorption spectroscopy and OES is applied to estimate the concentration of graphene flakes in NMP and concentrations of BP in different solvents, respectively. The morphologies of the samples are characterized by using TEM (flake size), and AFM (thickness of flakes). The structural properties of all samples are revealed by Raman spectroscopy (diameter of SWNTs, thickness of flakes), high resolution-TEM (HRTEM) (inter-spacing of layers), and XRD (phase, orientation and thickness of flakes). In addition, XPS is carried out to assess the surface chemical composition of graphene after the solvent exchange process as well as to determine the oxidation stage of elements (Mo and S) in $MoS_2$ flakes after LPE process. TGA is performed to quantify the content of carbon on the $MoS_2$/C hybrid. To measure the specific surface area of graphene flakes, I exploited BET. The energy dispersive X-ray spectroscopy is carried out to analyse the composition of BP flakes, whereas the EFTEM and EELS is exploited to evaluate the aging of BP flakes after exfoliation. The information obtained from the characterization techniques listed above enables a comprehensive evaluation of the material properties, which provide an insightful understanding of their electrochemical properties for applications in LIBs.

### 3.1. Graphene flakes

#### 3.1.1. Characterizations of graphene flakes in N-Methyl-2-pyrrolidone and ethanol

As mentioned in **chapter 2**, the graphene flakes are produced by LPE of graphite in NMP, followed by the exchange of graphene flakes from NMP to EtOH (section **2.1.3.1**). The graphene flakes in NMP and EtOH are characterized by means of OAS, TEM, Raman spectroscopy and XPS. Figure 3.1 plots the OAS of the graphene-based NMP ink. The absorption peak located at ~275 nm is attributed to inter-band electronic transitions from the unoccupied $\pi^*$ states at the M point of the Brillouin zone. [260, 261] The concentration of the dispersions is determined according to the Beer Lambert law, as shown in equation 3.1: [241, 262]

$$A = \alpha c l \tag{3.1}$$

in which $A$ is the absorbance; $\alpha$ is the optical absorption coefficient (L $g^{-1}m^{-1}$); $c$ is the concentration of the dispersed flakes; $l$ is the path length of the cuvette in which the sample is contained.

Using the experimentally derived absorption coefficient of 1390 L $g^{-1}$ $m^{-1}$ at 660 nm, [202, 241] a concentration of graphitic flakes is estimated to be ~ 0.18 g $L^{-1}$. Besides, the exchange of graphene flakes from NMP into EtOH [263] promotes the precipitation of the graphene flakes due to its low $\gamma$ (22 mN $m^{-1}$) [241] with respect to the surface energy of graphene, [241] resulting in a metastable ink in EtOH. For the estimation of the concentration of the graphitic flakes in the EtOH-based ink, the average mass loading of the graphitic film (1 mg), after solvent evaporation at room temperature, is divided by a known volume (250 μL) of the drop-cast EtOH-based ink onto the Cu foil. Following this procedure, a concentration of graphitic flakes is calculated to be ~ 5.6 g $L^{-1}$ in the EtOH-based ink. The low $\gamma$ of EtOH (22 mN $m^{-1}$) [241] with respect to the surface energy of graphene (46.7 mN $m^{-1}$), [241] promotes the precipitation of the graphene flakes, resulting in a metastable ink in EtOH. The high concentration of the graphitic flakes in the EtOH-based ink enables the fabrication of anodes using a simple one-step process for LIB anode fabrication by directly drop-casting the as-obtained graphitic flakes onto a Cu foil followed by drying at room temperature.

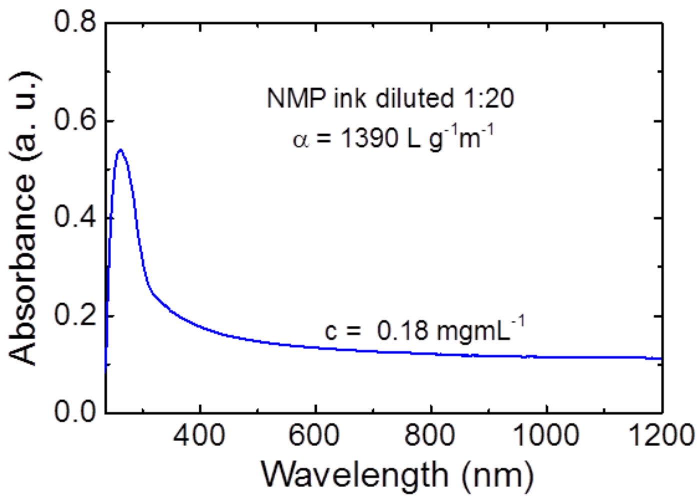


Figure 3.1. *Optical absorption spectra of the graphene ink in NMP.*

The morphological properties of the graphitic flakes dispersed in the NMP-based ink and in the EtOH-based ink are characterized by means of TEM and Raman spectroscopy. Transmission electron microscopy bright field images of the graphitic flakes before (NMP) and after the solvent exchange (EtOH) process are reported in Figure 3.2a and b, respectively. Both samples are formed by graphitic flakes with a lateral size ranging from 100 to 600 nm (see Figure 3.2c and d for statistical analysis). The statistical analysis demonstrates that the solvent exchange process does not induce modification in the lateral size of the graphitic flakes. Electron diffraction patterns, shown in the insets of Figure 3.2a and b, collected on aggregated flakes indicate that the flakes are crystalline in both samples. All the rings are indexed as *h, k, -h -k,* and 0 reflections of a hexagonal lattice with $a$ = 0.244(1) nm, in agreement with the graphite structure. [261]

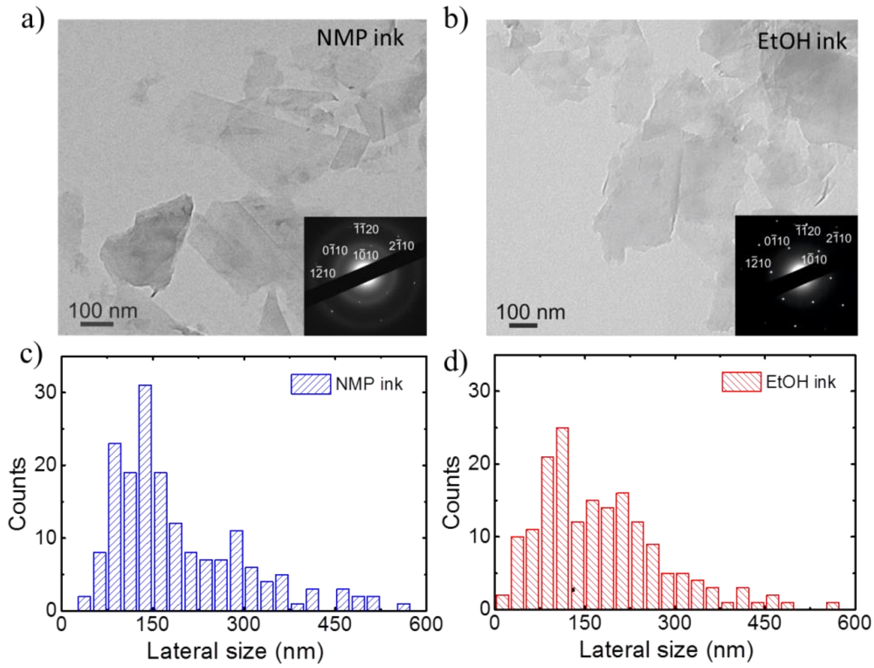


Figure 3.2. *Bright- field TEM image of graphene flakes dispersed from the (a) NMP ink and (b) EtOH ink; the insets show the electron diffraction patterns collected on an area of 2 mm in diameter with the peaks labelled by Miller – Bravais indices. (c) and (d) are lateral size distribution, extracted by statistical analysis on TEM images, of graphitic flakes dispersed in NMP (blue) and after solvent exchange in EtOH (red).*

Raman analysis is carried out in order to gain insight into the number of layers in the flakes and presence of defects. [264, 265] Figure 3.3a plots the typical Raman spectra of the graphite/graphene flakes deposited on Si/$SiO_2$ for both the NMP-based and the EtOH-based inks. In a typical Raman spectrum of graphene, the G peak corresponds to the $E_{2g}$ phonon at the Brillouin zone center; [265] the D peak is due to the breathing modes of the $sp^2$ rings and requires a defect for its activation by double resonance; [266-269] the 2D peak is the second order of the D peak. [266] For pristine graphene, the 2D peak has a single Lorentzian component, whereas it splits (upshifting also in position) for multi-layer graphene (MLG), reflecting the evolution of the band structure. [266, 270, 271] An estimation of the number of layers of the flakes can be derived from a statistical Raman analysis (based on 20 measurements for both NMP- and EtOH-based inks) of the full width at half maximum of the 2D peak (FWHM(2D)), see Figure 3.3b, the average position of the 2D peak (Pos(2D))

(Figure 3.3c) and the I(2D)/I(G) ratio (Figure 3.3d). For more details, the Raman spectra of both NMP and EtOH based-inks show that an average value of FWHM(2D) lower than 70 $cm^{-1}$, Pos(2D) around 2700 $cm^{-1}$ and the I(2D)/I(G) ratio higher than 0.5 (the value for graphite), [266] indicate that both samples are composed of a combination of SLG and FLG flakes. [202, 241, 262, 272] Additionally, the high I(D)/I(G) ratio (Figure 3.3e) is attributed to the edges of sub-micrometer flakes, [267] (see Figure 3.2) rather than to the presence of a large amount of structural defects within the flakes, otherwise the D peak would be much broader, and G and D' would merge in a single band. [265] Indeed, FWHM(G) always increases with defects. [265] As detailed in ref. [119, 273, 274] the lack of a clear correlation between I(D)/I(G) and FWHM(G) in both samples (Figure 3.3e) further supports the absence of structural defects also after the solvent exchange process.

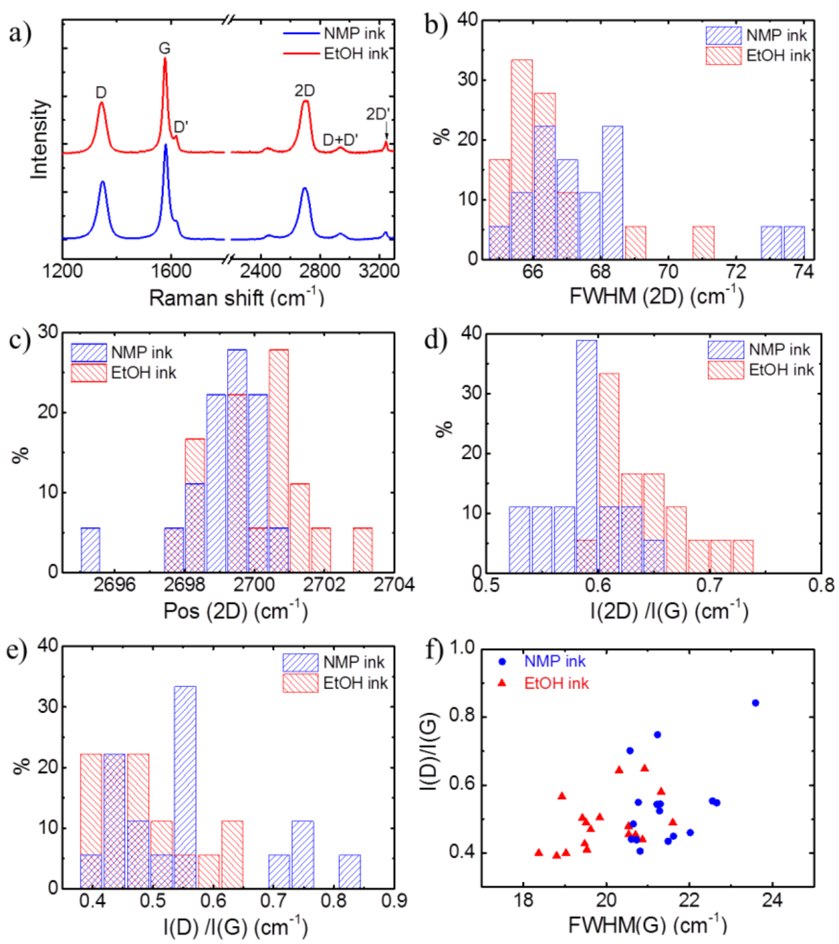


Figure 3.3. *(a) Raman spectra at a 532 nm excitation wavelength for representative flakes in the NMP ink (blue curve) and EtOH ink (red curve). Distribution of (b) FWHM(2D), (c) Pos(2D), (d) I(2D)/ I (G), and (e) I(D)/I(G), and (f) distribution of I(D)/I(G) as a function of FWHM(G), for the NMP ink (blue dashed histograms and dots) and EtOH ink (red dashed histograms and triangles), respectively.*

In order to obtain information about the surface chemistry of the SLG/FLG-based films deposited before and after the solvent exchange process, the NMP and EtOH-based inks are investigated by XPS. The signal of C 1s and N 1s core-levels are focused to obtain information on the chemical state and the atomic bonding of the two elements (Figure 3.4).

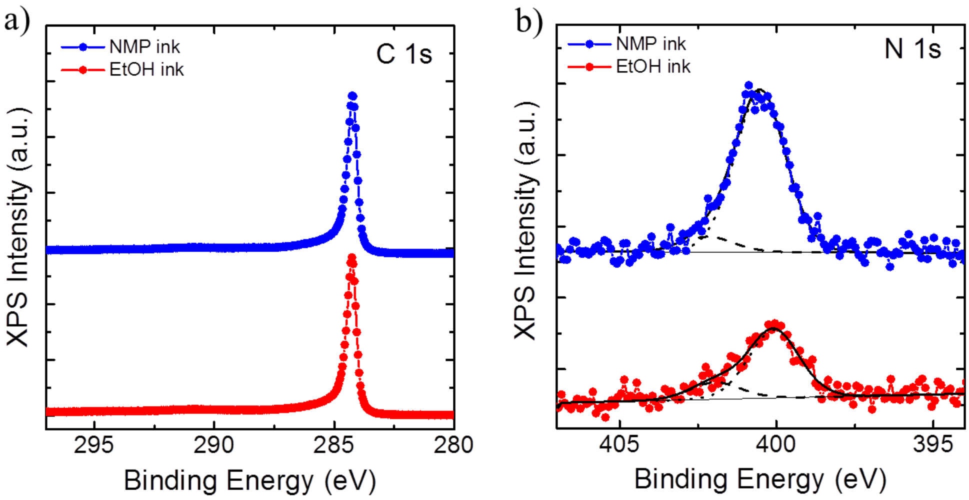


Figure 3.4. *XPS data of the (a) C 1s and (b) N 1s core-levels acquired on graphene films obtained from NMP (blue curve) and EtOH (red curve) inks.*

Indeed, the shape and position of the C 1s peak can provide information on the local environment and oxidation states of graphene, since binding energies are sensitive to the chemical environment. [3] The C 1s profiles collected on the two samples are reported in Figure 3.4a; in both cases, C 1s has an asymmetric shape with the C – C component centred at ~284.3 eV, as typically reported for pristine graphene and graphite flakes. [275] The peak shape and the absence of a C – O component, usually centred at ~286.2 eV, prove that the SLG and FLG flakes have not undergone oxidation during neither the exfoliation nor the solvent exchange process. [241, 276] As shown in Figure 3.4b, the N : C atomic ratio is 0.8 : 100 for the NMP ink, while it decreases to 0.4 : 100 after the solvent exchange process. For both NMP- and EtOH-based inks, the N 1s signal can be fitted with two components (Figure 3.4b). The main component (dotted profiles) is centred at 400.3 $\pm$0.3 eV for both samples and can be assigned to pyrrolic N (*i.e.*, N coordinated as in the pyrrole molecule), [268] consistent with the presence of NMP molecules, [270, 277] likely trapped between the SLG and FLG flakes. [241] The pyrrolic N component accounts for ~ 90% and ~ 80% of the total N content of the SLG and FLG flakes in the NMP-based ink and in the EtOH-based ink, respectively. The second, minor component (dashed profiles) is centred at 402.2 $\pm$ 0.3 eV, close to the position of the N peak observed in the related system of trimethylamine when adsorbed onto an electron acceptor substrate. [278] Therefore, this component is assigned to the N of the

NMP molecules adsorbed onto the SLG and FLG flakes. [279] In summary, the XPS analysis indicates that from one hand the solvent exchange process does not induce oxidation of the SLG and FLG flakes and from the other hand, it allows the removal of 50% of the NMP molecules adsorbed onto the SLG and FLG flakes, see Figure 3.4b. Such a small amount of residual NMP (less than 3.2 wt%, calculated from the N : C atomic ratio) demonstrates the feasibility of the proposed solvent exchange process for the NMP removal.

Briefly, the characterizations of graphene flakes in NMP and EtOH confirms that the solvent exchange process does not affect to the physical and chemical properties of the exfoliated flakes. Importantly, the Raman results indicate that both samples are composed of SLG and FLG flakes without defects on the basal planes. The high crystallinity of LPE graphene flakes is the key feature for assuring fast electron transport within LIB electrode.

### 3.1.2. Characterizations of graphene flakes having different lateral size and thickness

The graphene flakes dispersion is firstly prepared via LPE of graphite in NMP, which contains a heterogeneous distribution of thin/thick and small/large lateral size graphitic flakes. [159, 280] A set of FLG and MLG flakes is obtained by means of SBS in centrifugal field, which are then used to prepare binder-free anodes. As reported in section **2.1.3.2**, the obtained graphene flakes dispersions in NMP are ultra-centrifuged with different centrifugal speed, *e.g.,* 2000 rpm (769 *g*), 4000 rpm (3076 *g*), 10000 rpm (17100 *g*) and 30000 rpm (153700 *g*) corresponding Sample #1, #2, #3, and #4, respectively. Taking the advantage of the solvent exchange process, the NMP solvent in the four samples are exchanged by EtOH resulting in the four EtOH-based dispersions. The four NMP-based dispersions are firstly characterized by OAS to estimate the concentrations of the four samples before the exchange solvent process. As mentioned in section **3.1.1**, the solvent exchange process does not affect to the physical and chemical properties of graphene flakes, so the four EtOH-based dispersions are characterized by TEM, AFM, XPS and Raman spectroscopy to observe the change in dimension of the graphene flakes according to the different centrifugal speeds. Figure 3.5 plots the OAS of the four NMP-based dispersions. The UV absorption peak located at ~268 nm is attributed to inter-band electronic transitions from the unoccupied $\pi^*$ states at the M point of the Brillouin zone. [262] The concentration of the four dispersions in NMP are determined by OAS, using the experimentally derived absorption coefficient of 1390 L $g^{-1}m^{-1}$ at 660 nm (considering that the scattering is negligible). [202, 241, 262] From Figure 3.5, the concentrations of the dispersions in Sample #1, #2, #3 and #4 in NMP are calculated to be 4.0, 2.4, 1.1 and 0.1 g $L^{-1}$, respectively. [241] The concentrations of the four dispersions decrease with the increase in centrifugal speed used for the preparation of the four samples.

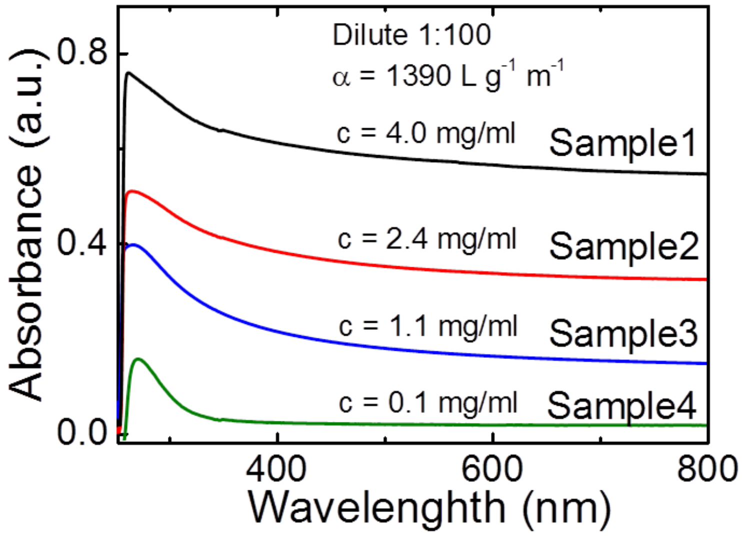


Figure 3.5. *Room temperature optical absorption spectra of the FLG and MLG graphene dispersions. For the measurements the samples are diluted 1:100 with NMP.*

The morphology of the samples is characterized by TEM and AFM analyses. The TEM images in Figure 3.6a and b show that the lateral size mode of the graphitic flakes decreases with the increase of the centrifugal force, passing from 380 nm to 75 nm, see Table 3.1. The XPS data of O 1s peaks and C 1s peaks is shown in Figure 3.7, giving surface chemical information for the FLG and MLG samples. As the flakes get smaller and thinner from

Table 3.1. *Analysis of the four samples prepared at different ultracentrifugation speeds*

| | Centrifuge speed (rpm) | Average lateral size (nm) | Average thickness (nm) | Surface area ($m^2\ g^{-1}$) | O/C ratio |
|---|---|---|---|---|---|
| **Sample#1** | 2000 | 380 | 20 | 114 ± 11 | 0.045 |
| **Sample#2** | 4000 | 180 | 10 | 236 ± 24 | 0.059 |
| **Sample#3** | 10000 | 120 | 5 | 317 ± 32 | 0.085 |
| **Sample#4** | 30000 | 75 | 2 | 414 ± 41 | 0.110 |

The AFM results shown in Figure 3.6c and d, demonstrate that both Sample#3 and #4 have narrower thickness distributions with respect to sample#1 and #2, *e.g.*, centered at 5 nm and 2 nm, respectively, (see Table 3.1). Accordingly, Sample#1 and #2 are mostly constituted by thick (20–50 layers) MLG flakes, while Sample#3 is composed of thinner MLG (10–15 layers) and Sample#4 comprised of FLG flakes. As also presented in Table 3.1, the surface area (SA) data obtained from BET measurement clearly demonstrate an increment of their values (SA from 114 ± 11 to 414 ± 41 $m^2$ $g^{-1}$) passing from Sample#1 to Sample#4, respectively.

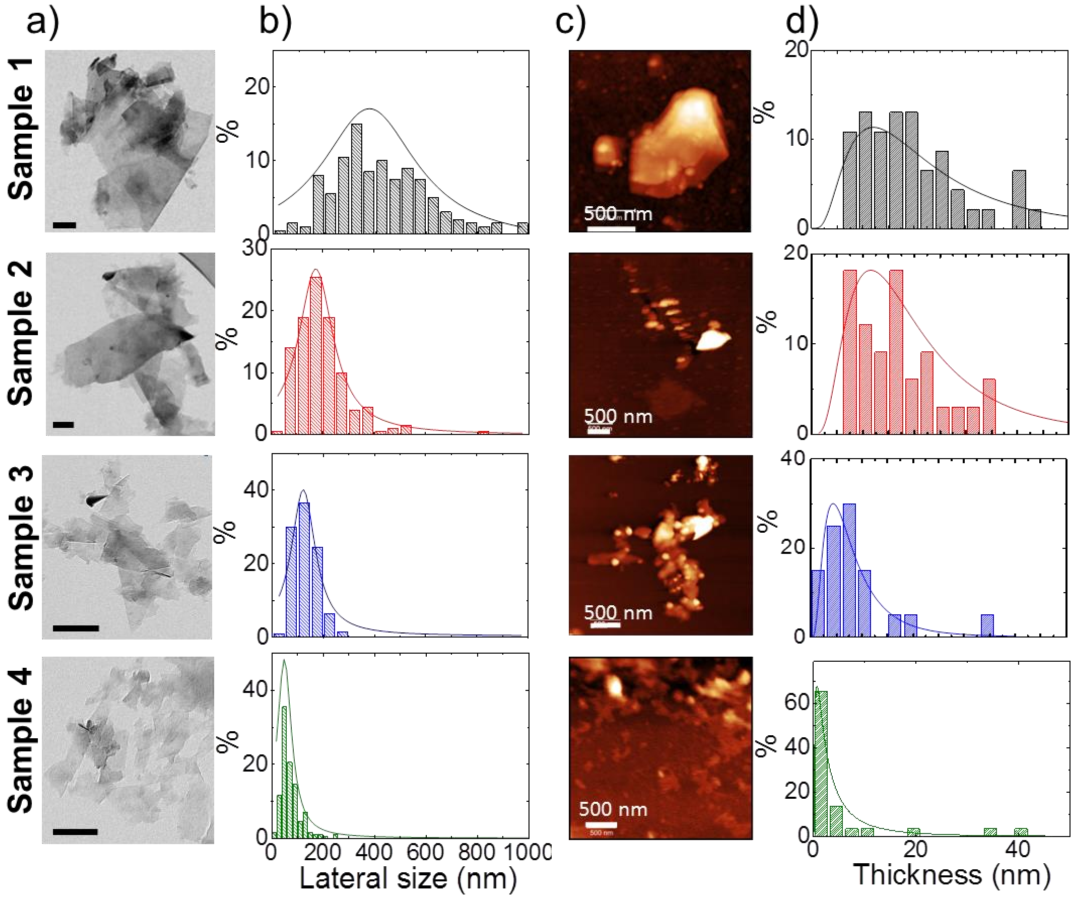


Figure 3.6. *Morphological analysis of the four samples, (a) Representative TEM images and (b) lateral size distribution of graphene flakes (black, Sample #1), (red, Sample #2), (blue, Sample #3), (green, Sample #4) showing a decreasing average distribution with maxima at 380 nm, 180 nm, 120 nm and 75 nm, respectively. The TEM scale bars are 100 nm. (c) Representative AFM images and (d) thickness distribution of the four as-produced samples.*

Sample #1 to Sample #4, the intensity of the oxygen peak on the O 1s region is increasing. The increase of oxygen presence in the smaller/thinner samples (Sample #3 and Sample #4), with respect to the larger/thicker ones (Sample #1 and Sample #2) is linked with the morphology of the flakes: Sample #3 and Sample #4 having more edges than Sample #1 and Sample #2 have consequently more active sites for the O attachment. The position of the XPS O 1s peak is at 532.1±0.2 eV, assigned to C-O moieties, in agreement with data reported in NIST XPS database (version 4.1). [281] Concerning the C 1s region, the four samples show similar C profile, characterized by an intense asymmetric peak centered at 284.5±0.2 eV. [3] It is worth to notice that C 1s profiles of the four samples differ in the 285~287 eV region, see inset in Figure 3.7b. In this region, the contribution of C-O moieties is expected (usually reported at 286.2 ± 0.2 eV). [282] In agreement with the O 1s results, the C signal in this region is increasing from Sample #1 to Sample #4. The O/C ratio is calculated from XPS analysis, demonstrating that the increase in dimension of graphene flakes results in the increase in O/C ratio, see Table 3.1.

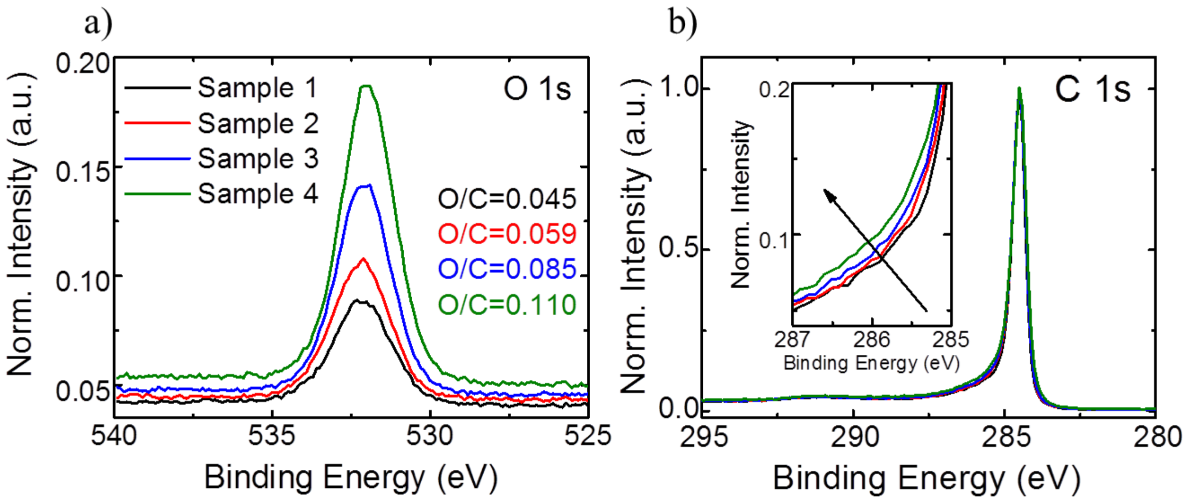


Figure 3.7. *XPS spectra of the four samples deposited onto a Cu substrate after normalization of the carbon signal. (a) O 1s peaks and (b) C 1s peaks. Inset: close up of the 285-287 eV range.*

The comparison of the Raman spectra of the as-prepared samples with that of graphite (Figure 3.8a) illustrates the evolution of the G, D and 2D peaks. There is an increase of both D and D' peaks intensity when passing from Sample #1 to Sample #4, which could be explained assuming an increase of defects, coupled with the reduction of FWHM(2D). The reduction of FWHM(2D) in turn indicates a decrease in the thickness of the flakes, [283] namely in the reduction of the number of layers of the initial graphite flakes. To corroborate these data, a statistical analysis is carried out. Figure 3.8b shows that the FWHM(2D) varies from 71 to 89 $cm^{-1}$ (Sample #1), 65 to 80 $cm^{-1}$ (Sample #2), 65 to 78 $cm^{-1}$ (Sample #3) and 65 to 75 $cm^{-1}$ (Sample #4), demonstrating the thickness reduction with the increase in centrifugal force.

The distribution between the I(2D)/I(G) is reported in Figure 3.8c, with integral intensity ratios, which range from 0.53-0.59 for Sample #1, 0.55-0.62 for Sample #2, 0.59-0.65 for Sample #3 and 0.63-0.77 for Sample #4. The progressive increase of the ratios, combined with the narrowing of FWHM(2D), suggests that the thickness of the flakes effectively decreases with the increase of the centrifugal force. The statistical analysis shows that Samples #1, #2 and #3 are composed by MLG, while Sample #4 mostly contains FLG flakes, in agreement with AFM data reported in Figure 3.5c-d. Besides, the analysis of I(D)/I(G) as a function of FWHM(G), and Disp(G), shown in Figure 3.8d and Figure 3.9, respectively, allows to discriminate between disorder localized at the edges and disorder in the bulk. [265]

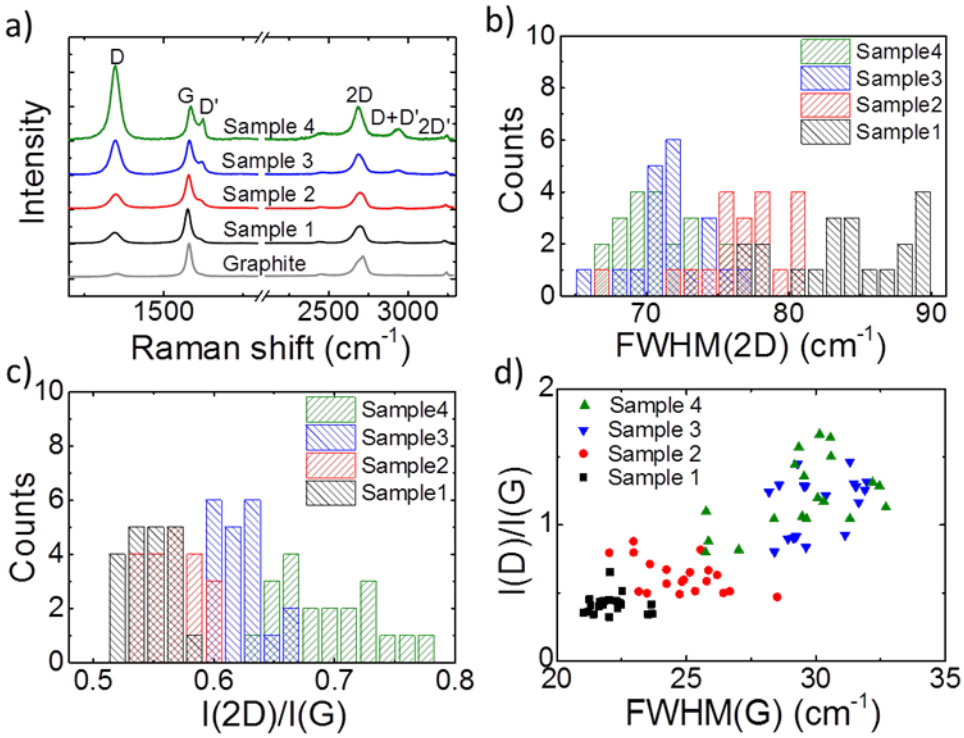


Figure 3.8. *Representative Raman spectra excited at 532 nm excitation wavelength for (a) the four graphene-based samples. Statistical distribution of (b) FWHM(2D), (c) I(2D)/I(G) and (d) I(D)/I(G) vs. FWHM(G) are also shown.*

In the latter case, a higher I(D)/I(G) would correspond to higher FWHM(G) and dispersion of the G peak (Disp(G)). Figure 3.8d and Figure 3.9 show that I(D)/I(G) is not correlated with both FWHM(G) and Disp(G). Moreover, the Disp(G) values (Figure 3.9) for all the samples are lower than 0.1 cm$^{-1}$ nm$^{-1}$, *e.g.*, the value expected for disordered carbons. [265] This is a proof that there is no in-plane defect caused during the exfoliation treatment, and the major contribution to the D peak comes from the sample edges, confirming that the LPE procedure does not introduce defects on the basal plane of the flakes.

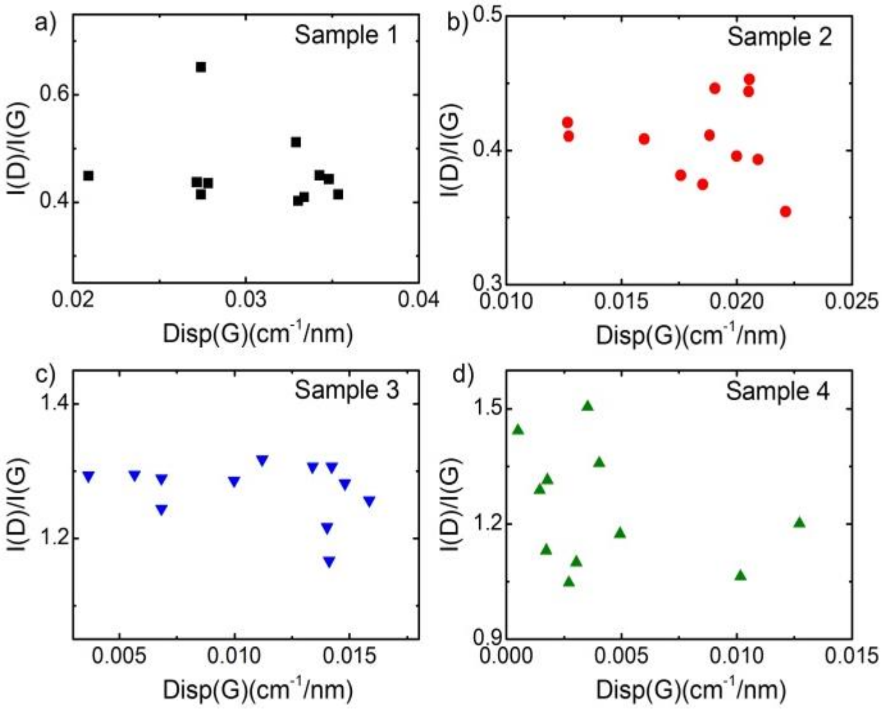


Figure 3.9. *I(D)/I(G) as a function of Disp(G). (a) Sample #1, (b) Sample #2, (c) Sample #3 and (d) Sample #4.*

In summary, the characterizations of the four samples confirm the efficient SBS process to sort defect-free graphene flakes by lateral size (from 380 to 75 nm) and thickness (from MLG to 2 nm FLG). The obtained results are essential for the further explanations of the electrochemical behaviors of graphene anodes based on FLG and MLG flakes, which will be reported in **chapter 4**.

### 3.2. Single wall carbon nanotubes

The dispersion of SWNTs in IPA is firstly characterize by optical absorption spectroscopy to point out various properties of SWNTs dispersions such as transition energies, [284, 285] bundling, [286] and concentration. [287] The OAS measurements of SWNT samples are carried out in the 400-1300 nm range. This range is sufficient to cover the second and third excitonic transitions of semiconducting SWNTs (s-SWNTs), i.e., $eh_{22}$ and $eh_{33}$, respectively, and the first of the metallic SWNTs (m-SWNTs), *i.e.*, $M_{11}$. [288, 289] The assignment of the optical transitions is based on the empirical Kataura plot. [290] This gives values of optical transition frequencies versus chirality for SWNTs in IPA dispersions, and is more appropriate than Kataura plots theoretically derived from tight binding and other models. [291] The OAS of SWNTs (Figure 3.10a) shows the $M_{11}$, the $eh_{22}$ and $eh_{33}$ regions.

Raman spectroscopy can be used to probe SWNTs structure within dispersions, see Figure 3.10b. In the low frequency region, the Radial Breathing Modes (RBMs) are observed. [292]

Their position, Pos(*RBM*), is inversely related to the SWNTs diameter, *d*, [293-295] as given by Equation 3.2:

$$Pos(RBM) = \frac{C_1}{d} + C_2 \qquad (3.2)$$

Combining *Pos(RBM)*, with excitation wavelength and the Kataura plot, [288] it is, in principle, possible to derive the SWNTs chirality. [296, 297]

Matching the diameter with excitation wavelength in the Kataura plot also gives information on the semiconducting or metallic character. A variety of $C_1$ and $C_2$ have been proposed for this relation. [285, 286, 288, 297] Here, we use the $C_1$=214.4 $cm^{-1}$ nm and $C_2$=18.7 $cm^{-1}$, from Ref. [298]. These were derived by plotting the resonance energy as a function of inverse RBM frequency without additional assumptions. The results are validated by using the parameters proposed in Refs. [284, 287, 299]

Raman spectroscopy also probes possible damage via the *D* peak. [283] The latter is due to the breathing modes of $sp^2$ rings and requires a defect for its activation by double resonance. [266, 300] The typical Raman spectrum of SWNTs in the 1500-1600 $cm^{-1}$ region consists of the $G^+$ and $G^-$ bands. In s-SWNTs, they originate from the longitudinal (LO) and tangential (TO) modes, respectively, derived from the splitting of the $E_{2g}$ phonon of graphene at the Brillouin zone centre. [265, 301] The positions of the $G^+$ and $G^-$ peaks, Pos($G^+$), Pos($G^-$), are diameter dependent and their separation increases with decreasing diameter. [302, 303] In m-SWNTs, the assignment of the $G^+$ and $G^-$ bands is the opposite, and the FWHM of the $G^-$ peak, FWHM($G^-$), is larger and Pos($G^-$) down-shifted with respect to the semiconducting counterpart. [292, 304] Thus, a wide, low frequency $G^-$ is a fingerprint of m-SWNTs. The absence of such a feature does not necessarily imply that only s-SWNTs are present, but could signify that m-SWNTs are off-resonance.

Doping could also modify positions and FWHMs. [305, 306] In m-SWNTs, a Pos($G^-$) blue-shift, accompanied by a FWHM($G^-$) decrease is observed with electron or hole doping. [271, 307] In s-SWNTs, doping upshifts Pos($G^+$), but does not affect FWHM($G^+$). [290, 295] Thus, a large number of excitation wavelengths are necessary for a complete characterization of SWNTs. [262, 305] Nevertheless; useful information can be derived even with few excitation wavelengths.

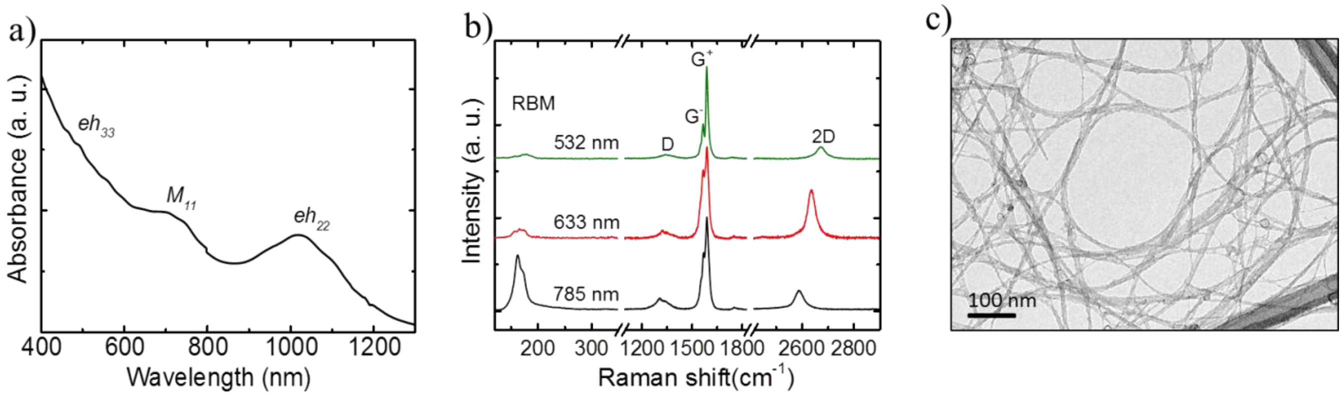


Figure 3.10. *(a) Absorption spectrum of SWNTs. The labels $eh_{22}$, $eh_{33}$ and $M_{11}$ refer to the second and third semiconducting and the first metallic excitonic transition. The spectra are normalized for a clear visualization. (b) Raman spectrum of pristine SWNTs. (c) Bright-field TEM images of pristine SWNTs.*

The Raman spectra of the SWNTs in the RBM region reported in Figure 3.10b show a distribution in the 100–200 $cm^{-1}$ range. This RBM range corresponds to SWNTs with ~1.37–1.45nm diameter. The Raman spectra in the D and G region of SWNTs, show a weak D band (*i.e.*, $I(D)/I(G)$~ 0.05), indicating a low number of defects, which could be linked with residual amorphous carbon from the synthesis process. [289, 291, 308]

The morphology of SWNTs is analysed by TEM. As shown in Figure 3.10c, from the TEM image of pristine SWNTs sample, it is possible to see the SWNTs aggregated in bundles, having a length exceeding the micrometre.

The characterizations of SWNTs provide the fundamental understanding about their physical properties, *e.g.*, diameters, defects and types of SWNTs (metallic or semiconducting) so that we can apply SWNTs for the proper applications. In this thesis, the SWNTs are used not only to improve the electrical conductivity of $MoO_3$/SWNTs electrode but also to buffer the volume change of $MoO_3$ flakes during lithiation and de-lithiation. The detail information of $MoO_3$/SWNTs electrodes will be provided in section **3.3**.

## 3.3. Molybdenum trioxide nanosheets and single wall carbon nanotube-bridged molybdenum oxide hybrid

The synthesis of the $MoO_3$/SWNTs hybrids for LIB anode starts with the solution processing of the two materials. The $MoO_3$ flakes obtained by LPE of bulk $MoO_3$, see section **2.1.3.3**, are characterized by TEM and Raman spectroscopy. The as-produced $MoO_3$ and SWNTs dispersions are then mixed to form hybrid structures of known weight percentage. The morphology of as-prepared $MoO_3$/SWNTs hybrid is characterized by TEM.

The structural properties of $MoO_3$ flakes are further carried out by Raman spectroscopy. As shown in Figure 3.11a, the Raman spectrum shows all typical peaks of $MoO_3$ in the 100-1200 $cm^{-1}$ range. The peak at 995 $cm^{-1}$ is attributed to terminal oxygen stretching mode (Mo=O) which results from unshared oxygen, [309] whereas the peak at 818 $cm^{-1}$ is assigned to the intermediate bridging O–Mo–O bonds, [310] which results from corner-shared oxygens in common to two $MoO_6$ octahedral. This peak shows a shift of 7 $cm^{-1}$ with respect to other $MoO_3$ reports. [311, 312] This shift is attributed to the coordination of oxygen atoms with other atoms *e.g.*, hydrogen. [210, 310]

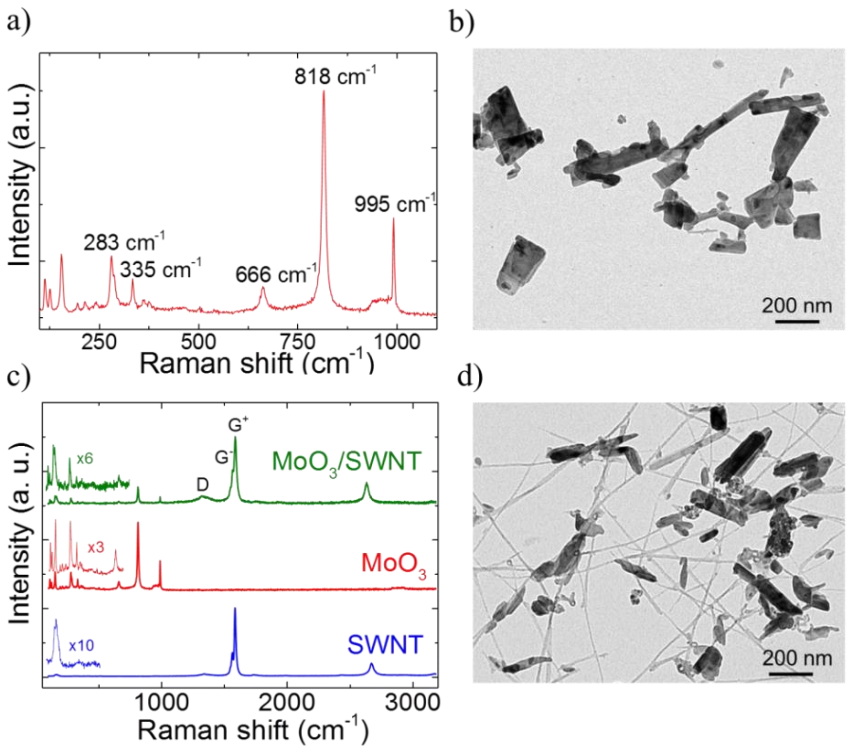


Figure 3.11. *(a) Raman spectrum of $MoO_3$, (b) Bright-field TEM image of $MoO_3$ flakes dispersed in IPA, (c) Raman spectrum of SWNTs, $MoO_3$ flakes and $MoO_3$/SWNTs hybrid and (d) Bright-field TEM image of $MoO_3$/SWNTs hybrid dispersed in IPA.*

The peak at 666 $cm^{-1}$ is assigned to $Mo_3$–O stretching mode caused by edge-shared oxygen atoms. [310, 313] The peaks located in the 200 - 400 $cm^{-1}$ range are attributed to the bending modes of $MoO_3$. [4] In particular, the peaks at 375 and 365 $cm^{-1}$ are scissor modes of O–Mo–O, the peak at 335 $cm^{-1}$ is a bending mode of O–Mo–O, and the 283 $cm^{-1}$ and 244 $cm^{-1}$ peaks are due to the wagging and twisting modes of O=Mo=O, respectively. [310-313] Finally, the peak at 156 $cm^{-1}$ is due to the translation of the ridged chains along the z axis. [314] The morphology of the as-produced $MoO_3$ are analyzed by TEM. Figure 3.11b shows $MoO_3$ flakes with lateral sizes ranging from 50 to 300 nm. The Raman spectra of $MoO_3$, SWNTs and $MoO_3$/SWNTs samples are shown in Figure 3.11c. The spectra are normalized to the signal of $G^+$ peak of the SWNTs. The spectrum of $MoO_3$/SWNTs sample shows the intensities of Raman peaks of $MoO_3$ in the region of 200-1000 $cm^{-1}$ decrease with respect to the $G^+$ peak of the SWNTs due to their high Raman cross section. [315-317] The TEM image of hybrid $MoO_3$/SWNTs sample (see Figure 3.11d), clearly shows the bundles of SWNTs acting as bridges to connect isolated $MoO_3$ flakes, forming an interconnected network in the mixture material of $MoO_3$/SWNTs. This structure is expected to bring the benefits of SWNTs to improve the electrical conductivity of electrode and prevent the volume change of $MoO_3$.

In short, the brief characterizations of morphology properties of $MoO_3$ flakes and $MoO_3$/SWNTs hybrid have shown the promising role of SWNTs in the hybrid structure. The network formed by SWNTs is expected to improve the electrical conductivity of electrode as well as to prevent the volume change of $MoO_3$ flakes. Also, the LPE of bulk $MoO_3$ is able to produce the $MoO_3$ flakes with lateral size ranging from 50-300 nm, bringing the benefit of nanostructure for LIB anode (as mentioned in section **1.3**).

### 3.4. Molybdenum disulfide flakes and molybdenum disulfide/amorphous carbon hybrids

#### 3.4.1. Molybdenum disulfide flakes

Similar to LPE graphene, NMP is found to be one of the most effective solvents for LPE of $MoS_2$, [150, 248]. However, as mentioned in section **2.1.2**, NMP shows issues related to environment and electrode fabrication, which can limit the development of LIB technology. In the case of $MoS_2$, the exfoliation of bulk $MoS_2$ in NMP results in the presence of superficial oxidized Mo species because the self-oxidation of NMP creates the formation of hydro peroxides, which oxidize $MoS_2$. [239] These oxidized Mo species can change the composition of electrode materials, leading to side electrochemical reactions during the cycling of battery. To address these limitations and implement $MoS_2$ flakes in the fabrication of LIB anode, the LPE of bulk $MoS_2$ is carried out in an environmentally friendly and low-b.p. solvent, *e.g.,* IPA, see section **2.1.3.4**.

The TEM images (Figure 3.12a) and the statistical analysis of the size distribution (the inset in Figure 3.12a) indicate that the exfoliated $MoS_2$ has lateral size mode of ~ 90 nm. The HR-TEM (Figure 3.12b) reveals the presence of few-layer $MoS_2$ flakes. The thickness of exfoliated $MoS_2$ flakes is characterized by AFM, see Figure 3.12b and c. The thickness distribution of $MoS_2$ flakes exfoliated in IPA peak at 3 nm, corresponding to ~ 4 stacked $MoS_2$ layers, see Figure 3.12c. To probe the structural property of exfoliated $MoS_2$, Raman spectroscopy is carried out on bulk and exfoliated $MoS_2$. Figure 3.12e shows the Raman spectra of bulk $MoS_2$, the two dominant peaks centered at ~ 379 $cm^{-1}$ and 405 $cm^{-1}$, corresponding to the $E^1_{2g}$ (in-plane vibration of Mo-S bonds) and $A_{1g}$ (out-plane vibration of

Mo-S bonds) modes, respectively. [318, 319] For the exfoliated $MoS_2$, the $E^1_{2g}$ and $A_{1g}$ modes appear at ~ 382 $cm^{-1}$ and 407 $cm^{-1}$, respectively. The Raman shift differences between these two peaks are 26 and 25 $cm^{-1}$ for bulk $MoS_2$ and exfoliated samples, respectively. [319-321] The decrease in $MoS_2$ layers is associated to the red-shift of the $A_{1g}$ peaks because the van der Waals force between two $MoS_2$ layers facilitate the atom vibration. The $E^1_{2g}$ peak exhibits blue-shift due to the long-range coulombic interlayer interactions. Therefore, Raman shift difference between $E^1_{2g}$ and $A_{1g}$ peaks in the case of $MoS_2$ (25 $cm^{-1}$) is lower than that of bulk $MoS_2$, suggesting the decrease in number of $MoS_2$ layers. [318, 319] Interestingly, the $E^1_{2g}$ and $A_{1g}$ peaks blue-shifts with respect to the bulk $MoS_2$. This observation is similar to the cases of chemical-assisted exfoliation of $MoS_2$, which is attributed to the adsorption of surfactants, intercalation agents or solvent molecules on the surface of $MoS_2$ flakes. [322-324] The crystalline structures of bulk $MoS_2$ and the exfoliated $MoS_2$ are also studied by XRD analysis (Figure 3.12f). The diffraction patterns of the bulk $MoS_2$ and exfoliated $MoS_2$ show strong, sharp peaks at $2\theta = 14.4^o$, $32.7^o$, $39.6^o$, $44.2^o$, $49.8^o$, $58.4^o$, $60.4^o$, which correspond to the (002), (100), (103), (006), (105), (110) and (008) planes of the hexagonal $MoS_2$ phase, respectively (JCPDS 37–1492). [163, 325] In particular, the distinct diffraction peak (002) at $2\theta = 14.4^o$ is characteristic of the ordered stacking of S-Mo-S layers, so the change in intensity of this peak can be associated with the thickness of $MoS_2$. [218, 326] However, the exfoliation of bulk $MoS_2$ does not affect the intensity of various peaks of $MoS_2$ flakes, *e.g*, (100), (103), (105), (110) planes, which are not orientated along the c-axis. Thus, the change in intensity of (002) can be evaluated by calculating the intensity ratio of (002) and (100) diffraction peaks ($I_{(002)}/I_{(100)}$). [218, 327] The XRD patterns of both materials are normalized according to the (002) diffraction peak for the realization of the change in intensity of (002) diffraction peak of exfoliated $MoS_2$ flakes with respect to bulk $MoS_2$. The $I_{(002)}/I_{(100)}$ ratios are calculated to be 4.94 and 2.08 for bulk $MoS_2$ and exfoliated $MoS_2$, respectively. It confirms the decrease in the crystallite size in the z direction (thickness). [172, 328, 329] Moreover, the size of crystallites is inversely proportional to the FWHM of the diffraction peaks according to Scherrer equation, see equation 3.3. [215, 221] The FWHM of (002) diffraction peak of exfoliated $MoS_2$ ($0.44^o$) is wider than that of bulk $MoS_2$ ($0.30^o$), suggesting that thickness of $MoS_2$ flakes are decreased after the LPE process. [218, 221, 329] These indications from XRD patterns are in agreement with the TEM, HR-TEM, AFM and Raman analysis (Figure 3.12a, b, c and d), confirming the LPE process provides smaller and thinner $MoS_2$ flakes with respect to its bulk counterpart.

$$\tau = \frac{K\,\lambda}{\beta\, cos\theta} \tag{3.3}$$

where $\tau$ is the mean size of the crystallites, $K$ is the dimensionless shape factor (0.9), $\lambda$ is the X-ray wavelength; $\beta$ is the line broadening at FWHM and $\theta$ is the Bragg angle (in degrees).

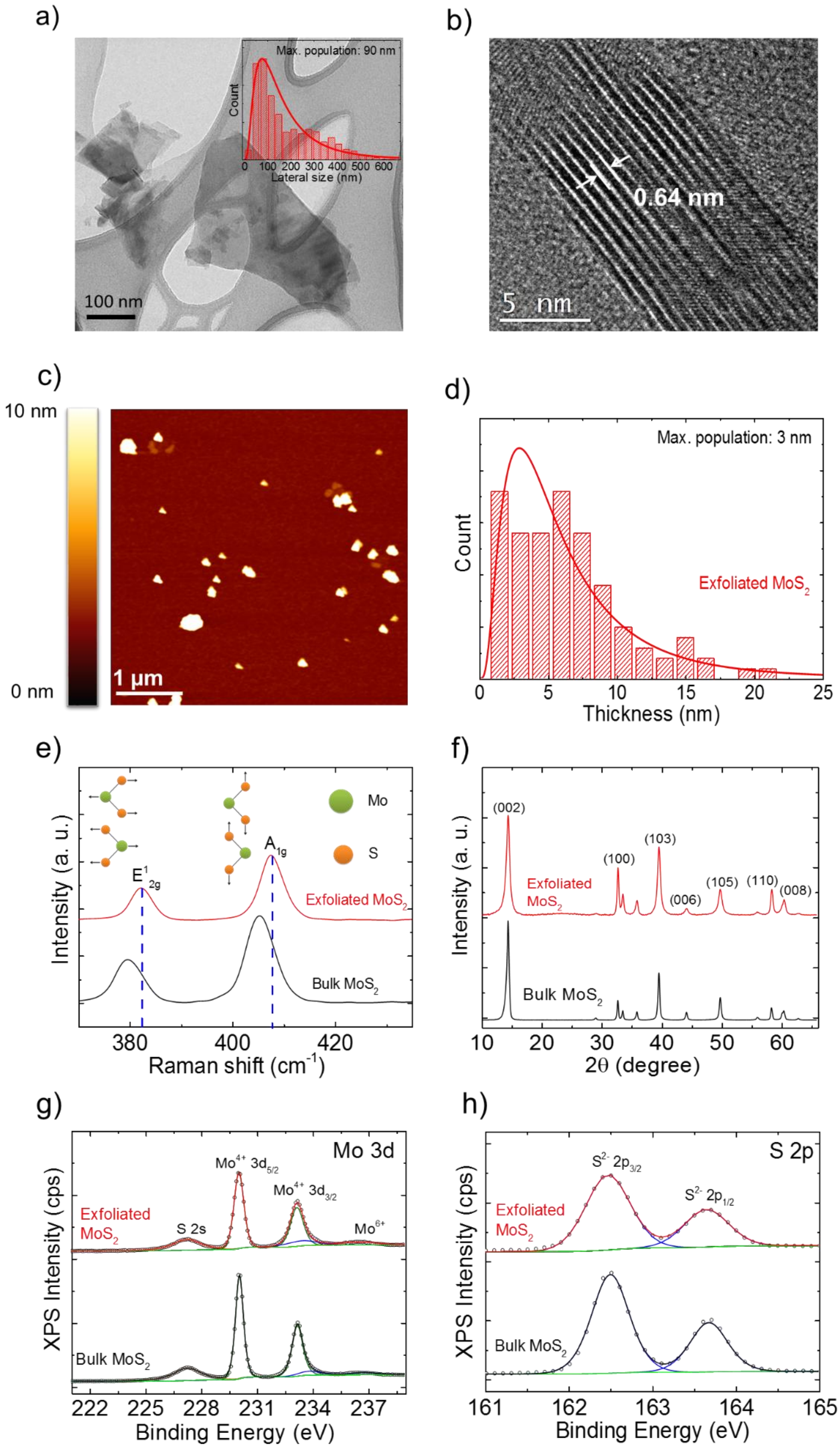

Figure 3.12. *(a) Transmission electron microscopy image of exfoliated $MoS_2$; the inset shows lateral size distribution, (b) High resolution-TEM image of exfoliated $MoS_2$, (c) Atomic force microscopy images of exfoliated $MoS_2$ and (d) its corresponding thickness distribution, (e) Raman spectra of bulk and exfoliated $MoS_2$, (f) X-ray diffraction patterns of bulk and exfoliated $MoS_2$, high resolution-XPS spectra for (g) Mo 3d and (h) S 2p of bulk and exfoliated $MoS_2$.*

The chemical content in $MoS_2$ before and after LPE process is analyzed by the XPS. In the XPS spectra of Mo 3d in bulk and exfoliated $MoS_2$ samples (Figure 3.12g), two peaks at 229.5 and 232.7 eV, are assigned to $3d_{5/2}$ and Mo $3d_{3/2}$ binding energies of $Mo^{4+}$, respectively, confirming the composition of $MoS_2$. [215, 330] The peak at 227.2 eV is ascribed to the 2s binding energies of S atoms in the $MoS_2$. [330, 331] The peak of $Mo^{6+}$ is observed in both XPS spectra of bulk and exfoliated $MoS_2$, the presence of which in case of bulk $MoS_2$ can be caused by partial surface oxidation of bulk $MoS_2$ by oxygen/water in air. Additionally, there is no change in intensity of the $Mo^{6+}$ peaks in both XPS spectra of bulk and exfoliated $MoS_2$, suggesting that the chemical structure of $MoS_2$ is not affected by the LPE process. [239] Figure 3.12h shows the XPS spectra of S 2p bulk and exfoliated $MoS_2$ samples, in which two peaks located at 162.5 and 163.7 eV correspond to $2p_{3/2}$ and $2p_{1/2}$ binding energies of $S^{2-}$ in $MoS_2$, respectively.[215, 332] By quantitative analysis of the XPS data over binding energy regions of Mo 3d and S 2p in both bulk and exfoliated $MoS_2$ samples, the Mo:S ratios in the two samples are estimated to be 1:1.9. This result indicates that the influence of the exfoliation process on the stoichiometry $MoS_2$ is negligible.

### 3.4.2. Molybdenum disulfide/amorphous carbon hybrids

As reported in section **2.2.2**, the $MoS_2$/PAA mixtures are formed by solution mixing of the exfoliated $MoS_2$ flakes and PAA in IPA. The $MoS_2$/C samples are formed by a thermal decomposition process of PAA. The $MoS_2$/C powders named as $MoS_2$/C-1, $MoS_2$/C-2, and $MoS_2$/C-3 corresponding to the different weight ratios of $MoS_2$/PAA as 1:1, 1:2 and 1:4, respectively.

The electrical conductivity and thickness of the carbon network are adjusted by either tuning the carbon source content, or the annealing temperature and time. [333] The amount of carbon in $MoS_2$/C samples is quantified by TGA in air. As shown in Figure 3.13a, the derivative weight curve of $MoS_2$ sample (red dash-curve) shows the first weight loss mainly occurring from ~ 350°C to 470°C, which is attributed to oxidation of $MoS_2$ to $MoO_3$. [334] Thus, the weight loss of $MoS_2$ is calculated ~ 11.2 wt%. The second weight loss at ~ 760 ℃ is attributed to the sublimation of $MoO_3$. [335] For the $MoS_2$/C samples, the derivative curves show a peak at ~ 360 ℃ corresponding to the first weight loss that is caused by the oxidation of $MoS_2$ to $MoO_3$. [335, 336] The second peak at ~ 420 ℃ is attributed to the combustion of carbon to form $CO_2$. [327, 337] The weight loss of these two processes is calculated approximately ~ 21.3, 27.3 and 41.1 wt% for the $MoS_2$/C-1, $MoS_2$/C-2, $MoS_2$/C-3 sample, respectively. Therefore, the carbon contents in $MoS_2$/C-1, $MoS_2$/C-2, and $MoS_2$/C-3 samples are estimated to be ~ 10.1, 16.1 and 29.9 wt% by subtracting the first weight loss of $MoS_2$ from the total weight loss of $MoS_2$ sample, see Table 3.2 for details. The weight loss of $MoS_2$/C samples at ~ 730 ℃ is attributed to the sublimation of $MoO_3$.

The structure of the $MoS_2$/C samples is further investigated by XRD and Raman measurements. Figure 3.13b shows the XRD patterns of the exfoliated $MoS_2$ and $MoS_2$/C samples, all the diffraction peaks are normalized according to (002) peak. The typical diffraction peaks of hexagonal $MoS_2$ phase are detected in the XRD patterns of $MoS_2$/C samples, suggesting the preservation of $MoS_2$ phase after the annealing process. The (002) diffraction peak is representative for the preferential orientation of $MoS_2$ layers along the z axis. The intensities of the (100), (103), (105) and (110) diffraction peaks significantly increase with the rise of carbon content. This indicates that the incorporation of amorphous carbon creates more disordered orientations of $MoS_2$ flakes, as reported in literatures. [163, 334, 337] In addition, there is no diffraction peak related to graphitic carbon, demonstrating that the carbon has amorphous nature. [163, 327] As shown in the Raman spectra of the $MoS_2$ and $MoS_2$/C samples (Figure 3.13c), the characteristic peaks of $MoS_2$ ($E^1_{2g}$ and $A_{1g}$) are observed in all samples and there are no shifts of these peaks in $MoS_2$/C with respect to the starting $MoS_2$ sample. These results suggest that the presence of carbon neither affect the crystalline structure of $MoS_2$, nor induces defects in the flakes. [163, 337] Compared to $MoS_2$ sample, the Raman spectra of $MoS_2$/C samples show two additional peaks at ~1360 and ~1599 $cm^{-1}$ corresponding to the D band and G band of carbon materials, respectively. The D band is attributed to $A_{1g}$ breathing mode of $sp^3$-hybridized disordered carbon or defective graphitic carbon, whereas the G band is associated with $E_{2g}$ stretching mode of the $sp^2$-hybridized graphitic carbon. [338] The presence of D and G band features the formation of amorphous carbon in $MoS_2$/C samples. [168, 169] To provide further insight into the morphology and structure of the amorphous carbon and $MoS_2$ flakes, HR-TEM measurement is performed. From HR-TEM images (Figure 3.13d, e and f), the interlayer distance of $MoS_2$ layers in $MoS_2$/C samples is ~ 0.64 nm, having similar value to the one of the exfoliated $MoS_2$ sample (Figure 3.12b). Also, the amorphous phase of carbon is observed in HR-TEM images of $MoS_2$/C samples. The HR-TEM images show that the thickness of carbon layer of $MoS_2$/C-1 (~ 0.8 nm) is smaller than that on $MoS_2$/C-2 (~ 2.4 nm) and $MoS_2$/C-3 (~ 13.8 nm).

Moreover, the carbon layer in $MoS_2$/C-1 sample does not cover completely the $MoS_2$ flakes due to the insufficient amount of initial PAA.

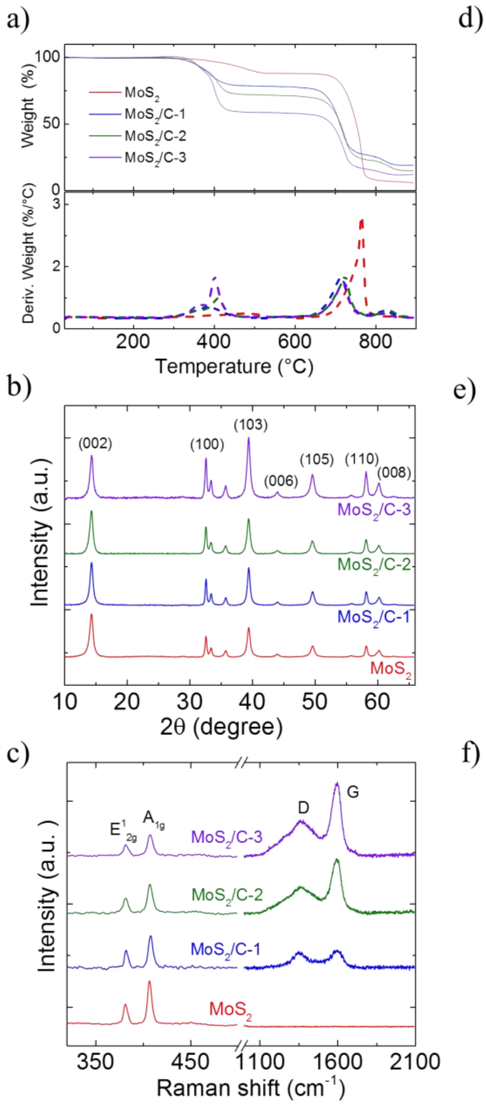


Figure 3.13. *(a) TGA and Derivative Weight curves, (b) X-ray diffraction patterns, (c) Raman spectra at 514.5 nm excitation wavelength exfoliated $MoS_2$, $MoS_2$/C-1, $MoS_2$/C-2 and $MoS_2$/C-3 samples. High resolution-TEM images of (d) $MoS_2$/C-1, (e) $MoS_2$/C-2 and (f) $MoS_2$/C-3 samples.*

Table 3.2. *Calculation of wt% of carbon based on TGA measurement*

| **Samples** | **Wt% of $MoS_2$ : PAA** | **Mass loss of Sulfur and Carbon (%)** | **Mass of carbon (%)** |
|---|---|---|---|
| $MoS_2$/C-1 | 1 : 1 | 21.22 | **10.00** |
| $MoS_2$/C-2 | 1 : 2 | 27.33 | **16.11** |

| | | | |
|---|---|---|---|
| $MoS_2$/C-3 | 1 : 4 | 41.08 | **29.86** |

In conclusion, the characterization of exfoliated $MoS_2$ flakes confirm that the LPE process is able to produce the nano-sized $MoS_2$ flakes (lateral size mode of ~ 90 nm) without any change in the structural phase and chemical composition. Moreover, the characterizations of $MoS_2$/C hybrids reveal the important information about the correlation between carbon content and the thickness of carbon layer in the $MoS_2$/C hybrid. The obtained results contribute to the further understanding of the electrochemical properties of $MoS_2$ and $MoS_2$/C electrodes in **chapter 5**.

### 3.5. Few-layer black phosphorous flakes

#### 3.5.1. Solvent analysis

In order to exfoliate and stabilize BP in a solvent, the Gibbs free energy of the mixture solvent/layered material must be minimized. [188, 241] This condition can be endorsed if the γ of the solvent is equivalent to the surface free energy of the material: [241]

$$\gamma = E_{Surface}^{Solvent} - TS_{Surface}^{Solvent} \tag{3.4}$$

in which $E$ is the solvent surface energy, $T$ is the absolute temperature and $S$ is the solvent surface entropy (which generally takes a value of $10^{-3}$ J m$^{-2}$ K$^{-1}$ [241, 339, 340]). Moreover, the matching of the Hansen or Hildebrand parameters of the solvent with the ones of the layered material facilitates the exfoliation process. [341-343] The Hildebrand parameter ($\delta_T$) is widely used in polymer science, and is defined as the square root of the cohesive energy density: [344, 345]

$$\delta_T = \sqrt{\frac{\Delta H_v - RT}{V_m}} \tag{3.5}$$

in which $\Delta H_v$ is the enthalpy of vaporization, $R$ is the ideal gas constant, and $V_m$ the molar volume. The Hildebrand parameter is used to evaluate the solubility or “dispersibility” of a material in a known solvent. [346, 347] However, in some specific cases, the Hildebrand parameter is not sufficient to describe and evaluate the dispersability of a material in a solvent. For example, the Hildebrand parameter of graphene is~23 MPa$^{1/2}$, [348] according to the solubility theory. A solvent with this $\delta_T$ value, *e.g.* IPA with $\delta_T \approx 23.8$, [341] should form a stable dispersion of graphene which, however, has not been experimentally demonstrated. The reason lies in the fact that the Hildebrand parameter does not consider the hydrogen bonding and polar interactions. [341] In contrast, the Hansen solubility parameter splits the cohesive energy ($\delta_T^2$) into three components: the polar contribution ($\delta_p$), the dispersive component ($\delta_d$) and the hydrogen-bonding ($\delta_h$) [341]

$$\delta_T^2 = \delta_d^2 + \delta_p^2 + \delta_h^2 \tag{3.6}$$

The γ, Hildebrand and Hansen parameters of the majority of solvents are reported in literature. [341] In contrast, the surface energy and the Hildebrand and Hansen parameters of the materials that are under consideration need an experimental estimation. A common way to obtain these data is to disperse the material in different solvents with a known γ, Hildebrand and Hansen parameters. The dispersed material is quantified either directly by evaporating the solvent and weighting the solid fraction, or indirectly by measuring the optical extinction of the material dispersed in the supernatant. Finally, when the solvent parameter value, *e.g.* the Hildebrand parameter, is plotted against the optical extinction, the maximum of the data distribution indicates the Hildebrand parameter of the dispersed material. The same analysis can be performed to estimate the Hansen parameters or to obtain the surface energy (see Equation 3.4).

Following this approach, the exfoliation of BP in different solvents (see section **2.1.3.4**) is tested, most of which had been previously used for the LPE of other layered crystals. [188, 241] Subsequently, the known values of γ and the Hansen and Hildebrand solubility parameters of the solvents (see Table 3.3) as well as the optical extinction of BP dispersed on each solvent allow estimating the surface energy, and the Hansen and Hildebrand parameters of the exfoliated BP flakes.

Table 3.3. *List of solvents with their corresponding surface tension, Hildebrand and Hansen parameters, and boiling points*

| **Solvent** | **Surface Tension ($mNm^{-1}$)** | **Hildebrand parameter ($MPa^{1/2}$)** | **Hansen parameter. Dispersive force ($MPa^{1/2}$)** | **Hansen parameter. Polar force ($MPa^{1/2}$)** | **Hansen parameter. Hydrogen bonding force ($MPa^{1/2}$)** | **Boiling point (℃)** |
|---|---|---|---|---|---|---|
| **Acetone** | 22.2 | 19.9 | 15.5 | 10.4 | 7.0 | 56.0 |
| **Toluene** | 28.4 | 18.2 | 18.0 | 1.4 | 2.0 | 110.6 |
| **Chloroform** | 25.8 | 18.9 | 17.8 | 3.1 | 5.7 | 61.2 |
| **2-Propanol** | 20.6 | 23.6 | 15.8 | 6.1 | 16.4 | 82.6 |
| **Trichloroethylene** | 28.7 | 19.0 | 18.0 | 3.1 | 5.3 | 87.2 |

| | | | | | | |
|---|---|---|---|---|---|---|
| **Methanol** | 21.8 | 29.8 | 15.1 | 12.3 | 22.5 | 64.7 |
| **Ethylene glycol** | 47.0 | 33.0 | 17.0 | 11.0 | 26.0 | 197.3 |
| **Acetonitrile** | 27.7 | 24.4 | 15.3 | 18.0 | 6.1 | 82.0 |
| **Ethanol** | 21.1 | 26.5 | 15.8 | 8.8 | 19.4 | 78.4 |
| **n-Hexane** | 18.7 | 14.9 | 14.9 | 0.0 | 0.0 | 68.0 |
| **N-Methyl-2-pyrrolidone** | 40.1 | 23.0 | 18.0 | 12.3 | 7.2 | 202.0 |
| **Dimethylfor-mamide** | 37.1 | 24.9 | 17.4 | 13.7 | 11.3 | 153.0 |
| **Diethyl carbonate** | 28.1 | 18.7 | 15.5 | 3.9 | 9.7 | 144.7 |
| **N-Cyclohexyl-2-pyrrolidone** | 43.2 | 20.5 | 18.2 | 6.8 | 6.5 | 284.0 |

Figure 3.14 shows the OES of BP flakes in 14 different solvents. By taking the value of the extinction at 680 nm of the dispersion in different solvents, and plotting them against the Hildebrand parameters and γ of each solvent, it is possible to estimate the Hildebrand parameter and γ of the dispersed material, respectively.

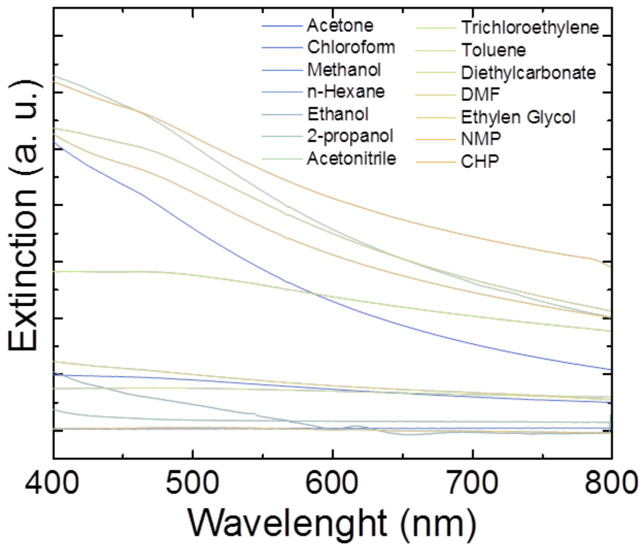


Figure 3.14. *Optical extinction spectra of BP after LPE in different solvents.*

Figure 3.15a and b show the solvent/BP dispersability analysis in terms of the Hildebrand parameter and γ, respectively. The dot distribution in Figure 3.15a fits a curve that peaks at a value close to 21 $MPa^{1/2}$. This value indicates the Hildebrand parameter of the BP, [343-345] which is in agreement with the previously report. [349] The data distribution in Figure 3.15b shows that the solvents that are able to exfoliate bulk BP have a γ in the range of 25-40 $mNm^{-1}$. By applying equation 3.4, these values give a BP surface energy in the range of 50-65 $mJ\ m^{-}$

[2]. The Hansen parameters of BP, shown in Figure 3.15c, d and e, provide $\delta_p$, $\delta_h$ and $\delta_d$ values in the range of 5-12 MPa$^{1/2}$, 5-10 MPa$^{1/2}$ and 15-18 MPa$^{1/2}$, respectively. This means that a solvent with these Hansen parameters should be able to exfoliate and suspend the FL-BP. In summary, the solvent analysis (Figure 3.14 and 3.15) demonstrates that from the selected solvent, seven solvents are able to exfoliate/disperse BP: CHP, NMP, DMF, diethyl-carbonate, acetonitrile, trichloroethylene and acetone. In particular, three of these solvents have a low-b.p. (< 100 °C), *i.e.* trichloroethylene, acetonitrile and acetone, from which acetone the only non-toxic solvent is (Health code ≤ 1 NFPA704). [231] Thus, in the following part of this section, the exfoliated flakes in acetone and in CHP are fully characterized, the latter being used as a reference solvent.

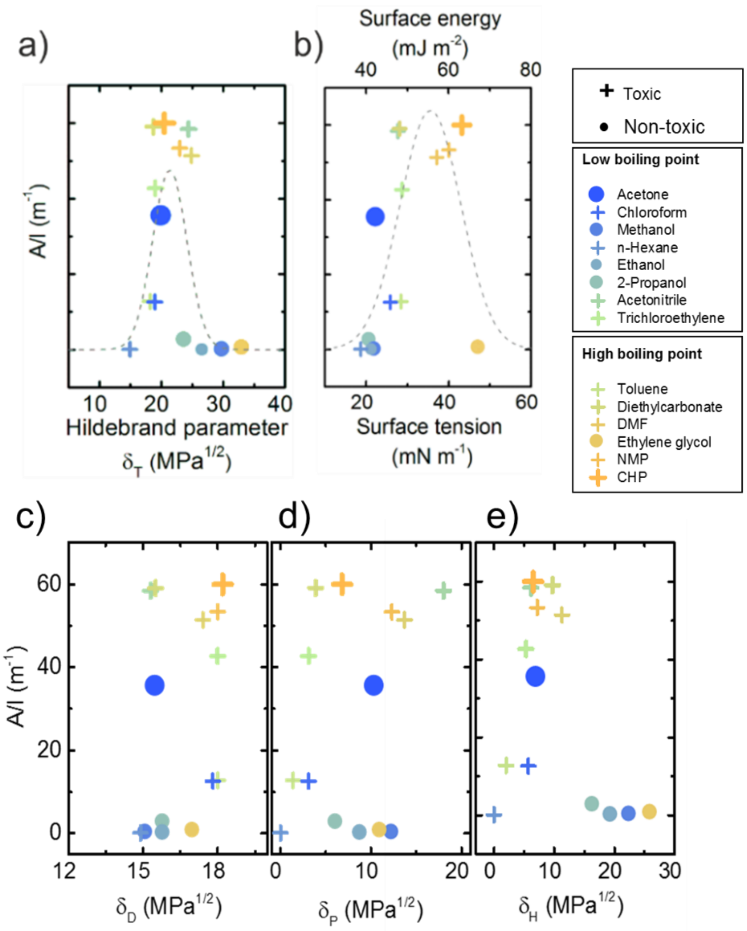


Figure 3.15. *The extinction coefficient of BP dispersed in different solvents after the LPE process, plotted as a function of (a) Hildebrand parameter, and (b) surface tension (lower axis) and surface energy (upper axis). Dots represent the low/non-toxic solvents (Health code ≤ 1 NFPA704), crosses denote the highly toxic solvents ((Health code ≥ 2 NFPA704). Dots and crosses with colours from blue to light-green represent the solvents with b.p. < 100° C, while the ones from turquoise to orange represents solvents with b.p. > 100° C. Estimation of the Hansen parameters of FL-BP, giving approximated parameters of (c) dispersive force: 15-18 MPa$^{1/2}$; (d) polar force: 5-12 MPa$^{1/2}$ and (e) hydrogen bonding force: 5-10 MPa$^{1/2}$.*

Figure 3.16a shows vials with the BP exfoliated in CHP (vial on the left) and the BP exfoliated in acetone at different dilution ratios (from the second left to right: no-dilution, 40%, 30%, 20%, 10% and 5%). Their corresponding extinction spectra are reported in Figure 3.16b, with the extinction coefficient for BP flakes dispersed in acetone being shown as an inset. The slope of this curve indicates that the extinction coefficient is 600 L g$^{-1}$ m$^{-1}$.

There is discrepancy between the extinction coefficient measured in this work and the previous values reported in literature, see Table 3.4. This difference is due to the diverse particle size distributions (thickness/lateral size), the refraction indexes of the solvents, and the wavelength at which the measurement is carried out. [350] The concentration of the FL-BP flakes in CHP (FL-BP$_{CHP}$) is obtained using extinction coefficient at 465nm = 1500 L g$^{-1}$ m$^{-1}$, [235] attaining 0.6 g L$^{-1}$, and the concentration of BP flakes in acetone is obtained with the estimated extinction coefficient at 660nm = 600 L g$^{-1}$ m$^{-1}$, indicating a concentration of 0.35 g L$^{-1}$.

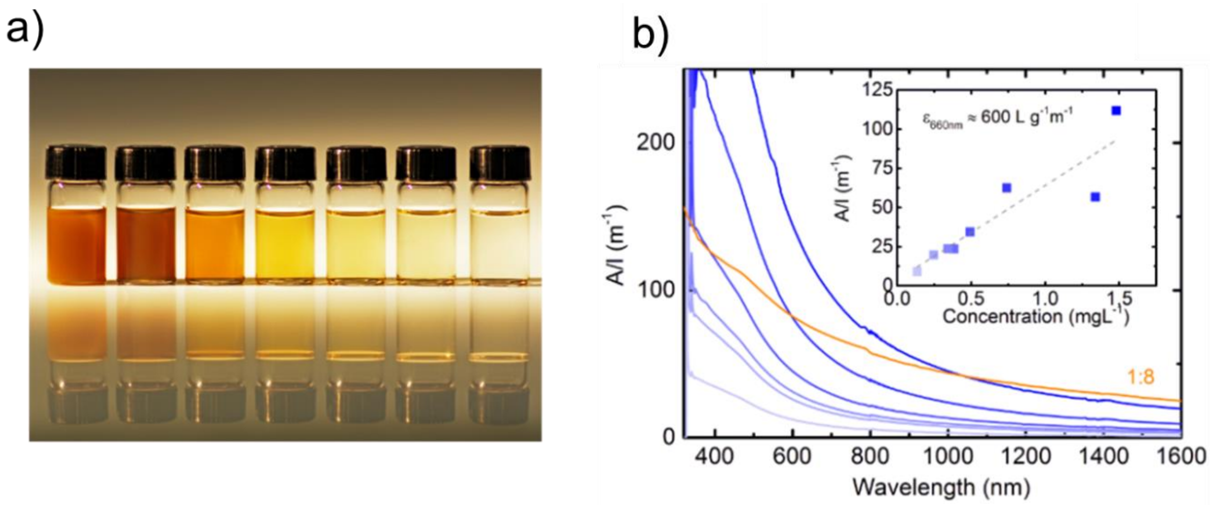


Figure 3.16. *(a) Photograph of the FL-BP dispersions in CHP (first from the left) and acetone at different concentrations (from the second left to right). (b) Extinction spectra of the FL-BP dispersions in acetone at different concentrations, in different blue tones, and FL-BP dispersions in CHP, in orange. The inset shows the calibration curve according to the Beer-Lambert law, yielding an extinction coefficient of ~600 L g$^{-1}$m$^{-1}$, at 660 nm.*

Table 3.4. *Reported extinction coefficients for liquid phase exfoliated FL-BP in diverse solvents*.

| Solvent | Thickness (nm) | Lateral size (nm) | Wavelength (nm) | Extinction coefficient (L g$^{-1}$m$^{-1}$) | Ref. |
|---|---|---|---|---|---|
| **DMF** | 10 | 200* | 1176 | 4819 | [234] |
| **DMSO** | 20 | 400* | 1176 | 5373 | [234] |

| | | | | | |
|---|---|---|---|---|---|
| **NMP** | 10 | 100 | 660 | 263 | [351] |
| **$H_2O$** | 5 | 100 | 660 | 209 | [352] |
| **CHP** | 6 | 100 | 465 | 1500§ | [235] |
| **Acetone** | 5 | 30 | 660 | 600 | This work |

* Lateral size estimated by dynamic light scattering. § Value of absorption coefficient.

### 3.5.2. Morphological characterization of BP flakes in CHP and acetone

Raman spectroscopy gives important information about the vibrational modes of exfoliated crystals. The Raman spectra of BP consists of three peaks, one out-of-plane mode ($A_g^1$, located at 365 $cm^{-1}$) and two in-plane modes ($A_g^2$ and $B_{2g}$, located at 471 $cm^{-1}$ and 440 $cm^{-1}$ respectively, Figure 3.17). [353, 354] The positions and the intensity ratios between these peaks change depending on the T, [355] oxidation, [356, 357] strain, [358, 359] and number of layers. [352, 360]

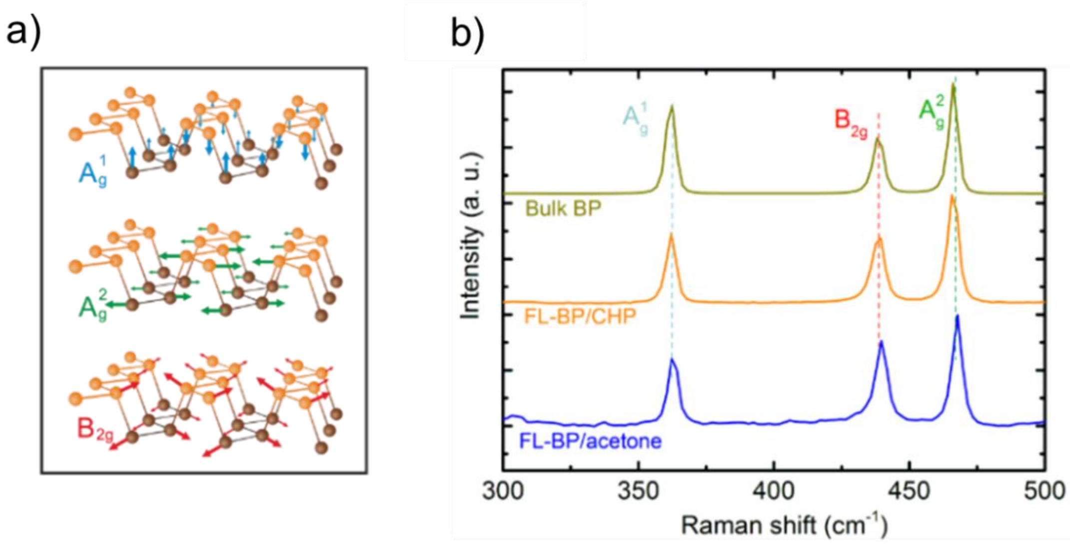


Figure 3.17. *(a) Scheme of the FL-BP Raman active modes. (b) Raman spectra of the Bulk BP (dark yellow line), of the FL-BP cast from a CHP dispersion (orange line) and of FL-BP cast from a dispersion in acetone (blue line).*

Figure 3.17b shows the Raman spectra of the starting bulk material (dark yellow), the BP exfoliated in CHP (orange) and the one in acetone (blue). The exfoliated samples display $A_g^1$ at ~362.0 $cm^{-1}$, $B_{2g}$ at ~434 $cm^{-1}$ and $A_g^2$ at ~467 $cm^{-1}$, which is consistent with previous studies on liquid phase exfoliated BP, obtaining FL-BP. [235, 351] The Raman spectra on both samples, compared with the one of bulk material, suggest that the LPE process does not damage the BP structure and the number of layers is reduced with respect to bulk BP. [357]

The TEM characterization provides a detailed insight into the morphology and structure of the exfoliated BP flakes. The lateral size distribution analysis indicates that the FL-BP flakes exfoliated in acetone are smaller, with a lateral size of 30 nm (Figure 3.18a and 3.18b), compared with the ones exfoliated in CHP, which are 60 nm (Figure 3.18c and 3.18d). The FL-BP flakes thickness distribution, estimated by AFM analysis, indicates that the BP flakes exfoliated in acetone peak at 7 nm (~13 staked phosphorene layers, Figure 3.18e and f), while the ones in CHP peak at 8.1 nm (~16 staked phosphorene layers, Figure 3.18g and h). The TEM and AFM analysis indicates that FL-BP can be produced either using CHP or acetone.

Figures 3.19a and 3.19f report the STEM analysis of FL-BP produced in acetone and CHP (FL-$BP_{acetone}$ and FL-$BP_{CHP}$, respectively). The compositional mapping by EDS, (Figure 3 b-d and g-i) shows that flakes are composed of P with no appreciable presence of O. Moreover, after the FL-$BP_{acetone}$ and FL-$BP_{CHP}$ production, both samples retained the crystal structure of FL-BP, as shown by HRTEM images in Figs. 3.19e and j.

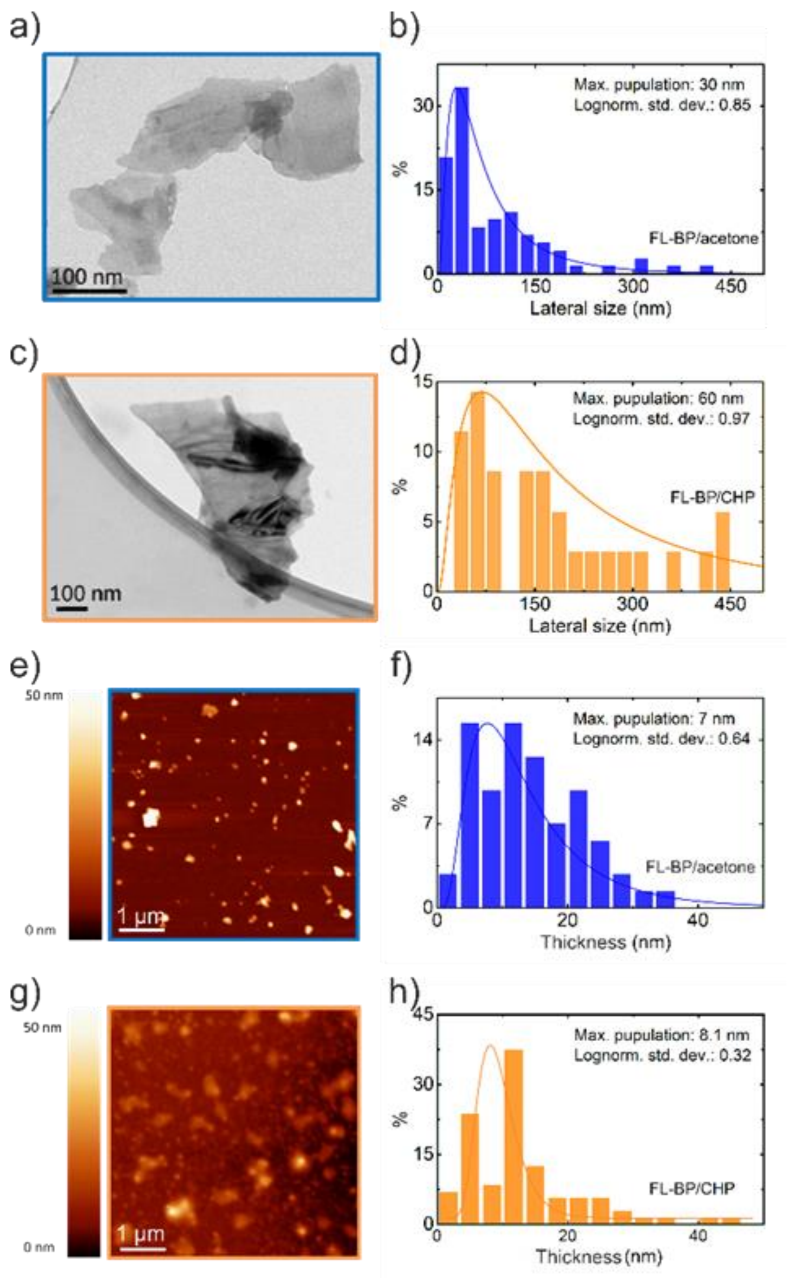


Figure 3.18. *Transmission electron microscopy of FL-BP in (a) acetone and (c) CHP, and their corresponding lateral size distributions (b and d). Atomic force microscopy images of (e) FL-BP$_{acetone}$ and (g) FL-BP$_{CHP}$, and (f and h) their corresponding thickness distributions.*

The structural analysis of the exfoliated flakes is a challenging task due to the crystalline degradation of the thinnest flakes upon exposure to ambient conditions. [357] The degradation of FL-BP flakes is due to the presence of oxygen groups favouring the formation of PO groups. [228, 234, 235] In the case of LPE–BP, it has been reported that CHP and NMP form solvation shells adjacent to the BP surface, which prevents oxidation. [235]

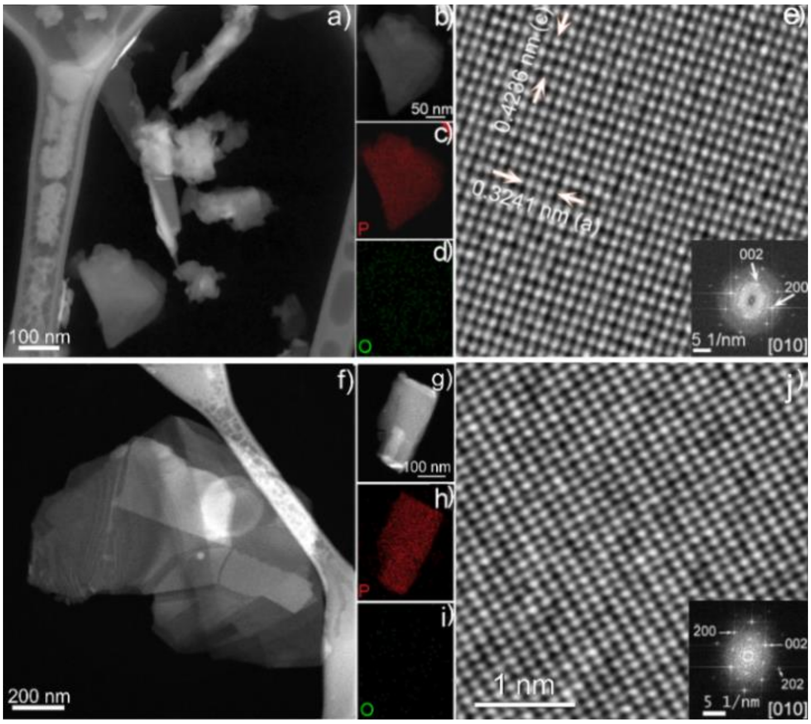


Figure 3.19. (a) *STEM image of FL-BP$_{acetone}$ sheets. (b) STEM image of a selected FL-BP$_{acetone}$ sheet and corresponding d) EDS maps showing the distribution of P (c) and O (d). e) HRTEM image of an FL-BP$_{acetone}$ sheet oriented in its 010 axis with the FT reported as an inset. (f) STEM image of several overlapping FL-BP$_{CHP}$ sheets, g) STEM image of an FL-BP$_{CHP}$ sheet with the EDS maps showing the distribution of P (h) and O (i). (j) HRTEM of the FL-BP$_{CHP}$ sheet in the 010 orientation with the FT as an inset.*

In light of this, an ageing study comparing FL-BP$_{acetone}$ with FL-BP$_{CHP}$ is performed. Electron energy loss spectroscopy (EELS) analysis is performed to determine the chemical bonding in the samples, at different storage times during a three months period. The comparison of the EELS collected from the flakes after different storage times in CHP (Figure 3.20a) and in acetone (Figure 3.20b) indicates that both samples undergo gradual oxidation over a three months period following the exfoliation process. This is evident from the rise of the peak at ~136 eV, in addition to the P $L_{2,3}$-edge at ~130 eV (labelled as $P^0$) which corresponds to elemental P (Figure 3.20a and b). The peak at ~136 eV (labelled as $P_XO_Y$) has previously been attributed to oxidation of BP flakes [227, 361, 362] and is also a dominant feature in the P $L_{2,3}$-edge from $P_2O_5$. [227, 361, 362] The corresponding EEL spectra focused on the oxygen K-edge region (Figure 3.20c) from the two samples following more than three months of ageing, exhibit weak but distinguishable signals associated with the presence of oxygen (arrowed). In contrast, no clear signal in the same energy range is observed in the spectra from the as-exfoliated samples.

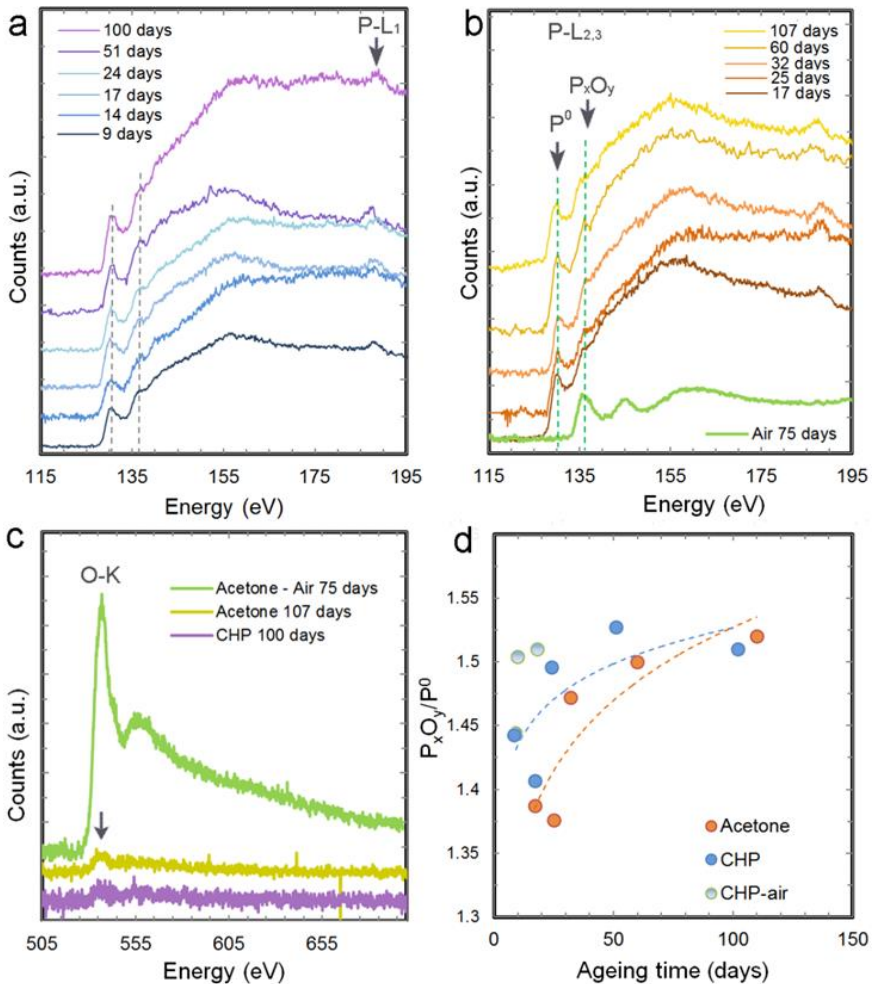


Figure 3.20. *The EELS characterization of the FL-BP degradation in acetone and in CHP. EEL spectra exhibiting the phosphorus L-edge, collected from the FL-BP flakes stored in (a) CHP and in (b) acetone for different time, indicated in the graphs, following the exfoliation in the respective solvents. An EEL spectrum from the flakes stored in air for 75 days following the exfoliation in acetone is included for comparison in (b). The P $L_{2,3}$-edge at ~130 eV corresponds to elemental P ($P^0$), while the appearance of this edge at higher energies indicates that P is in a higher oxidation state. The additional peak observed here at ~136 eV has been attributed to oxidation of FL-BP flakes,* [227, 361, 362] *hence it is labelled $P_XO_Y$. (c) EEL spectra in the oxygen K-edge region collected from the FL-BP flakes stored in CHP and in acetone for 100 and 107 days, respectively. The oxygen K-edge signal from the flakes after storage in the respective solvents is considerably weaker than the oxygen signal from the acetone-exfoliated flakes stored in air for 75 days, included for comparison in (c). (d) Evolution of the intensity ratio of the $P_XO_Y$ to $P^0$ signals in the EEL spectra collected after different storage times in CHP (blue circles) and in acetone (orange circles). Additional data from the CHP-exfoliated sample stored in air up to two weeks are also included for comparison in (d) (open blue circles). Each data point is an average of six measurements. The dashes lines are power-low fits to the experimental data points.*

Although no significant differences are immediately visible between the EEL spectra from the two samples after comparable storage times in their respective solvents, the intensity ratio of the $P_XO_Y$ signal at 136 eV versus the $P^0$ signal at 130 eV, plotted in Figure 3.20d, is slightly but consistently higher in the spectra collected from the FL-$BP_{CHP}$ over the initial two months. After more than three months of storage (~100 days of storage in the respective solvents), both samples reach a similar level of oxidation (1.52 $P_XO_Y$ to $P^0$ ratio, Figure 3.20d). The rate of oxidation of the FL-BP in both solvents is nevertheless significantly lower than in air (additional data points from the FL-$BP_{CHP}$ left in air for two weeks are included for comparison; light blue circles in Figure 3.20 d). This is evident from the prominent oxygen K-edge in the spectrum from the acetone-exfoliated sample left in air for 75 days (the topmost spectrum in Figure 3.20c) compared to the oxygen signals from flakes stored in the two solvent for more than three months.

The FL-BP flakes exposed to air in the present work retained their crystalline structure and most of the phosphorous in the elemental form within the initial couple of weeks, however the prolonged exposure to air gradually lead to their oxidation and structural degradation. The EEL spectrum from the acetone-exfoliated sample left in air for 75 days included in Figure 3.20b (green line) indicates a chemical shift from 130 eV to ~136 eV and exhibits additional features at higher energies, both consistent with the formation of phosphorus oxide. [227, 361, 362] The oxidation is accompanied by a significant structural transformation. What are initially fine crystalline FL-BP flakes in aggregates (Figure 3.21a), after exposure to air for 75 days transformed into amorphous clusters (Figure 3.21b), similar to droplet-like features reported previously. [227, 361-363] The compositional analysis based on EELS indicates that the composition of the amorphous clusters is approximately $P_{54}O_{46}$ (expressed in at%; Figure 3.21c). The compositional analysis is based on the P L-edge found here at 136 eV and O K-edge at ~532 eV, both extracted from the raw spectra by removing the background fitted according to a power law model and using the Hartree-Slater model for the cross-section calculation.

After 12 weeks of aging time, both FL-$BP_{acetone}$ and FL-$BP_{CHP}$ samples retain their crystallinity, as is evident from the HRTEM image of an FL-$BP_{acetone}$ flake, shown in the 110 zone axis (Figure 3.22a). However, the degradation of the flakes is visible as a surface-localized amorphous coating which is 2 to 5 nm thick, as can be appreciated from the side-view image of the flake reported in Figure 3.22b.

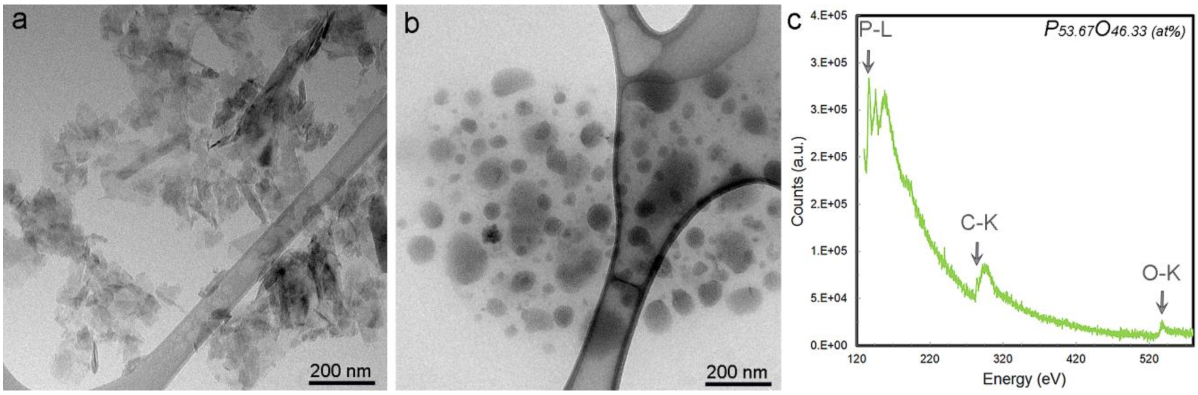


Figure 3.21.*The degradation of the FL-BP flakes in air. (a) An aggregate of flakes after exfoliation in acetone and (b) a similar aggregate after exposure to air for 75 days. (c) An EEL spectrum from the flakes after oxidation in air for 75 days exhibiting prominent phosphorus and oxygen edges used for quantification. The carbon K-edge at 284 eV originates from the amorphous carbon TEM grid support.*

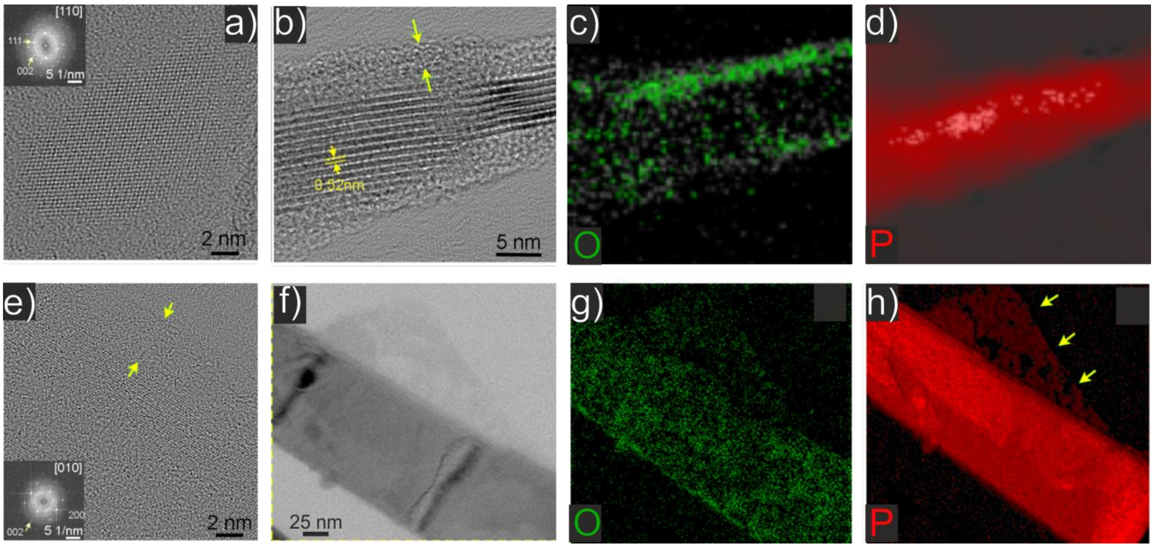


Figure 3.22. *Study on the structural degradation of FL-BP$_{acetone}$ (a to d) and FL-BP$_{CHP}$ (e to h) flakes after 12 weeks of storage in the respective solvents. (a) A FL-BP$_{acetone}$ flake in the 110 zone axis exhibiting the structure of bulk BP. The corresponding FT is shown as an inset to (a). (b) An 8 layered thick flake shown edge-on, in which the individual phosphorene monolayers of ~ 0.52 nm in thickness within the flake can be clearly resolved. The same flake also exhibits an amorphous layer on the surface (see yellow arrow) and the corresponding (c) oxygen and (d) phosphorus EFTEM elemental maps indicate that this layer is oxygen-rich. A thick amorphous layer is also present on the FL-BP$_{CHP}$ flakes (see arrows in e). The flake shown in (e) is in the 010 zone axis, with the corresponding FT shown as an inset. Additionally, a thinner (brighter in contrast in TEM image in (f)) flake overlapping the flake shown in (e) exhibits clear signs of structural degradation. The corresponding (g) oxygen and in particular (h) phosphorus EFTEM elemental maps clearly indicate the fragmentation of the thinner flake (yellow arrows in h).*

The distance between two adjacent BP layers is 0.52 nm, [364] as is shown by the arrows (see Figure 3.22b). The compositional analysis of this flake (Figure 3.22c and d) by EFTEM indicates that the amorphous surface layer is oxygen-rich (Figure 3.22c), while the central crystalline part of the flake remains phosphorus-rich (Figure 3.22d). The presence of a thick amorphous layer is also evident on the FL-$BP_{CHP}$ (see arrows in Figure 3.22e). Fragmentation accompanying oxidation is also observed with thin flakes, such as the one shown in Fig 3.22f and g, overlapping the thicker (darker in contrast) flake. The degradation of the thinner flake (light contrast) is clearly visible from the EFTEM map of phosphorus (see arrows in Figure 3.22h).

The spectroscopic and morphological characterizations show that the exfoliation of bulk BP can be performed in acetone as successfully as in high-b.p. solvents such as CHP. Detailed structural and compositional characterization of the exfoliated material also demonstrates that the oxidation by aging FL- $BP_{acetone}$ is similar to aging FL-$BP_{CHP}$. The exfoliation of BP in acetone is therefore an affordable alternative to the exfoliation process carried out exploiting high-b.p. and toxic solvents, offering a safe and sustainable route for the exfoliation, storage and deposition processes of FL-BP flakes.

In conclusion, it is demonstrated the exfoliation of bulk black phosphorus with acetone, creating a new way to formulate functional inks to be exploited for the designing of few-layers BP-based devices. The exfoliation of BP and its dispersion in 14 different solvents give us the possibility to evaluate the dispersability properties of few-layers BP. It has been estimated: (*i*) the surface energy to be in the range of 55-70 $mJm^{-2}$; (*ii*) the Hildebrand parameter to be 21 $MPa^{1/2}$ and (*iii*) the Hansen parameters to be 15-18 $MPa^{1/2}$ for a dispersive force, 5-12 $MPa^{1/2}$ for a polar force and 5-10 $MPa^{1/2}$ for a hydrogen bonding force. Among the different trials, it has been found that exfoliation in acetone leads to exfoliated FL-BP flakes with average lateral size of 30 nm and thickness of 7 nm (corresponding to 13 layers). Additionally, The EELS and Raman spectroscopies demonstrates that the exfoliated BP flakes in acetone show an aging (oxidation and degradation) that is comparable with the one obtained by using high-b.p. solvents, *e.g.*, CHP. These results will give an opportunity for the exploitation of FL-BP flakes in acetone as an active material for the realization of LIB anodes which will be reported in **chapter 6.**

# Chapter 4:

# Application of graphene for lithium ion batteries

## 4.1. Introduction

Graphene flakes, obtained from the LPE of pristine graphite, represent an ideal yet not fully explored material platform for LIB anodes. [202] Besides all the properties of graphene that are beneficial for LIB applications, such as large surface to mass ratio (2600 $m^2/g$),[192] high electrical conductivity, [193] and high mechanical strength, [194] the LPE graphene flakes have high crystallinity, [159] a key feature for promoting fast electron transport in the electrode. [129] Moreover, the high specific surface area [192] of graphene flakes could allow $Li^+$ uptake on both basal planes and at the edges, providing more active sites for $Li^+$ storage. [196] Thus, graphene flakes prepared by LPE of graphite are emerging as a promising anode material for LIB. [198] As mentioned in **chapter 2**, LPE exploited the ultra-sonication process to exfoliate 2D flakes from their bulk counterparts in a specific solvent, having the γ as close as to the surface energy of 2D flakes. [188, 365] So far, NMP has been considered as one of the most-effective solvents for the production of graphene flake via LPE because its γ is 41.2 mN $m^{-1}$, which is close to graphene's surface energy (46.7 mN $m^{-1}$). (detailed discussion in section **2.1.2**). However, NMP is not an environmentally friendly solvent. [249, 250] Moreover, NMP has high b.p. (202 ℃), [3] therefore its evaporation process usually requires high temperature, (>150 ℃) [67, 249] coupled with high vacuum conditions to avoid the oxidation of the graphene flakes. [159, 249] These issues limit the LPE graphene based ink obtained in NMP for the application of energy conversion and storage devices. [159] Non-toxic and low-b.p. solvents such as water [243, 366, 367] and some alcohols, [368] which would be crucial to develop a fully environmentally compatible deposition/coating process, [159, 249] require the addition of stabilizing agents, *e.g.*, polymers or surfactants, [287, 367] for the optimal dispersion of the flakes. Unfortunately, the presence of such stabilizers in the ink compromises the graphene flake electrochemical properties once deposited onto the current collector. [272] A viable strategy to overcome the aforementioned issues relies in the exploitation of co-solvents, *e.g.*, water/EtOH, [249, 369] and water/isopropanol, [251, 370] to tune the rheological properties of low-b.p. solvents for the formulation of graphene flake-based inks. However, the concentration of the as-produced ink is still low (< 1 g $L^{-1}$), [249, 251] thus not ideal for applications where highly concentrated ink is needed, *e.g.*, the production of battery electrodes.

Besides the issues on the development of novel and high-performance anode materials, advances in the electrode fabrication processes are also important. In fact, the electrode preparation [371-376] is time-consuming and expensive with a strong impact on the cost of the LIB technology. [377-379] Additionally, the composition and morphology of the electrode are critical for LIB operation, because both composition and morphological inhomogeneity can hinder the diffusion of $Li^+$ throughout the electrode itself, resulting in a high charge transfer resistance of electrode materials during lithiation/de-lithation process. [380] Finally, the weight of the binder, being a material not involved in the lithiation/de-lithiation processes, has a negative effect on the electrochemical performance of the anode, limiting both the specific capacity and the energy density of LIBs. [381] For instance, PVdF is reported to swell, *e.g.*, the PVdF binder in a Si battery has shown a 20% thickness change in the electrolyte during the charge/discharge process) [382] in contact with electrolytes based on carbonate solvents. This phenomenon causes solvent decomposition, resulting in capacity fading of LIBs during operation. [382-384] Moreover, PVdF requires the use of toxic and expensive organic solvents, coupling with extra steps to mix and combine with active materials to form a complete electrode material. [371, 385] In this regard, tremendous efforts have been made to develop binder-free electrodes for LIBs, [377] mostly exploiting the direct deposition of the active materials onto the current collectors. [371-374] However, most of the proposed methods such as electrophoretic deposition of hollow $Co_3O_4$, [371] sputtering of Ge embedded in carbon matrix, [372] CVD of CNT and Si nanowire, [373, 374] have not met the requirements in terms of scalability and low-cost production. Another route, *e.g.*, vacuum filtration, has been reported as promising method for low-cost and mass production of the binder-free carbon-based anodes, without any current collector support substrate. Nevertheless, the anodes are still facing limitation of large irreversible capacity and low reversible capacity. For example, the binder-free SWNTs anode shows an irreversible capacity of 1000 mAh $g^{-1}$, while the RGO and CNT/GO free-standing anodes show the capacity of 300 and 330 mAh $g^{-1}$, respectively.

Besides the issues of solvent and electrode fabrication, the performance of graphene-based LIBs is still controversial. In fact, graphene and its derivatives, such as GO [386-388] and RGO, [117, 160, 389] are widely investigated for the realization of LIB electrodes. Recently, RGO, GO and their hybrids/composites with electrochemically active material have been the most investigated materials as promising choices of anodes for LIB. [117, 160, 389-391] Although RGO can provide large initial capacity value (> 2000 mAh $g^{-1}$), [392] it suffers large irreversible capacity and high voltage hysteresis upon lithiation/de-lithiation. This phenomena is due to the heteroatoms/functional groups, *e.g.*, O- and H-containing in functional groups, and the presence of defects, *e.g.*, micro-pores, vacancies, etc., which diminish the conductivity and act as $Li^+$ traps during lithiation/de-lithiation. [393, 394] In order to avoid such negative effects of the functional groups and defects, pristine graphene flakes produced by the LPE of graphite, [202] are a viable replacement for graphite, GO and RGO as anode active material. The anode composed by pristine SLG flakes have shown a promising specific capacity of 744 mAh $g^{-1}$, with the assumption of $Li^+$ adsorbed on both sides of graphene, forming a $Li_2C_6$ stoichiometry. [196] However, the $Li^+$ storage is thermodynamically unstable in pristine SLG electrode during lithiation/de-lithiation, where only low $Li^+$ occupancy levels can be achieved. [157, 395] In contrast, MLG has shown several improvements in terms of electrochemical and thermal stability within the LIBs operational temperature range (-20/60$^o$ C), [201, 396] as well as mechanical stability of the electrode. [397] However, there are no considerable gains in specific capacity of MLG-based anode with respect to that of graphite anode. [5, 396] This raises a natural question. What about what lies in between? Is there a critical flakes size where both beneficial properties of graphite, *e.g.*, low operating voltage, and graphene (high conductivity and short diffusion paths) are found? Is FLG a good active material for next-generation Li-ion batteries? Despite the fact that it is well accepted that dimensions (lateral size and thickness) of the flakes [202] as well as their edges, [198] are expected to play key roles on the $Li^+$ storage mechanisms [36, 44, 198, 202, 398] the link between these morphological properties, and electrochemical performances has not been established yet, neither for RGO, [159, 392, 399-402] nor with the less investigated un-functionalized flakes.

This chapter presents the investigation on the electrochemical performance of binder-free single SLG/ FLG flakes based anode for LIB and the study on the role of graphene flake dimensionality on the electrochemical performance of anodes based on FLG and MLG flakes. The graphene flakes are obtained by LPE of graphite in NMP. A solvent exchange process is exploited to first remove the NMP and then to re-disperse the exfoliated SLG/FLG flakes in EtOH. The binder-free SLG/FLG flakes based anode is successful formed via a one-step fabrication of LIB anodes (drop-casting an environmentally friendly graphene flake-based ink on a Cu substrate at room temperature), without the addition of conductive additives. The anode is assembled in half-cell configuration, achieving a reversible specific capacity of 503 mA h $g^{-1}$ after 100 cycles. Moreover, the full LIB configuration using binder-free SLG/FLG flakes anode and commercial LNMO cathode, exhibits the reversible specific capacity of ~100 mA h $g^{-1}$. This process is able to avoid the conventional time-consuming preparation and deposition of the anode electrodes, promoting a novel strategy to produce graphene based electrodes in fast and efficient way. Additionally, the binder-free anodes based on FLG and

MLG flakes are fabricated to explored role of flake dimensionality on the lithiation/de-lithiation processes and electrochemical properties. The electrochemical results show that decreasing graphene flake dimension (lateral size and thickness) leads to an increase of the initial specific capacity from ~590 to ~1270 $mAhg^{-1}$ which is however linked with a significant increase of the irreversible capacity. Especially, the $Li^+$ storage by adsorption is predominant compared with intercalation for the $Li^+$ storage in the case of anodes composed of small flake size (< 100 nm). In this thesis, the study of the role of graphene flakes dimension on its $Li^+$ storage ability provides insightful guidelines practical exploitation of graphene-based electrodes.

### 4.2. Graphene-based binder-free anode for lithium ion batteries

This section provides a protocol to design binder-free graphene-based anodes for LIBs, starting from LPE of pristine graphite, solvent exchange process and drop-casting, opening the way to the optimization of energy/power densities and lifetime environmentally friendly LIBs. Briefly, graphite is exfoliated in NMP via ultra-sonication process, [260, 403] producing a heterogeneous dispersion of thin/thick and small/large graphitic flakes. [159] The obtained dispersion is subsequently ultra-centrifuged (10000 rpm), exploiting the SBS process, [202, 261] result in an ink enriched in SLG and FLG flakes. A solvent exchange process is exploited to replace NMP with EtOH, in order to obtain an environmentally friendly graphene ink for the deposition onto the current collector (see section **2.1.3.1**). Comparing the structural analysis by TEM and Raman (Figure 3.2a and b) characterizations of graphene flakes in both NMP and EtOH (see section **3.1.1**), it is demonstrated that the solvent exchange process does not affect the structural and morphological properties of the graphene flakes. Then, the graphene-based ink in EtOH is drop-casted onto Cu substrate under air atmosphere at room temperature and then dried at 120 ℃ and $10^{-3}$ bar for 30 min in a vacuum oven. The as-produced binder-free electrodes have a mass loading of SLG and FLG flakes of 1 mg. The film covers homogeneously the Cu substrate, both at macroscopic (Figure 4.1a) and microscopic (Figure 4.1b) levels, with a thickness of 15 μm (inset to Figure 4.1b).

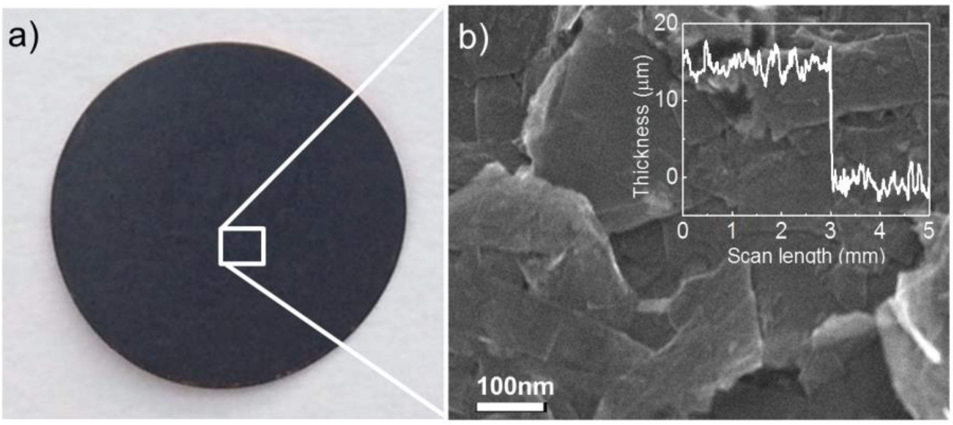


Figure 4.1. *(a) Photograph of the Cu-supported SLG- and FLG-based electrode. (b) SEM image of the graphene electrode. The inset shows the thickness of the SLG- and FLG-based electrode measured by using a profilometer.*

The as-produced anode is also characterized by Raman spectroscopy in order to evaluate the quality of the flakes composing the electrode. Figure 4.2a shows typical Raman spectra of grapheme flakes (in EtOH) deposited onto the $SiO_2$ substrate and binder-free graphene anode. Besides, Figure 4.2b exhibits no correlation in the distributions of the I(D)/I(G) vs. FWHM(G) in the both cases of graphene ink and graphene anode, indicating that no additional defects on SLG and FLG flakes are caused by the deposition process. [277, 404, 405] Moreover, the 2D peak still shows a Lorentzian line-shape distinctly different from that of graphite. In fact, the statistical analysis of I(2D)/I(G) (Figure 4.2c) and Pos(2D) (Figure 4.2d) of the as-prepared electrode indicates that the electrode is composed of a collection of SLG and FLG flakes,[202, 262] which, also if stacked together, are however electronically decoupled.

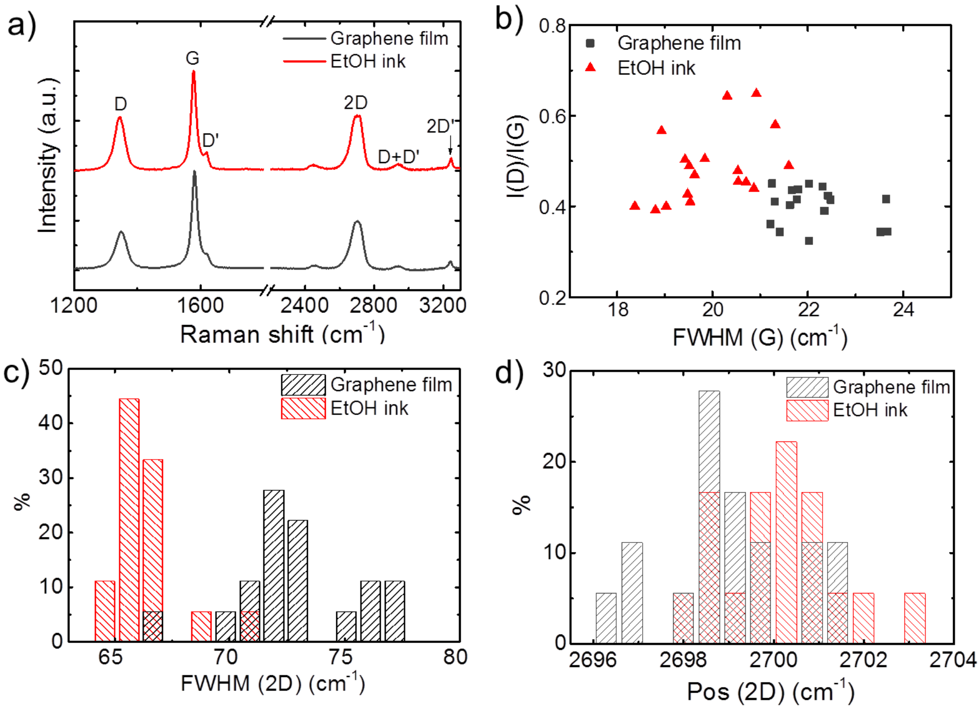


Figure 4.2. *(a) Raman spectra of the graphene EtOH ink (red) and the graphene electrode (dark gray), (b) I(D)/I(G) ratios as a function of FWHM(G), and histograms of (c) I(2D)/I(G) and (d) Pos(2D).*

The anode based on SLG and FLG flakes are tested against metallic Li in a half-cell configuration. Figure 4.3a reports the CVs performed at a scan rate of 50 μV $s^{-1}$, carried out to get a complete electrochemical response for the Li ion transfer. [406] The scan range is from 1 V to 5 mV vs. $Li/Li^+$, covering the formation of the SEI [407] and the lithiation/de-lithiation process for carbon materials. [408] The first CV scan shows a broad reduction peak with a maximum at 0.55 V and an onset at 0.8 V, which is associated with the SEI formation due to side reactions or the reduction of the electrolyte at the surface of the electrode. [407] The absence of this peak in the following scans indicates that the SEI formation is stable, which guarantees a good cycle life of the anode, without further decomposition reactions. [407] Additionally, there is a current increase (~20%) in the 0.1 – 0.3 V range passing from the $1^{st}$ to the $5^{th}$ cycle. This electrochemical behavior can be associated with a slow activation of the lithiation/de-lithiation processes that gradually enhance the capacity of the SLG/FLG-based anode over cycling. [396]

The binder-free electrode based on SLG and FLG flakes shows a specific capacity of 503 mA h $g^{-1}$ at a current density of 0.1 A $g^{-1}$ after the $100^{th}$ charge/discharge cycle in the range from 50 mV to 3 V vs. $Li/Li^+$ and a coulombic efficiency of 99.5% (Figure 4.3b). Moreover, the half-cell cycled at different current densities presents excellent charge/discharge cyclability as well. In fact, a specific capacity of 610 mA h $g^{-1}$ is reached when the graphene-based anode is cycled at 0.05 A $g^{-1}$. Additionally, specific capacity values of 260 mA h $g^{-1}$ and 150 mA h $g^{-1}$ have been reached after 20 cycles at current densities of 0.5 A $g^{-1}$ and 1 A $g^{-1}$, respectively. Figure 4.3b and c, presents the voltage profiles of the electrodes during the 1$^{st}$, 10$^{th}$, 50$^{th}$ and 100$^{th}$ galvanostatic charge/discharge cycles. The latter are performed at a current density of 0.1 A $g^{-1}$ between 5 mV and 3 V vs. $Li/Li^+$, in order to complete the lithiation/de-lithiation (charge/discharge) process in the SLG/FLG-based anode during each cycle. From the first voltage profile, the irreversible specific capacity is calculated to be 500 mA h $g^{-1}$, which represents about half of the total charge capacity. Such a high irreversible charge capacity value is typical for graphene-based anodes and it is presumably due to the large surface area [195, 396] (325 $m^2$ $g^{-1}$, measured by BET) and edge reactivity of the SLG/FLG flakes compared to graphite-based anodes. [392]

The voltage profiles show that more than 50% of the electrode capacity is delivered at a potential lower than 0.25 V vs. Li /$Li^+$ with a flat plateau up to the 100$^{th}$ cycle (Figure 4.3c). Such a low potential is comparable to the values obtained using graphite (0 – 0.4 V vs. $Li/Li^+$), leading to a high energy efficiency of batteries. [396] In order to understand the effect of voltage cut-off on both the specific capacity and coulombic efficiency of the graphene-based anode, we tested the electrode cycled at two different cut-off voltages, one between 50 mV and 2 V and the other one between 50 mV and 3 V. As shown in Figure 4.3d, the specific capacities of the electrode tested in these two different voltage ranges are similar, with a capacity loss lower than 5% for the first 50 cycles for both test conditions. Also the coulombic efficiency is quite similar, with a value >99% achieved after 8 and 5 cycles for the electrode cycled up to 2 V and 3 V, respectively. Moreover, the electrode cycled up to 2 V shows no gradual increase of the specific capacity upon cycling as instead shown by the electrode cycled up to 3 V. As mentioned before, this specific capacity increase is linked to the slow activation of the anode. [396] It indicates that a small quantity of irreversible capacity, which may be related to the edge effects of the graphene flakes, [202] requires high voltage (2 – 3 V) to be completed.

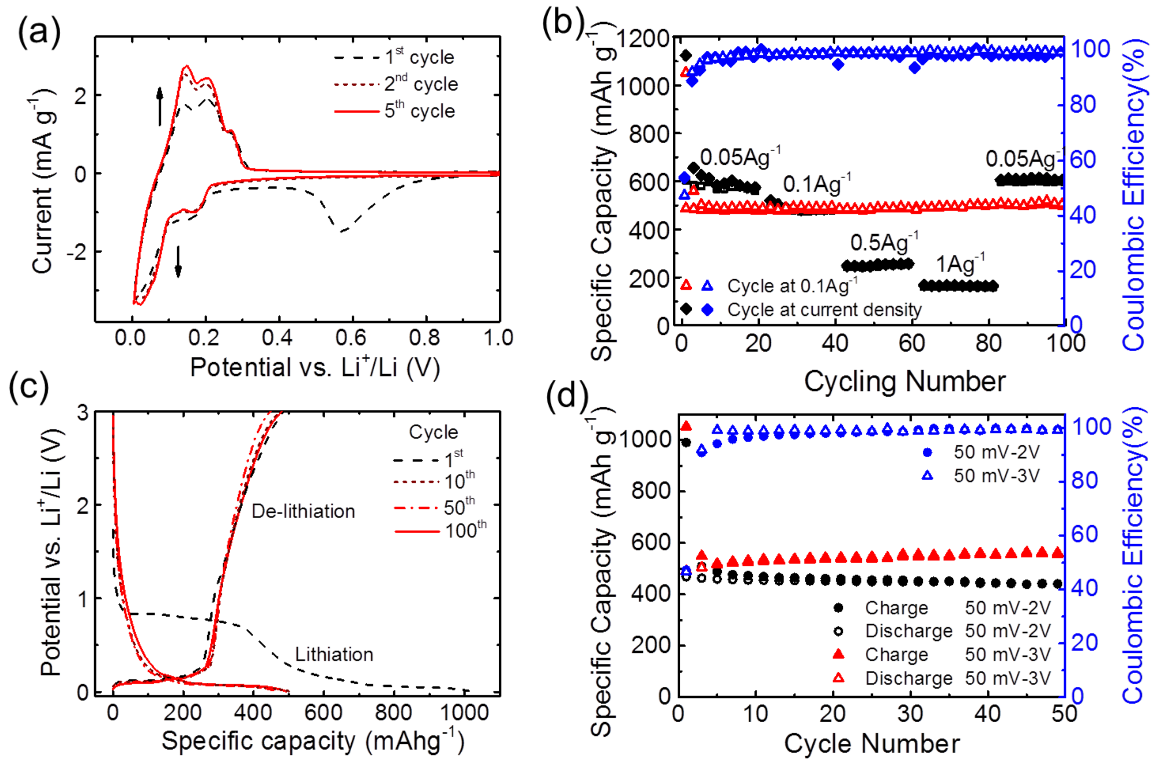


Figure 4.3. *(a) Cyclic voltammetries at a scan rate of 50 µVs$^{-1}$. (b) Specific capacity and Coulombic efficiency over charge/ discharge galvanostatic cycles between 50mV and 3V. The galvanostatic cycling at 0.1 A g$^{-1}$ (triangles) is compared with the one at different current densities (diamond). (c) Voltage profile upon galvanostatic charge/discharge of graphene electrodes at 0.1 A g$^{-1}$ between 50mV and 3V. (d) Specific capacity and Coulombic efficiency over galvanostatic cycles at current density of 0.1 A g$^{-1}$ between 50 mV and 2 V (circle) and between 50 mV and 3 V (triangles), respectively.*

The binder-free SLG/FLG-based anode is further studied in LIB configuration, coupling it with a commercial cathode material, *e.g.*, LNMO. The latter is considered as one of the most promising candidates in the development of high energy/power LIBs, [409, 410] thanks to its high theoretical specific capacity (146.7 mAh g$^{-1}$) [411] and high working voltage (around 4.7 V vs. Li/Li$^+$). [412] Before the full LIB assembly, the pre-lithiation step is carried out on the anode to improve the working voltage and the energy density as well as to reduce the irreversible capacity loss, increasing the Li$^+$ concentration of the electrolyte. [413] The aforementioned properties positively contribute to the cell cycling stability. [414] The reason behind the choice for the pre-lithiation process of the anode only for the full battery configuration and not for the half-cell configuration, relies on the fact that the LNMO cathode has limited Li$^+$ source compared to the metallic Li foil (used for the half-cell configuration tests). [413] Thus, the LNMO cathode is not able to provide sufficient Li$^+$ for the formation of SEI film without negatively affecting the cell cycling stability. [413] Moreover, in designing the battery, it is of paramount importance to reach an optimal balance of cathode and anode electrodes both in term of weight and electrochemical properties. [413-415] The weight ratio we used in trying to optimize the anode/cathode balancing is 1/3.5, which takes into account the difference in specific capacity of the two electrodes. As shown in Figure 4.4a, the SLG/FLG-LNMO full battery operates at a high voltage (~ 4.5 V) with a voltage profile similar to the typical LNMO one, [411] confirming appreciable anode performance with a substantially constant working voltage lower than 0.20 V vs. $Li/Li^+$. [412] The plot of the specific capacity as a function of the galvanostatic charge/discharge cycles (Figure 4.4b) shows a rather stable specific capacity of ~100 mAh $g^{-1}$ with respect to the mass of LNMO, and a coulombic efficiency of ~ 99 % achieved after 5 cycles. A major drawback of the LNMO-based batteries is their capacity fade, [416, 417] which is caused by the decomposition of the electrolyte at the electrode/electrolyte interface at the high working voltage (~ 4.7 V). [416] The capacity and the stability of SLG-FLG/LNMO full battery are comparable to those of state of the art LNMO-based batteries. [418-421] Although further research needs to be done on the optimization of LNMO cathodes and electrolyte, the results obtained by using the binder-free SLG/FLG-based electrodes, both in half- and full-cell configuration, strongly encourage their exploitation as advanced and high performance anode in LIBs.

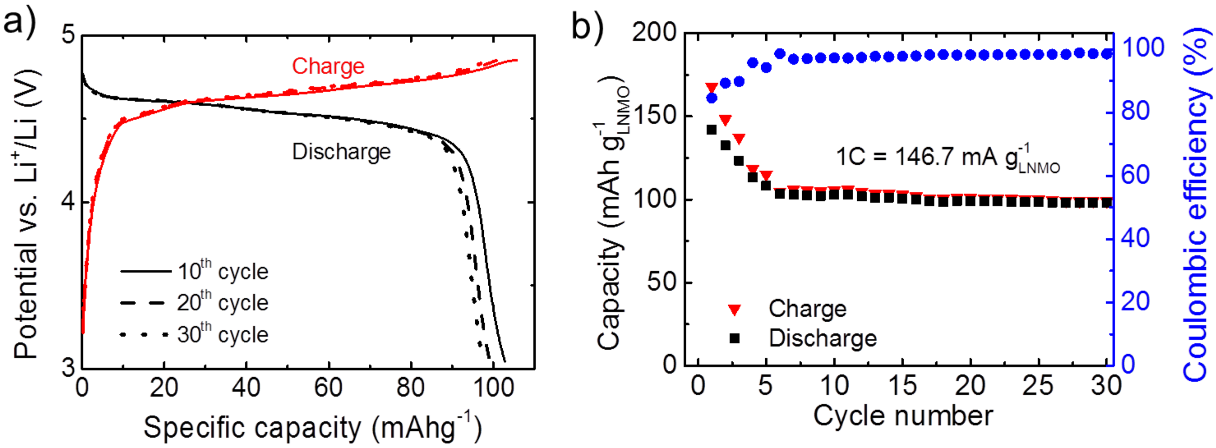


Figure 4.4. *(a) Voltage profile upon galvanostatic charge/ discharge of graphene/LNMO full battery. 10th, 20th and 30th cycle at 1 C (146 mA $g^{-1}$ vs. LNMO). (b) Specific capacity and coulombic efficiency over charge/discharge galvanostatic cycles at 1 C between 3 V and 5 V of graphene/LNMO full battery.*

### 4.3. The influence of graphene flake morphology on electrochemical properties of graphene based anode in lithium ion batteries

This section brings out the answers for the questions about the role of graphene flake morphology (i.e., lateral size and thickness) on the electrochemical properties of anodes based on FLG and MLG flakes, as mentioned in section **4.1.** As reported in section **3.1.2**, a set of

FLG and MLG flake dispersions (in NMP) are obtained and marked as Sample #1, #2, #3 and #4, corresponding to the lateral size (ranging from 75 to 380 nm) and thickness (from 2 to 20 nm), see Figure 3.6. The Raman results of these samples in Figure 3.8 confirm that Samples #1, #2 and #3 are composed of MLGs, while Sample #4 mostly contains FLG. In order to meet the requirements of fast deposition and non-toxicity, [150, 249] the sediments of the four samples are collected and dispersed in EtOH, allowing the simple one-step fabrication of binder-free electrodes. [3] The electrodes do not contain any additional conductive carbon, *e.g.*, carbon black, which is widely used in literature, [422] in order to avoid interfering with the electrochemical response of the graphene flakes, *e.g.*, by contributing to the $Li^+$ storage capacity. The graphene dispersions deposited onto the Cu substrates are characterized by SEM, see Figure 4.5.

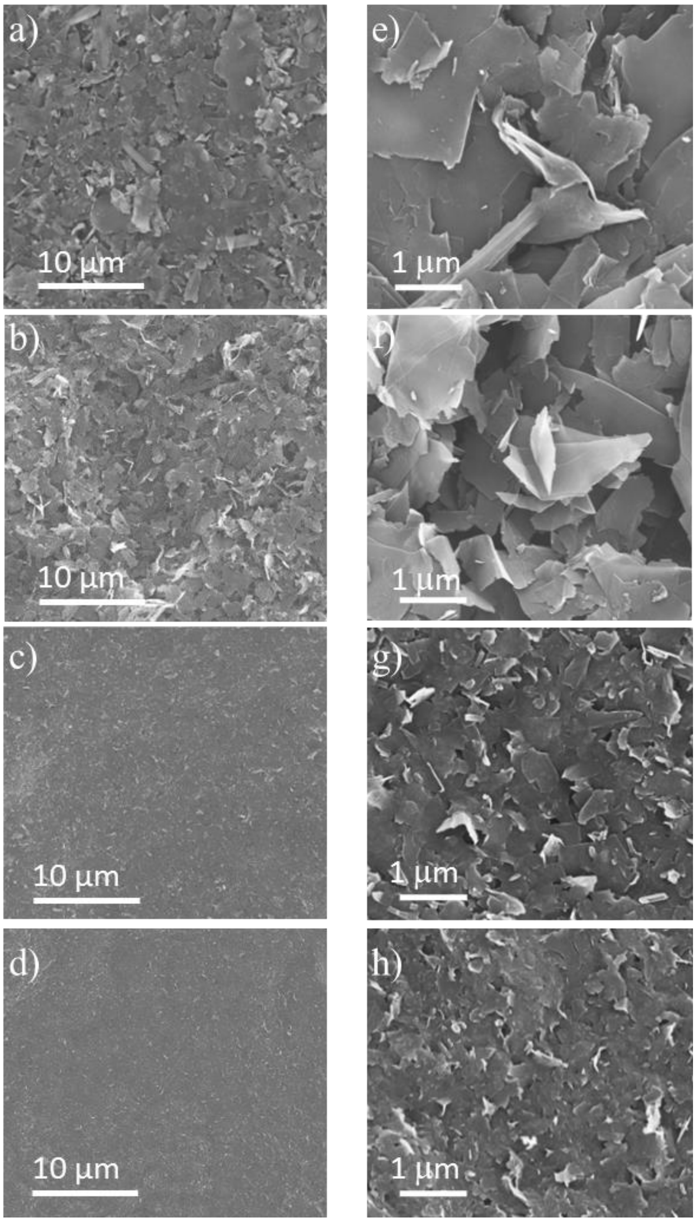


Figure 4.5. *(a), (b), (c), (d) Low resolution SEM images and (e), (f), (g), (h) high resolution SEM images of Sample #1, #2, #3 and #4 deposited onto a Cu substrate, respectively.*

The micrographs recorded at low magnification (Figure 4.5a, b, c and d), and representative for the whole area, testify the homogeneity of the binder-free electrodes, independently from the flake size. Higher magnification images (Figure 4.5e, f, g and h) reveal that, as the flake dimension decreases, the electrodes surface becomes more flat and compact, which from one hand could improve the electronic transport amongst the flakes, but, on the other hand, may not be beneficial for the lithium storage capacity and transport. The lateral sizes and thickness of the graphene flakes are expected to have a significant influence on their $Li^+$ storage characteristics. [5, 195] The voltage profiles of Figure 4.6a show that upon the first lithiation, the specific capacity of the electrode increases from 591 mAh $g^{-1}$ to 1267 mAh $g^{-1}$ as the average lateral size and thickness of the flake decreases from Sample #1 to Sample #4. However, in the following opposite process, $Li^+$ ions are released only to a certain extent, revealing a significant irreversible capacity, *e.g.*, 40% for Sample #1. As the flakes get smaller in both lateral size and thickness, more amount of charge is irreversibly consumed in the first cycle, resulting in only 35% coulombic efficiency for Sample #4, see Figure 4.6a. Accordingly, the loss of capacity may be ascribed to the irreversible electrolyte decomposition process leading to the formation of a solid electrolyte interphase (SEI) on the electrode surface. As previously discussed, changes in dimensions naturally leads to changes in surface area and edge defects (see Table 3.1 and Figure 3.7), and thus in turn, of electrode reactivity. [423] In fact, as confirmed by the evident plateau evolving in all samples below 0.9 V (Figure 4.6a), the charge associated to such irreversible process increases with decreasing flake sizes.

From the 2$^{nd}$ cycle onward, the specific capacity of Sample #1 and Sample #2 rapidly stabilizes without considerable fade, setting on values of 341 and 366 mAh $g^{-1}$, respectively, at the 20th cycle. The higher capacity provided by the smaller/thinner flakes appears to be partially lost upon cycling (Fig 6b). The flake size has a noticeable influence on the potential window in which the capacity is delivered. During lithiation and de-lithiation cycles, Samples #1 and Sample #2 provide more stable capacities, mainly delivered at low potentials in the 0.005-0.2 V and 0.005-0.25 V range for lithiation and de-lithiation, respectively), compared to Samples #3 and Sample #4 (Figure 4.6b). As the flakes dimension decreases, larger contributions arise from the more positive potential range instead (namely, 0.2-3 V and 0.25-3 V for lithiation and de-lithiation). Such behavior suggests that adsorption of $Li^+$ (on the flakes' surface or edges) is the mechanism primarily responsible for charge storage in small lateral size FLG flakes, [202, 394] whereas, intercalation of $Li^+$ (in between the layers) is the main process occurring in MLG flakes. By analyzing the capacity evolution upon the first 20 cycles (see Figure 6b), the $Li^+$ adsorption mechanism (between 0.2/0.25-3 V) appears to be rather stable, and does not affect the electrodes cyclability in the case of big flake size based anodes (Samples #1 and Sample #2). Differently, it is evident that the decay observed for small flakes arises, for the largest extent, from the low potential region (below 0.25/0.2 V). This suggests that Li intercalation in small size MLG (sample #3) and FLG (sample #4) is somehow less reversible than in larger graphene flakes.

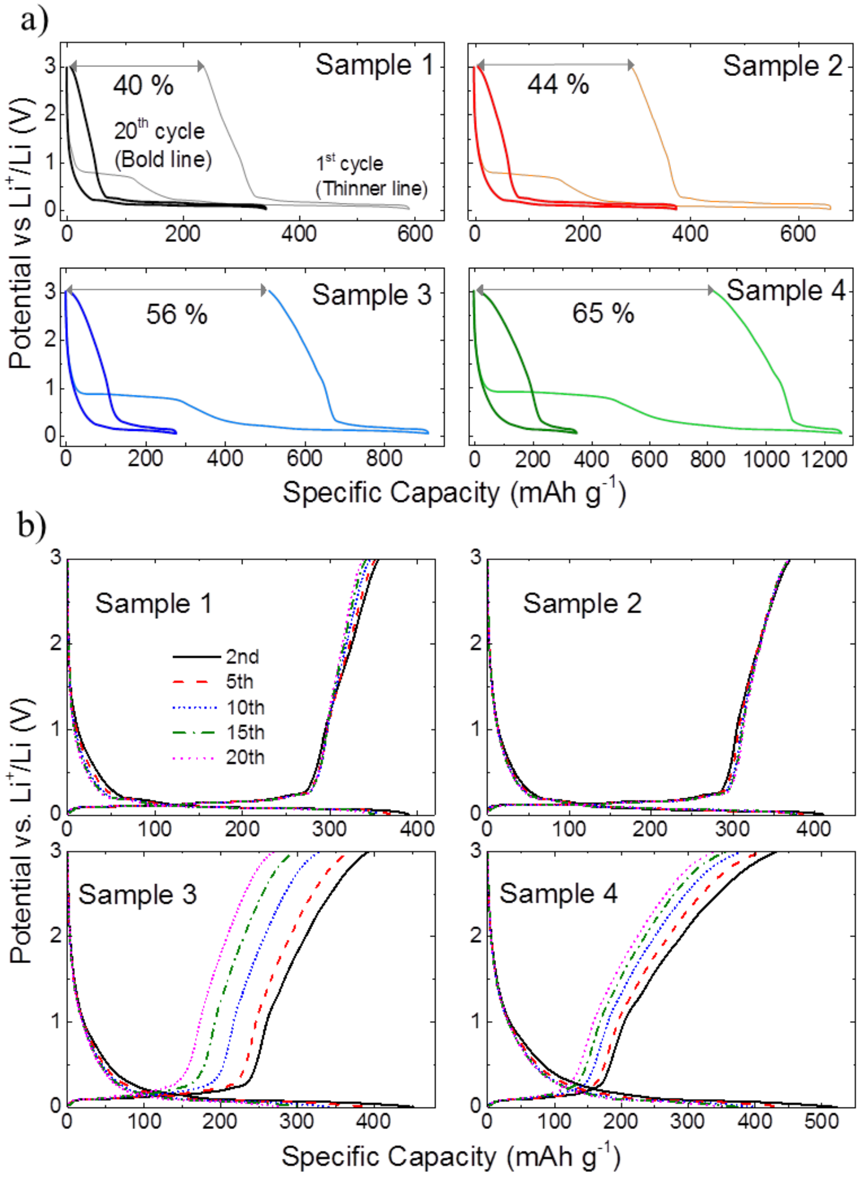


Figure 4.6. *(a) Voltage profiles ( $1^{st}$ cycle and $20^{th}$ cycle) and (b) Voltage profiles evolution (in the cycle range 2-20) of the electrodes based on Sample #1, Sample #2, Sample #3, and Sample #4 (current density: 0.1 A $g^{-1}$).*

In order to get further understanding in the $Li^+$ storage process in FLG- and MLG-based electrodes, a differential capacity analysis is carried out in the 0.005-0.3 V potential range, see Figure 4.7. For Samples #1 and #2 the $Li^+$ storage process evolves with a series of very sharp peaks, demonstrating fast kinetics and high reversibility. As extensively reported in literature, [424-426] the voltage peak sequence may be explained with the co-existence of phases, similar to those observed for graphite (*four-stage* or *staging mechanism*). [425] From the more diluted phase (>IV) to the fully lithiated one (I), all the main intercalation stages can be clearly detected in the samples with larger flakes (Samples #1 and #2). The different lithiation/de-lithiation stages are still detectable in Sample #3, however with weaker peaks for the IV to III and III to II stage-transitions. The former transition almost completely vanishes by further reducing the dimension of the flakes, *e.g.*, for Sample #4, suggesting that the majority of the flakes possesses a thickness lower than six layers, as indeed confirmed by the AFM (Figure 3.6 c and d) and Raman results (see Figure 3.8). The good news here is that the polarization associated with each intercalation stage, which is a kinetic parameter associated to the energy required to expand the van der Waals gap across two adjacent graphene layers by contrasting the repulsive interactions between guest species, [425] is not affected by the flake size. However, while large and thick flakes (Samples #1 and #2) show stable and highly reversible intercalation behavior, Samples #3 and #4 display a loss of such feature upon the first 20 cycles, which accounts for the aforementioned capacity fading (see Figure 4.6).

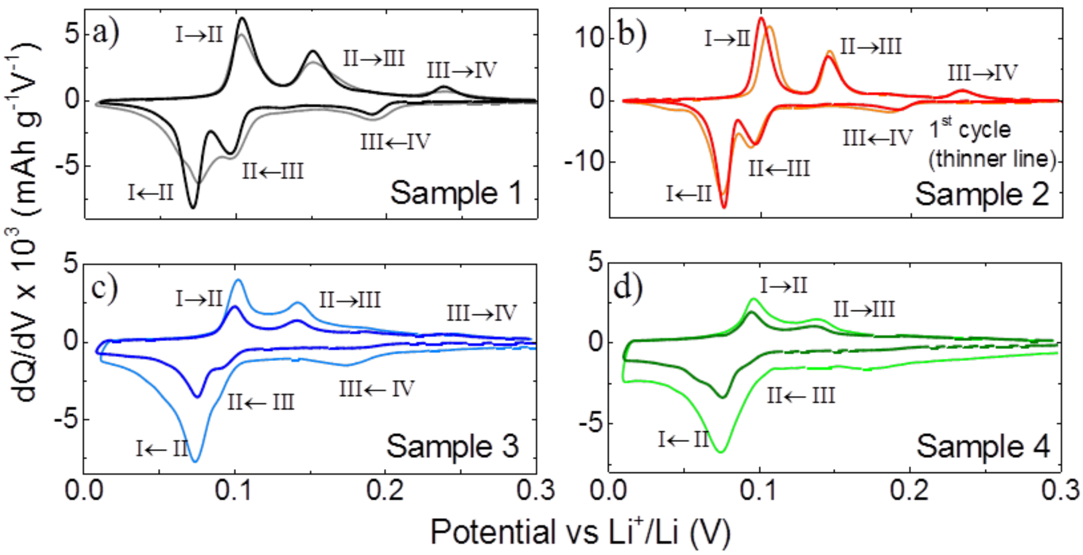


Figure 4.7. *Differential capacity plots for the 1st (dash) and 20th (solid) cycle (current rate: 0.1 $Ag^{-1}$) of the electrodes based on Sample #1, Sample #2, Sample #3, and Sample #4.*

Small lateral size MLG- and FLG-flakes (Samples #3 and #4) would be expected to enable faster $Li^+$ diffusion due to the shorter diffusion lengths for ion transport compared to the large lateral size flakes. However, the rate capability test in Figure 4.8a shows that the capacities of Samples#3 and #4 are inferior to those of Samples#1 and #2 under all different current loads (0.1 to 10 A $g^{-1}$). Noteworthy, Samples#1 and #2 provide good capacity retention up to 2 A $g^{-1}$ with respect to Samples #3 and #4. Unexpectedly, Sample#3 shows anomalously poor (but reproducible) rate performance, whose cause remains unknown and will be investigated further. After the rate capability test, the electrodes based on Samples#1 and #2 show a full capacity recovery at 0.1 A $g^{-1}$, with a coulombic efficiency approaching 100%, whereas Samples#3 and #4 show a steeper capacity fading, *e.g.*, only 74% capacity retention for Sample#3).

A further contribution to a deeper understanding of the $Li^+$ storage mechanism of MLG- and FLG-based electrodes is provided by EIS, see Figure 4.8b, c, d and e, which shows the typical signature of insertion electrodes, *e.g.*, a redox reaction which involves charge transfer resistance ($R_{CT}$) coupled with insertion of guest ions contained in an electrolyte into the physical structure of a solid host). [195] The first feature, occurring at high frequency expressed for a phenomena such as $Li^+$ diffusion through the SEI and/or with particle-particle and particle-collector contact resistances [427] both of which might indeed be in force in this study, with FLG- and MLG-flakes taking the role of the aforementioned particles. In fact, the slightly distorted shape of the semicircle suggests a scattered distribution of time constants, which makes it difficult to separate each contribution, as the sub-semicircles are highly overlapped due to very similar time constants.

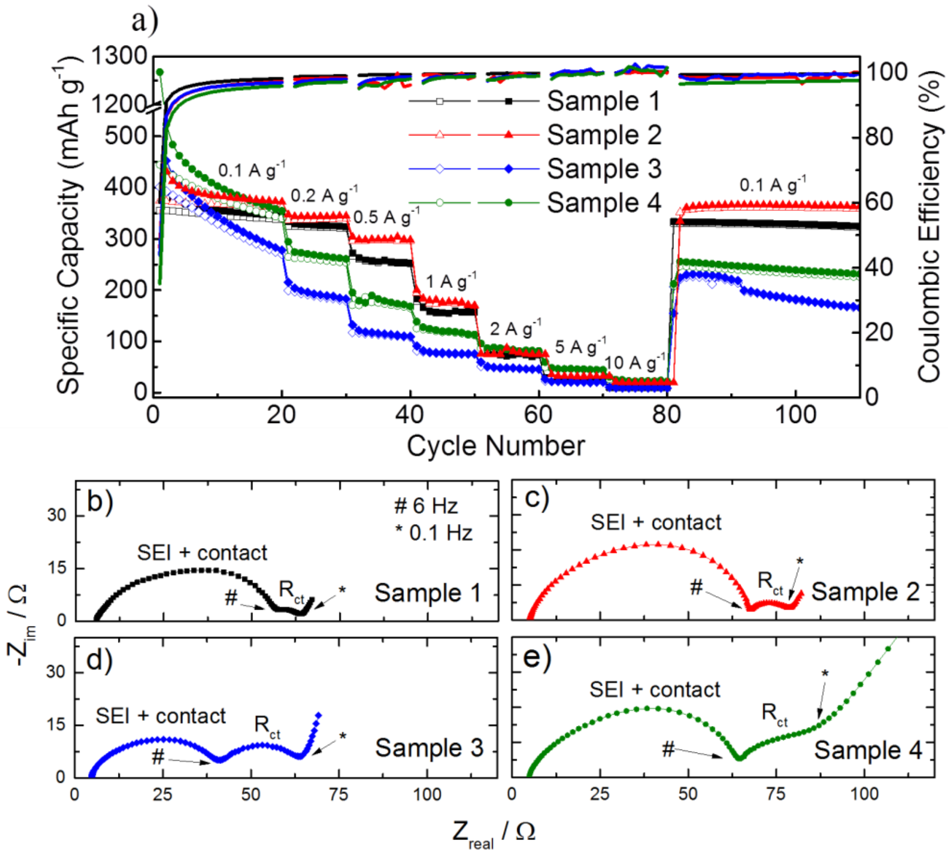


Figure 4.8. *(a) Rate capability test of the graphene flake electrode samples. (b)-(e) Nyquist plots of partially lithiated graphene flake electrode samples (collected at 0.075 V) with the main contributions of SEI, contact, and charge transfer resistances are highlighted.*

Moreover, both SEI and contact resistances are influenced by the flake dimension in a complex manner. Remarkably, the resistance of the mid-frequency semi-circle (from ca. 6-10 Hz to 0.1 Hz), attributed to the $R_{CT}$ of the $Li^+$ uptake process in the FLG- and MLG-based electrodes, displays a significant increase upon the decrease in the flake dimensions. This behavior is in agreement with several literature reports, [195, 428-430] where both theoretical and experimental results have in fact demonstrated that, as the (defect-free) graphene thickness approaches the single-layer limit, the lower Li-to-C binding energy and the stronger coulombic repulsions amongst $Li^+$ may hinder high occupancy. [157, 430] It is evident that changes in dimensions can have great influences on the $Li^+$ storage capability of FLG- and MLG- flakes. However, besides looking at the bare capacity values, we should not forget other parameters, which are equally important for practical application in LIBs. As the flakes size decreases, more capacity is delivered at high potentials. As a matter of fact, high lithiation/de-lithiation potential and sloping voltage profiles, however, might result in reduced and non-constant voltage output from the battery. The normalized charge and discharge cycles reported in Figure 4.9a and b clearly highlight to which extent the intercalation ( < 0.2 and < 0.25 V) and adsorption ( > 0.2 and > 0.25 V) storage contribute to the total state of charge (SOC) or depth of discharge (DOD) of the FLG- and MLG-based anodes. As summarized in Figure 4.9c, the intercalation is predominant in large and thick flakes, while it becomes less evident in the smaller and thinner ones. The contribution of adsorption in small and thin flakes is particularly relevant during $Li^+$ extraction, where it can account for up to 65% of the whole delivered capacity, *e.g.*, in Sample#4). Such discrepancy between charge and discharge gives rise to a voltage hysteresis, common for carbonaceous materials. [408, 431] As shown in Figure 4.9d, the higher de-lithiation potentials, associated with the reduction in dimensions of the flakes, do increase considerably the electrode average voltage during discharge. This has a detrimental effect on the voltage efficiency which, ultimately, is reduced from 40% (Sample#1 and #2) to 25% (Sample#4).

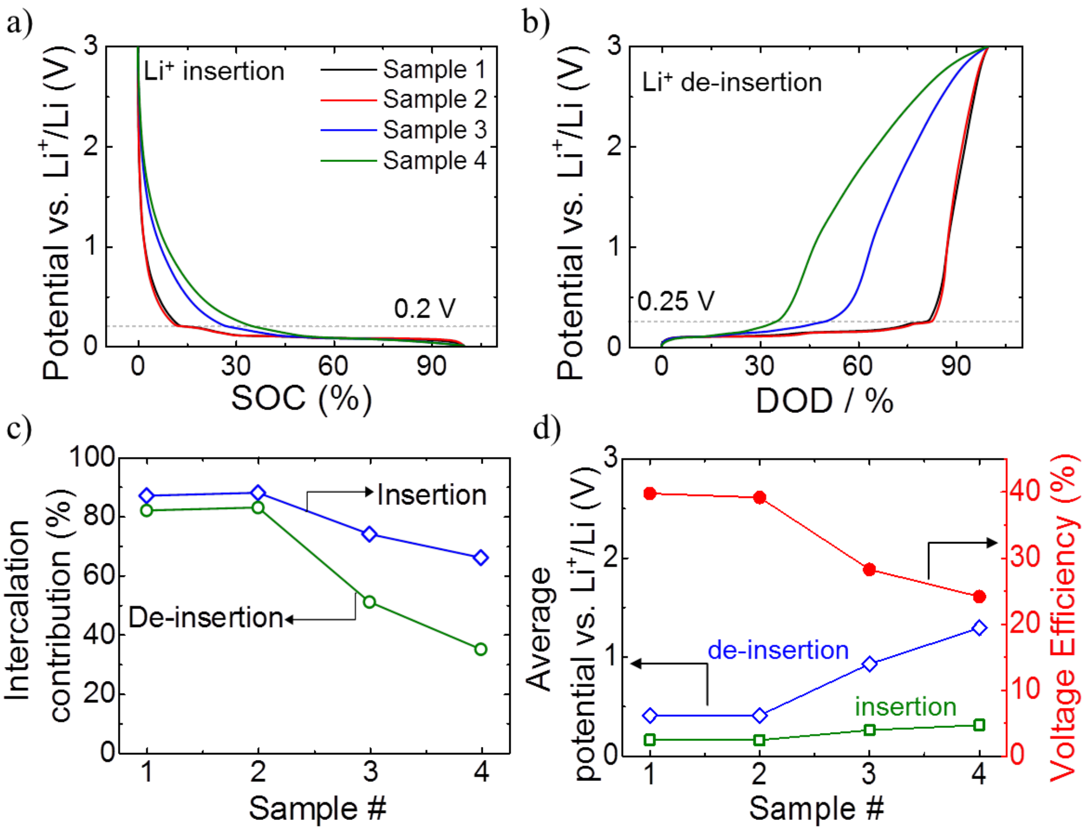


Figure 4.9. *Normalized voltage profiles of the four graphene-based samples in terms of (a) SOC and (b) DOD (obtained from the 20th cycle at 0.1 A g*$^{-1}$*). (c) Contribution of the intercalation mechanism to the total charge (calculated as the percentage of charge stored below 0.2 V or delivered above 0.25 V for lithiation and de-lithiation, respectively). (d) Effect of lithiation and de-lithiation average potentials on the voltage efficiency of the graphene anodes (the average potentials are obtained by the integral of the voltage profiles divided by the specific gravimetric capacity. The voltage efficiency is calculated as the ratio between de-lithiation and lithiation average potentials).*

### 4.4. Conclusion

In this chapter, graphene flakes (SLG/FLG) obtained by LPE of graphite in NMP and then followed by a solvent exchange process to re-disperse in environmentally friendly solvent, *e.g.*, EtOH, are used to fabricate a binder-free SLG/FLG-based anode for LIBs. This approach has several advantages in the production of anode for lithium ion batteries. First of all, the solvent exchange process can be considered as a fast, efficient and low-cost method to remove NMP from the graphene flakes, prior the deposition on the current collector. The solvent changes from NMP to EtOH can reduce the pollution and also facilitate the electrode deposition, leading to recycle the solvent (NMP) and then use for another LPE process of graphite. Secondly, the absence of any conductive agent and binder allows using a simple, one-step process to deposit the SLG/FLG-based film onto the Cu substrate, avoiding time-consuming and costly preparation procedures. The binder-free SLG/FLG-based anode exhibits a reversible specific capacity of 503 mA h $g^{-1}$ after 100 cycles at a current density of 100 mA $g^{-1}$ with a coulombic efficiency > 99.5% (Figure 4.3b). Moreover, this anode is also used in a full-cell configuration (commercial LNMO as cathode), exhibiting a working voltage around 4.7 V and a reversible specific capacity of 100 mA h $g^{-1}$. The one-step fabrication of binder-free SLG/FLG-based anode is paving the way to produce high energy/power density electrodes for LIBs through a facile coating process, with consequent reduction of the environmental impact and production costs.

Taking the advantages of the fabrication of binder-free graphene anode, a systematic and comprehensive study on the role of the morphology of MLG- to FLG-flakes on their electrochemical properties as anode for LIB is carried out. The results demonstrate that changes in the flakes dimension have indeed a significant impact into their capability of $Li^+$ storage. The decrease in flake lateral size/thickness does enable higher specific capacity values in the first cycle. Nevertheless, the capacity loss due to the SEI formation dramatically increases with the decrease in flake lateral size/thickness. Smaller flakes also show slower charge transfer kinetics attributable to lower Li-to-C binding energies and stronger coulombic repulsion among $Li^+$, with respect to the larger counterparts. It should be noted that the staging behavior of graphite, the typical “fingerprint” of the intercalation mechanism, is always observed in all samples (Figure 4.7). However, the intercalation mechanism becomes less reversible with the shrinking of flake sizes. This phenomenon arises from surface passivation, trapping of $Li^+$ due to defects, or other effects that still need to be clarified by further studies. Furthermore, a larger contribution of $Li^+$ adsorption to the overall storage capacity can be clearly noticed passing from MLG to FLG flakes. This has a detrimental effect on the average de-lithiation voltage, which substantially increases with decreasing the flake dimension, resulting on lower voltage efficiency with respect to anodes based on MLG layer graphene. In general, the results in section **4.3** demonstrate that the mission of finding the ultimate anode material for LIBs is still on-going. Graphene is probably a part of it, but, may not be the main character for the task. Fully exploiting the advantages of graphene, *e.g.*, high conductivity and large surface area, to composite with other types of anode materials, *e.g*, Si, TMOs and TMSs, can be more promising than graphene alone.

# Chapter 5:

# Application of molybdenum trioxide and molybdenum disulfide for lithium ion batteries

## 5.1. Introduction

Since graphene has been recognized more suitable as a supporting material in anodes for LIBS, the ever-increasing efforts have been devoted toward seeking promising 2D materials as active material in anodes to replace graphite. As discussed in **Chapter 1**, TMOs and TMSs are found to be the potential substitutions for graphite due to their very high specific capacity with respect to graphite. However, the issues of poor rate-capability and fast capacity fading, resulting from volume change and low intrinsic conductivity, are still limiting these materials for practical application in LIB anode. To overcome these issues, the strategies of nanostructure and composite/hybrid are proposed. This chapter introduces the studies on the production, processing and electrochemical properties of layered $MoO_3$ and $MoS_2$, which are the typical representatives of TMOs and TMSs, respectively, for LIB anode.

In the field of LIBs, orthorhombic $MoO_3$ ($\alpha$-$MoO_3$), the most thermodynamically stable phase of $MoO_3$, [432, 433] has been demonstrated as a very promising anode material, thanks to its high theoretical specific capacity of 1117 mAh $g^{-1}$. [203, 204] Additionally, the interlayer spacing as large as 0.69 nm of $\alpha$-$MoO_3$ with respect to that of graphite (0.34 nm) guarantees its $Li^+$ host capability. [434, 435] Moreover, its higher intercalation voltages (1.5 – 2.3V vs. $Li/Li^+$) compared to that of graphite (< 0.4 vs $Li/Li^+$) could reduce the safety problems caused by the electrolyte decomposition, especially for the utilization in EVs, HEVs. [436] Similar to $\alpha$-$MoO_3$, $MoS_2$ has drawn significant interest as promising substitutes for the graphite thanks to its high theoretical capacity (670 mAh $g^{-1}$), [437] large interlayer spacing (0.62 nm) [72] and high intercalation voltages (~ 0.5-1.1 V vs. $Li/Li^+$). [216] Nevertheless, there are issues that still need to be solved for these materials: (*i*) the fast capacity fading of the bulk $MoO_3$ and $MoS_2$ because of the volume change during lithiation/de-lithiation, [72, 217, 218] (*ii*) the low rate-capability due to the low electrical conductivity of $MoO_3$ and $MoS_2$. [214, 219-221] To overcome these issues, one of the most encouraging strategies for these 2D materials are reducing the lateral size of their bulk counterpart by nanostructuring, [4, 182, 438-441] and mixing the resulting nanostructures of $MoO_3$ and $MoS_2$ with carbon-based nanomaterials, such as amorphous carbon, [330, 442, 443] CNTs [167, 209, 444] and graphene, [211, 241, 445] to form composite/hybrid materials. Recently, the exploitation of various nanostructures of both $MoO_3$ and $MoS_2$ composite/hybrid material as anode materials have demonstrated significant improvements, with respect to the bulk $MoO_3$ and $MoS_2$, in term of specific capacity [446-449] and electrochemical stability. [438, 442, 450] Nevertheless, the costly production processes used, [438, 439, 442, 445] *e.g.*, CVD [206, 438, 451] or hydrothermal methods, [168, 330, 439, 440, 442] pose scalability challenges towards practical industrial application. [155, 206, 452] Additionally, the use of toxic materials [306, 453, 454] as well as binders [4, 455, 456] are also limiting factors for practical use.

This chapter firstly presents the investigation on production of nano-sized $MoO_3$, $MoS_2$ flakes and their carbon-based hybrid/composite. Secondly, the insightful studies on their electrochemical performances are carried out to demonstrate the effects of carbon-based nanomaterials on the electrochemical performances of $MoO_3$ and $MoS_2$. The LPE processes [237, 238] of bulk $MoO_3$ and $MoS_2$ in IPA are exploited as a facile and effective method for producing nano-sized $MoO_3$ and $MoS_2$ flakes, see section **2.1.3.3** and **2.1.3.4** for the detailed procedures. The hybrid structure of SWNTs-bridged $MoO_3$ is synthesized by mixing multilayer $MoO_3$ flakes with solution processed SWNTs and used as an active binder-free material for LIBs. Both the $MoO_3$ exfoliation process and the SWNTs dispersing are carried out in isopropanol, allowing a simple deposition onto the Cu substrate. The designed binder-free solution processed hybrid $MoO_3$/SWNTs anode displays a specific capacity of 865 $mAhg^{-1}$ at 100 $mAg^{-1}$ after 100 cycles, with a columbic efficiency of 99.7%. The SWNTs addition determines a network structure with the $MoO_3$ providing (*i*) long channels for electronic charge transport; (*ii*) an active anode material, instead of polymeric binder, offering extra capacity for $Li^+$ storage: (*iii*) a buffer frame in the electrode, which reduces the capacity fading caused by the volume variation of $MoO_3$ flakes during the lithiation/delithiation process. To further confirm the essential roles of SWNTs, the electrochemical properties of the multilayers $MoO_3$ combined with CB nanoparticles are characterized. This structure is not able to create the network structure seen with SWNTs, yielding a significant capacity fading of the resulting battery. These results set the basis for the exploitation of exfoliated 2D $MoO_3$ sheets as anodic materials in LIBs. Meanwhile, the $MoS_2$/C hybrids with three different weight ratios of carbon are formed by thermal decomposition of PAA (as carbon source) in Ar atmosphere. The hybrid structures consist of exfoliated $MoS_2$ flakes incorporated in carbon network. The as-prepared $MoS_2$/C hybrids are deposited onto Cu substrate, in order to investigate the effect of different carbon contents on the electrochemical properties of $MoS_2$. The $MoS_2$/C electrode with optimized carbon content features a high reversible specific capacity of 521 mAh $g^{-1}$ after 100 cycles, with a columbic efficiency of 99.7%. The results confirm that carbon network not only improves the electrical conductivity of electrode by facilitating the electron transport, but also acting as a buffer layer for active materials to avoid its volume change upon cycling. Through the optimization of the electrochemical properties, our study demonstrates a process that is promising for a production of $MoS_2$/C hybrid for $Li^+$ storage application.

### 5.2. Carbon nanotubes-bridged $MoO_3$ hybrid structure as high performance anode for lithium ion batteries

This section provides a simple, low-cost, non-toxic method to fabricate binder-free hybrid $MoO_3$/SWNTs electrode, by a solution processing of SWNTs, and then mixing with $MoO_3$ flakes and depositing the mixture on Cu substrate. This is a promising strategy for exploiting the exfoliated $MoO_3$ flakes in LIB anodes, delivering high energy and power densities as well as long lifetime. As discussed in section **2.1.3.3**, the $MoO_3$ flakes in dispersion are obtained by LPE of pristine $MoO_3$ in IPA, while the SWNTs and CB are dispersed in IPA by sonication. The diameter of SWNTs is estimated to be in the ~1.37–1.45 nm range by Raman spectroscopy whereas the diameter of the SWNTs bundle is ~10 nm according to TEM images and the corresponding statistical analysis, see Figure 3.10. The TEM images of Figure 3.11b display the $MoO_3$ flakes with lateral sizes ranging from 50 to 300 nm. The hybrid $MoO_3$/SWNTs shown in Figure 3.11d clearly demonstrates that the bundles of SWNTs act as bridges to connect isolated $MoO_3$ flakes, forming an interconnected network in the mixture of these two materials. The as-prepared samples are then exploited for the realization of electrodes, *e.g.*, anodes, for LIBs. In particular, solution processed $MoO_3$ flakes and the hybrid $MoO_3$/SWNTs mixed with ratio of 9:1 are deposited onto Cu substrates. A reference sample, *e.*g., $MoO_3$ mixed with 10% CB, is also prepared by using the same process. The mass loading of $MoO_3$, $MoO_3$/SWNTs and $MoO_3$/CB in the corresponding electrodes has been calculated as 0.80 mg, 0.74 mg and 0.75 mg, respectively. The morphology of the $MoO_3$/SWNTs and $MoO_3$/CB electrodes is characterized by SEM. The SEM image of the $MoO_3$ electrode (Figure 5.1a) shows $MoO_3$ flakes with regular polygonal shapes, which are homogenously distributed onto the Cu substrate. Figure 5.1b shows how the morphology of the hybrid $MoO_3$/SWNTs is dominated by the $MoO_3$ flakes inserted in the mesoporous network of SWNTs bundles. In contrast, the morphology of the $MoO_3$/CB electrode is dominated by large aggregates of CB, ~ 400 nm in diameter, with a few $MoO_3$ flakes observed and pointed with white arrows in the image of Figure 5.1c. In order to corroborate the presence of SWNTs, $MoO_3$ or CB, Raman spectroscopy is performed on the three electrodes of $MoO_3$, $MoO_3$/SWNTs and $MoO_3$/CB samples deposited onto Cu substrates. In Figure 5.1d, the typical Raman features of $MoO_3$, which has been shown in Figure 3.11a, [310, 457, 458] can be observed in all three samples. However, it is worth to mention that the

Raman signals of SWNTs and CB dominates the Raman spectra of the $MoO_3$/SWNTs and $MoO_3$/CB electrodes, respectively.

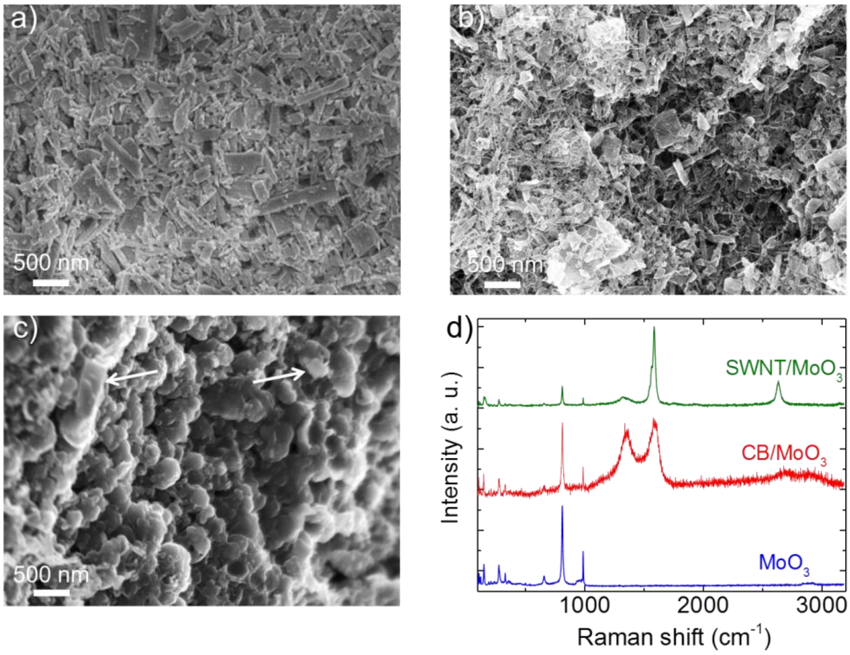


Figure 5.1. *Scanning electron microscope images of (a) $MoO_3$, (b) $MoO_3$/SWNTs and (c) $MoO_3$/CB deposited onto Cu substrates. (d) Raman spectra of the $MoO_3$/SWNTs (green), $MoO_3$/CB (red) and $MoO_3$ (blue) electrodes, deposited onto Cu substrates.*

The CV results (Figure 5.2a) of the three samples, *e.g.*, $MoO_3$, $MoO_3$/CB and $MoO_3$/SWNTs are collected at a scan rate of 50 $\mu Vs^{-1}$ starting from 5 mV vs $Li/Li^+$ potential, to cover the lithiation processes in both $MoO_3$ and SWNTs. [459] In the first reduction sweep, the $MoO_3$ exhibits two peaks at 2.3 and 2.7 V, which can be linked with the insertion of Li ions into the interlayers of the $MoO_3$ structure to form $Li_xMoO_3$, and another peak at 0.4 V, which corresponds to the conversion reaction of $Li_xMoO_3$ into Mo and $Li_2O$. [210, 460] The two processes determine, the accommodation of six Li ions in each $MoO_3$, reaching theoretical specific capacity of 1117 $mAhg^{-1}$, [203, 204] as summarized by equation 5.1 and 5.2. [210, 460]

$$MoO_3 + xLi^+ + xe^- \rightarrow Li_xMoO_3 \quad (5.1)$$

$$Li_xMoO_3 + (6-x)Li^+ + (6-x)e^- \rightarrow Mo + 3Li_2O \quad (5.2)$$

In the reverse oxidation process, metallic Mo is converted into amorphous $MoO_2$, in the 1.0 V to 2.2 V range. [210] From the 2nd cycle onward, a clear a shift is observed in the conversion reaction peak at 0.4 V, which is consistent with the formation, upon oxidation, of $MoO_2$ with lower reactivity with respect to $MoO_3$. [171] Furthermore, in the second cycle a new peak, at 1.5 V, appears which can be assigned to the lithium insertion into amorphous $MoO_2$. [171, 461] For the $MoO_3$ and the hybrid $MoO_3$/CB samples, the reduction peaks at 1.5 V and 0.4 V rapidly disappear during the following 8 cycles. On the contrary, in the case of $MoO_3$/SWNTs sample the intensity of these two peaks is maintained from cycle 2 to cycle 10, leading to a remarkable improvement on its electrochemical stability with respect to the other two samples.

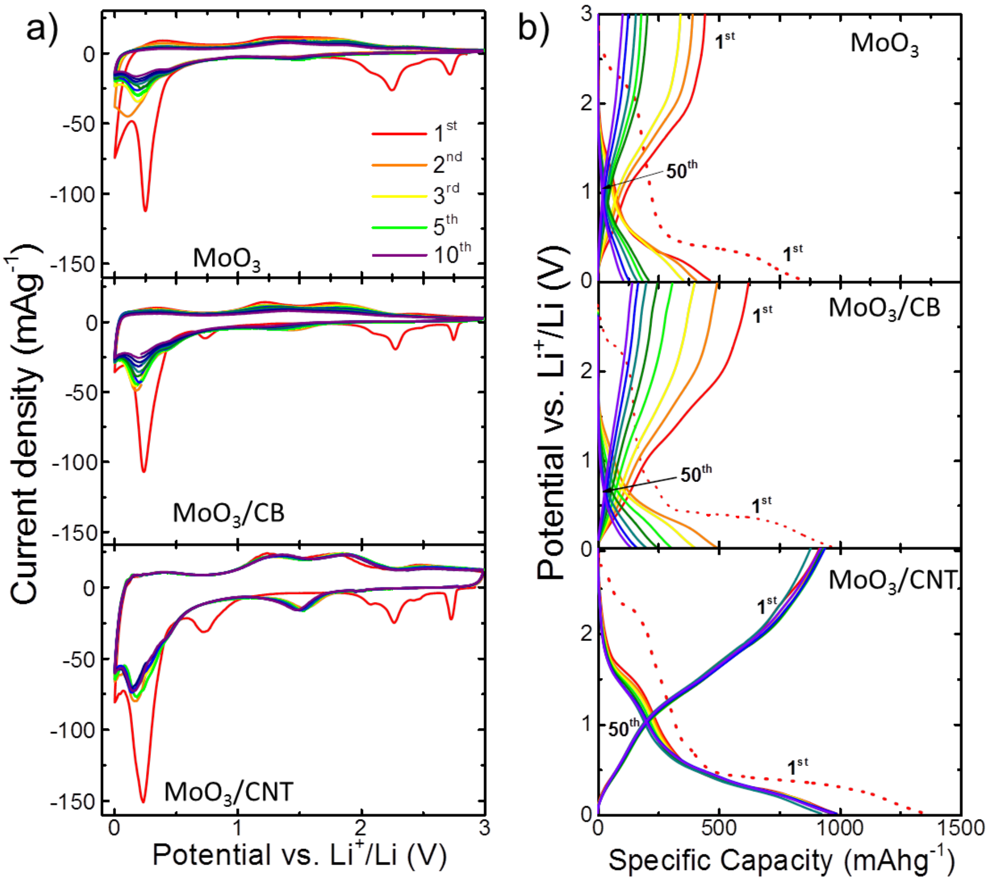


Figure 5.2. *(a) Cyclic voltammograms and (b) Charge/discharge voltage profiles of $MoO_3$, $MoO_3$/CB and $MoO_3$/SWNTs as anodes against Li foil in half cell configuration.*

Figure 5.2b shows the charge/discharge voltage profiles of bulk $MoO_3$ at 100 $mAg^{-1}$, in order to get a complete electrochemical response for the Li ion transfer, [462] during the lithiation/de-lithiation process at the anode. In the 1$^{st}$ charge (lithiation) process, two plateaus at 2.3 V and 0.4 V are observed in all the three samples. These two plateaus have already been attributed to the formation of $Li_xMoO_3$ and its following conversion reaction into metallic Mo and $LiO_2$, respectively. [210, 460] These reactions have also contribution on the large initial specific capacity obtained in the three samples, *e.g.*, 864 $mAhg^{-1}$ for $MoO_3$, 1332 $mAhg^{-1}$ for $MoO_3$/CB, and 1357 $mAhg^{-1}$ for $MoO_3$/SWNTs. The higher initial specific capacity shown by both the $MoO_3$/SWNTs and $MoO_3$/CB samples, compared with the $MoO_3$ sample, can be associated to the enhanced electrical conductivity in the hybrid electrodes due to the presence of the carbon nanomaterials. [439, 463] On the contrary, significant differences for the three samples are shown by the specific capacities obtained at the 1st discharge (de-lithiation) process. In fact, initial specific capacities of 481, 625 and 962 mAhg$^{-1}$ are achieved for the $MoO_3$, $MoO_3$/CB, and $MoO_3$/SWNT samples, respectively. For all the 3 samples, the capacity drop between the 1st charge and discharge processes (Figure 5.3a), is caused by the combination of several irreversible processes, including: (*i*) the SEI formation; [155] (*ii*) the structural modulation during $Li^+$ insertion/extraction into the inter-layers and intra-layers of $MoO_3$; [171] (*iii*) the conductivity loss caused by the electrode pulverization upon lithiation/de-lithiation. [464]

For the $MoO_3$ and $MoO_3$/CB samples, a coulombic efficiency as low as 55.7% and 46.9% is observed at the 1st cycle, respectively, see Figure 5.3a. Moreover, both samples show capacity fading upon cycling, which is the main drawback of $MoO_3$ anodes due to the pulverization of the electrode, [439] with capacity loss of 84% and 64%, respectively, after 60 cycles. Alternatively, the $MoO_3$/SWNTs sample shows a coulombic efficiency as high as 70.9% at the 1st cycle, a value which is significantly enhanced compared to the $MoO_3$ and $MoO_3$/CB samples. Additionally, the $MoO_3$/SWNTs sample shows a tangible improvement on the stability of the electrochemical performance, delivering reversible capacity of ~950 mAh g$^{-1}$ at 50th cycle, with only a 1.2% capacity loss from the 1st cycle.

In order to further understand the different electrochemical performance of the three $MoO_3$-based electrodes, the EIS for all the three samples at charged state, after 60 cycles are carried out. The Nyquist plots of the electrodes are presenting a semi-circle at high-to-medium frequency, [465] demonstrating the different interface resistances in the three samples. The interface resistance occurring at high frequency is associated with phenomena such as $Li^+$ ion diffusion through the SEI film and/or in the active material, and the contact layer between the electrode and current collector. [427, 466, 467] As obtained from Figure 5.3b, the interface resistance of the $MoO_3$ sample is ~160 $\Omega$, which is significantly reduced to ~ 80 $\Omega$ for the $MoO_3$/CB sample. The $MoO_3$/SWNTs hybrid structure gives the lowest value of interface resistance, *e.g.*, ~ 40 $\Omega$, which is one fourth and one half with respect to the ones shown by the $MoO_3$- and $MoO_3$/CB-based electrodes, respectively. The reduction of the interface resistance upon the addition of carbon additives, especially SWNTs, compared with the $MoO_3$, might be attributed to the different structural morphology of the electrodes after lithiation/de-lithiation processes. [439, 465]

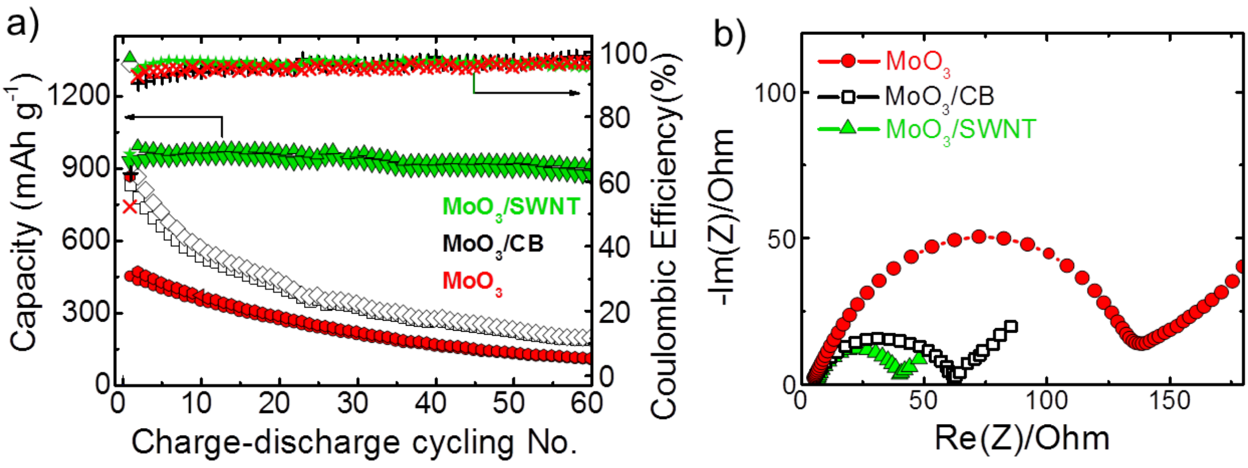


Figure 5.3. *(a) Specific capacity and coulombic efficiency over charge/discharge galvanostatic cycles, and (b) Electrochemical impedance spectroscopy of $MoO_3$ (red), $MoO_3$/SWNTs (green) and $MoO_3$/CB (black) as anodes against Li foil in half cell configuration.*

Therefore, in order to understand the relation between the electrochemical performance of the three samples and their structural morphology after charge-discharge cycles, the post-mortem SEM measurements on $MoO_3$, $MoO_3$/CB and $MoO_3$/SWNTs electrodes after 60 charge/discharge cycles are carried out. As shown in Figure 5.4a, the $MoO_3$ electrode clearly presents cracks and fractures with width of 200-400 nm, likely caused by the volume change during the charge/discharge cycles. These cracks determine a drop in the electrical conductivity, with consequent capacity fading, [204, 468] as clearly presented in Figure 5.3. As shown in Figure 5.4b, large cracks over 1 μm are observed in the $MoO_3$/CB electrode as well.

Even if, compared to free $MoO_3$, the presence of CB seems able to furnish better electrical conductivity during the first cycles, the $MoO_3$/CB electrodes still suffer a remarkable capacity fading upon cycling. This is likely due to the inability of CB to keep the anode material in continuous contact with the current collector. [468, 469] Although the $MoO_3$/SWNTs sample shows cracks after 60 cycles, the cracks are much narrower with respect to the ones presented by the $MoO_3$ and $MoO_3$/CB electrodes. Moreover, the carbon network of nanotubes ensures high electrical conductivity upon the expansion/contraction processes of $MoO_3$. This conductive framework is therefore beneficial for both mechanical stability [470] and the specific capacity of the anodes.

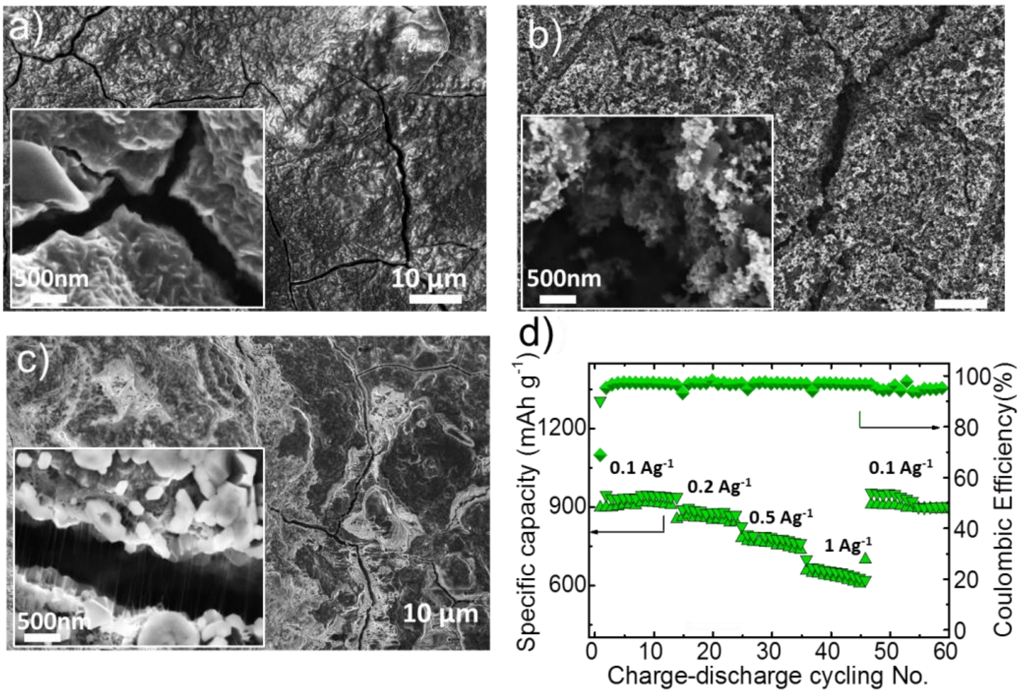


Figure 5.4. *SEM images of (a) $MoO_3$, (b) $MoO_3$/CB, (c) $MoO_3$/SWNTs electrodes after 60 charge/discharge galvanostatic cycles and (d) Specific capacity at different current densities of $MoO_3$/SWNTs anodes measured against Li foil in half cell configuration.*

In order to further investigate the electrochemical activities of the $MoO_3$/SWNTs hybrid electrode at fast charge/discharge processes, the $MoO_3$/SWNTs electrode is charged/discharged at different specific currents. As shown in Figure 5.4d, the specific capacities of $MoO_3$/SWNTs electrode after 10 cycles at each specific current have been recorded as ~956 mAh g$^{-1}$, to ~863 mAh g$^{-1}$, ~757 mAh g$^{-1}$, ~645 mAh g$^{-1}$, when the specific currents varies from 0.1 to 0.2, 0.5 and 1 A g$^{-1}$, respectively. A drop of ~30% with the specific current rising from 0.1 to 1 A g$^{-1}$, and a coulombic efficiency of ~99 % strongly suggested that the $MoO_3$/SWNTs hybrid electrode is very promising for the application of fast charge-discharge devices.

From the obtained results of $MoO_3$, $MoO_3$ CB and $MoO_3$/SWNTs electrodes, it is clear that the SWNTs addition (10% with respect to the $MoO_3$ flakes) is beneficial for the electrochemical properties of the as-produced electrodes. Thus, in order to further investigate the contribution of the SWNTs to the $MoO_3$/SWNTs hybrid anode, another two electrodes with weight ratios of 20% and 30% for SWNTs, are prepared following the preparation processes described in section **2.4.1.2**. As shown in Figure 5.5a, b and c, the three $MoO_3$/SWNTs hybrid anodes show a homogenous coverage of SWNTs and $MoO_3$ flakes onto the Cu substrates. The presence of the hybrids SWNTs and $MoO_3$ flakes is confirmed by the

Raman spectra of the three samples shown in Figure 5.5d. The spectra are normalized to the signal of $G^+$ peak of the SWNTs. The spectra show the Raman peaks of the $MoO_3$ in the region of 200-1000 $cm^{-1}$, which decrease in intensity, with respect to the $G^+$ peak of the SWNTs, as the percentage of SWNTs increases in the $MoO_3$/SWNTs hybrid. For the $MoO_3$/SWNTs-30% hybrid anode the Raman spectrum is dominated by the SWNTs signal due to their high Raman cross section. [29, 471, 472]

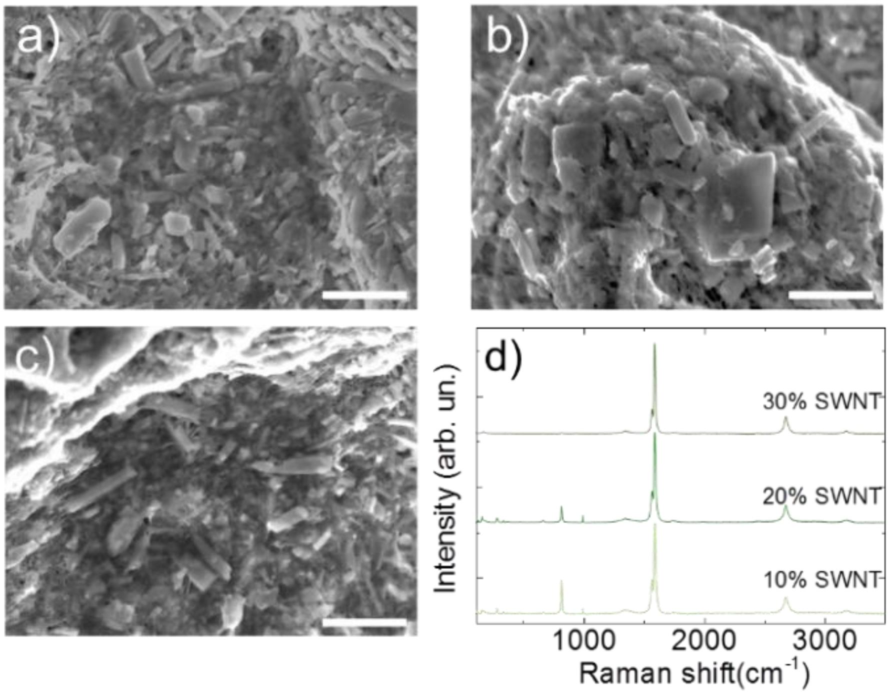


Figure 5.5. *Scanning electron microscope images of $MoO_3$/SWNTs hybrids coated onto Cu substrates with SWNTs weight ratio of (a) 10%, (b) 20% and (c) 30%, with respect to the $MoO_3$ flakes. All scale bars are 1 μm. (d) Raman spectra, acquired with an excitation wavelength of 514.5 nm, of $MoO_3$/SWNTs hybrids with 10% (light green), 20% (green), and 30% (dark green) SWNTs relative content with respect to $MoO_3$.*

The CV, galvanostatic charge/discharge and EIS measurements are carried out to understand the effects of SWNTs/$MoO_3$ weight ratio on the electrochemical performances of the $MoO_3$/SWNTs hybrid anodes. As shown in Figure 5.6a, the CV curves of the three $MoO_3$/SWNTs hybrid samples have clearly demonstrated the insertion of Li ions into the interlayers of the $MoO_3$ structure to form $Li_xMoO_3$ at 2.3 V. Additionally, the irreversible reduction peak at 0.4 V observed in all the three samples can be attributed to the conversion reaction of $Li_xMoO_3$ into Mo and $LiO_2$. A new peak at 1.5 V is appearing from the second cycle onward, representing the Li ion insertion into amorphous $MoO_2$. Moreover, the intensity of the aforementioned peak drops significantly at the second cycle, due to the lower reactivity of $MoO_2$ compared to the one of $MoO_3$. [3, 473] However, the intensity drop of this peak (at

0.4 V) is reducing with the increase of the SWNTs percentage in the $MoO_3$/SWNTs, as a result of the decreasing contribution from $MoO_3$ reaction in the hybrid structure. Moreover, two peaks at 1.5 V and 0.4 V in all three samples are observed without any shift or intensity drop in the following cycles from 2 to 10, leading to the stable electrochemical performance of the $MoO_3$/SWNTs hybrid anodes.

The post-mortem SEM images of the three $MoO_3$/SWNTs electrodes shown in Figure 5.6b, c and d clearly demonstrate that the SWNTs in the $MoO_3$/SWNTs electrode create a network between the cracked "islands" following the $MoO_3$ volume change during charge/discharge cycles. [439, 465] Notably, the width of the cracks is reducing with the percentage increase of SWNTs in the $MoO_3$/SWNT hybrids. A possible explanation could be linked with the fact that the increasing amount of SWNTs, as buffer between the $MoO_3$ flakes, can efficiently attenuate the volume change during charge/discharge cycles, reducing the mechanical degradation of the electrodes and leading to stable electrochemical performances.

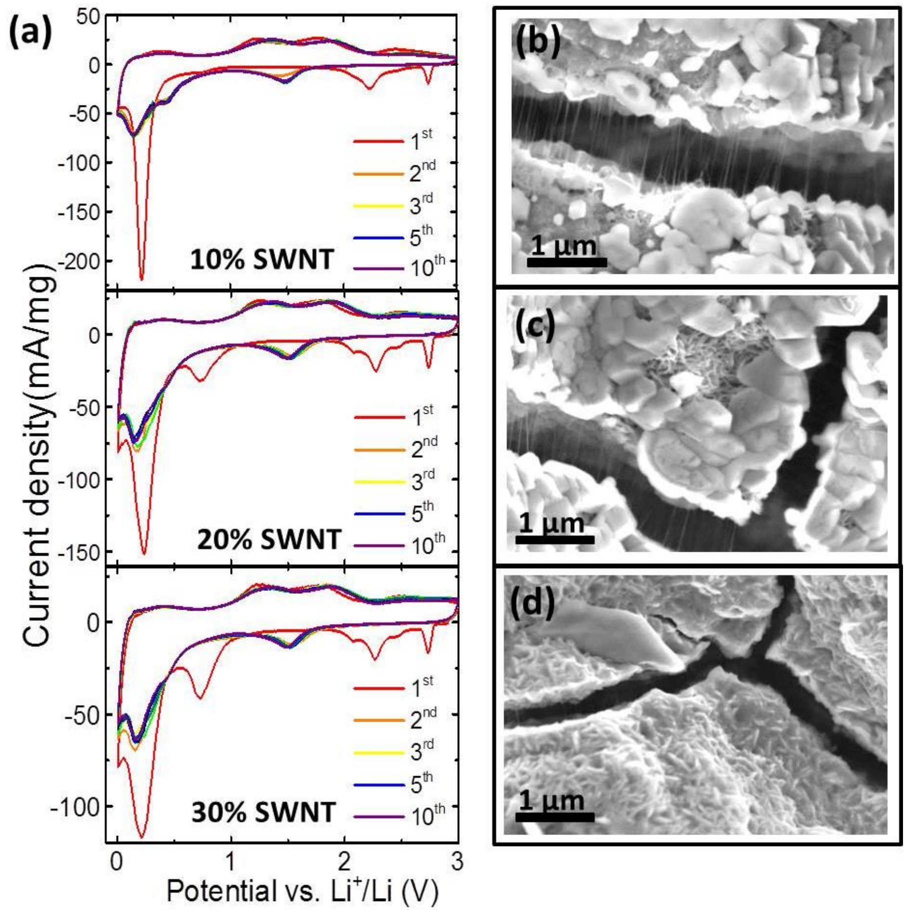


Figure 5.6. *(a) Cyclic voltammograms of $MoO_3$/SWNTs* hybrids *with different SWNT weight ratios as anodes against Li foil in half cell configuration. Scanning electron microscope images of (b) $MoO_3$/10%SWNTs, (c) $MoO_3$/20%SWNTs and (d) $MoO_3$/30%SWNTs electrodes after 100 charge/discharge galvanostatic cycles.*

As shown in Figure 5.7a, while the percentage of SWNTs in the $MoO_3$/SWNT electrodes rises from 10% to 30%, the initial capacities of the three samples reach 1357, 1161 and 1044 $mAhg^{-1}$, with corresponding discharge capacity at the first cycle of 927, 675, and 566 $mAhg^{-1}$, respectively. The specific capacity and coulombic efficiency (Figure 5.6a) demonstrate that all the hybrid electrodes with different mixed ratios show remarkable stable cyclability up to 50 cycles, if compared with the $MoO_3$ anode.

The EIS results of the 3 samples shown in Figure 5.7b, demonstrates how the higher is the percentage of SWNTs in the hybrid $MoO_3$/SWNTs electrodes, the lower is their $R_{CT}$. In fact, $R_{CT}$ values of ~40 Ω, ~30 Ω and ~17 Ω have been obtained for the sample with 10%, 20% and 30% of SWNTs with respect to the $MoO_3$ flakes, respectively. However, although higher percentage of SWNTs, *e.g.*, 20-30%, in the hybrid structure can provide better electrical conductivity, *e.g.*, $R_{CT}$ of 30 Ω and 17 Ω for the electrodes containing 20% and 30% of SWNTs with respect to the $MoO_3$ flakes) this is not directly associated to an increase of the electrode specific capacity. In fact, the increasing percentage of SWNTs has determined a tangible decrease of the specific capacity with respect to the total loading of $MoO_3$/SWNT hybrid electrodes. This could be linked with the high irreversible capacity that affect CNTs-based anode for LIBs. [254] In fact, the irreversible capacity increases from 32% for the 10% $MoO_3$/SWNTs sample to 46% in the case of 30% $MoO_3$/SWNTs one. Moreover, the 10% $MoO_3$/SWNTs sample shows the highest capacity retention (71.6% after 50 cycles) over charge/discharge cycles, obtained by dividing the charge-capacity to the initial capacity (Figure 5.2a), amongst the electrodes, *e.g.*, the hybrids $MoO_3$/SWNTs and the $MoO_3$ one.

Moreover, the specific capacity of each electrode is calculated, as shown in Figure 5.7d, labeled by different SWNTs content from 0 to 30%. The specific capacities are calculated using the mass loading of $MoO_3$ and $MoO_3$/SWNTs, respectively. In both cases, the 10% SWNTs sample reaches the highest specific capacity of 1028 $\mathrm{mAhg}_{\mathrm{MoO3}}^{-1}$ and 926 $\mathrm{mAhg}_{\mathrm{MoO3/SWNTS}}^{-1}$, see Figure 5.7d, which represent the 92% and 82%, respectively, of the theoretical specific capacity of $MoO_3$. [203, 204] The $MoO_3$/SWNTs binder-free anode in this work favorably compares with state of the art $MoO_3$-based LIB, as reported in literature. [154, 211, 432, 439, 474, 475] The reported electrochemical analysis indicates that the addition of 10% SWNTs in the hybrid structure with $MoO_3$ flakes represents the best compromise in term of mechanical and electrochemical properties of the as-produced anodes.

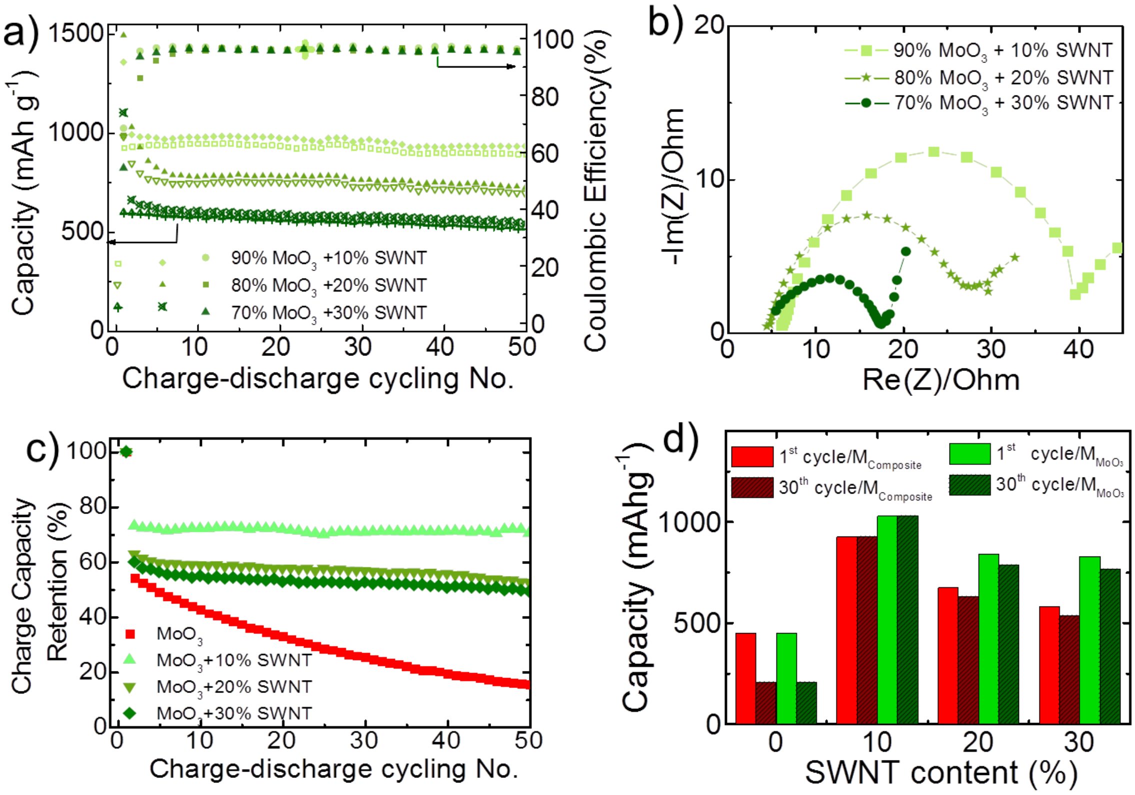


Figure 5.7. *(a) Specific capacity and coulombic efficiency over charge/discharge galvanostatic cycles, and (b) Electrochemical impedance spectroscopy of $MoO_3$/SWNTs hybrid electrodes with different SWNTs weight ratios as anodes against Li foil in half cell configuration. (c) Capacity retention of $MoO_3$/SWNTs hybrid anodes and d) Specific capacity of $MoO_3$/SWNTs hybrid anode calculated with respect the weight of $MoO_3$ (red) and the hybrid structures, respectively (green).*

### 5.3. Molybdenum disulfide flakes/amorphous carbon hybrid as anode for lithium ion batteries

Similar to $MoO_3$/SWNTs hybrid system, the goal of $MoS_2$/C in $MoS_2$ based anode is to exploit the key features of amorphous carbon in improving the electrical conductivity of electrode and accommodating the volume change of $MoS_2$ during lithiation/de-lithiation. The production of $MoS_2$ flakes via LPE and the synthesis of $MoS_2$/C hybrid via thermal decomposition of a carbon source (PAA) provide a promising strategy to obtain 2D crystals/carbon hybrid for LIB anode. In this work, the $MoS_2$ flakes obtained by LPE of bulk $MoS_2$ having an average lateral size of ~ 90 nm, see Figure 3.12a, which is advantageous for $Li^+$ diffusion due to the decrease in diffusion length. The AFM analysis, XRD and Raman spectroscopy (Figure 3.12c, d, e and f) demonstrate the reduction in thickness of $MoS_2$ layers without any change in crystal structure, with respect to its bulk counterpart, whereas the XPS results (Figure 3.12g and h) confirm the stable chemical structure of $MoS_2$ flakes after the LPE process. These results suggest that the physical and chemical properties of the obtained

$MoS_2$ flakes are not affected by the LPE process. As reported in section **2.2.2,** The $MoS_2$/C hybrids obtained by the thermal decomposition of $MoS_2$/PAA mixtures are named as $MoS_2$/C-1, $MoS_2$/C-2, and $MoS_2$/C-3, corresponding to the different mixing ratios of $MoS_2$ and PAA by weight at 1:1, 1:2 and 1:4, respectively. The carbon content in $MoS_2$/C-1, $MoS_2$/C-2, and $MoS_2$/C-3 samples is estimated to be ~ 10.1, 16.1 and 29.9 wt% with respect to the total weights of hybrid samples by TGA results (Figure 3.13a). The HR-TEM images (Figure 3.13d, e and f) demonstrate that the thickness of carbon layer in $MoS_2$/C hybrids increase with the increase in carbon content.

The $MoS_2$ flakes and $MoS_2$/C powders are mixed with CB, and a binder (PAA) in IPA, forming the slurry. The electrodes are made by depositing the slurry onto Cu disks, see section **2.2.2**. The surface morphology of the electrodes is evaluated by HR-SEM, Figure 5.8. In the case of $MoS_2$ electrode, the $MoS_2$ flakes are distributed in random orientations, as indicated by the arrows in Figure 5.8a. This feature is favorable for $Li^+$ storage due to the increase in active sites at the surface of electrode. [327] The SEM images of $MoS_2$/C electrodes show the formation of particles, suggesting the covering of carbon onto the $MoS_2$ flakes, see Figure 5.8b, c and d.

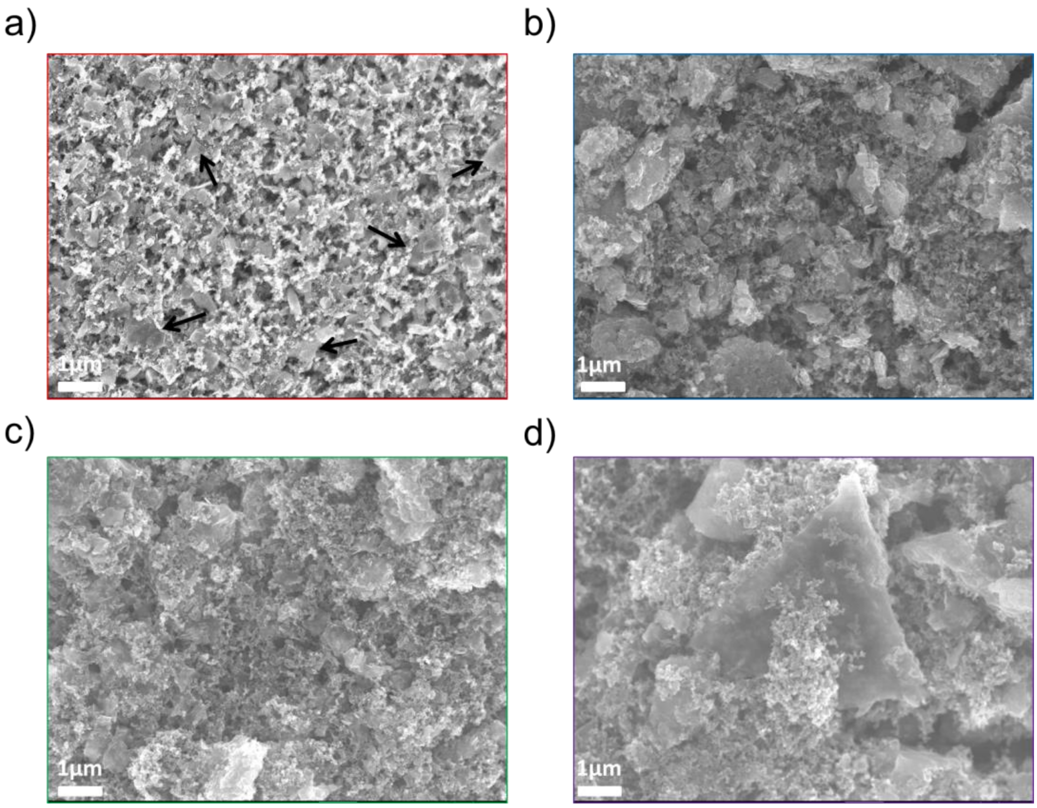


Figure 5.8. *High-Resolution-SEM of (a) $MoS_2$, (b) $MoS_2$/C-1, (c) $MoS_2$/C-2 and (d) $MoS_2$/C-3 electrodes.*

The covering of carbon onto the $MoS_2$ flakes is expected to form an electrical conductive network, which acting as a buffer prevents the volume change of $MoS_2$ during lithiation/de-lithiation. However, a large amount of carbon content also increases the thickness of carbon layer onto the $MoS_2$ flakes (Figure 5.8d), hindering the diffusion of $Li^+$ during lithiation/de-lithiation. [163, 337] Therefore, the appropriate portion of carbon on $MoS_2$ flakes need to be optimized in order to not only provide an effective conductive network between the $MoS_2$ flakes, but also allow a facile $Li^+$ diffusion during cycling process. The electrochemical properties of $MoS_2$ and $MoS_2$/C electrodes as anode for LIBs assembled in a half-cell configuration are firstly investigated by means of CV technique. The CV measurement is carried out with the scan rate of 50 $\mu Vs^{-1}$ over the potential range from 3.00 to 0.005 V vs Li/$Li^+$. Figure 5.9a shows the CV curves of $MoS_2$ electrode. In the 1$^{st}$ cycle, the first reduction peak at ~1.03 V links to the formation of $Li_xMoS_2$ by the intercalation of $Li^+$ into $MoS_2$ layers. The small reduction peak at ~0.70 V may be caused by the formation of SEI onto the surface of the $MoS_2$ electrode. [72] The reduction peak at ~ 0.46 V is instead associated to the formation of $Li_2S$ and metallic Mo nanoparticles via a conversion reaction of $Li_xMoS_2$. [72, 334, 476] The oxidation peak at ~ 2.32 V is attributed to oxidation of $Li_2S$ into $Li^+$ and sulphur (S). [72, 334, 476] Meanwhile, the broad and weak peak at ~ 1.63 V indicates the partial oxidation of metallic Mo to form $MoS_2$. [214, 327] The CV result of $MoS_2$ electrode shows a new reduction peak at ~ 1.90 V in the 2$^{nd}$ cycle, which corresponds to the reduction of S to form $Li_2S$. Besides, the oxidation peak observed at ~ 2.32 V is attributed to oxidation of $Li_2S$. The two reduction and oxidation peaks in 2$^{nd}$ cycle constitute a reversible redox couple. [72, 334, 476] From the 2$^{nd}$ cycle, the electrochemical mechanism of $MoS_2$ is mainly dominated by the reversible conversion reaction of S to $Li_2S$. [477] In general, the redox processes of $MoS_2$ can be summarized according to the following reactions: [72]

$$MoS_2 + xLi^+ \rightarrow Li_xMoS_2 \quad (5.3)$$

$$Li_xMoS_2 + (4\text{-}x)Li+ + (4\text{-}x)e^- \rightarrow Mo + 2Li_2S \quad (5.4)$$

$$Li_2S \rightarrow S + 2Li + 2e^- \quad (5.5)$$

$$S + 2Li + 2e^- \rightarrow Li_2S \quad (5.6)$$

However, the intensities of two reduction peaks (at ~ 1.03 and ~ 0.45 V) drastically decrease in the 2$^{nd}$ and 3$^{rd}$ cycles because of the consumption of residual $MoS_2$, which is not completely reduced during the 1$^{st}$ cycle. From 3$^{rd}$ cycle, the intensity of reduction peak at ~ 1.90 V is slightly increased (24.9 mA $g^{-1}$) with respect to the 2$^{nd}$ cycle, which is attributed to an activation process of the electrode materials. [478] Importantly, in the case of $MoS_2$ and

$MoS_2$/C-1 electrodes, it is observed that the intensities of oxidation peaks at ~ 2.32 V significantly decrease with the increasing of cycle number. In specific, the intensity differences of these peaks between 1$^{st}$ and 2$^{nd}$ cycles are 45 mA g$^{-1}$ and 18 mA g$^{-1}$ for $MoS_2$ and $MoS_2$/C-1 electrodes, respectively. These CV behaviors suggest that in the case of $MoS_2$ electrode, irreversible electrochemical processes take place due to irreversible redox reactions during lithiation/de-lithiation, see equations 5.3 and 5.4. [327] These irreversible redox reactions progressively produce insulated S, see equation 5.5 and 5.6, which can hinder the electron transport of $MoS_2$ electrode during cycling, resulting in its irreversible electrochemical processes. [479] The irreversible electrochemical processes are alleviated in the case of $MoS_2$/C-1 electrode due to the support of carbon network. However, these processes are still observed because the insufficient carbon content cannot completely cover all the $MoS_2$ flakes in the case of $MoS_2$/C-1 electrode (see HR-TEM image in Figure 3.13d), which still cannot completely improve the electron transport within the electrode.

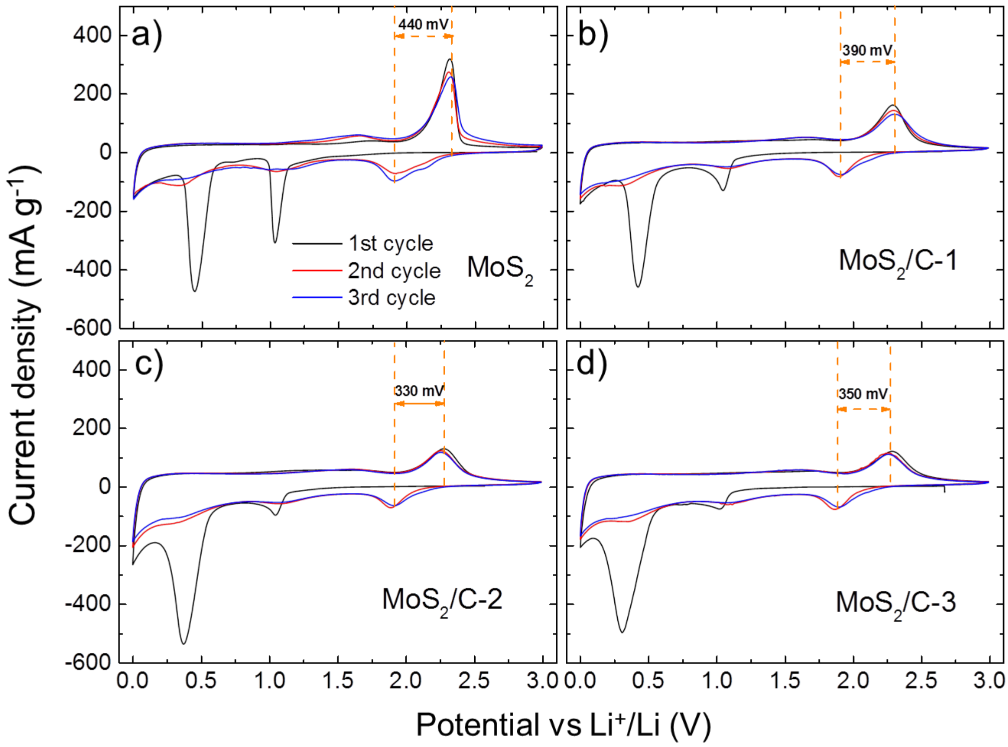


Figure 5.9. *Cyclic voltammograms of (a) $MoS_2$, (b) $MoS_2$/C-1, (c) $MoS_2$/C-2 and (d) $MoS_2$/C-3 electrodes at a scan rate of 50 μV s$^{-1}$.*

For $MoS_2$/C-2 and $MoS_2$/C-3 electrodes (Figure 5.9c and d), the intensities of oxidation peaks at ~ 2.32 V in the initial three cycles are overlapped. The $MoS_2$/C-2 and $MoS_2$/C-3 electrodes exhibit a reversible electrochemical process, in contrast to $MoS_2$ and $MoS_2$/C-1 electrodes which do not present this process, indicating that the sufficient carbon content improves the electrical conductivity of $MoS_2$. It is noteworthy to mention that the potential differences between redox peaks at ~ 1.92 and 2.32 V, after 3 cycles, is 440, 390, 330 and 350 mV, for $MoS_2$, $MoS_2$/C-1, $MoS_2$/C-2 and $MoS_2$/C-3 electrodes, respectively. This fact confirms that $MoS_2$/C electrodes have lower overall resistance and better electrochemical reversibility than in the $MoS_2$ electrode. [215, 480] As the carbon content increase, a broadening of the reduction peak set at ~0.46 V Li/$Li^+$, together with a slight decrease in the peak current, is observed. This modification finds its explanation in kinetics limitation, *e.g.*, $Li^+$ diffusion through carbon thickness, of $Li_xMoS_2$ – $Li_2S$ conversion buffered by carbon matrix. [481]

Galvanostatic charge/discharge cycling measurements are carried out at a current density of 100 mA $g^{-1}$ over the potential range from 3.00 to 0.005 V vs Li/$Li^+$ in order to fully investigate the electrochemical response for the $Li^+$ storage of the $MoS_2$ and $MoS_2$/C electrodes. In Figure 5.10, the charge/discharge voltage profiles of $MoS_2$ and $MoS_2$/C electrodes show similar electrochemical behaviours. They clearly indicate two distinct voltage plateaus at ~ 1.05 and 0.54 V in the 1$^{st}$ charge process (lithiation), which correspond to the $Li^+$ intercalation and conversion reaction of $Li_xMoS_2$ to metallic Mo and $Li_2S$, respectively, see equations 5.3 and 5.4. [336, 482, 483] Simultaneously, a severe reduction in the 1.05 V plateau length happens. This is because the $Li^+$ intercalation reaction (equation 1), corresponding to 1.05V plateau, is progressively limited as the thickness of carbon layers increase (~ 0.8, 2.4 and 13.8 nm for $MoS_2$/C-1, $MoS_2$/C-2 and $MoS_2$/C-3, respectively), see Figure 3.13c, d and f. Carbon matrix tortuosity and thickness might be responsible for the limited lithium diffusion and the direct switch to a conversion mechanism yielding metallic Mo and $Li_2S$. Thus, the increase in thickness of carbon layer can be considered as a drawback for the intercalation of $Li^+$ into $MoS_2$ layers.

A voltage plateaus at ~ 2.25 V is observed in the 1$^{st}$ discharge process (de-lithiation), the voltage plateaus at ~ 1.92 V in the 2$^{nd}$ charge process, associated with the reversible redox reaction of $Li_2S$/S couple, which always appears in the subsequent cycles. [218, 336, 482, 483] The voltage plateaus in the charge/discharge voltage profiles are consistent with the reduction and oxidation peaks in the CV results of the $MoS_2$ and $MoS_2$/C electrodes (Figure 5.9). Nevertheless, the $MoS_2$/C electrodes exhibit a good overlapped charge and discharge potential curves, upon 100 cycles with respect to $MoS_2$ electrode, a sign of a good reversible reaction during lithiation/de-lithiation. The initial irreversible capacities (the capacity difference between 1$^{st}$ charge and discharge) of the $MoS_2$, $MoS_2$/C-1, $MoS_2$/C-2 and $MoS_2$/C-3 electrodes are 295, 338, 416 and 444 mAh $g^{-1}$, respectively. The rise of the initial irreversible capacities with the increasing of carbon content could be due to the fact that the amount of amorphous carbon offers more active sites, *e.g.*, defects, for irreversible $Li^+$ storage in the 1$^{st}$ lithiation. [162, 168, 169, 484]

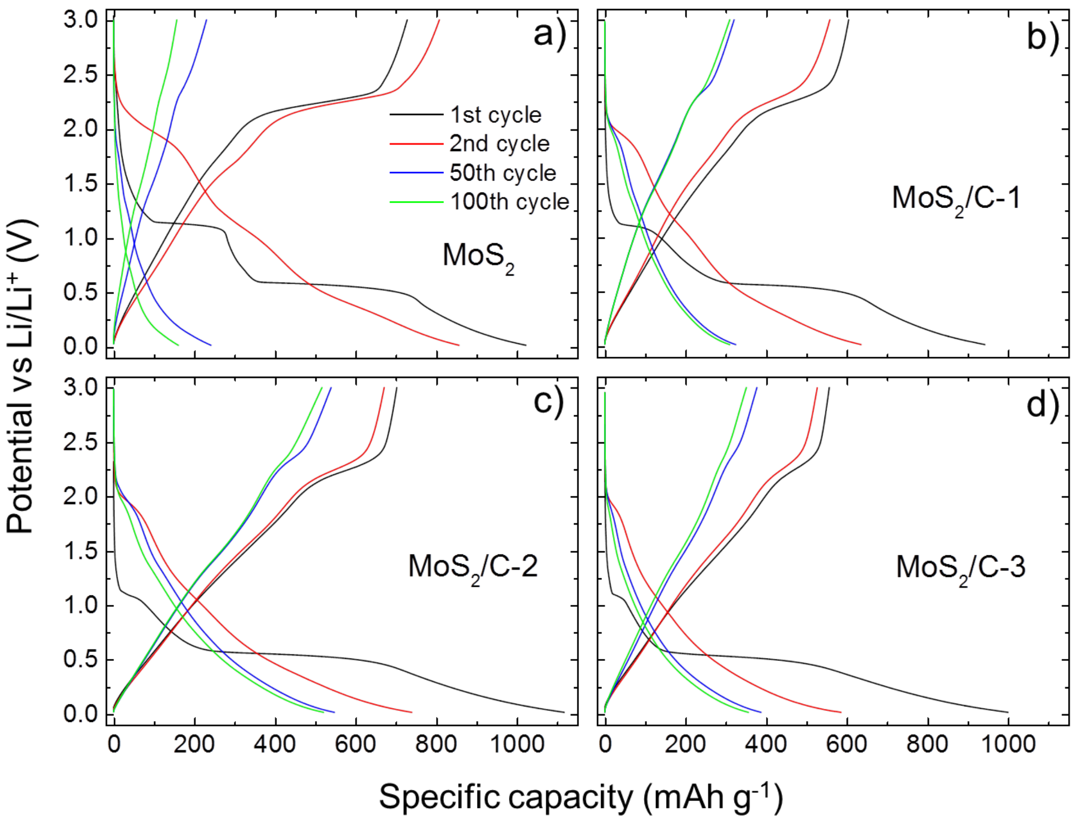


Figure 5.10. *Voltage profiles upon galvanostic charge/discharge of (a) $MoS_2$, (b) $MoS_2$/C-1, (c) $MoS_2$/C-2 and (d) $MoS_2$/C-3 electrodes at 0.1 A $g^{-1}$ between 3.00 to 0.005 V vs Li/$Li^+$.*

In order to clarify the Li+ storage capability of carbon network which may contribute to the irreversible specific capacity of $MoS_2$/C electrodes, the galvanostatic charge/discharge measurement of amorphous carbon electrode is carried out at a current density of 0.1 A $g^{-1}$ over the potential range from 3.00 to 0.005 V vs Li/$Li^+$. The amorphous carbon is obtained by the thermal decomposition of PAA, and the preparation of amorphous carbon electrode is following the preparation steps of $MoS_2$ and $MoS_2$/C electrodes reported in section **2.4.1.3**. As shown in Figure 5.11a, the charge/discharge voltage profile of amorphous carbon electrode shows the specific capacity of ~ 285 mAh $g^{-1}$ in the initial charge process. From subsequent charge processes, the electrode exhibits the continuously capacity fading of ~ 145, 117 and 94 mAh $g^{-1}$ corresponding to the $2^{nd}$, $5^{th}$ and $20^{th}$ cycles, respectively. The capacity fading during cycling suggests the irreversible $Li^+$ storage process of amorphous carbon electrode, associated to the presence of active sites, *e.g.*, defects, in amorphous carbon. [162, 168, 169, 484] The irreversible $Li^+$ storage in amorphous carbon contributes to the increase in irreversible capacities of $MoS_2$/C electrodes, as shown in Figure 5.10.

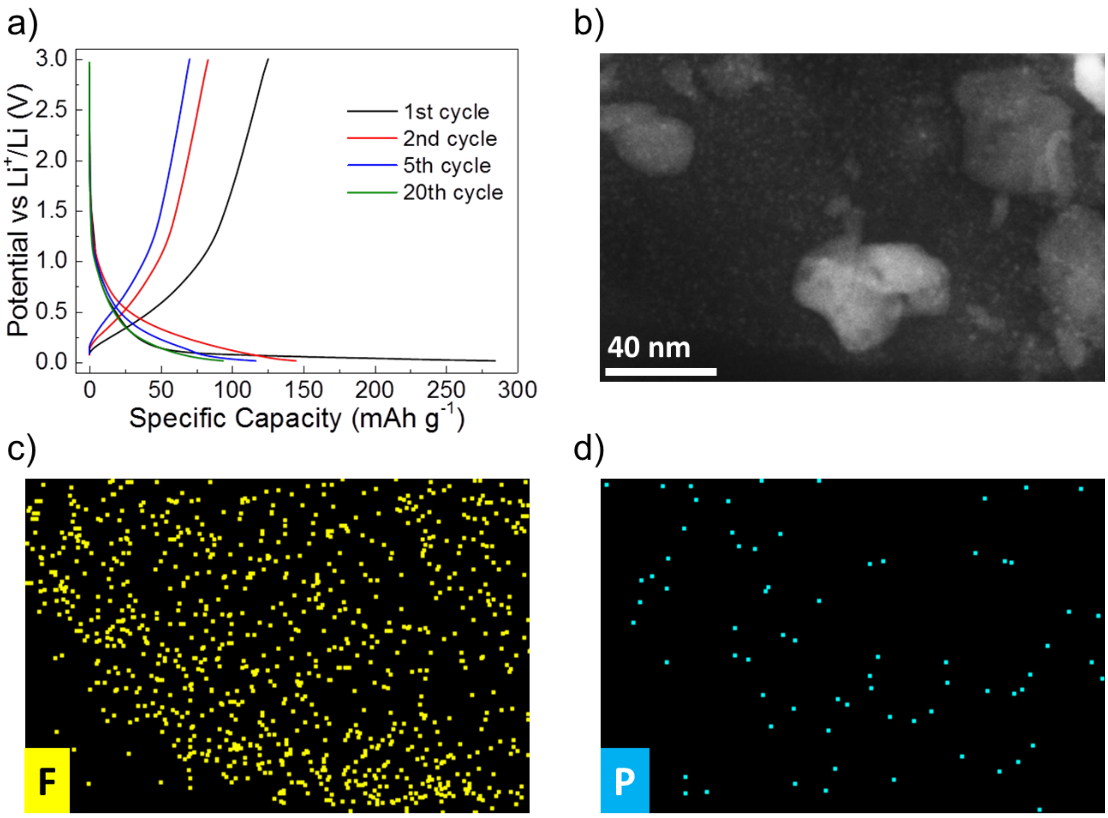


Figure 5.11. *(a) Voltage profiles upon galvanostic charge/discharge of amorphous carbon electrode at 0.1 A $g^{-1}$ between 5 mV and 3 V; (b) HAADF-STEM image of $MoS_2$ electrode after 100 charge/discharge galvanostatic cycles and elemental maps of (c) F and (d) P acquired by STEM-EDS.*

A further contribution to the initial irreversible capacity can be attributed to the formation of SEI on the surface of the electrodes. To confirm the formation of SEI, the elemental mapping of $MoS_2$ electrode after 100 charge/discharge cycles is carried out by STEM-EDS measurements. Figure 5.11b shows a high angular annular dark field - scanning TEM (HAADF)-STEM image of $MoS_2$ electrode materials, for which the corresponding elemental maps are demonstrated in Figure 5.11c and d. The distribution of fluorine (F) and phosphor (P) on the electrode can be used to identify the formation of SEI. The components of SEI are always contributed from the reduction and decomposition of the electrolyte. In this work, the $LiPF_6$ is used as the lithium salt (see section **2.4.2**), which decomposes into LiF and a small portion of $PF_5$ through the reactions 5.7 and 5.8, see the equation 5.7. [485, 486] The presence of F confirms the formation of LiF, while P is barely visible probably due to small amount of $PF_5$ in the observed area.

$$LPF_6\ (solv) \rightarrow LiF\ (s) + PF_5\ (s) \qquad (5.7)$$

The formation of SEI in $MoS_2$ electrode is in agreement with the small broad peak at ~ 0.7 V in the first cycle of its CV curve (see Figure 5.9a). In the cases of $MoS_2$/C electrodes, the increase in irreversible capacity with higher content of carbon can be attributed to the excessive interphase between $MoS_2$/amorphous carbon and electrolyte, leading to considerable side reactions of SEI formation on $MoS_2$/amorphous carbon. [330, 483, 487]

To further understand the mechanism for the effect of carbon content on the electrochemical performance of the $MoS_2$/C electrode, the EIS of $MoS_2$, $MoS_2$/C electrodes are acquired from a frequency of 10 kHz to 10 mHz. The Nyquist plots of all electrodes, Figure 5.12, consist of a depressed semi-circle in the high frequency region and a sloping straight line in the low-frequency region. The semi-circles are described by means of a generalized RC-circuit (the inset in Figure 5.12a) with electrolyte resistance $R_E$ (resistance caused by the mass transport of $Li^+$ through electrolyte), $R_{CT}$ (including the electron transfer to the reactive center $MoS_2$), and a constant phase element (CPE) for the electrode/electrolyte interface. [162, 488] The high frequency region is associated with the $R_{CT}$, whereas the low-frequency line is descriptive of the $Li^+$ diffusion impedance within the electrode which is described by the Warburg circuit element ($Z_W$) in RC-circuit. [337, 488-490] Figure 5.12a shows the Nyquist plots of $MoS_2$ and $MoS_2$/C electrodes after the 1$^{st}$ lithiation/de-lithiation, at charged state. The $R_{CT}$ values are ~ 85, 37, 29 and 70 Ω for $MoS_2$, $MoS_2$/C-1, $MoS_2$/C-2 and $MoS_2$/C-3 electrodes, respectively. The $R_{CT}$ of the $MoS_2$/C electrodes are thus lower than that of the $MoS_2$ electrode. This clearly indicates that the electrical conductivity of the $MoS_2$/C electrodes is higher than that of $MoS_2$ electrodes. This fact confirms that the incorporation of carbon improves the electrical conductivity of the $MoS_2$/C electrodes by constructing a conductive network between $MoS_2$ flakes, and thus greatly enhance electron transport within electrode during the lithiation/de-lithiation process. [306, 327] The $MoS_2$/C-2 electrode shows the lowest value of $R_{CT}$ with respect to $MoS_2$/C-1 and $MoS_2$/C-3 electrodes, suggesting that $MoS_2$/C-2 is endowed with the proper amount of carbon content so that a reasonable compromise between improved electrical conductivity of the electrode and the limited $Li^+$ diffusion through the carbon is obtained. [327, 491] Besides, among the three $MoS_2$/C electrodes, the $MoS_2$/C-3 electrode exhibits the highest $R_{CT}$ value. The increase in carbon content results in the increase in the thickness of carbon layer covering the flakes (Figure 3.13d, e and f). This feature prolongs the pathway for electron transfer across the $MoS_2$/C in the $MoS_2$/C electrode with respect to that of $MoS_2$/C-1 and $MoS_2$/C-2 electrodes, leading to the increase of the $R_{CT}$. The Nyquist plots of $MoS_2$ and $MoS_2$/C electrodes after the 100 cycles, at charged state in Figure 5.12b shows the same trend as the plots in Figure 5.12a. The $R_{CT}$ value of $MoS_2$/C-1, $MoS_2$/C-2 and $MoS_2$/C-3 electrodes exhibit the values of ~ 26, 21, and 58 Ω. The decrease in the $R_{CT}$ values of $MoS_2$/C electrodes after 100 cycles with respect to the 1st cycle can be explained based on the CV data and voltage profiles, as shown in Figure 5.9 and 5.10. According to the voltage profiles of $MoS_2$/C electrodes, the voltage plateaus at ~ 1.05 and 0.54 V related to the intercalation and conversion reactions (equation 5.3 and 5.4), are observed at the 1st charge process, see Figure 5.10b, c and d. From the 2nd charge, these voltage plateaus are still observed as the sloping curves. This is because the $MoS_2$ has not been completely consumed after the 1st charge process, therefore, the residual $MoS_2$ continuously contribute to the intercalation and conversion reactions at the 2nd charge process. These features can also be observed by the broadened shape of reduction peaks at ~ 1.03 and 0.45 V in the 2nd cycle of CV data with respect to that of 1st cycle (Figure 5.9b, c and d). Compare to the 1st charge process, the diminished voltage plateau at ~ 1.05 and 0.54 V are diminished at the 100th charge process, (Figure 5.10b, c and d) suggesting the complete consumption of residual $MoS_2$ via the intercalation and conversion reactions. [492-494] Thus, the high $R_{CT}$ values after the 1st cycle compared to that of the 100th cycle in $MoS_2$/C electrodes are attributed to the formation of residual $MoS_2$ which can limit the electron transfer across $MoS_2$/C. However, the $R_{CT}$ value of the $MoS_2$ electrode increases strictly after 100 cycles (~ 174 Ω) because of structural destruction of the active material upon cycling. The EIS results confirm the effects of carbon on the electrochemical performances of the $MoS_2$/C electrodes after cycling.

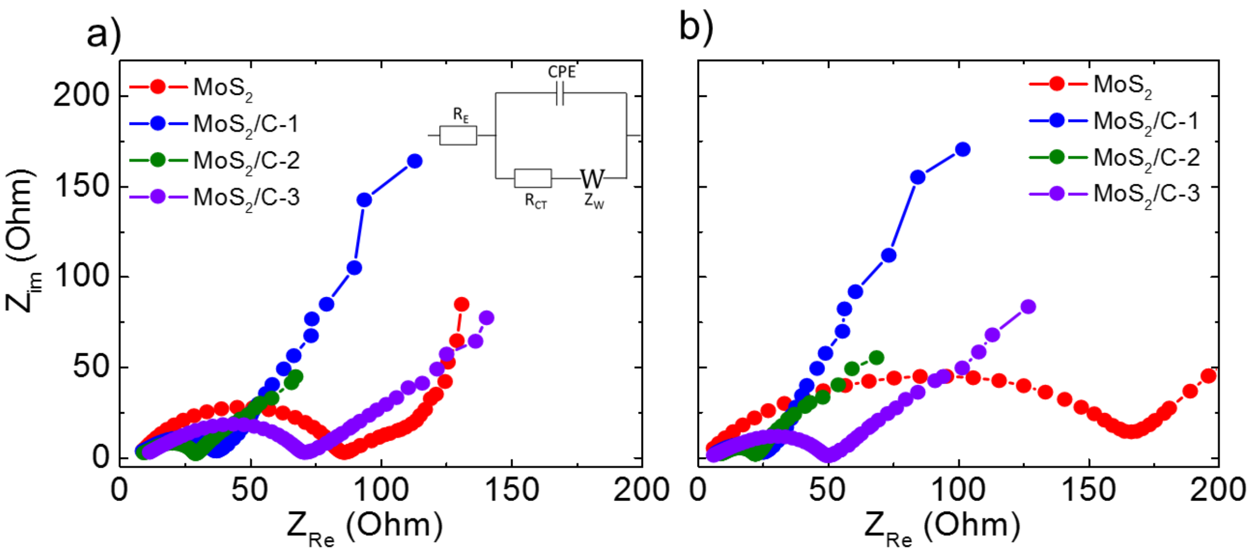


Figure 5.12. *Electrochemical impedance spectroscopy of $MoS_2$, $MoS_2$/C-1, $MoS_2$/C-2 and $MoS_2$/C-3 electrodes at charge state (a) after the 1st cycle and (b) after the 100th cycles.*

The specific capacity and coulombic efficiency over charge/discharge galvanostatic cycles at 100 mA $g^{-1}$ of $MoS_2$, $MoS_2$/C electrodes are shown in Figure 5.13a. Remarkably, the specific capacity of the $MoS_2$ electrode increases from 859 to 939 mAh $g^{-1}$ from 2nd to 9th cycle, but rapidly decrease to 161 mAh $g^{-1}$ after 100 cycles. The increase in specific capacity of $MoS_2$ electrode in the few initial cycles is due to the continuous conversion reactions of $Li_xMoS_2$, recognized also in the reduction peaks at ~ 1.03 and 0.45 V in CV data (Figure 5.9a). These reactions trigger the volume change of $MoS_2$, leading to the electrode pulverization, resulting in the introduction of defect sites. These sites may serve to trap more $Li^+$ during subsequent lithiation processes, and could explain the gradual increase in specific capacity. [163, 168, 174, 495] However, this phenomenon takes place in the initial cycles because the electrode pulverises rapidly, resulting in an electrical contact loss between $MoS_2$ and current collector, leading to a significant capacity fading in the following cycles. [72, 489] It is notable that the cyclability and specific capacities of the $MoS_2$/C electrodes is superior to that of the $MoS_2$ electrode. This demonstrates that carbon network not only hinders the capacity fading of $MoS_2$ flakes by buffering the volume change, but also enhances the electrical conductivity of electrode, by forming the carbon matrix as a conductive network. [334, 478, 491] The $MoS_2$/C-1, $MoS_2$/C-2 and $MoS_2$/C-3 electrodes retain stable specific capacities of 310, 521, 356 mAh $g^{-1}$, with a coulombic efficiency of ~ 99.6, 99.7 and 98.2 %, respectively, after 100 cycles. It is notable that the $MoS_2$/C-1 electrode exhibits a low specific capacity with respect to that of $MoS_2$/C-2 and $MoS_2$/C-3 electrodes. This result is attributed to the partial carbon covering on $MoS_2$ flakes, due to the insufficient carbon content, which is confirmed by HR-TEM image (Figure 3.13d). The incomplete embedding of $MoS_2$ flakes into carbon network is associated to capacity loss of ~ 698 mAh $g^{-1}$ (~ 80% of initial capacity) after 100 cycles, due to the structural failure by pulverization. However, the $MoS_2$/C-1 electrode is still able to preserve the reversible capacity (~310 mAh $g^{-1}$), as shown in Figure 5.13a. [336, 483] In contrast, the $MoS_2$/C-2 electrodes exhibits a significant higher specific capacities (521 mAh $g^{-1}$) with respect to $MoS_2$/C-1 and $MoS_2$/C-3 electrodes, demonstrating the high reversible $Li^+$ storage ability and good structural stability of $MoS_2$/C-2, due to the sufficient carbon content providing the complete conductive carbon network which can effectively accommodate the volume change as a buffered layer, and also improve the electrical conductivity of the electrode. However, although the $MoS_2$/C-3 electrode shows a stable cycling performance, its specific capacity (356 mAh $g^{-1}$) is drastically lower than that of $MoS_2$/C-2 electrode (521 mAh $g^{-1}$). The thickness of carbon layer induces an elongated diffusion pathway of $Li^+$, leading to low specific capacity. [166, 337]

The electrochemical characterization at varying current densities are performed (Figure 5.13b) to investigate the rate capabilities of the $MoS_2$/C electrodes. The $MoS_2$/C-2 achieves the best rate capability among the three $MoS_2$/C electrodes, with ~ 546 mAh $g^{-1}$ at 100 mA $g^{-1}$ and ~272 mAh $g^{-1}$ at 2000 mA $g^{-1}$. The specific capacity restores to ~ 500 mAh $g^{-1}$ when the current rate is changed back to 100 mA g$^{-1}$, featuring capacity retention of ~ 91.6 %. The $MoS_2$/C-3 electrode exhibits a specific capacity of ~ 402 mAh g$^{-1}$ at 100 mA g$^{-1}$ and ~ 156 mAh g$^{-1}$ at 2000 mA g$^{-1}$. The specific capacity restores to ~ 371 mAh g$^{-1}$ when the current rate is changed back to 100 mA g$^{-1}$, displaying capacity retention of ~ 92.3 %. The high values of capacity retention of $MoS_2$/C-2 and MoS2/C-3 electrodes confirm the role of carbon in structural preservation of $MoS_2$ flakes, protecting the electrode from pulverization during lithiation/de-lithiation. [337] On the contrary, $MoS_2$/C-1 electrode shows rapid capacity decay as the current density increases, indicating a capacity retention of 32.6 % when the current rate is reset from 2000 mA g$^{-1}$ to 100 mA g$^{-1}$. This is attributed to the insufficient carbon content, which is in agreement with the galvanostatic charge/discharge cycling test (Figure 5.13a).

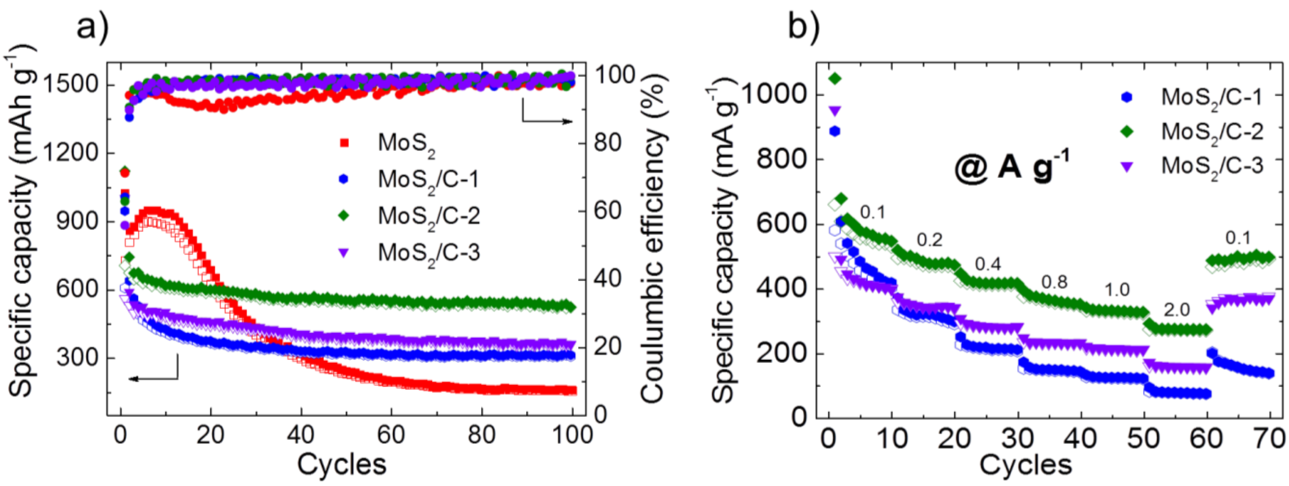


Figure 5.13. *(a) Specific capacity and Coulombic efficiency over charge/discharge galvanostatic cycles at 100 mA g$^{-1}$ and (b) rate performance at different current densities from 0.1 to 2.0 A g$^{-1}$ of $MoS_2$, $MoS_2$/C-1, $MoS_2$/C-2 and $MoS_2$/C-3 electrodes. The specific capacity capacities are normalized by the mass of $MoS_2$/C hybrids.*

To further study the effect of carbon content on the electrochemical behaviors of the electrodes, the morphologies of $MoS_2$, $MoS_2$/C-1, $MoS_2$/C-2 and $MoS_2$/C-3 electrodes after 100 charge/discharge cycles are examined by post-mortem SEM. As shown in Figure 5.14a, the $MoS_2$ electrode clearly exhibits fractures with width of ~ 3 µm (indicated by arrows), likely caused by the volume change during the charge/discharge cycles. These fractures contribute to the decrease in electrical conductivity (Figure 5.12b), and the significant capacity fading of the electrode (Figure 13a) [468, 496, 497]. On the surface of $MoS_2$/C-1 electrode the small fractures with the width of ~ 800 nm are observed as shown in Figure 5.14b. This apparently shows that the pulverization of $MoS_2$/C-1 electrode is less severe than that of the $MoS_2$ electrode. These small fractures in $MoS_2$/C-1 electrode are caused by partial pulverization during cycling due to lacking of carbon covered on flakes which is confirmed by HR-TEM images (Figure 3.13d) and galvanostatic charge/discharge cycling test (Figure 5.13a). By contrast, the surface of $MoS_2$/C-2 and $MoS_2$/C-3 electrode show a homogenous morphology and the presence of fractures mostly cannot be observed, demonstrating that the pulverization is hindered by carbon network. Thanks to the structure stability, both electrical conductivity and reversible specific capacity of $MoS_2$/C electrodes are improved if compared with the $MoS_2$ electrode, as clearly shown in Figure 5.12 and 5.13a, respectively.

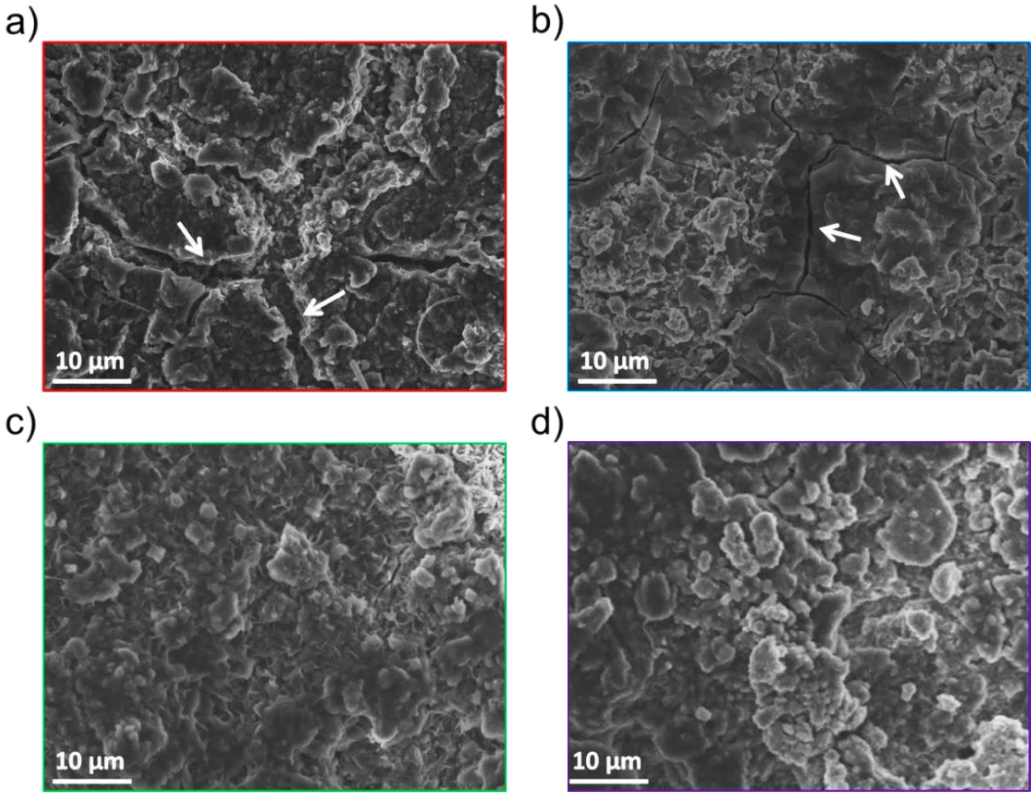


Figure 5.14. *High resolution SEM images of (a) $MoS_2$, (b) $MoS_2$/C-1, (c) $MoS_2$/C-2 and (d) $MoS_2$/C-3 electrodes after 100 charge/discharge galvanostatic cycles.*

## 5.4. Conclusion

In this chapter, I described the experimental procedure for the realization of a high performance binder-free $MoO_3$/SWNTs hybrid anode for LIBs, based on $MoO_3$ flakes obtained via LPE method, combined with solution processed SWNTs. Contrary to CB nanoparticles, the SWNTs addition determines a network structure with the $MoO_3$, which is beneficial for the mechanical and electrochemical performances of the as-produced anode by providing (*i*) long channels for electronic charge transport; (*ii*) an active anode material, instead of polymeric binder, offering extra capacity for Li ions storage: (*iii*) a buffer frame in the electrode, which reduce the capacity fading caused by the volume expansion of $MoO_3$ flakes during the lithiation process. The designed binder-free solution processed hybrid

$MoO_3$/SWNTs (90:10) anode has demonstrated a specific capacity of 865 mAh$g^{-1}$ at 100 m$Ag^{-1}$ after 100 cycles, with a columbic efficiency of 99.7% and a capacity fading of 0.02% per cycle. This work exhibits that the low-cost, non-toxic, binder-free hybrid $MoO_3$/SWNTs can boost the development of high-performance anodes for LIBs.

The LPE process of bulk $MoS_2$ in IPA is also used to produce $MoS_2$ flakes with lateral size of ~ 90 nm. A subsequent thermal composition of PAA in the mixture with $MoS_2$ flakes successfully created the $MoS_2$/C hybrids for LIB anodes. The $MoS_2$/C electrodes exhibited high capacity, an improved cyclability, and high rate cycling compared with $MoS_2$ electrode. In particular, $MoS_2$/C-2 electrode, with a ~16.11%wt of carbon content delivers a reversible specific capacity of 521 mAh $g^{-1}$ at 100 mA $g^{-1}$ after 100 charge/discharge cycles. These aspects unveiled an optimum value of carbon content in effectively embedding $MoS_2$ flakes With respect to that of $MoS_2$ electrode (~ 174 Ω) after 100 cycles, the low $R_{CT}$ value of $MoS_2$/C-2 electrode (~ 26 Ω), confirms that the proper carbon portion provides an effective conductive network. These results are ascribed to (*i*) a conductive network of carbon connecting the $MoS_2$ flakes, and facilitating the $Li^+$ diffusion and the electron transport; (*ii*) the carbon network acts as a buffer layer, easing the volume change of $MoS_2$ flakes during the lithiation/de-lithiation process. Therefore, the $MoS_2$/C hybrid fabrication protocol is a promising tool for the production of $MoS_2$/carbon hybrids and also can be easily extended to the construction of other 2D nano-crystals dispersed in amorphous carbon networks for LIB application.

# Chapter 6:

# Application of black phosphorous for lithium ion batteries

## 6.1. Introduction

Black phosphorous (BP) has recently attracted a great deal of interest because of its extremely high theoretical specific capacity of 2596 mA h $g^{-1}$. [147-149] This high theoretical specific capacity can be achieved thanks to the puckered structure of BP which allows uptaking three $Li^+$ to form $Li_3P$ compounds. [186] Additionally, the BP can exhibit outstanding charge/discharge rate because the  puckered structure allows the fast $Li^+$ diffusion is $10^4$ times faster than it is in graphene [226], *e.g.*, the diffusion energy barrier in BP is 0.09eV [498] and in graphene is 0.327eV [198]. Moreover, when exfoliated into single layer (phosphorene) or into FL-BP flakes, the increased available surface area can further enhance the electrochemical activity, which is beneficial for energy storage applications. [186]

The exfoliation of bulk BP into single- or few-layer flakes can be achieved by several strategies, such as MC, BM and LPE [183, 184] methods. The MC method exfoliate BP based on consecutively peeling off crystal layers by using adhesive tape, [142] but it is only suitable for research activities due to both the limited scalability and morphological heterogeneity of the exfoliated flakes. [142] The other exfoliation technique, *e.g.*, BM [185, 186] can meet the requirement of scalable production, but usually introduces impurities in the obtained products. [145, 187] In contrast, LPE [150, 241, 499] is an affordable and scalable alternative to MC. [183, 184] The LPE of BP in both aqueous [500] and organic solvents [235, 360, 369] has been recently demonstrated which opened up possibilities to use the exfoliated BP in applications as light absorbers, [501, 502] and energy storage devices. [500, 503] However, current approaches for the LPE of BP present several issues especially in aqueous environment, where the chemical integrity of the exfoliated flakes is compromised due to the oxidation promoted by the presence of $O_2$/$H_2O$. [227-229] The formation of phosphorus-oxide species, *i.e.* $P_2O_5$ and $P_2O_4$, [230] has been reported when the BP is exposed to air. These processes increase the roughness of the flakes and accelerate their degradation. [231] Performing the LPE in pure organic solvents solves this issue, since the presence of water and $O_2$ is avoided. The organic solvents that commonly used to exfoliate BP are generally toxic (Health code ≥ 2 NFPA704), [232] and have a b.p. usually above 100 °C, *e.g.* NMP, b.p. = 202°C, [233] DMF, b.p. = 153°C [234] CHP, b.p. = 284°C [235] or formamide (b.p. =

210 °C). [236] The solvent b.p. is critical for several applications because the solvent removal is of paramount importance for the realization of high performance anodes of batteries, [3, 504] and it is also relevant for the development of electronic, [249, 505] and optoelectronic devices. [161, 502] In general, the solvent removal is performed by heating the deposited sample or device above the solvent b.p. However, annealing procedures always run the risk of either degrading the material or damaging the device. Furthermore, in some cases the solvent degrades when heated, i.e. NMP, [506] thus it leaves contaminants or impurities on the as-prepared devices, [507] which are detrimental to their performance. [508] A possible solution for these problems is to use an easy-to-remove solvent, preferably one that is not toxic, not degrading with the annealing temperature. To date, however, a clear solution to overcome such an issue has not been found.

As discussed in section **3.5**, the importance of the solvent selection, which is of paramount importance for the ink storage, treatment, deposition and drying, crucial for the application as anodes for LIBs. In specific, the selected solvent should be able to: (*i*) exfoliate BP; (*ii*) keep a stable dispersion of the exfoliated flakes, i.e. the exfoliated flakes should not flocculate or precipitate; (*iii*) prevent the degradation of the exfoliated flakes by oxidation; (*iv*) be easily removed without leaving impurities. Interestingly, the exfoliation is also possible in acetone (see section **3.5.1**), a well-known non-toxic solvent with a low-b.p. [231] The exfoliation in acetone is attractive for real applications, *e.g.* polymer composites and functional inks, for both of which the drying time and toxicity are key factors to be considered. The exfoliation of BP in acetone is a feasible and up-scalable approach which allows fast deposition of homogeneous films of FL-BP flakes onto Cu substrate as anodes for LIBs. The study on electrochemical properties of FL-BP exfoliated in acetone indicates that it is promising with regards to the fast charge/discharge LIBs. Overall, the presented process is a step forward towards the fabrication of phosphorene-based devices.

### 6.2. Few-layer black phosphorous as anode for lithium ion batteries

The successful exfoliation of BP in acetone exploiting a low-b.p. solvent, not toxic, not degrading with the annealing temperature, offers the possibility to scale-up the production, [150, 241] for applications in the energy storage sector. To further highlight this point, this section will analyse the electrochemical properties of FL-$BP_{acetone}$-based anode, comparing to the one based on FL-$BP_{CHP}$. To this end, both dispersions are mixed with a conductive agent and a binding material, *i.e.* CB and PVdF, respectively, then deposited onto Cu substrates (see section **2.4.1.4**). The SEM images of the samples show the mixture of the FL-BP, PVdF and CB, covering the copper substrates (see Figure 6.1a and b, obtained from acetone and CHP dispersions, respectively). The optical pictures, reported as insets in Figure 6.1a and b, show the copper substrate coated with the FL-BP/CB/PVdF. These images demonstrate that a complete and uniform coverage of the substrate is achieved with the FL-$BP_{acetone}$ sample. In contrast, for the deposited FL-$BP_{CHP}$, the substrate is not uniformly coated. This inhomogeneous material distribution is attributed to the slow drying/evaporation of the CHP (hours timescale), and the temperature required to dry the electrode (~180°C). The heterogeneity in terms of material distribution, *e.g.*, FL-BP and CB/PVdF, on the electrodes is also analysed by using EDS and Raman mapping. The presence of FL-BP is characterized by means of EDS, analysing the $K_\alpha$ energy of phosphorus (2.013 eV), while the presence of CB or PVdF is identified by investigating the $K_\alpha$ energy of carbon (0.277 eV). In the FL-$BP_{acetone}$ sample, the EDS mapping (Figure 6.1c) shows that the phosphorus, in red, is homogenously distributed onto the substrate and evenly spread with the carbon, in cyan. On the contrary, for the FL-$BP_{CHP}$ sample (Figure 6.1d), the phosphorus distribution suggests that the FL-BP is aggregated, while the carbon is uniformly distributed. The Raman mapping of the film-like deposited samples further support the different distribution of FL-BP in the two samples by monitoring the signal to baseline ratio of the $A_g^1$ peak. The Raman mappings of FL-$BP_{acetone}$ and FL-$BP_{CHP}$ are shown in Fig. 6e and Fig. 6f, respectively. The Raman mapping of FL-$BP_{acetone}$ shows the homogenous presence of the $A_g^1$ peak, with an average intensity of 0.5, which confirms the uniform distribution of FL-BP crystals crystals onto the substrate. On the contrary, the FL-$BP_{CHP}$ Raman mapping presents preferential areas where the $A_g^1$ peak is concentrated (intensity 1) and others where the $A_g^1$ peak is not present (intensity 0), indicating aggregation of the FL-BP flakes.

The FL-BP-based anodes are then tested against a Li foil in a half-cell configuration, as described in the methods section. The electrochemical results of the FL-BP anodes are summarized in Figure 6.2. The CV measurement (Figure 6.2a) are performed at a rate of 30 $\mu Vs^{-1}$ in order to get an electrochemical response for the Li ion transfer from the Li foil to the FL-BP-based anodes. [509, 510] The CV scan ranges from 0.05 V to 3 V vs $Li^+/Li$, which is within the reaction range of both the formation of the solid-electrolyte interface (SEI) and the lithiation/de-lithiation processes for the BP material. [147] The first CV reduction cycle shows multiple peaks around 0.6-1.0 V, which are attributed to the phase change from BP → $Li_xP$ → LiP → $Li_2P$ → $Li_3P$. [147]

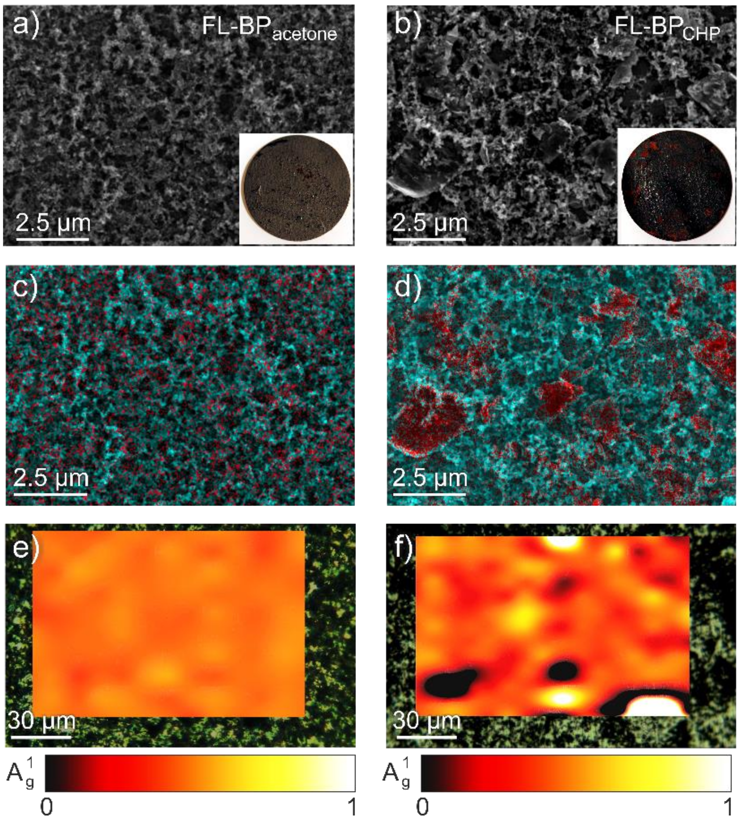


Figure 6.1. *Scanning electron microscopy images of electrodes made of a) FL-BP$_{acetone}$ and b) FL-BP$_{CHP}$, mixed with CB and PVdF deposited onto copper substrates. c) Energy-dispersive X-ray spectrometry elemental mapping of carbon (cyan) and phosphorus (red) of FL-BP$_{acetone}$ and d) FL-BP$_{CHP}$. Raman mapping on the electrodes plotting the signal to baseline intensity of the $A_g^1$ peak of e) FL-BP$_{acetone}$ and f) FL-BP$_{CHP}$.*

The voltage profiles of the FL-BP electrodes during the 1$^{st}$, and 20$^{th}$ galvanostatic charge/discharge cycles are performed at a specific current of 100 mA g$^{-1}$ between 50 mV and 3 V vs Li$^+$/Li, in order to complete the lithiation/de-lithiation (charge/discharge) process during each cycle (Figure 6.2b). From the first voltage profile of the FL-BP$_{acetone}$ anode, an initial capacity of 1732 mAh g$^{-1}$ and a discharge capacity of ~510 mAh g$^{-1}$ are measured. Such a high irreversible capacity (~1220 mAh g$^{-1}$) is typical of nanoflake size-based anodes, [5, 511] and similar behaviour has already been reported for BP-based anodes. [148, 234] The high irreversible capacity is associated to the large quantity of Li ions that are consumed for the SEI formation on the FL-BP large surface area and trapped by the high energy binding on the edges. [5, 511] The voltage profiles of both FL-BP anodes show that more than 80% of the electrode capacity is delivered at a potential that is lower than 1 V vs Li$^+$/Li over the 20 cycles. Such a low potential is beneficial for the application of the FL-BP anode material to target high energy-efficiency LIBs. [191]

As shown in Figure 6.2c, both FL-BP anodes present a significant capacity which fades within the first 10 cycles. This could be caused by the large volume change that originates from the lithiation/de-lithiation processes during different $Li_XP$ phases. [147] However, the FL-$BP_{acetone}$ anode stabilizes at a specific capacity of ~480 mAh $g^{-1}$, with a coulombic efficiency of 99.6% after 100 charge/discharge cycles, taken at a current density of 0.1 A $g^{-1}$. Meanwhile, the anode based on FL-$BP_{CHP}$, tested under the same experimental conditions, shows a specific capacity of ~200 mAh $g^{-1}$ with a coulombic efficiency of 99.6%. To get further insights on the performances, the two FL-BP electrodes are cycled between 50 mV to 3 V vs Li+/Li at specific currents ranging from 0.1 to 1 A $g^{-1}$ in order to investigate the electrochemistry activities of the samples during fast lithiation/de-lithiation (charge/discharge) processes. The results, presented in Figure 6.2d, demonstrate that the FL-$BP_{acetone}$ electrode presents stable discharge cyclability with a specific capacity of 447 mAh $g^{-1}$ at a specific current of 0.2 A $g^{-1}$ after the $20^{th}$ charge/discharge and a coulombic efficiency of 99.7%. On the other hand, under the same experimental conditions, the FL-$BP_{CHP}$ electrode reaches a specific capacity of 185 mAh $g^{-1}$ and a coulombic efficiency of 99.4% (Figure 6.2c and d).

Furthermore, for the FL-$BP_{acetone}$ based anode, specific capacities of 382 mAh $g^{-1}$ and 345 mAh $g^{-1}$ are reached at current densities of 0.5 A $g^{-1}$ and 1 A $g^{-1}$, respectively. Only less than a 30% drop in the specific capacities (from 480 mA $g^{-1}$ to 345 mAh $g^{-1}$) is observed for the FL-$BP_{acetone}$ anode which was tested at both a low (0.1 A $g^{-1}$) and a high current density (1 A $g^{-1}$), indicating that the FL-$BP_{acetone}$ based battery is a promising option for fast charge/discharge devices. [149, 195, 512] Although the specific capacity of the FL-$BP_{CHP}$ anode also presents a drop of 10% with the specific current varying from 0.1 to 1 A $g^{-1}$, its specific capacity still remains below 200 mAh $g^{-1}$, *i.e.* 50% lower than the one based on FL-$BP_{acetone}$. Moreover, the FL-$BP_{acetone}$-based anode outperforms previously reported anodes based on solution processed BP (*i.e.* ~200 mAh $g^{-1}$ at 0.1 A $g^{-1}$ after the second discharge cycle, [500] and ~250 mAh $g^{-1}$ at 0.1 A $g^{-1}$ after the first discharge cycle [234]). The difference in the electrochemical performances of the two different anodes, *i.e.* the specific capacity, is attributed to the aggregation of the FL-$BP_{CHP}$ after the deposition, as demonstrated by both the SEM and Raman mappings reported in Figure 6.1. In contrast, the FL-$BP_{acetone}$ flakes do not aggregate after the deposition onto the copper substrate.

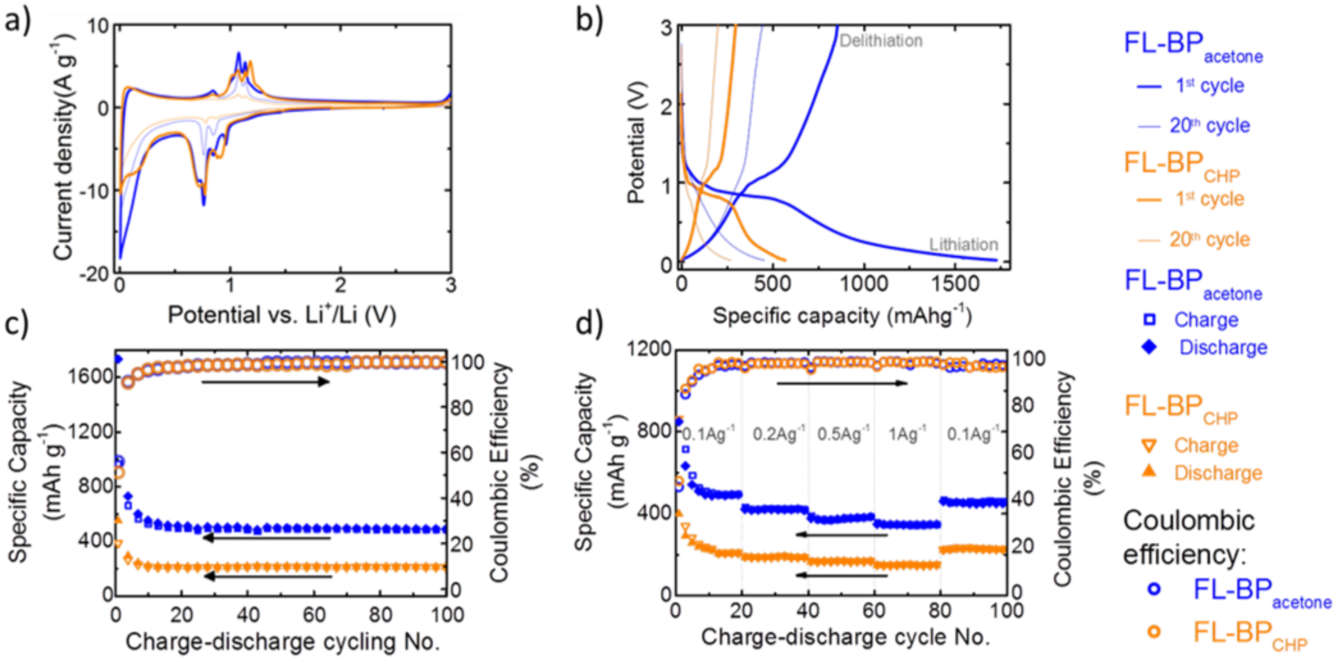


Figure 6.2. *The electrochemical analysis of the FL-BP film (acetone exfoliated sample data points shown in blue; CHP exfoliated sample data points shown in orange). (a) Cyclic voltrammetries at a scan rate of 30 µVs$^{-1}$ and (b) voltage profile upon galvanostatic charge/discharge of BP-based electrodes at 0.1 A g$^{-1}$ between 50 mV and 3 V. Thick and thin lines correspond to 1$^{st}$ and 20$^{th}$ cycle, respectively. (c) Specific capacity and coulombic efficiency over galvanostatic charge/ discharge and cycling between 50 mV and 3 V at 0.1 Ag$^{-1}$ (d) and different specific currents, for both the FL-BP$_{acetone}$- and FL-BP$_{CHP}$-based electrode*

### 6.3. Conclusion

In conclusion, the exfoliation of bulk BP in acetone has been exploited for the realization of LIB anodes. The FL-BP$_{acetone}$ flakes are homogenously distributed onto the current collector substrate thanks to the fast solvent removal. The FL-BP$_{acetone}$ based anodes, tested in half-cell configuration, achieved a specific capacity of 480 mA g$^{-1}$ at a current density of 0.1 A g$^{-1}$, with a coulombic efficiency of 99.6% after 100 charge/discharge cycles. The FL-BP$_{acetone}$-based anode outperformed the FL-BP$_{CHP}$- based one (~200 mAh g$^{-1}$ after 100 cycles at 0.1 A g$^{-1}$, achieving a coulombic efficiency of ~99.0%). The proposed liquid phase exfoliation process can also be scaled-up since the use of acetone does not present environmental risks, whereas both CHP and NMP do. Finally, the exfoliation of BP in acetone can be further improved by the addition of acetone-soluble polymers, thus enabling the large-scale production of FL-BP/polymer composites.

# Chapter 7:

# Conclusion and outlook

Up to date, the search for novel materials is still one of the crucial quests for the development of high-performance lithium ion batteries (LIBs). In this context, two dimensional materials (2D) have been recognized as promising candidates for future LIB applications because their unique structure not only provides the efficient ion transport channels between the layers, facilitating the diffusion of $Li^+$, but also offers the large surface area for $Li^+$ storage. Graphene, transition metal oxides (TMOs) and transition metal sulfides (TMSs) and black phosphorous (BP) have been recognized as promising materials for future LIB technology. Therefore, this thesis focused on the production of graphene, $MoO_3$ (as a representative for TMOs) and $MoS_2$ (as a representative for TMSs) and BP by liquid phase exfoliation (LPE) of their bulk counterparts for LIB anodes. The study of graphene anode provides a fast and simple preparation route to fabricate binder-free graphene anode for the improvement of specific capacity with respect to commercial graphite anode. Moreover, the study on the effects of flakes dimensions (lateral size and thickness) on the electrochemical performance of graphene flakes as anode material provides the guidelines for the practical exploitation of graphene-based electrodes. In addition to graphene, the understanding of the electrochemical properties of $MoO_3$ and $MoS_2$ provides a strategy in material synthesis, *e.g.*, single wall carbon nanotube bridge-$MoO_3$ flakes ($MoO_3$/SWNTs) hybrid and $MoS_2$ flakes/amorphous carbon hybrid ($MoS_2$/C), to overcome the current issues of these materials for LIB anode, *e.g.*, volume change upon cycling, low electrical conductivity. Furthermore, the activity on the exfoliation of BP in different solvents offers the opportunity to understand the role of solvent parameters on exfoliation and dispersability of BP flakes. Based on this, we can determine the ideal solvent which can meet the requirement for the exfoliation of BP and the realization of LIBs. The aim of this chapter is to summarize the most relevant results achieved on graphene, $MoO_3$, $MoS_2$ and BP based anodes. In addition, the future developments for each of these materials in LIB technology are discussed.

### 7.1. Graphene-based anode for lithium ion batteries

The aim of my research on graphene based LIB anode relied on the exploitation of LPE to produce graphene flakes from graphite (LPE graphene) because the LPE graphene flakes have high crystallinity, that is, a key feature for assuring fast electron transport to the electrode support. In this work, the obtained graphene ink after LPE process is enriched in single- (SLG) and few-layer (FLG) graphene flakes. However, the drawback of LPE graphene is the use of high boiling-point, toxic solvent, *e.g*, N-Methyl-2-pyrrolidone (NMP) which is a critical issue both for the electrode deposition and the health and environment. Therefore, the solvent-exchange process of graphene flakes by using vacuum filtration was exploited to exchange NMP into a low-b.p. and environmental-friendly solvent, *e.g*, ethanol (EtOH). In addition, it is important to evaluate the influence of solvent exchange process on the physical and chemical properties of the graphene flakes. To this aim, transmission electron microscopy (TEM), X-ray photoelectron spectroscopy (XPS) and Raman spectroscopy have been used. In particular, comparing the TEM and Raman characterizations of graphene flakes in NMP and EtOH, it is clearly demonstrated that the solvent exchange process does not affect the structural and morphological properties of the graphene flakes. Besides, the XPS analysis indicates that from one hand the solvent exchange process does not induce oxidation of the graphene flakes and from the other hand, it allows the removal of ~50% of the NMP molecules adsorbed onto the graphene flakes. Briefly, the solvent exchange process allows obtaining high crystallinity graphene flakes in EtOH, which enables the fast electrode fabrication at room temperature with respect to graphene flakes in NMP.

Taking the advantage of solvent exchange process, I fabricated the binder-free graphene anode via drop-casting graphene flakes in EtOH at room temperature (one-step fabrication) and studied its electrochemical properties. The graphene electrode in half-cell configuration exhibits remarkable electrochemical performance and stability, a charge/discharge specific capacity of 503 mA $hg^{-1}$ after 100 cycles at a current density of 100 mA $g^{-1}$ with a coulombic efficiency > 99.5%. Moreover, the graphene anode shows its functionality also in a full-cell configuration, exploiting commercial $LiNi_{0.5}Mn_{1.5}O_4$ (LNMO) as cathode, with a reversible specific capacity of ~ 100 mAh $g^{-1}$. The results obtained by using the binder-free graphene electrodes, both in half- and full-cell configuration, provides useful guidelines for the practical exploitation not only for graphene but also for other 2D materials as stand-alone anode materials in LIBs. Moreover, compared to the commercial graphite anode the one-step preparation route of binder-free graphene anode is opening the way to the improvement of capacity (by utilizing 100% the weight of active material) through a low-cost, facile coating process (drop-casting of graphene dispersion at room temperature), with consequent reduction of the environmental impact (using environmental friendly solvents).

The dimension (lateral size and thickness) of the graphene flakes has an important role in the $Li^+$ storage mechanisms, but the link between these morphological properties, and electrochemical performances were not established yet. Therefore, the sorting of graphene flakes after the exfoliation of graphite with various dimensions by means of sedimentation based separation (SBS) has been carried to clarify the roles of graphene flakes dimension on electrochemical performance of LIB anode. The SBS exploiting different centrifugal speeds, coupling with the solvent exchange process allows producing four dispersions of graphene flakes in NMP. The TEM and AFM measurements have been exploited for the characterization of the flakes morphology of the four samples. In particular, the graphene flakes dimension decreases, from Sample#1 to #4, with the increase in centrifugal speed. The Raman spectroscopies of graphene flakes in the four samples show that Sample#1 and #2 are mostly formed of thick (20–50 layers) MLG flakes, while Sample#3 is composed of thinner multi-layer graphene (MLG) (10–15 layers) and Sample#4 comprised of FLG flakes. Importantly, the obtained electrochemical results demonstrate that the MLG flakes (20–50 layers) having average lateral size ranging from 180-380 nm, have not yet demonstrated considerable gain in maximum specific capacity (~ 341–366 mAh $g^{-1}$) compared to the theoretical specific capacity of graphite (372 mAh $g^{-1}$). Meanwhile, more capacity is delivered at high potentials (> 0.2 V vs $Li/Li^+$) upon graphene flake size reduction, due to the preferential $Li^+$ storage by adsorption rather than intercalation in small lateral size (~100 nm) and thin (< 15 layers) flakes, resulting in reduced and non-constant voltage output, which is a detrimental factor for voltage efficiency. This study demonstrates that graphene might be still involved in the list of ultimate LIB electrode materials, but it may not be considered as the active materials. Nevertheless, graphene can be used as a supporting platform for other types of active materials in composite or hybrid structures, *e.g.*, conductive agent, buffered layer for volume change of active material, etc.

## 7.2. Molybdenum oxides- and molybdenum disulfide-based anode for lithium ion batteries

In the second part of my PhD program, I started to investigate the electrochemical properties of $MoO_3$, $MoS_2$ flakes and their carbon-based hybrid structures with the aim to contribute in the understanding on the effects of carbon materials on $Li^+$ storage ability of $MoO_3$ and $MoS_2$. Although $MoO_3$ and $MoS_2$ exhibit high theoretical capacity with respect to that of graphite, these materials are still commonly facing the issues of volume change upon cycling and low electrical conductivity. Thus, nanostructuring and hybrid synthesis were proposed to be the viable strategies to overcome the current issues of $MoO_3$ and $MoS_2$. In particular, the nano-sized $MoO_3$ and $MoS_2$ flakes reduce the length for $Li^+$ diffusion and mitigate the volume change during charging/discharging process with respect to their bulk counterparts. In addition to nanostructuring, the synthesis of $MoO_3$/SWNTs and $MoS_2$/C hybrid is an effective strategy to exploit the preeminent properties of carbon-based materials, *e.g.*, high electrical conductivity and mechanical strength, to compensate for the limited properties of active materials, *e.g.*, buffering the volume change and enhancing the conductivity of electrodes.

In the case of $MoO_3$ flakes-based anode, the $MoO_3$/SWNTs hybrid was formed by exploiting a simple solution mixing process. The SWNTs in $MoO_3$/SWNTs hybrid play a role of bridging the isolated $MoO_3$ flakes, forming an interconnected network in the mixture of $MoO_3$/SWNTs. This structure enables long channels for electron transport and a buffered frame for accommodating the volume change of active material during lithiation/de-lithiation process. Indeed, the surface morphology of the $MoO_3$/SWNTs hybrid electrode after 100 charge/discharge cycles demonstrates that the SWNTs in the $MoO_3$ /SWNT electrode create a network between the cracked 'islands' following the $MoO_3$ volume change during charge/discharge cycles. Hence, the $MoO_3$/SWNTs hybrid anode displays a high specific capacity of ~ 865 mAh $g^{-1}$ at 100 mA $g^{-1}$ after 100 cycles, with a columbic efficiency of ~99.7%. This study set the basis for the exploitation of exfoliated $MoO_3$ flakes as anode materials in high LIB. Moreover, the binder-free $MoO_3$/SWNTs hybrid anode prepared by a simple method can boost the development of high performance anodes for LIBs.

Taking advantages of the knowledge on the use of carbon based material in $MoO_3$/SWNTs hybrid, I successfully synthesized the amorphous carbon/$MoS_2$ flakes hybrid. The hybrid structure consists of $MoS_2$ flakes incorporated in an amorphous carbon network. The carbon in the $MoS_2$/C hybrid plays the role of conductive network, promoting the electron transport and also acts as a buffer layer for the active material, accommodating its volume variation upon cycling. However, controlling the carbon content (wt%) in $MoS_2$/C hybrids is also an important task because it determines the thickness of carbon layer which highly influence to the $Li^+$ diffusion in the electrode. To do so, I synthesized three $MoS_2$/C hybrids with different carbon contents of ~10.00%, 16.11% and 29.86% corresponding to sample $MoS_2$/C-1, $MoS_2$/C-2 and $MoS_2$/C-3, respectively. The thickness of the carbon layer is found to increase with the increase in carbon content in the $MoS_2$/C hybrids. Especially in the $MoS_2$/C-1 hybrid, the low carbon content is unable to completely cover the $MoS_2$ flakes. The electrochemical performance of $MoS_2$/C hybrids demonstrates that all hybrid electrodes feature a stable reversible capacity and low charge transfer resistances ($R_{CT}$) upon 100 charge/discharge cycles with respect to that of pristine $MoS_2$. This indicates the role of carbon in improving the electrode conductivity and buffering volume change of $MoS_2$. Indeed, the morphology of the electrode surface after 100 cycles show that with the increase in carbon content, the formation of fractures gradually disappears on the surface of hybrid electrodes, confirming the role of carbon network in the structural preservation, avoiding pulverization of electrodes. Moreover, it has been observed that the insufficient carbon content in $MoS_2$/C-1 sample leads to the pulverization of electrode, whereas the excess carbon content in $MoS_2$/C-3 sample limits the $Li^+$ diffusion. As a result, both $MoS_2$/C-1 and -3 electrodes exhibit lower reversible specific capacity than that of the $MoS_2$/C-2 one, which features a proper amount of carbon covering on $MoS_2$ flakes. The improved electrochemical performance of $MoS_2$/C-2 sample with respect to $MoS_2$/C-1 and -3 ones indicates that proper carbon content not only improves the electrical conductivity of the electrode by facilitating the electron transport, but also acts as a buffer layer for active materials to avoid its volume change upon cycling.

In summary, the electrochemical performances of $MoO_3$/SWNTs and $MoS_2$/C electrodes demonstrate an effective strategy in hybrid/composite synthesis to produce high performance LIB anode. Both the $MoO_3$/SWNTs and $MoS_2$/C hybrids are produced by facile fabrication protocols that can also be easily extended to the construction of hybrid structures of other 2D nano-crystals in carbon-based material networks for LIB application.

### 7.3. Black phosphorous based anode for lithium ion batteries

In the last activity of my thesis, the production of FL-BP was carried out via LPE to investigate the solvent parameters which are relevant to the selection of an ideal solvent for the exfoliation of BP. In specific, the selected solvent should be able to: (*i*) exfoliate BP; (*ii*) keep a stable dispersion of the exfoliated flakes, *i.e.* the exfoliated flakes should not flocculate or precipitate; (*iii*) prevent the degradation of the exfoliated flakes by oxidation; (*iv*) be easily removed without leaving impurities. The exfoliation of BP in 14 different solvents were carried out and then the dispersability properties of few-layers BP (FL-BP) where evaluated, based on $\gamma$, Hansen solubility and Hildebrand parameters. Among the different trials, although the N-Cyclohexyl-2-pyrrolidone (CHP) is the solvent that promotes the highest concentration compared with all the other solvents, but it still showing the drawbacks of toxicity and high-boiling point (b.p.), the detrimental factors in LIB technology. Importantly, it has been recognized that the BP exfoliation is also possible in acetone, a well-known non-toxic solvent with a low-b.p. The morphological and structural characterization reveals that the exfoliated BP flakes in acetone are undamaged by the LPE process, and have an average lateral size of ~30 nm and an average thickness of ~7 nm. More importantly, by using electron energy loss (EEL) and Raman spectroscopies, it is demonstrated that the aging of exfoliated BP flakes in acetone is comparable with the one obtained by using high-b.p. solvent, *e.g.*, CHP. The successful exfoliation of BP in acetone creates the feasible and up-scalable approach for fast electrode deposition in LIB technology. The FL-$BL_{acetone}$-based anode outperformed the FL-$BP_{CHP}$ - based one. These findings indicate that the FL-$BP_{acetone}$ - based LIB anode is promising with regards to the design of fast charge/discharge devices. Overall, the presented process is a step forward towards the fabrication of phosphorene-based devices.

### 7.4. Future development

Liquid phase exfoliation of layered material is an effective strategy to produce 2D materials with low-cost, simplicity and high output, which can be applied for LIBs to reach the industrial-scale. This method can not only be used for $MoO_3$ and $MoS_2$, but can also be extended to other 2D crystals. The key parameter of LPE is the solvent used in the process which determines the production yield. The current solvents to exfoliate 2D crystal are mostly high-b.p. and toxic organic solvents, *e.g.*, NMP, DMF, CHP, benzyl benzoate, etc. which are not favourable for future LIB technology. Therefore, the searching and the new solvents and modifying the composition of solvents to meet the requirements of exfoliation of 2D crystals, *e.g.*, the surface energy of solvents have to be close to the surface tension ($\gamma$) of 2D flakes, the solvents have to be non-toxic, low-b.p., etc., is one of the future missions for research community to further develop the industrial-scale production of LIB materials.

In this thesis, the solvent exchange process of graphene flakes via vacuum filtration technique was explored as a promising route to the processing of environmentally friendly graphene ink, which allows one step fabrication of binder-free electrode for LIBs. This approach should be further exploited for other 2D materials, *e.g.*, TMOs, TMSs for the realization of LIB anode with high capacity. However, the vacuum filtration technique still has a drawback of losing material in filtering membrane. Thus, the solvent exchange process can be realized by other techniques, which should be further investigated for the realization of the simple, fast, effective and low-cost electrode fabrication.

Furthermore, the understanding of the role of graphene flakes dimension on their $Li^+$ storage ability provides the guidelines for the practical exploitation of graphene-based electrodes. One of the potential future directions in graphene-based LIB is exploiting hybrid structures of graphene with an active material with high theoretical capacity, *e.g.*, alloying materials, TMOs and TMSs, to fully utilize the novel properties of graphene, *e.g.*, high electrical conductivity, large surface area and high mechanical strength for the improvement of the $Li^+$ storage ability. As discussed in section **1.2.3**, although exhibiting the large theoretical capacities, Si, TMOs, TMSs alone are still facing with the issues of low conductivity and large volume change. Owing to the impressive electrical conductivity, graphene was proposed as a conductive agent to improve the conductivity of these electrodes. [513] Moreover, the large surface area of graphene can buffer the volume change of active materials in Si, TMOs and TMSs electrodes. Besides, superior thermal conductivity of graphene can be advantageous for dissipating the heat generated in LIBs in the case of high current loads. [514] Recently, six models of graphene-based composites have been reported: encapsulated, mixed, wrapped, anchored, sandwich-like and layered models [513], see Figure 7.1. The uses of each model depend on the design of active materials. For example, the graphene/nanoparticles based composites are commonly described by the encapsulated, mixed, wrapped and anchored models, whereas sandwich-like and layered models are associated to the composites of graphene and other 2D materials. In the case of LPE graphene flakes, the mixed model can be the ideal case for designing LIB anode material. [515]

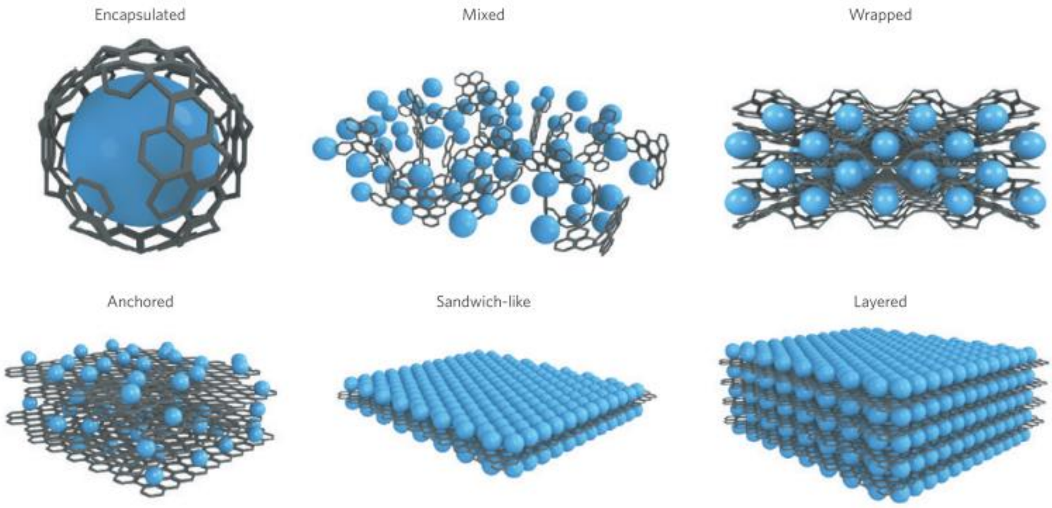


Figure 7.1. *Structural models of graphene composites. [191]*

The activities on $MoO_3$ and $MoS_2$ based anodes enable the use of carbon based materials in improving the electrochemical performance of anodes based on 2D materials. It should be noted that the electrochemical performances of $MoO_3$/SWNTs and $MoS_2$/C highly depend on the characteristics of adopted carbon based materials, such as the structure, morphology and content. Hence, optimization of the carbon network and synthesis of novel hybrid/composite structures, are the critical strategies for the future development of $MoO_3$ and $MoS_2$ for high performance LIB anodes. The choice of carbon-based materials for hybrid/composite structure with $MoO_3$ or $MoS_2$ is not limited to SWNTs and amorphous carbon. For example, the hybrid structures of $MoO_3$/graphene or $MoS_2$/graphene should be exploited for the realization of high performance LIB anode. Moreover, the development of well-designed architectures based on $MoO_3$ and $MoS_2$ materials could bring a new way to develop advanced TMOs- and TMSs-based electrodes with high energy density, high power density, and long cycle life for LIBs. Also, it is necessary to further develop and optimize the protocols for large-scale and environmentally friendly production of TMOs, TMSs and their hybrid/composites for LIBs applications. In addition, the control of lateral size and thickness of layered TMOs and TMSs via SBS can provide an enhanced specific surface area, increased number of active sites, and a faster ion transport, which could generate electrode materials for high rate electrochemical energy storage. The electrochemical properties of the 2D flakes can be further improved by a rational structure design based on nanoscale manipulation of 2D flakes, such as aligning 2D nanosheets or constructing 3D nanosheets interconnected networks. To some extent, although the rechargeable performance of TMO-and TMSs-based materials has been studied, the correspondence between structure and performance is needed to be further clarified. The actual mechanism underlying these electrochemical properties is somewhat unclear to researchers. Further investigations into the trigger origin of electrochemical reaction and the principle of capacity retention need to be carried out. In this regard, in-situ TEM observation and operando X-ray techniques combined with cyclic voltammetry technology are strong tools for researches of electrochemical mechanism. The above proposed studies will pave a way for the innovative design of high performance LIB anodes based on TMOs and TMSs.

As for BP exfoliation, the LPE of BP in acetone still can be further improved by the addition of acetone-soluble polymers which can scale-up the production. Thus, formulating the acetone-based solvents is one of the essential works for future development of large-scale production of FL-BP based anode for LIBs and other applications. In the field of LIBs, the low-b.p. of acetone allows fast fabrication of FL-$BL_{acetone}$ based anode which exhibiting the stable specific capacity. However, the anode also shows large irreversible capacity during the first few cycles before getting a stable performance, resulting in a relatively low specific capacity with respect to the report from Cui *et al.* [149] In this regard, further studies need to be realized to investigate the morphology of BP flakes which is able to plays a very important role in irreversible $Li^+$ storage. The defeats on the flakes edges may trap the $Li^+$ producing the observed capacity loss. Besides, the FL-BP flakes in this thesis have favorable panel structure with controllable dimension can not only fully exploit the large inter-layer space for the fast charge-discharge approaching, but also minimize the damage caused by its volume change during cycles. Moreover, its high rate capacity and stability is attractive for industrial applications. Therefore, I believe that the FL-$BL_{acetone}$ based anode is promising and can be further improved for high-performance LIBs. Several strategies have been considered to improve BP batteries. For instance, by coating or bonding the BP flakes surface/edges with carbon materials and increasing the percentage of BP flakes in the electrode. In this way the battery is expected to exhibit better performances in terms of capacity and energy density. However, the additives have to be selected properly. The 2D or 3D structured additives, such as CNTs and graphene networks, are also expected to improve the conductivity of the anode materials and prevent the volume change. Binder materials with high elastic property may also take into the further investigation list.

# References


1. Kasperson, R.E. and B.J. Ram, *The Public Acceptance of New Energy Technologies.* Daedalus, 2013. **142**(1): p. 90-96.
2. Tarascon, J.M. and M. Armand, *Issues and challenges facing rechargeable lithium batteries.* Nature, 2001. **414**(6861): p. 359-367.
3. Sun, H.Y., et al., *Binder-free graphene as an advanced anode for lithium batteries.* Journal of Materials Chemistry A, 2016. **4**(18): p. 6886-6895.
4. Sun, Y.X., et al., *Binder-free alpha-MoO3 nanobelt electrode for lithium-ion batteries utilizing van der Waals forces for film formation and connection with current collector.* Journal of Materials Chemistry A, 2013. **1**(15): p. 4736-4746.
5. Sun, H., et al., *How much does size really matter? Exploring the limits of graphene as Li ion battery anode material.* Solid State Communications, 2017. **251**: p. 88-93.
6. Ratso, S., et al., *Transition metal-nitrogen co-doped carbide-derived carbon catalysts for oxygen reduction reaction in alkaline direct methanol fuel cell.* Applied Catalysis B-Environmental, 2017. **219**: p. 276-286.
7. Kim, B., et al., *Self-recoverable voltage reversal in stacked microbial fuel cells due to biofilm capacitance.* Bioresource Technology, 2017. **245**: p. 1286-1289.
8. Zhuang, Q., et al., *An integrated natural gas power cycle using hydrogen and carbon fuel cells.* Fuel, 2017. **209**: p. 76-84.
9. Ravuri, S., et al., *Wet Chemical Synthesis of SnS/Graphene Nanocomposites for High Performance Supercapacitor Electrodes.* International Journal of Nanoscience, 2018. **17**(1-2).
10. Samuel, E., et al., *Flexible and freestanding core-shell SnOx/carbon nanofiber mats for high-performance supercapacitors.* Journal of Alloys and Compounds, 2017. **728**: p. 1362-1371.
11. Ates, M., et al., *Reduced graphene oxide/Titanium oxide nanocomposite synthesis via microwave-assisted method and supercapacitor behaviors.* Journal of Alloys and Compounds, 2017. **728**: p. 541-551.
12. Lashtabeg, A. and S.J. Skinner, *Solid oxide fuel cells - a challenge for materials chemists?* Journal of Materials Chemistry, 2006. **16**(31): p. 3161-3170.
13. Wang, G.P., L. Zhang, and J.J. Zhang, *A review of electrode materials for electrochemical supercapacitors.* Chemical Society Reviews, 2012. **41**(2): p. 797-828.
14. Felderhoff, M., et al., *Hydrogen storage: the remaining scientific and technological challenges.* Physical Chemistry Chemical Physics, 2007. **9**(21): p. 2643-2653.
15. Etacheri, V., et al., *Challenges in the development of advanced Li-ion batteries: a review.* Energy & Environmental Science, 2011. **4**(9): p. 3243-3262.
16. Gonzalez, A., et al., *Review on supercapacitors: Technologies and materials.* Renewable & Sustainable Energy Reviews, 2016. **58**: p. 1189-1206.
17. Huang, W., et al., *Discussion on Application of Super capacitor Energy Storage System in Microgrid.* 2009 International Conference on Sustainable Power Generation and Supply, Vols 1-4, 2009: p. 1719-+.
18. Ghaviha, N., et al., *Review of Application of Energy Storage Devices in Railway Transportation.* 8th International Conference on Applied Energy (Icae2016), 2017. **105**.
19. Nitta, N., et al., *Nanostructured composite electrodes for Li-ion batteries with enhanced energy density.* Abstracts of Papers of the American Chemical Society, 2014. **248**.
20. Nitta, N., et al., *Li-ion battery materials: present and future.* Materials Today, 2015. **18**(5): p. 252-264.
21. PaulRuetschi, *Review on the lead—acid battery science and technology.* Journal of Power Sources, 1977. **2**(1): p. 3-120.
22. Bernardes, A.M., D.C.R. Espinosa, and J.A.S. Tenorio, *Recycling of batteries: a review of current processes and technologies.* Journal of Power Sources, 2004. **130**(1-2): p. 291-298.
23. Young, K.-H., *Research in Nickel/Metal Hydride Batteries 2016.* Batteries, 2016. **2**(4): p. 31.
24. Deng, D., *Li-ion batteries: basics, progress, and challenges.* Energy Science & Engineering, 2015. **3**(5): p. 385-418.

25. Goodenough, J.B. and K.S. Park, *The Li-Ion Rechargeable Battery: A Perspective.* Journal of the American Chemical Society, 2013. **135**(4): p. 1167-1176.
26. Marom, R., et al., *A review of advanced and practical lithium battery materials.* Journal of Materials Chemistry, 2011. **21**(27): p. 9938-9954.
27. Armand, M. and J.M. Tarascon, *Building better batteries.* Nature, 2008. **451**(7179): p. 652-657.
28. PILLOT, C., *Battery Market Development for Consumer Electronics, Automotive, and Industrial: Materials Requirements and Trends.* avicenne energy, 2015.
29. Whittingham, M.S., *Electrical Energy Storage and Intercalation Chemistry.* Science, 1976. **192**(1126-1127).
30. Levine, S., *The Great Battery Race.* Foreign Policy, 2010. **182**: p. 88-95.
31. Mizushima, K., P. C. Jones, P. J. Wiseman, and J. B. Goodenough, *LixCoO2 (0<x≤1): A new cathode material for batteries of high energy density.* Solid State Ionics, 1981. **3-4**: p. 171-174.
32. Besenhard, J.O., and G. Eichinger. , *Besenhard, J. O., and G. Eichinger. 1976. High energy density lithium cells: Part I. Electrolytes and anodes. .* J. Electroanal. Chem. Interfacial Electrochem., 1976. **68**: p. 1-18.
33. Abdalla, A.M., et al., *NdBaMn2O5+delta layered perovskite as an active cathode material for solid oxide fuel cells.* Ceramics International, 2017. **43**(17): p. 15932-15938.
34. Basu, S., C. Zeller, P. J. Flanders, C. D. Fuerst, W. D. Johnson, and J. E. Fischer, *Synthesis and properties of lithium-graphite intercalation compounds.* Mat. Sci. Eng., 1979. **38**: p. 275-283.
35. Yoshino, A., K. Sanechika, and T. Nakajima, USP4, 1987. **668**: p. 595.
36. Roy, P. and S.K. Srivastava, *Nanostructured anode materials for lithium ion batteries.* Journal of Materials Chemistry A, 2015. **3**(6): p. 2454-2484.
37. Shah, K., et al., *State of the Art and Future Research Needs for Multiscale Analysis of Li-Ion Cells.* Journal of Electrochemical Energy Conversion and Storage, 2017. **14**(2).
38. Wang, W.W., S. Yang, and C. Lin, *Clay-like mechanical properties for the jellyroll of cylindrical Lithium-ion cells.* Applied Energy, 2017. **196**: p. 249-258.
39. Siva P.V. Nadimpalli, V.A.S., Daniel P. Abraham, Allan F. Bower, and Pradeep R. Guduru *Stress Evolution in Lithium-Ion Composite Electrodes during Electrochemical Cycling and Resulting Internal Pressures on the Cell Casing.* Journal of The Electrochemical Society, 2015. **162**(14): p. A2656-A2663.
40. *Types of Battery Cells.* Battery University Group: p. http://batteryuniversity.com/learn/article/types_of_battery_cells.
41. Kovalenko, M.V., *Basics of Materials Science (for batteries)* Empa -Swiss Federal Laboratories for Materials Science and Technology, 2015.
42. Wu, Y., *LITHIUM-ION BATTERIES: Fundamentals and Applications.* ELECTROCHEMICAL ENERGY STORAGE AND CONVERSION, CRC Press Taylor & Francis Group 2015.
43. Christian Julien, A.M., Ashok Vijh, Karim Zaghib, *Lithium Batteries: Science and Technology.* Springer Science and Business Media, 2016.
44. Goriparti, S., et al., *Review on recent progress of nanostructured anode materials for Li-ion batteries.* Journal of Power Sources, 2014. **257**: p. 421-443.
45. Zhang, B.A., et al., *Correlation Between Microstructure and Na Storage Behavior in Hard Carbon.* Advanced Energy Materials, 2016. **6**(1).
46. Licht, S., et al., *Carbon Nanotubes Produced from Ambient Carbon Dioxide for Environmentally Sustainable Lithium-Ion and Sodium-Ion Battery Anodes.* Acs Central Science, 2016. **2**(3): p. 162-168.
47. Zhong, Z.Y., et al., *Ab initio studies on Li4+xTi5O12 compounds as anode materials for lithium-ion batteries.* Chemphyschem, 2008. **9**(14): p. 2104-2108.
48. Tang, Y.X., et al., *Rational material design for ultrafast rechargeable lithium-ion batteries.* Chemical Society Reviews, 2015. **44**(17): p. 5926-5940.
49. Cabana, J., et al., *Beyond Intercalation-Based Li-Ion Batteries: The State of the Art and Challenges of Electrode Materials Reacting Through Conversion Reactions.* Advanced Materials, 2010. **22**(35): p. E170-E192.

50. Linden, D.a.R., T. B., *Handbook of Batteries.* McGraw Hill, 1995.
51. Smith, A.J., et al., *Precision Measurements of the Coulombic Efficiency of Lithium-Ion Batteries and of Electrode Materials for Lithium-Ion Batteries.* Journal of the Electrochemical Society, 2010. **157**(2): p. A196-A202.
52. Helmenstine, A.M., *Table of Electrical Resistivity and Conductivity.* ThoughtCo., 2017.
53. Armstrong, A.R., et al., *The lithium intercalation process in the low-voltage lithium battery anode Li1+xV1-xO2.* Nature Materials, 2011. **10**(3): p. 223-229.
54. Xue, D.J., et al., *Improving the Electrode Performance of Ge through Ge@C Core-Shell Nanoparticles and Graphene Networks.* Journal of the American Chemical Society, 2012. **134**(5): p. 2512-2515.
55. Mahmood, N., et al., *Hybrid of Co3Sn2@Co Nanoparticles and Nitrogen-Doped Graphene as a Lithium Ion Battery Anode.* Acs Nano, 2013. **7**(11): p. 10307-10318.
56. Kim, M.G. and J. Cho, *Reversible and High-Capacity Nanostructured Electrode Materials for Li-Ion Batteries.* Advanced Functional Materials, 2009. **19**(10): p. 1497-1514.
57. Pharr, M., et al., *Measurements of stress and fracture in germanium electrodes of lithium-ion batteries during electrochemical lithiation and delithiation.* Journal of Power Sources, 2016. **304**: p. 164-169.
58. Chan, M.K.Y., C. Wolverton, and J.P. Greeley, *First Principles Simulations of the Electrochemical Lithiation and Delithiation of Faceted Crystalline Silicon.* Journal of the American Chemical Society, 2012. **134**(35): p. 14362-14374.
59. Yoon, T., et al., *Capacity Fading Mechanisms of Silicon Nanoparticle Negative Electrodes for Lithium Ion Batteries.* Journal of the Electrochemical Society, 2015. **162**(12): p. A2325-A2330.
60. Ikonen, T., et al., *Electrochemically anodized porous silicon: Towards simple and affordable anode material for Li-ion batteries.* Scientific Reports, 2017. **7**.
61. Chan, C.K., et al., *High-performance lithium battery anodes using silicon nanowires.* Nature Nanotechnology, 2008. **3**(1): p. 31-35.
62. Tokranov, A., et al., *Control and Optimization of the Electrochemical and Mechanical Properties of the Solid Electrolyte Interphase on Silicon Electrodes in Lithium Ion Batteries.* Advanced Energy Materials, 2016. **6**(8).
63. Kennedy, T., M. Brandon, and K.M. Ryan, *Advances in the Application of Silicon and Germanium Nanowires for High-Performance Lithium-Ion Batteries.* Advanced Materials, 2016. **28**(27): p. 5696-5704.
64. Yu, S.H., et al., *Conversion Reaction-Based Oxide Nanomaterials for Lithium Ion Battery Anodes.* Small, 2016. **12**(16): p. 2146-2172.
65. Mahmood, N., T.Y. Tang, and Y.L. Hou, *Nanostructured Anode Materials for Lithium Ion Batteries: Progress, Challenge and Perspective.* Advanced Energy Materials, 2016. **6**(17).
66. Rowsell, J.L.C., V. Pralong, and L.F. Nazar, *Layered lithium iron nitride: A promising anode material for Li-ion batteries.* Journal of the American Chemical Society, 2001. **123**(35): p. 8598-8599.
67. Poizot, P., et al., *Nano-sized transition-metaloxides as negative-electrode materials for lithium-ion batteries.* Nature, 2000. **407**(6803): p. 496-499.
68. Palacin, M.R., *Recent advances in rechargeable battery materials: a chemist's perspective.* Chemical Society Reviews, 2009. **38**(9): p. 2565-2575.
69. Yang, J., et al., *Unique synthesis of hollow Co3O4 nanoparticles embedded in thin Al2O3 nanosheets for enhanced lithium storage.* Nanoscale, 2015. **7**(38): p. 15983-15989.
70. Malini, R., et al., *Conversion reactions: a new pathway to realise energy in lithium-ion battery-review.* Ionics, 2009. **15**(3): p. 301-307.
71. Xu, X., et al., *Nanostructured transition metal sulfides for lithium ion batteries: Progress and challenges.* Nano Today, 2014. **9**(5): p. 604-630.
72. Stephenson, T., et al., *Lithium ion battery applications of molybdenum disulfide (MoS2) nanocomposites.* Energy & Environmental Science, 2014. **7**(1): p. 209-231.
73. Liang, C.D., N.J. Dudney, and J.Y. Howe, *Hierarchically Structured Sulfur/Carbon Nanocomposite Material for High-Energy Lithium Battery.* Chemistry of Materials, 2009. **21**(19): p. 4724-4730.

74. Su, Y.S. and A. Manthiram, *Lithium-sulphur batteries with a microporous carbon paper as a bifunctional interlayer.* Nature Communications, 2012. **3**.
75. Cuisinier, M., et al., *Unique behaviour of nonsolvents for polysulphides in lithium-sulphur batteries.* Energy & Environmental Science, 2014. **7**(8): p. 2697-2705.
76. Xu, B., et al., *Recent progress in cathode materials research for advanced lithium ion batteries.* Materials Science & Engineering R-Reports, 2012. **73**(5-6): p. 51-65.
77. Shao-Horn, Y., et al., *Structural fatigue in spinel electrodes in Li/Li-x[Mn-2]O-4 cells.* Journal of Power Sources, 1999. **81**: p. 496-499.
78. Thackeray, M.M., *Spinel electrodes for lithium batteries.* Journal of the American Ceramic Society, 1999. **82**(12): p. 3347-3354.
79. Du Pasquier, A., et al., *A comparative study of Li-ion battery, supercapacitor and nonaqueous asymmetric hybrid devices for automotive applications.* Journal of Power Sources, 2003. **115**(1): p. 171-178.
80. Dahn, J.N.R.a.J.R., *Electrochemical and In Situ X-Ray Diffraction Studies of Lithium Intercalation in Li x CoO2.* J. Electrochem. Soc., 1992. **139**: p. 2091-2097.
81. Ceder, G., et al., *Identification of cathode materials for lithium batteries guided by first-principles calculations.* Nature, 1998. **392**(6677): p. 694-696.
82. Madhavi, S., et al., *Effect of Cr dopant on the cathodic behavior of LiCoO2.* Electrochimica Acta, 2002. **48**(3): p. 219-226.
83. Stoyanova, R., E. Zhecheva, and L. Zarkova, *Effect of Mn-Substitution for Co on the Crystal-Structure and Acid Delithiation of Limnyco1-Yo2 Solid-Solutions.* Solid State Ionics, 1994. **73**(3-4): p. 233-240.
84. Park, O.K., et al., *Who will drive electric vehicles, olivine or spinel?* Energy & Environmental Science, 2011. **4**(5): p. 1621-1633.
85. Pieczonka, N.P.W., et al., *Understanding Transition-Metal Dissolution Behavior in LiNi0.5Mn1.5O4 High-Voltage Spinel for Lithium Ion Batteries.* Journal of Physical Chemistry C, 2013. **117**(31): p. 15947-15957.
86. Xiao, J., et al., *High-Performance LiNi0.5Mn1.5O4 Spinel Controlled by Mn3+Concentration and Site Disorder.* Advanced Materials, 2012. **24**(16): p. 2109-2116.
87. Manthiram, A., K. Chemelewski, and E.S. Lee, *A perspective on the high-voltage LiMn1.5Ni0.5O4 spinel cathode for lithium-ion batteries.* Energy & Environmental Science, 2014. **7**(4): p. 1339-1350.
88. Chung, S.Y., J.T. Bloking, and Y.M. Chiang, *Electronically conductive phospho-olivines as lithium storage electrodes.* Nature Materials, 2002. **1**(2): p. 123-128.
89. Malik, R., et al., *Particle Size Dependence of the Ionic Diffusivity.* Nano Letters, 2010. **10**(10): p. 4123-4127.
90. Hsu, K.F., S.Y. Tsay, and B.J. Hwang, *Synthesis and characterization of nano-sized LiFePO4 cathode materials prepared by a citric acid-based sol-gel route.* Journal of Materials Chemistry, 2004. **14**(17): p. 2690-2695.
91. Guyomard, D. and J.M. Tarascon, *Li Metal-Free Rechargeable Limn2o4/Carbon Cells - Their Understanding and Optimization.* Journal of the Electrochemical Society, 1992. **139**(4): p. 937-948.
92. Yang, L., A. Xiao, and B.L. Lucht, *Investigation of solvation in lithium ion battery electrolytes by NMR spectroscopy.* Journal of Molecular Liquids, 2010. **154**(2-3): p. 131-133.
93. Xu, K., *Nonaqueous liquid electrolytes for lithium-based rechargeable batteries.* Chemical Reviews, 2004. **104**(10): p. 4303-4417.
94. Long, L.Z., et al., *Polymer electrolytes for lithium polymer batteries.* Journal of Materials Chemistry A, 2016. **4**(26): p. 10038-10069.
95. Li, Y., et al., *A highly elastic and flexible solid-state polymer electrolyte based on ionic liquid-decorated PMMA nanoparticles for lithium batteries.* New Journal of Chemistry, 2017. **41**(21): p. 13096-13103.
96. Meyer, W.H., *Polymer Electrolytes for Lithium-Ion Batteries.* Adv. Mater., 1998. **6**: p. 10.
97. Stephan, A.M., *Review on gel polymer electrolytes for lithium batteries.* European Polymer Journal, 2006. **42**(1): p. 21-42.

98. Fergus, J.W., *Ceramic and polymeric solid electrolytes for lithium-ion batteries.* Journal of Power Sources, 2010. **195**(15): p. 4554-4569.
99. Porcarelli, L., et al., *Super Soft All-Ethylene Oxide Polymer Electrolyte for Safe All-Solid Lithium Batteries.* Scientific Reports, 2016. **6**.
100. Yoshio, M., Brodd, R. J., and Kozawa, A., *Lithium-Ion Batteries.* Springer, 2009. **1**.
101. Nam, D.H., et al., *Electrochemical performances of Sn anode electrodeposited on porous Cu foam for Li-ion batteries.* Electrochimica Acta, 2012. **66**: p. 126-132.
102. Lee, H., et al., *A review of recent developments in membrane separators for rechargeable lithium-ion batteries.* Energy & Environmental Science, 2014. **7**(12): p. 3857-3886.
103. Xiang, H.F., et al., *An inorganic membrane as a separator for lithium-ion battery.* Journal of Power Sources, 2011. **196**(20): p. 8651-8655.
104. Zhang, Y.C., et al., *A thin inorganic composite separator for lithium-ion batteries.* Journal of Membrane Science, 2016. **509**: p. 19-26.
105. Daniel, C.a.B., J. O. , *Handbook of Battery Materials.* Wiley-VCH, 2011.
106. Kim, S.W. and K.Y. Cho, *Current Collectors for Flexible Lithium Ion Batteries: A Review of Materials.* Journal of Electrochemical Science and Technology, 2015. **6**(1): p. 1-6.
107. Myung, S.T., Y. Hitoshi, and Y.K. Sun, *Electrochemical behavior and passivation of current collectors in lithium-ion batteries.* Journal of Materials Chemistry, 2011. **21**(27): p. 9891-9911.
108. Jeon, H., et al., *Highly rough copper current collector: improving adhesion property between a silicon electrode and current collector for flexible lithium-ion batteries.* Rsc Advances, 2017. **7**(57): p. 35681-35686.
109. Kang, S.W., et al., *Enhancing Performance of a Lithium Ion Battery by Optimizing the Surface Properties of the Current Collector.* International Journal of Electrochemical Science, 2015. **10**(3): p. 2324-2335.
110. ANDERSEN, H.F., *NEW MATERIALS FOR LITHIUM-ION BATTERIES.* Fraunhofer-Institut für Silicatforschung ISC, 2013.
111. Yang, C.G., et al., *Nickel foam supported Sn-Co alloy film as anode for lithium ion batteries.* Journal of Power Sources, 2011. **196**(24): p. 10673-10678.
112. Goodenough, J.B., *Evolution of Strategies for Modern Rechargeable Batteries.* Accounts of Chemical Research, 2013. **46**(5): p. 1053-1061.
113. Dai, X.Y., et al., *Extending the High-Voltage Capacity of LiCoO2 Cathode by Direct Coating of the Composite Electrode with Li2CO3 via Magnetron Sputtering.* Journal of Physical Chemistry C, 2016. **120**(1): p. 422-430.
114. Oszajca, M.F., M.I. Bodnarchuk, and M.V. Kovalenko, *Precisely Engineered Colloidal Nanoparticles and Nanocrystals for Li-Ion and Na-Ion Batteries: Model Systems or Practical Solutions?* Chemistry of Materials, 2014. **26**(19): p. 5422-5432.
115. Liu, X.H., et al., *Size-Dependent Fracture of Silicon Nanoparticles During Lithiation.* Acs Nano, 2012. **6**(2): p. 1522-1531.
116. He, M., et al., *Monodisperse Antimony Nanocrystals for High-Rate Li-ion and Na-ion Battery Anodes: Nano versus Bulk.* Nano Letters, 2014. **14**(3): p. 1255-1262.
117. Wang, H.L., et al., *Mn3O4-Graphene Hybrid as a High-Capacity Anode Material for Lithium Ion Batteries.* Journal of the American Chemical Society, 2010. **132**(40): p. 13978-13980.
118. Qi, W., et al., *Nanostructured anode materials for lithium-ion batteries: principle, recent progress and future perspectives.* Journal of Materials Chemistry A, 2017. **5**(37): p. 19521-19540.
119. Bruce, P.G., B. Scrosati, and J.M. Tarascon, *Nanomaterials for rechargeable lithium batteries.* Angewandte Chemie-International Edition, 2008. **47**(16): p. 2930-2946.
120. Arico, A.S., et al., *Nanostructured materials for advanced energy conversion and storage devices.* Nature Materials, 2005. **4**(5): p. 366-377.
121. Hwang, T.H., et al., *Electrospun Core-Shell Fibers for Robust Silicon Nanoparticle-Based Lithium Ion Battery Anodes.* Nano Letters, 2012. **12**(2): p. 802-807.
122. Qiu, L., et al., *Mechanically Robust, Electrically Conductive and Stimuli-Responsive Binary Network Hydrogels Enabled by Superelastic Graphene Aerogels.* Advanced Materials, 2014. **26**(20): p. 3333-+.

123. Worsley, M.A., et al., *Synthesis of Graphene Aerogel with High Electrical Conductivity.* Journal of the American Chemical Society, 2010. **132**(40): p. 14067-14069.
124. Zhai, C.X., et al., *Assembling CoSn3 nanoparticles on multiwalled carbon nanotubes with enhanced lithium storage properties.* Nanoscale, 2011. **3**(4): p. 1798-1801.
125. Su, H.P., et al., *Colloidal Synthesis of Silicon-Carbon Composite Material for Lithium-Ion Batteries.* Angewandte Chemie-International Edition, 2017. **56**(36): p. 10780-10785.
126. Fang, S., et al., *Ge-graphene-carbon nanotube composite anode for high performance lithium-ion batteries.* Journal of Materials Chemistry A, 2015. **3**(4): p. 1498-1503.
127. Gao, X.W., et al., *Novel Germanium/Polypyrrole Composite for High Power Lithium-ion Batteries.* Scientific Reports, 2014. **4**.
128. Zhang, S.S., *A review on the separators of liquid electrolyte Li-ion batteries.* Journal of Power Sources, 2007. **164**(1): p. 351-364.
129. Scrosati, B. and J. Garche, *Lithium batteries: Status, prospects and future.* Journal of Power Sources, 2010. **195**(9): p. 2419-2430.
130. Zhang, X., et al., *Synthesis of MnO@C core-shell nanoplates with controllable shell thickness and their electrochemical performance for lithium-ion batteries.* Journal of Materials Chemistry, 2012. **22**(34): p. 17864-17869.
131. Long, P., et al., *Facile synthesis of Co9S8 nanosheets for lithium ion batteries with enhanced rate capability and cycling stability.* New Journal of Chemistry, 2017. **41**(17): p. 9184-9191.
132. Qi, W., et al., *Facile Synthesis of Layer Structured GeP3/C with Stable Chemical Bonding for Enhanced Lithium-Ion Storage.* Scientific Reports, 2017. **7**.
133. Kim, S.Y., et al., *Facile Synthesis of Carbon-Coated Silicon/Graphite Spherical Composites for High-Performance Lithium-Ion Batteries.* Acs Applied Materials & Interfaces, 2016. **8**(19): p. 12109-12117.
134. Luo, B., et al., *Reduced Graphene Oxide-Mediated Growth of Uniform Tin-Core/Carbon-Sheath Coaxial Nanocables with Enhanced Lithium Ion Storage Properties.* Advanced Materials, 2012. **24**(11): p. 1405-1409.
135. Xu, Y.H., et al., *Electrochemical Performance of Porous Carbon/Tin Composite Anodes for Sodium-Ion and Lithium-Ion Batteries.* Advanced Energy Materials, 2013. **3**(1): p. 128-133.
136. Novoselov, K.S., et al., *Electric field effect in atomically thin carbon films.* Science, 2004. **306**(5696): p. 666-669.
137. Kalantar-zadeh, K., et al., *Two dimensional and layered transition metal oxides.* Applied Materials Today, 2016. **5**: p. 73-89.
138. Wu, S.P., Y. Du, and S.J. Sun, *Transition metal dichalcogenide based nanomaterials for rechargeable batteries.* Chemical Engineering Journal, 2017. **307**: p. 189-207.
139. Ralf Riedel, W.L., *Handbook of Ceramic Hard Materials: Chapter 7. Transition Metal Carbides, Nitrides, and Carbonitrides.* wiley online library, 2008.
140. Mas-Balleste, R., et al., *2D materials: to graphene and beyond.* Nanoscale, 2011. **3**(1): p. 20-30.
141. Liu, J.H. and X.W. Liu, *Two-Dimensional Nanoarchitectures for Lithium Storage.* Advanced Materials, 2012. **24**(30): p. 4097-4111.
142. Novoselov, K.S., et al., *Two-dimensional atomic crystals.* Proceedings of the National Academy of Sciences of the United States of America, 2005. **102**(30): p. 10451-10453.
143. Peng, L.L., et al., *Two-Dimensional Materials for Beyond-Lithium-Ion Batteries.* Advanced Energy Materials, 2016. **6**(11).
144. Xiong, P., et al., *Two-dimensional nanosheets based Li-ion full batteries with high rate capability and flexibility.* Nano Energy, 2015. **12**: p. 816-823.
145. Shi, L. and T.S. Zhao, *Recent advances in inorganic 2D materials and their applications in lithium and sodium batteries.* Journal of Materials Chemistry A, 2017. **5**(8): p. 3735-3758.
146. Sahoo, R., A. Pal, and T. Pal, *2D materials for renewable energy storage devices: Outlook and challenges.* Chemical Communications, 2016. **52**(93): p. 13528-13542.
147. Park, C.M. and H.J. Sohn, *Black phosphorus and its composite for lithium rechargeable batteries.* Advanced Materials, 2007. **19**(18): p. 2465-+.
148. Sun, L.Q., et al., *Electrochemical Activity of Black Phosphorus as an Anode Material for Lithium-Ion Batteries.* Journal of Physical Chemistry C, 2012. **116**(28): p. 14772-14779.

149. Sun, J., et al., *Formation of Stable Phosphorus-Carbon Bond for Enhanced Performance in Black Phosphorus Nanoparticle-Graphite Composite Battery Anodes.* Nano Letters, 2014. **14**(8): p. 4573-4580.
150. Bonaccorso, F., et al., *Production and processing of graphene and 2d crystals.* Materials Today, 2012. **15**(12): p. 564-589.
151. Dillon, A.C., et al., *HWCVD MoO3 nanoparticles and a-Si for next generation Li-ion anodes.* Thin Solid Films, 2011. **519**(14): p. 4495-4497.
152. Huang, Z.X., et al., *3D graphene supported MoO2 for high performance binder-free lithium ion battery.* Nanoscale, 2014. **6**(16): p. 9839-9845.
153. Noerochim, L., et al., *Rapid synthesis of free-standing MoO3/Graphene films by the microwave hydrothermal method as cathode for bendable lithium batteries.* Journal of Power Sources, 2013. **228**: p. 198-205.
154. Ji, W.X., et al., *MoO3 Nanobelts/Reduced Graphene Oxide (RGO) Composites as a High-Performance Anode Material for Lithium Ion Batteries.* Chinese Journal of Inorganic Chemistry, 2015. **31**(4): p. 659-665.
155. Feng, C.Q., et al., *Synthesis and electrochemical properties of MoO3/C nanocomposite.* Electrochimica Acta, 2013. **93**: p. 101-106.
156. Yu, Z., et al., *A New Way to Prepare MoO3/C as Anode of Lithium ion Battery for Enhancing the Electrochemical Performance at Room Temperature.* Journal of Electrochemical Science and Technology, 2016. **7**(2): p. 170-178.
157. Pollak, E., et al., *The Interaction of Li+ with Single-Layer and Few-Layer Graphene.* Nano Letters, 2010. **10**(9): p. 3386-3388.
158. Shokhen, V., et al., *On the impact of Vertical Alignment of MoS2 for Efficient Lithium Storage.* Scientific Reports, 2017. **7**.
159. Bonaccorso, F., et al., *Graphene, related two-dimensional crystals, and hybrid systems for energy conversion and storage.* Science, 2015. **347**(6217).
160. Yoo, E., et al., *Large reversible Li storage of graphene nanosheet families for use in rechargeable lithium ion batteries.* Nano Letters, 2008. **8**(8): p. 2277-2282.
161. Mattevi, C., et al., *Evolution of Electrical, Chemical, and Structural Properties of Transparent and Conducting Chemically Derived Graphene Thin Films.* Advanced Functional Materials, 2009. **19**(16): p. 2577-2583.
162. Qiu, W.D., et al., *Facile Synthesis of Hollow MoS2 Microspheres/Amorphous Carbon Composites and Their Lithium Storage Properties.* Electrochimica Acta, 2014. **117**: p. 145-152.
163. Lee, G.H., et al., *In situ formation of MoS2/C nanocomposite as an anode for high-performance lithium-ion batteries.* Rsc Advances, 2016. **6**(95): p. 92259-92266.
164. Youngkuk Bae, C.-Y.S., Suyeon Yoo, Seung-Keun Park, Yuanzhe Piao, *Solvothermal Synthesis of a Molybdenum Disulfide/Reduced Porous Graphene Oxide Nanocomposite as a High-Performance Anode Material for Lithium-Ion Batteries.* Energy teachnology, 2017. **5**: p. 1-9.
165. Wang, S.Q., et al., *Solvothermal Synthesis of MoS2/Carbon Nanotube Composites with Improved Electrochemical Performance for Lithium Ion Batteries.* Nanoscience and Nanotechnology Letters, 2012. **4**(4): p. 378-383.
166. Jin, J., et al., *Template synthesis of hollow MoS2-carbon nanocomposites using microporous organic polymers and their lithium storage properties.* Nanoscale, 2015. **7**(26): p. 11280-11285.
167. Patel, M.D., et al., *Vertically oriented MoS2 nanoflakes coated on 3D carbon nanotubes for next generation Li-ion batteries.* Nanotechnology, 2016. **27**(49).
168. Chang, K., et al., *Graphene-like MoS2/amorphous carbon composites with high capacity and excellent stability as anode materials for lithium ion batteries.* Journal of Materials Chemistry, 2011. **21**(17): p. 6251-6257.
169. Chang, K. and W.X. Chen, *Single-layer MoS2/graphene dispersed in amorphous carbon: towards high electrochemical performances in rechargeable lithium ion batteries.* Journal of Materials Chemistry, 2011. **21**(43): p. 17175-17184.
170. Zhou, L., et al., *alpha-MoO3 Nanobelts: A High Performance Cathode Material for Lithium Ion Batteries.* Journal of Physical Chemistry C, 2010. **114**(49): p. 21868-21872.

171. Sen, U.K. and S. Mitra, *Electrochemical activity of alpha-MoO3 nano-belts as lithium-ion battery cathode.* Rsc Advances, 2012. **2**(29): p. 11123-11131.
172. Pham, V.H., et al., *Liquid phase co-exfoliated MoS2-graphene composites as anode materials for lithium ion batteries.* Journal of Power Sources, 2013. **244**: p. 280-286.
173. Qin, W., et al., *MoS2-reduced graphene oxide composites via microwave assisted synthesis for sodium ion battery anode with improved capacity and cycling performance.* Electrochimica Acta, 2015. **153**: p. 55-61.
174. Choi, M., et al., *A route to synthesis molybdenum disulfide-reduced graphene oxide (MoS2-RGO) composites using supercritical methanol and their enhanced electrochemical performance for Li-ion batteries.* Journal of Power Sources, 2016. **309**: p. 202-211.
175. Jing, Y., et al., *Layer-by-Layer Hybrids of MoS2 and Reduced Graphene Oxide for Lithium Ion Batteries.* Electrochimica Acta, 2014. **147**: p. 392-400.
176. Wang, Z., et al., *Facile synthesis of MoS2/graphene composites: effects of different cationic surfactants on microstructures and electrochemical properties of reversible lithium storage.* Rsc Advances, 2013. **3**(44): p. 21675-21684.
177. Nguyen, D.N., et al., *Crystallization of Amorphous Molybdenum Sulfide Induced by Electron or Laser Beam and Its Effect on H-2-Evolving Activities.* Journal of Physical Chemistry C, 2016. **120**(50): p. 28789-28794.
178. Zhang, L. and X.W. Lou, *Hierarchical MoS2 Shells Supported on Carbon Spheres for Highly Reversible Lithium Storage.* Chemistry-a European Journal, 2014. **20**(18): p. 5219-5223.
179. Guo, J., et al., *Synthesis of graphene-like MoS2 nanowall/graphene nanosheet hybrid materials with high lithium storage performance.* Catalysis Today, 2015. **246**: p. 165-171.
180. Hou, Y., et al., *N-doped graphene/porous g-C3N4 nanosheets supported layered-MoS2 hybrid as robust anode materials for lithium-ion batteries.* Nano Energy, 2014. **8**: p. 157-164.
181. Ma, L., et al., *Cationic surfactant-assisted hydrothermal synthesis of few-layer molybdenum disulfide/graphene composites: Microstructure and electrochemical lithium storage.* Journal of Power Sources, 2014. **264**: p. 262-271.
182. Wang, Z., et al., *CTAB-assisted synthesis of single-layer MoS2-graphene composites as anode materials of Li-ion batteries.* Journal of Materials Chemistry A, 2013. **1**(6): p. 2202-2210.
183. Qiao, J.S., et al., *High-mobility transport anisotropy and linear dichroism in few-layer black phosphorus.* Nature Communications, 2014. **5**.
184. Tran, V., et al., *Layer-controlled band gap and anisotropic excitons in few-layer black phosphorus.* Physical Review B, 2014. **89**(23).
185. Dahbi, M., et al., *Black Phosphorus as a High-Capacity, High-Capability Negative Electrode for Sodium-Ion Batteries: Investigation of the Electrode/Interface.* Chemistry of Materials, 2016. **28**(6): p. 1625-1635.
186. Qiu, M., et al., *Current progress in black phosphorus materials and their applications in electrochemical energy storage.* Nanoscale, 2017. **9**(36): p. 13384-13403.
187. Jeon, I.Y., et al., *Large-Scale Production of Edge-Selectively Functionalized Graphene Nanoplatelets via Ball Milling and Their Use as Metal-Free Electrocatalysts for Oxygen Reduction Reaction.* Journal of the American Chemical Society, 2013. **135**(4): p. 1386-1393.
188. Coleman, J.N., et al., *Two-Dimensional Nanosheets Produced by Liquid Exfoliation of Layered Materials.* Science, 2011. **331**(6017): p. 568-571.
189. Paton, K.R., et al., *Scalable production of large quantities of defect-free few-layer graphene by shear exfoliation in liquids.* Nature Materials, 2014. **13**(6): p. 624-630.
190. Wei, Y. and Z.Y. Sun, *Liquid-phase exfoliation of graphite for mass production of pristine few-layer graphene.* Current Opinion in Colloid & Interface Science, 2015. **20**(5-6): p. 311-321.
191. Raccichini, R., et al., *The role of graphene for electrochemical energy storage.* Nature Materials, 2015. **14**(3): p. 271-279.
192. Stoller, M.D., et al., *Graphene-Based Ultracapacitors.* Nano Letters, 2008. **8**(10): p. 3498-3502.
193. Geim, A.K. and K.S. Novoselov, *The rise of graphene.* Nature Materials, 2007. **6**(3): p. 183-191.
194. Lee, C., et al., *Measurement of the elastic properties and intrinsic strength of monolayer graphene.* Science, 2008. **321**(5887): p. 385-388.

195. Winter, M., et al., *Insertion electrode materials for rechargeable lithium batteries.* Advanced Materials, 1998. **10**(10): p. 725-763.
196. Dahn, J.R., et al., *Mechanisms for Lithium Insertion in Carbonaceous Materials.* Science, 1995. **270**(5236): p. 590-593.
197. Liu, Y.H., et al., *Mechanism of lithium insertion in hard carbons prepared by pyrolysis of epoxy resins.* Carbon, 1996. **34**(2): p. 193-200.
198. Uthaisar, C. and V. Barone, *Edge Effects on the Characteristics of Li Diffusion in Graphene.* Nano Letters, 2010. **10**(8): p. 2838-2842.
199. Wang, D.H., et al., *Self-Assembled TiO2-Graphene Hybrid Nanostructures for Enhanced Li-Ion Insertion.* Acs Nano, 2009. **3**(4): p. 907-914.
200. Elia, G.A., et al., *An Advanced Lithium-Air Battery Exploiting an Ionic Liquid-Based Electrolyte.* Nano Letters, 2014. **14**(11): p. 6572-6577.
201. Raccichini, R., et al., *Boosting the power performance of multilayer graphene as lithium-ion battery anode via unconventional doping with in-situ formed Fe nanoparticles.* Scientific Reports, 2016. **6**.
202. Hassoun, J., et al., *An Advanced Lithium-Ion Battery Based on a Graphene Anode and a Lithium Iron Phosphate Cathode.* Nano Letters, 2014. **14**(8): p. 4901-4906.
203. Li, H., P. Balaya, and J. Maier, *Li-storage via heterogeneous reaction in selected binary metal fluorides and oxides.* Journal of the Electrochemical Society, 2004. **151**(11): p. A1878-A1885.
204. Riley, L.A., et al., *Optimization of MoO3 nanoparticles as negative-electrode material in high-energy lithium ion batteries.* Journal of Power Sources, 2010. **195**(2): p. 588-592.
205. Hosono, K., et al., *Synthesis of polypyrrole/MoO3 hybrid thin films and their volatile organic compound gas-sensing properties.* Chemistry of Materials, 2005. **17**(2): p. 349-354.
206. Leroux, F. and L.F. Nazar, *Uptake of lithium by layered molybdenum oxide and its tin exchanged derivatives: high volumetric capacity materials.* Solid State Ionics, 2000. **133**(1-2): p. 37-50.
207. Tao, T., et al., *MoO3 nanoparticles dispersed uniformly in carbon matrix: a high capacity composite anode for Li-ion batteries.* Journal of Materials Chemistry, 2011. **21**(25): p. 9350-9355.
208. Ding, J., et al., *Facile synthesis of carbon/MoO3 nanocomposites as stable battery anodes.* Journal of Power Sources, 2017. **348**: p. 270-280.
209. Wang, G.B., et al., *High-performance CNT-wired MoO3 nanobelts for Li-storage application.* Journal of Materials Chemistry A, 2013. **1**(12): p. 4112-4118.
210. Ni, J.F., et al., *Carbon nanotube-wired and oxygen-deficient MoO3 nanobelts with enhanced lithium-storage capability.* Journal of Power Sources, 2014. **247**: p. 90-94.
211. Liu, C.L., et al., *In situ synthesis of alpha-MoO3/graphene composites as anode materials for lithium ion battery.* Materials Chemistry and Physics, 2014. **143**(3): p. 1111-1118.
212. Lu, P.J., M. Lei, and J. Liu, *Graphene nanosheets encapsulated alpha-MoO3 nanoribbons with ultrahigh lithium ion storage properties.* Crystengcomm, 2014. **16**(29): p. 6745-6755.
213. Wang, T.Y., et al., *MoS2-Based Nanocomposites for Electrochemical Energy Storage.* Advanced Science, 2017. **4**(2).
214. Jiang, H., et al., *2D Monolayer MoS2-Carbon Interoverlapped Superstructure: Engineering Ideal Atomic Interface for Lithium Ion Storage.* Advanced Materials, 2015. **27**(24): p. 3687-3695.
215. Hu, S., et al., *Mesoporous Carbon Nanofibers Embedded with MoS2 Nanocrystals for Extraordinary Li-Ion Storage.* Chemistry-a European Journal, 2015. **21**(50): p. 18248-18257.
216. Maruyama, H., et al., *Improving battery safety by reducing the formation of Li dendrites with the use of amorphous silicon polymer anodes.* Scientific Reports, 2015. **5**.
217. Chang, K. and W.X. Chen, *L-Cysteine-Assisted Synthesis of Layered MoS2/Graphene Composites with Excellent Electrochemical Performances for Lithium Ion Batteries.* Acs Nano, 2011. **5**(6): p. 4720-4728.
218. Wan, Z.M., et al., *Core-Shell Structure of Hierarchical Quasi-Hollow MoS2 Microspheres Encapsulated Porous Carbon as Stable Anode for Li-Ion Batteries.* Small, 2014. **10**(23): p. 4975-4981.

219. Zhang, C.F., et al., *Synthesis of MoS2-C One-Dimensional Nanostructures with Improved Lithium Storage Properties.* Acs Applied Materials & Interfaces, 2012. **4**(7): p. 3765-3768.
220. George, C., et al., *Structural Evolution of Electrochemically Lithiated MoS2 Nanosheets and the Role of Carbon Additive in Li-Ion Batteries.* Chemistry of Materials, 2016. **28**(20): p. 7304-7310.
221. Kong, J.H., et al., *MoS2 Nanosheets Hosted in Polydopamine-Derived Mesoporous Carbon Nanofibers as Lithium-Ion Battery Anodes: Enhanced MoS2 Capacity Utilization and Underlying Mechanism.* ACS Applied Materials & Interfaces, 2015. **7**(43): p. 24279-24287.
222. Song, H.J., et al., *Preparation and tribological properties of MoS2/graphene oxide composites.* Applied Surface Science, 2017. **419**: p. 24-34.
223. Yang, M., et al., *Free-standing molybdenum disulfide/graphene composite paper as a binder- and carbon-free anode for lithium-ion batteries.* Journal of Power Sources, 2015. **288**: p. 76-81.
224. Zhu, C.B., et al., *Fast Li Storage in MoS2-Graphene-Carbon Nanotube Nanocomposites: Advantageous Functional Integration of 0D, 1D, and 2D Nanostructures.* Advanced Energy Materials, 2015. **5**(4).
225. Ding, S.J., J.S. Chen, and X.W. Lou, *Glucose-Assisted Growth of MoS2 Nanosheets on CNT Backbone for Improved Lithium Storage Properties.* Chemistry-a European Journal, 2011. **17**(47): p. 13142-13145.
226. Antonio Esau Del Rio Castillo, V.P., Haiyan Sun, Joka Buha, Duc Anh Dinh, Emanuele Lago, Alberto Ansaldo, Andrea Capasso, Liberato Manna, and Francesco Bonaccorso, *Exfoliation of Few-Layer Black Phosphorus in Low Boiling Point Solvents and its Application in Li-ion Batteries.* Chem. Mater., 2017. **Just Accepted Manuscript**.
227. Favron, A., et al., *Photooxidation and quantum confinement effects in exfoliated black phosphorus.* Nature Materials, 2015. **14**(8): p. 826-+.
228. Zhao, Y.T., et al., *Surface Coordination of Black Phosphorus for Robust Air and Water Stability.* Angewandte Chemie-International Edition, 2016. **55**(16): p. 5003-5007.
229. Illarionov, Y.Y., et al., *Long-Term Stability and Reliability of Black Phosphorus Field-Effect Transistors.* Acs Nano, 2016. **10**(10): p. 9543-9549.
230. Edmonds, M.T., et al., *Creating a Stable Oxide at the Surface of Black Phosphorus.* Acs Applied Materials & Interfaces, 2015. **7**(27): p. 14557-14562.
231. Koenig, S.P., et al., *Electric field effect in ultrathin black phosphorus.* Applied Physics Letters, 2014. **104**(10).
232. Sun, D.X., et al., *Thermal risk assessment and grading of chemicals with instantaneous power density.* Journal of Thermal Analysis and Calorimetry, 2012. **109**(3): p. 1373-1377.
233. Brent, J.R., et al., *Production of few-layer phosphorene by liquid exfoliation of black phosphorus.* Chemical Communications, 2014. **50**(87): p. 13338-13341.
234. Yasaei, P., et al., *High-Quality Black Phosphorus Atomic Layers by Liquid-Phase Exfoliation.* Advanced Materials, 2015. **27**(11): p. 1887-+.
235. Hanlon, D., et al., *Liquid exfoliation of solvent-stabilized few-layer black phosphorus for applications beyond electronics.* Nature Communications, 2015. **6**.
236. Zhang, Y., et al., *An Air-Stable Densely Packed Phosphorene-Graphene Composite Toward Advanced Lithium Storage Properties.* Advanced Energy Materials, 2016. **6**(12).
237. Chabot, V., et al., *High yield production and purification of few layer graphene by Gum Arabic assisted physical sonication.* Scientific Reports, 2013. **3**.
238. Bonaccorso, F., et al., *2D-Crystal-Based Functional Inks.* Advanced Materials, 2016. **28**(29): p. 6136-6166.
239. Jawaid, A., et al., *Mechanism for Liquid Phase Exfoliation of MoS2.* Chemistry of Materials, 2016. **28**(1): p. 337-348.
240. Kakavelakis, G., et al., *Size-Tuning of WSe2 Flakes for High Efficiency Inverted Organic Solar Cells.* Acs Nano, 2017. **11**(4): p. 3517-3531.
241. Hernandez, Y., et al., *High-yield production of graphene by liquid-phase exfoliation of graphite.* Nature Nanotechnology, 2008. **3**(9): p. 563-568.
242. Israelachvili, J., *Intermolecular and surface force.* Boston: Academic Press third edition, 2011.

243. Lotya, M., et al., *Liquid Phase Production of Graphene by Exfoliation of Graphite in Surfactant/Water Solutions.* Journal of the American Chemical Society, 2009. **131**(10): p. 3611-3620.
244. Rosoff, M., Nano-surface chemistry, 2001. **CRC Press**.
245. Svedberg, T., Pedersen, K. O., *The Ultracentrifuge.* Oxford, 1940.
246. Khan, U., et al., *Solvent-Exfoliated Graphene at Extremely High Concentration.* Langmuir, 2011. **27**(15): p. 9077-9082.
247. Svedberg, T.P., K. O., *The Ultracentrifuge.* Oxford

University Press: Oxford, U.K., 1940.

248. Gupta, A., V. Arunachalam, and S. Vasudevan, *Liquid-Phase Exfoliation of MoS2 Nanosheets: The Critical Role of Trace Water.* Journal of Physical Chemistry Letters, 2016. **7**(23): p. 4884-4890.
249. Capasso, A., et al., *Ink-jet printing of graphene for flexible electronics: An environmentally-friendly approach.* Solid State Communications, 2015. **224**: p. 53-63.
250. Reisch, M., *Solvent users look to replace NMP.* Chemical & Engineering News, 2008. **86**(29): p. 32-32.
251. Halim, U., et al., *A rational design of cosolvent exfoliation of layered materials by directly probing liquid-solid interaction.* Nature Communications, 2013. **4**.
252. Liang, Y.T. and M.C. Hersam, *Highly Concentrated Graphene Solutions via Polymer Enhanced Solvent Exfoliation and Iterative Solvent Exchange.* Journal of the American Chemical Society, 2010. **132**(50): p. 17661-17663.
253. Xiong, Z., Y.S. Yun, and H.J. Jin, *Applications of Carbon Nanotubes for Lithium Ion Battery Anodes.* Materials, 2013. **6**(3): p. 1138-1158.
254. Landi, B.J., et al., *Carbon nanotubes for lithium ion batteries.* Energy & Environmental Science, 2009. **2**(6): p. 638-654.
255. Allen J. Bard, L.R.F., *Electrochemical Methods: Fundamentals and Applications.* JOHN WILEY & SONS, INC., 2001.
256. *https://chem.libretexts.org/Core/Analytical_Chemistry/Instrumental_Analysis/Cyclic_Voltammetry*.
257. https://www.comsol.com/blogs/modeling-electroanalysis-cyclic-voltammetry/.
258. Barsoukov, E.M., J. R., *Impedance Spectroscopy Theory, Experiment, and Applications.* JOHN WILEY & SONS, INC., 2005.
259. Quan-Chao Zhuang, X.-Y.Q., Shou-Dong Xu, Ying-Huai Qiang and Shi-Gang Sun, *Diagnosis of Electrochemical Impedance Spectroscopy in Lithium-Ion Batteries. Lithium Ion Batteries - New Developments.* InTech, 2012.
260. D. Greenaway, G.H., F. Bassani and E. Tosatti, Phys. Rev., 1969. **178**: p. 1340.
261. Meyer, J.C., et al., *The structure of suspended graphene sheets.* Nature, 2007. **446**(7131): p. 60-63.
262. Torrisi, F., et al., *Inkjet-Printed Graphene Electronics.* Acs Nano, 2012. **6**(4): p. 2992-3006.
263. Zhang, X.Y., et al., *Dispersion of graphene in ethanol using a simple solvent exchange method.* Chemical Communications, 2010. **46**(40): p. 7539-7541.
264. Yang, L., et al., *Excitonic Effects on the Optical Response of Graphene and Bilayer Graphene.* Physical Review Letters, 2009. **103**(18).
265. Ferrari, A.C. and D.M. Basko, *Raman spectroscopy as a versatile tool for studying the properties of graphene.* Nature Nanotechnology, 2013. **8**(4): p. 235-246.
266. Ferrari, A.C., et al., *Raman spectrum of graphene and graphene layers.* Physical Review Letters, 2006. **97**(18).
267. Ferrari, A.C. and J. Robertson, *Resonant Raman spectroscopy of disordered, amorphous, and diamondlike carbon.* Physical Review B, 2001. **64**(7).
268. Nolan, H., et al., *Nitrogen-doped reduced graphene oxide electrodes for electrochemical supercapacitors.* Physical Chemistry Chemical Physics, 2014. **16**(6): p. 2280-2284.
269. Thomsen, C. and S. Reich, *Doable resonant Raman scattering in graphite.* Physical Review Letters, 2000. **85**(24): p. 5214-5217.

270. Neoh, K.G., E.T. Kang, and K.L. Tan, *Limitations of the X-ray photoelectron spectroscopy technique in the study of electroactive polymers.* Journal of Physical Chemistry B, 1997. **101**(5): p. 726-731.
271. Das, A., et al., *Monitoring dopants by Raman scattering in an electrochemically top-gated graphene transistor.* Nature Nanotechnology, 2008. **3**(4): p. 210-215.
272. Ferrari, A.C., et al., *Science and technology roadmap for graphene, related two-dimensional crystals, and hybrid systems.* Nanoscale, 2015. **7**(11): p. 4598-4810.
273. Liu, J. and D.F. Xue, *Hollow Nanostructured Anode Materials for Li-Ion Batteries.* Nanoscale Research Letters, 2010. **5**(10): p. 1525-1534.
274. Cheng, F.Y., et al., *Functional Materials for Rechargeable Batteries.* Advanced Materials, 2011. **23**(15): p. 1695-1715.
275. Jiang, B.J., et al., *Facile fabrication of high quality graphene from expandable graphite: simultaneous exfoliation and reduction.* Chemical Communications, 2010. **46**(27): p. 4920-4922.
276. Eda, G., G. Fanchini, and M. Chhowalla, *Large-area ultrathin films of reduced graphene oxide as a transparent and flexible electronic material.* Nature Nanotechnology, 2008. **3**(5): p. 270-274.
277. Peng, H.L., et al., *Effect of Transition Metals on the Structure and Performance of the Doped Carbon Catalysts Derived From Polyaniline and Melamine for ORR Application.* Acs Catalysis, 2014. **4**(10): p. 3797-3805.
278. Cao, X.P. and R.J. Hamers, *Silicon surfaces as electron acceptors: Dative bonding of amines with Si(001) and Si(111) surfaces.* Journal of the American Chemical Society, 2001. **123**(44): p. 10988-10996.
279. Charlier, J., et al., *Adsorption of substituted pyrrolidone molecules on Au(111): an STM and XPS study.* Surface and Interface Analysis, 2000. **30**(1): p. 283-287.
280. Yang, L., B. Ravdel, and B.L. Lucht, *Electrolyte Reactions with the Surface of High Voltage LiNi0.5Mn1.5O4 Cathodes for Lithium-Ion Batteries.* Electrochemical and Solid State Letters, 2010. **13**(8): p. A95-A97.
281. Kalisky, B., et al., *Scanning Probe Manipulation of Magnetism at the LaAlO3/SrTiO3 Heterointerface.* Nano Letters, 2012. **12**(8): p. 4055-4059.
282. Chu, P.K. and L.H. Li, *Characterization of amorphous and nanocrystalline carbon films.* Materials Chemistry and Physics, 2006. **96**(2-3): p. 253-277.
283. Ferrari, A.C., *Raman spectroscopy of graphene and graphite: Disorder, electron-phonon coupling, doping and nonadiabatic effects.* Solid State Communications, 2007. **143**(1-2): p. 47-57.
284. Tan, P.H., et al., *Optical properties of nanotube bundles by photoluminescence excitation and absorption spectroscopy.* Physica E-Low-Dimensional Systems & Nanostructures, 2008. **40**(7): p. 2352-2359.
285. Tan, P.H., et al., *Photoluminescence spectroscopy of carbon nanotube bundles: Evidence for exciton energy transfer.* Physical Review Letters, 2007. **99**(13).
286. Hagen, A. and T. Hertel, *Quantitative analysis of optical spectra from individual single-wall carbon nanotubes.* Nano Letters, 2003. **3**(3): p. 383-388.
287. Bonaccorso, F., et al., *Density Gradient Ultracentrifugation of Nanotubes: Interplay of Bundling and Surfactants Encapsulation.* Journal of Physical Chemistry C, 2010. **114**(41): p. 17267-17285.
288. Kataura, H., et al., *Optical absorption and resonance Raman scattering of carbon nanotubes.* Electronic Properties of Novel Materials - Science and Technology of Molecular Nanostructures, 1999. **486**: p. 328-332.
289. Weisman, R.B. and S.M. Bachilo, *Dependence of optical transition energies on structure for single-walled carbon nanotubes in aqueous suspension: An empirical Kataura plot.* Nano Letters, 2003. **3**(9): p. 1235-1238.
290. Kataura, H., et al., *Optical properties of single-wall carbon nanotubes.* Synthetic Metals, 1999. **103**(1-3): p. 2555-2558.
291. Bachilo, S.M., et al., *Structure-assigned optical spectra of single-walled carbon nanotubes.* Science, 2002. **298**(5602): p. 2361-2366.

292. Rao, A.M., et al., *Diameter-selective Raman scattering from vibrational modes in carbon nanotubes.* Science, 1997. **275**(5297): p. 187-191.
293. Telg, H., et al., *Chirality distribution and transition energies of carbon nanotubes (vol 93, art no 177401, 2004).* Physical Review Letters, 2004. **93**(18).
294. Meyer, J.C., et al., *Raman modes of index-identified freestanding single-walled carbon nanotubes.* Physical Review Letters, 2005. **95**(21).
295. Fantini, C., et al., *Optical transition energies for carbon nanotubes from resonant Raman spectroscopy: Environment and temperature effects.* Physical Review Letters, 2004. **93**(14).
296. Paillet, M., et al., *Raman active phonons of identified semiconducting single-walled carbon nanotubes.* Physical Review Letters, 2006. **96**(25).
297. Jorio, A., et al., *Structural (n, m) determination of isolated single-wall carbon nanotubes by resonant Raman scattering.* Physical Review Letters, 2001. **86**(6): p. 1118-1121.
298. Shi, Z.J., et al., *Mass-production of single-wall carbon nanotubes by arc discharge method.* Carbon, 1999. **37**(9): p. 1449-1453.
299. Araujo, P.T., et al., *Diameter Dependence of the Dielectric Constant for the Excitonic Transition Energy of Single-Wall Carbon Nanotubes.* Physical Review Letters, 2009. **103**(14).
300. Ferrari, A.C. and J. Robertson, *Interpretation of Raman spectra of disordered and amorphous carbon.* Physical Review B, 2000. **61**(20): p. 14095-14107.
301. Mohiuddin, T.M.G., et al., *Uniaxial strain in graphene by Raman spectroscopy: G peak splitting, Gruneisen parameters, and sample orientation.* Physical Review B, 2009. **79**(20).
302. Piscanec, S., et al., *Optical phonons in carbon nanotubes: Kohn anomalies, Peierls distortions, and dynamic effects.* Physical Review B, 2007. **75**(3).
303. Jorio, A., et al., *G-band resonant Raman study of 62 isolated single-wall carbon nanotubes.* Physical Review B, 2002. **65**(15).
304. Lazzeri, M., et al., *Phonon linewidths and electron-phonon coupling in graphite and nanotubes.* Physical Review B, 2006. **73**(15).
305. Hasan, T., et al., *Solution-phase exfoliation of graphite for ultrafast photonics.* Physica Status Solidi B-Basic Solid State Physics, 2010. **247**(11-12): p. 2953-2957.
306. Zhou, J.W., et al., *2D Space-Confined Synthesis of Few-Layer MoS2 Anchored on Carbon Nanosheet for Lithium-Ion Battery Anode.* Acs Nano, 2015. **9**(4): p. 3837-3848.
307. Shiozawa, H., et al., *Screening the Missing Electron: Nanochemistry in Action.* Physical Review Letters, 2009. **102**(4).
308. Miyata, Y., K. Mizuno, and H. Kataura, *Purity and Defect Characterization of Single-Wall Carbon Nanotubes Using Raman Spectroscopy.* Journal of Nanomaterials, 2011.
309. C. W. Bret, W.G.S., D. W. Hahn, 2011. **42**: p. 301.
310. Siciliano, T., et al., *Characteristics of molybdenum trioxide nanobelts prepared by thermal evaporation technique.* Materials Chemistry and Physics, 2009. **114**(2-3): p. 687-691.
311. G. Mestl, P.R., B. Delmon, H. Knozinger, 1994. **98**: p. 11269.
312. M. A. Py, K.M., Phys. B, 1981. **105**: p. 370.
313. TaoHe, J., *Photochromism of molybdenum oxide.* Journal of Photochemistry and Photobiology C: Photochemistry Reviews, 2003. **4**(2): p. 125-143.
314. Wang, D., et al., *Van der Waals epitaxy of ultrathin alpha-MoO3 sheets on mica substrate with single-unit-cell thickness.* Applied Physics Letters, 2016. **108**(5).
315. Bohn, J.E., et al., *Estimating the Raman Cross Sections of Single Carbon Nanotubes.* Acs Nano, 2010. **4**(6): p. 3466-3470.
316. Heifets, E., et al., *Electronic structure and thermodynamic stability of double-layered SrTiO3(001) surfaces: Ab initio simulations.* Physical Review B, 2007. **75**(11).
317. Klar, P., et al., *Raman scattering efficiency of graphene.* Physical Review B, 2013. **87**(20).
318. Li, H., et al., *From Bulk to Monolayer MoS2: Evolution of Raman Scattering.* Advanced Functional Materials, 2012. **22**(7): p. 1385-1390.
319. Lee, C., et al., *Anomalous Lattice Vibrations of Single- and Few-Layer MoS2.* Acs Nano, 2010. **4**(5): p. 2695-2700.
320. Yu, Y.F., et al., *Controlled Scalable Synthesis of Uniform, High-Quality Monolayer and Few-layer MoS2 Films.* Scientific Reports, 2013. **3**.

321. McCreary, K.M., et al., *Large-Area Synthesis of Continuous and Uniform MoS2 Monolayer Films on Graphene.* Advanced Functional Materials, 2014. **24**(41): p. 6449-6454.
322. Balendhran, S., et al., *Atomically thin layers of MoS2 via a two step thermal evaporation-exfoliation method.* Nanoscale, 2012. **4**(2): p. 461-466.
323. Zhu, J.Y., et al., *Exfoliation of MoS2 and h-BN nanosheets by hydrolysis of LiBH4.* Nanotechnology, 2017. **28**(11).
324. Bindhu, B., et al., *Molybdenum disulfide nanoflakes through Li-AHA assisted exfoliation in an aqueous medium.* Rsc Advances, 2016. **6**(26): p. 22026-22033.
325. Ravula, S., J.B. Essner, and G.A. Baker, *Kitchen-Inspired Nanochemistry: Dispersion, Exfoliation, and Hybridization of Functional MoS2 Nanosheets Using Culinary Hydrocolloids.* Chemnanomat, 2015. **1**(3): p. 167-177.
326. Du, G.D., et al., *Superior stability and high capacity of restacked molybdenum disulfide as anode material for lithium ion batteries.* Chemical Communications, 2010. **46**(7): p. 1106-1108.
327. Hu, S., et al., *Preparation of carbon coated MoS2 flower-like nanostructure with self-assembled nanosheets as high-performance lithium-ion battery anodes.* Journal of Materials Chemistry A, 2014. **2**(21): p. 7862-7872.
328. Gao, D.Q., et al., *Ferromagnetism in freestanding MoS2 nanosheets.* Nanoscale Research Letters, 2013. **8**.
329. Ibrahem, M.A., et al., *High quantity and quality few-layers transition metal disulfide nanosheets from wet-milling exfoliation.* Rsc Advances, 2013. **3**(32): p. 13193-13202.
330. Chen, G., et al., *Facile synthesis of hierarchical MoS2-carbon microspheres as a robust anode for lithium ion batteries.* Journal of Materials Chemistry A, 2016. **4**(24): p. 9653-9660.
331. Shi, Y.M., et al., *Self-assembly of hierarchical MoSx/CNT nanocomposites (2 < x < 3): towards high performance anode materials for lithium ion batteries.* Scientific Reports, 2013. **3**.
332. Park, S.K., et al., *Scalable Synthesis of Few-Layer MoS2 Incorporated into Hierarchical Porous Carbon Nanosheets for High-Performance Li- and Na-Ion Battery Anodes.* Acs Applied Materials & Interfaces, 2016. **8**(30): p. 19456-19465.
333. Li, H.Q. and H.S. Zhou, *Enhancing the performances of Li-ion batteries by carbon-coating: present and future.* Chemical Communications, 2012. **48**(9): p. 1201-1217.
334. Zhang, Y.F., et al., *MoS2 coated hollow carbon spheres for anodes of lithium ion batteries.* 2d Materials, 2016. **3**(2).
335. Wang, J.J., et al., *An Advanced MoS2/Carbon Anode for High-Performance Sodium-Ion Batteries.* Small, 2015. **11**(4): p. 473-481.
336. Zhao, C.Y., et al., *Thin MoS2 Nanoflakes Encapsulated in Carbon Nanofibers as High-Performance Anodes for Lithium-Ion Batteries.* Acs Applied Materials & Interfaces, 2014. **6**(9): p. 6392-6398.
337. Sun, W.Y., et al., *Effects of Carbon Content on the Electrochemical Performances of MoS2-C Nanocomposites for Li-Ion Batteries.* Acs Applied Materials & Interfaces, 2016. **8**(34): p. 22168-22174.
338. Pimenta, M.A., et al., *Studying disorder in graphite-based systems by Raman spectroscopy.* Physical Chemistry Chemical Physics, 2007. **9**(11): p. 1276-1291.
339. Klein, A., et al., *Electronic band structure of single-crystal and single-layer WS2: Influence of interlayer van der Waals interactions.* Physical Review B, 2001. **64**(20).
340. Horie, C. and H. Miyazaki, *Atomic-Force-Microscopy Images of Graphite Due to Vanderwaals Interactions.* Physical Review B, 1990. **42**(18): p. 11757-11761.
341. Hansen, C., *Hansen Solubility Parameters: A user's handbook, Second Edition.* Boca Raton, Fla: CRC Press, 2007: p. 978-0-8493-7248-3.
342. Lyklema, J., *The surface tension of pure liquids - Thermodynamic components and corresponding states.* Colloids and Surfaces a-Physicochemical and Engineering Aspects, 1999. **156**(1-3): p. 413-421.
343. Del Rio-Castillo, A.E., et al., *Selective suspension of single layer graphene mechanochemically exfoliated from carbon nanofibres.* Nano Research, 2014. **7**(7): p. 963-972.
344. Coleman, J.N., *Liquid-Phase Exfoliation of Nanotubes and Graphene.* Advanced Functional Materials, 2009. **19**(23): p. 3680-3695.

345. Hildebrand, J.H.S., R. L., *Solubility of Non-Electrolites. 3rd ed.* New York, Reinhold Corp. , 1950.
346. Vandenburg, H.J., et al., *A simple solvent selection method for accelerated solvent extraction of additives from polymers.* Analyst, 1999. **124**(11): p. 1707-1710.
347. Barton, A., *AFM. Handbook of Solubility Parameters and Other Cohesion Parameters 2nd edition.* CRC Press 1991.
348. Hernandez, Y., et al., *Measurement of Multicomponent Solubility Parameters for Graphene Facilitates Solvent Discovery.* Langmuir, 2010. **26**(5): p. 3208-3213.
349. Woomer, A.H., et al., *Phosphorene: Synthesis, Scale-Up, and Quantitative Optical Spectroscopy.* Acs Nano, 2015. **9**(9): p. 8869-8884.
350. Garciarubio, L.H., *Refractive-Index Effects on the Absorption-Spectra of Macromolecules.* Macromolecules, 1992. **25**(10): p. 2608-2613.
351. Kang, J., et al., *Solvent Exfoliation of Electronic-Grade, Two-Dimensional Black Phosphorus.* Acs Nano, 2015. **9**(4): p. 3596-3604.
352. Kang, J., et al., *Stable aqueous dispersions of optically and electronically active phosphorene.* Proceedings of the National Academy of Sciences of the United States of America, 2016. **113**(42): p. 11688-11693.
353. Vanderborgh, C.A. and D. Schiferl, *Raman Studies of Black Phosphorus from 0.25 to 7.7 Gpa at 15-K.* Physical Review B, 1989. **40**(14): p. 9595-9599.
354. Lu, W.L., et al., *Plasma-assisted fabrication of monolayer phosphorene and its Raman characterization.* Nano Research, 2014. **7**(6): p. 853-859.
355. Zhang, S., et al., *Extraordinary Photoluminescence and Strong Temperature/Angle-Dependent Raman Responses in Few-Layer Phosphorene.* Acs Nano, 2014. **8**(9): p. 9590-9596.
356. Ziletti, A., et al., *Phosphorene oxides: Bandgap engineering of phosphorene by oxidation.* Physical Review B, 2015. **91**(8).
357. Sun, J., et al., *A phosphorene-graphene hybrid material as a high-capacity anode for sodium-ion batteries.* Nature Nanotechnology, 2015. **10**(11): p. 980-U184.
358. Fei, R.X. and L. Yang, *Lattice vibrational modes and Raman scattering spectra of strained phosphorene.* Applied Physics Letters, 2014. **105**(8).
359. Cai, Y.Q., et al., *Giant Phononic Anisotropy and Unusual Anharmonicity of Phosphorene: Interlayer Coupling and Strain Engineering.* Advanced Functional Materials, 2015. **25**(15): p. 2230-2236.
360. Guo, Z.N., et al., *From Black Phosphorus to Phosphorene: Basic Solvent Exfoliation, Evolution of Raman Scattering, and Applications to Ultrafast Photonics.* Advanced Functional Materials, 2015. **25**(45): p. 6996-7002.
361. Wu, R.J., et al., *Atomic and electronic structure of exfoliated black phosphorus.* Journal of Vacuum Science & Technology A, 2015. **33**(6).
362. Liu, X.L., et al., *In Situ Thermal Decomposition of Exfoliated Two-Dimensional Black Phosphorus.* Journal of Physical Chemistry Letters, 2015. **6**(5): p. 773-778.
363. Huang, Y., et al., *Interaction of Black Phosphorus with Oxygen and Water.* Chemistry of Materials, 2016. **28**(22): p. 8330-8339.
364. Brent, J.R., et al., *On the stability of surfactant-stabilised few-layer black phosphorus in aqueous media.* Rsc Advances, 2016. **6**(90): p. 86955-86958.
365. Nicolosi, V., et al., *Liquid Exfoliation of Layered Materials.* Science, 2013. **340**(6139): p. 1420-+.
366. Green, A.A. and M.C. Hersam, *Solution Phase Production of Graphene with Controlled Thickness via Density Differentiation.* Nano Letters, 2009. **9**(12): p. 4031-4036.
367. Marago, O.M., et al., *Brownian Motion of Graphene.* Acs Nano, 2010. **4**(12): p. 7515-7523.
368. O'Neill, A., et al., *Graphene Dispersion and Exfoliation in Low Boiling Point Solvents.* Journal of Physical Chemistry C, 2011. **115**(13): p. 5422-5428.
369. Bonaccorso, F. and Z.P. Sun, *Solution processing of graphene, topological insulators and other 2d crystals for ultrafast photonics.* Optical Materials Express, 2014. **4**(1): p. 63-78.
370. Zhou, D., Q.Y. Cheng, and B.H. Han, *Solvothermal synthesis of homogeneous graphene dispersion with high concentration.* Carbon, 2011. **49**(12): p. 3920-3927.

371. Ha, D.H., M.A. Islam, and R.D. Robinson, *Binder-Free and Carbon-Free Nanoparticle Batteries: A Method for Nanoparticle Electrodes without Polymeric Binders or Carbon Black.* Nano Letters, 2012. **12**(10): p. 5122-5130.
372. Li, W., et al., *One step preparation of a high performance Ge-C nanocomposite anode for lithium ion batteries by tandem plasma reactions.* Chemical Communications, 2014. **50**(16): p. 2052-2054.
373. Liu, B., et al., *Hierarchical silicon nanowires-carbon textiles matrix as a binder-free anode for high-performance advanced lithium-ion batteries.* Scientific Reports, 2013. **3**.
374. Li, N., et al., *ZnO Anchored on Vertically Aligned Graphene: Binder-Free Anode Materials for Lithium-Ion Batteries.* Acs Applied Materials & Interfaces, 2014. **6**(23): p. 20590-20596.
375. Abouimrane, A., et al., *Non-Annealed Graphene Paper as a Binder-Free Anode for Lithium-Ion Batteries.* Journal of Physical Chemistry C, 2010. **114**(29): p. 12800-12804.
376. Hu, Y.H., et al., *Free-standing graphene-carbon nanotube hybrid papers used as current collector and binder free anodes for lithium ion batteries.* Journal of Power Sources, 2013. **237**: p. 41-46.
377. Scrosati, B., J. Hassoun, and Y.K. Sun, *Lithium-ion batteries. A look into the future.* Energy & Environmental Science, 2011. **4**(9): p. 3287-3295.
378. Dunn, B., H. Kamath, and J.M. Tarascon, *Electrical Energy Storage for the Grid: A Battery of Choices.* Science, 2011. **334**(6058): p. 928-935.
379. Scrosati, B., *Recent advances in lithium ion battery materials.* Electrochimica Acta, 2000. **45**(15-16): p. 2461-2466.
380. Bueno, P.R. and E.R. Leite, *Nanostructured Li ion insertion electrodes. 1. Discussion on fast transport and short path for ion diffusion.* Journal of Physical Chemistry B, 2003. **107**(34): p. 8868-8877.
381. Luo, S., et al., *Binder-Free LiCoO2/Carbon Nanotube Cathodes for High-Performance Lithium Ion Batteries.* Advanced Materials, 2012. **24**(17): p. 2294-2298.
382. Kovalenko, I., et al., *A Major Constituent of Brown Algae for Use in High-Capacity Li-Ion Batteries.* Science, 2011. **334**(6052): p. 75-79.
383. Peled, E., et al., *The Sei Model - Application to Lithium Polymer Electrolyte Batteries.* Electrochimica Acta, 1995. **40**(13-14): p. 2197-2204.
384. Han, J.T., et al., *Lithium Ion Intercalation Performance of Niobium Oxides: KNb5O13 and K6Nb10.8O30.* Chemistry of Materials, 2009. **21**(20): p. 4753-4755.
385. Chou, S.L., et al., *Small things make a big difference: binder effects on the performance of Li and Na batteries.* Physical Chemistry Chemical Physics, 2014. **16**(38): p. 20347-20359.
386. Ji, L.W., et al., *Graphene Oxide as a Sulfur Immobilizer in High Performance Lithium/Sulfur Cells.* Journal of the American Chemical Society, 2011. **133**(46): p. 18522-18525.
387. Lee, J.K., et al., *Silicon nanoparticles-graphene paper composites for Li ion battery anodes.* Chemical Communications, 2010. **46**(12): p. 2025-2027.
388. Zhang, J.X., et al., *Graphite/graphene oxide composite as high capacity and binder-free anode material for lithium ion batteries.* Journal of Power Sources, 2013. **241**: p. 619-626.
389. Lian, P.C., et al., *Large reversible capacity of high quality graphene sheets as an anode material for lithium-ion batteries.* Electrochimica Acta, 2010. **55**(12): p. 3909-3914.
390. Qu, B.H., et al., *Layered SnS2-Reduced Graphene Oxide Composite - A High-Capacity, High-Rate, and Long-Cycle Life Sodium-Ion Battery Anode Material.* Advanced Materials, 2014. **26**(23): p. 3854-3859.
391. Zhu, X.J., et al., *Nanostructured Reduced Graphene Oxide/Fe2O3 Composite As a High-Performance Anode Material for Lithium Ion Batteries.* Acs Nano, 2011. **5**(4): p. 3333-3338.
392. Vargas, O.A., A. Caballero, and J. Morales, *Can the performance of graphene nanosheets for lithium storage in Li-ion batteries be predicted?* Nanoscale, 2012. **4**(6): p. 2083-2092.
393. Zhou, L.J., Z.F. Hou, and L.M. Wu, *First-Principles Study of Lithium Adsorption and Diffusion on Graphene with Point Defects.* Journal of Physical Chemistry C, 2012. **116**(41): p. 21780-21787.
394. Xiang, H.F., et al., *Graphene sheets as anode materials for Li-ion batteries: preparation, structure, electrochemical properties and mechanism for lithium storage.* Rsc Advances, 2012. **2**(17): p. 6792-6799.

395. Tossici, R., et al., *Electrochemical behavior of superdense 'LiC2' prepared by ballmilling.* Electrochimica Acta, 2003. **48**(10): p. 1419-1424.
396. Raccichini, R., et al., *Enhanced low-temperature lithium storage performance of multilayer graphene made through an improved ionic liquid-assisted synthesis.* Journal of Power Sources, 2015. **281**: p. 318-325.
397. Li, N., et al., *Flexible graphene-based lithium ion batteries with ultrafast charge and discharge rates.* Proceedings of the National Academy of Sciences of the United States of America, 2012. **109**(43): p. 17360-17365.
398. Wang, G.X., et al., *Graphene nanosheets for enhanced lithium storage in lithium ion batteries.* Carbon, 2009. **47**(8): p. 2049-2053.
399. Evanoff, K., et al., *Nanosilicon-Coated Graphene Granules as Anodes for Li-Ion Batteries.* Advanced Energy Materials, 2011. **1**(4): p. 495-498.
400. Wu, Z.S., et al., *High-Energy MnO2 Nanowire/Graphene and Graphene Asymmetric Electrochemical Capacitors.* Acs Nano, 2010. **4**(10): p. 5835-5842.
401. Shi, Y., et al., *Hollow Structured Li3VO4 Wrapped with Graphene Nanosheets in Situ Prepared by a One-Pot Template-Free Method as an Anode for Lithium-Ion Batteries.* Nano Letters, 2013. **13**(10): p. 4715-4720.
402. Zhou, G.M., et al., *Graphene-Wrapped Fe3O4 Anode Material with Improved Reversible Capacity and Cyclic Stability for Lithium Ion Batteries.* Chemistry of Materials, 2010. **22**(18): p. 5306-5313.
403. Mason, T.J., Sonochemistry, Oxford University Press, New York, 1999. **1**.
404. Wang, Y.Y., et al., *Raman studies of monolayer graphene: The substrate effect.* Journal of Physical Chemistry C, 2008. **112**(29): p. 10637-10640.
405. Tsukamoto, T., et al., *Effects of Surface Chemistry of Substrates on Raman Spectra in Graphene.* Journal of Physical Chemistry C, 2012. **116**(7): p. 4732-4737.
406. Levi, M.D., E.A. Levi, and D. Aurbach, *The mechanism of lithium intercalation in graphite film electrodes in aprotic media .2. Potentiostatic intermittent titration and in situ XRD studies of the solid-state ionic diffusion.* Journal of Electroanalytical Chemistry, 1997. **421**(1-2): p. 89-97.
407. Verma, P., P. Maire, and P. Novak, *A review of the features and analyses of the solid electrolyte interphase in Li-ion batteries.* Electrochimica Acta, 2010. **55**(22): p. 6332-6341.
408. Kaskhedikar, N.A. and J. Maier, *Lithium Storage ion Carbon Nanostructures.* Advanced Materials, 2009. **21**(25-26): p. 2664-2680.
409. Liu, D., et al., *Spinel materials for high-voltage cathodes in Li-ion batteries.* RSC Advances, 2014. **4**(1): p. 154-167.
410. Hassoun, J., et al., *A New, Safe, High-Rate and High-Energy Polymer Lithium-Ion Battery.* Advanced Materials, 2009. **21**(47): p. 4807-4810.
411. Kim, J.-H., et al., *Comparative Study of LiNi0. 5Mn1. 5O4-δ and LiNi0. 5Mn1. 5O4 Cathodes Having Two Crystallographic Structures: Fd 3 m and P 4332.* Chemistry of materials, 2004. **16**(5): p. 906-914.
412. Zhong, Q., et al., *Synthesis and Electrochemistry of LiNi x Mn2− x O 4.* Journal of The Electrochemical Society, 1997. **144**(1): p. 205-213.
413. Zhang, J., Z. Shi, and C. Wang, *Effect of pre-lithiation degrees of mesocarbon microbeads anode on the electrochemical performance of lithium-ion capacitors.* Electrochimica Acta, 2014. **125**: p. 22-28.
414. Sivakkumar, S. and A. Pandolfo, *Evaluation of lithium-ion capacitors assembled with pre-lithiated graphite anode and activated carbon cathode.* Electrochimica Acta, 2012. **65**: p. 280-287.
415. Hassoun, J., et al., *An advanced lithium-ion battery based on a graphene anode and a lithium iron phosphate cathode.* Nano letters, 2014. **14**(8): p. 4901-4906.
416. Monaco, S., et al., *Electrochemical performance of LiNi 0.5 Mn 1.5 O 4 composite electrodes featuring carbons and reduced graphene oxide.* Journal of Power Sources, 2015. **278**: p. 733-740.
417. Song, J., et al., *Role of Oxygen Vacancies on the Performance of Li [Ni0. 5–x Mn1. 5+ x] O4 (x= 0, 0.05, and 0.08) Spinel Cathodes for Lithium-Ion Batteries.* Chemistry of Materials, 2012. **24**(15): p. 3101-3109.

418. Yang, L., et al., *Excitonic effects on the optical response of graphene and bilayer graphene.* Physical review letters, 2009. **103**(18): p. 186802.
419. Zhou, L., D. Zhao, and X.D. Lou, *LiNi0. 5Mn1. 5O4 Hollow Structures as High-Performance Cathodes for Lithium-Ion Batteries.* Angewandte Chemie, 2012. **124**(1): p. 243-245.
420. Arrebola, J.C., et al., *Crystallinity Control of a Nanostructured LiNi0. 5Mn1. 5O4 Spinel via Polymer-Assisted Synthesis: A Method for Improving Its Rate Capability and Performance in 5 V Lithium Batteries.* Advanced Functional Materials, 2006. **16**(14): p. 1904-1912.
421. Yang, L., B. Ravdel, and B.L. Lucht, *Electrolyte reactions with the surface of high voltage LiNi0. 5Mn1. 5O4 cathodes for lithium-ion batteries.* Electrochemical and Solid-State Letters, 2010. **13**(8): p. A95-A97.
422. M. Yoshio, R.J.B., A. Kozawa, *Lithium-Ion Batteries.* Springer, 2009.
423. Pan, D., et al., *Li Storage Properties of Disordered Graphene Nanosheets.* Chemistry of Materials, 2009. **21**(14): p. 3136-3142.
424. Roy, P. and S.K. Srivastava, *Nanostructured anode materials for lithium ion batteries.* J. Mater. Chem. A, 2015. **3**(6): p. 2454-2484.
425. Winter, M., et al., *Insertion Electrode Materials for Rechargeable Lithium Batteries.* Adv. Mater., 1998. **10**(10): p. 725-763.
426. Kaskhedikar, N.A. and J. Maier, *Lithium Storage in Carbon Nanostructures.* Adv. Mater., 2009. **21**(25-26): p. 2664-2680.
427. Holzapfel, M., et al., *First lithiation and charge/discharge cycles of graphite materials, investigated by electrochemical impedance spectroscopy.* Journal of Electroanalytical Chemistry, 2003. **546**: p. 41-50.
428. Ferre-Vilaplana, A., *Storage of hydrogen adsorbed on alkali metal doped single-layer all-carbon materials.* Journal of Physical Chemistry C, 2008. **112**(10): p. 3998-4004.
429. Liu, Y.Y., et al., *Feasibility of Lithium Storage on Graphene and Its Derivatives.* Journal of Physical Chemistry Letters, 2013. **4**(10): p. 1737-1742.
430. Ataca, C., et al., *High-capacity hydrogen storage by metallized graphene.* Applied Physics Letters, 2008. **93**(4).
431. de las Casas, C. and W.Z. Li, *A review of application of carbon nanotubes for lithium ion battery anode material.* Journal of Power Sources, 2012. **208**: p. 74-85.
432. Wang, Z.Y., S. Madhavi, and X.W. Lou, *Ultralong alpha-MoO3 Nanobelts: Synthesis and Effect of Binder Choice on Their Lithium Storage Properties.* Journal of Physical Chemistry C, 2012. **116**(23): p. 12508-12513.
433. Lou, X.W. and H.C. Zeng, *Hydrothermal synthesis of alpha-MoO3 nanorods via acidification of ammonium heptamolybdate tetrahydrate.* Chemistry of Materials, 2002. **14**(11): p. 4781-4789.
434. J.O.Besenhard, R.S., *The discharge reaction mechanism of the MoO3 electrode in organic electrolytes.* Journal of Power Sources, 1976–1977. **1**: p. 267-276.
435. Qiu, J.Y.C., Z.X. Yang, and Y. Li, *N-doped carbon encapsulated ultrathin MoO3 nanosheets as superior anodes with high capacity and excellent rate capability for Li-ion batteries.* Journal of Materials Chemistry A, 2015. **3**(48): p. 24245-24253.
436. Haiyan Sun, D.H., Duc Anh Dinh, John B. Boland, Antonio Esau Del Rio Castillo, Carlo Di Giovanni, Alberto Ansaldo, Vittorio Pellegrini, Jonathan N. Coleman and Francesco Bonaccorso, *Carbon nanotubes-bridged molybdenum trioxide nanosheets as high performance anode for lithium ion batteries.* 2D Materials, 2017. **In Press**.
437. Gao, M.R., et al., *Nanostructured metal chalcogenides: synthesis, modification, and applications in energy conversion and storage devices.* Chemical Society Reviews, 2013. **42**(7): p. 2986-3017.
438. Chen, J.S., et al., *Fast Synthesis of alpha-MoO3 Nanorods with Controlled Aspect Ratios and Their Enhanced Lithium Storage Capabilities.* Journal of Physical Chemistry C, 2010. **114**(18): p. 8675-8678.
439. Hassan, M.F., et al., *Carbon-coated MoO3 nanobelts as anode materials for lithium-ion batteries.* Journal of Power Sources, 2010. **195**(8): p. 2372-2376.
440. Maier, J., *Nanoionics: ion transport and electrochemical storage in confined systems.* Nature Materials, 2005. **4**(11): p. 805-815.

441. Yoo, H., et al., *Cylindrical nanostructured MoS2 directly grown on CNT composites for lithium-ion batteries.* Nanoscale, 2015. **7**(8): p. 3404-3409.
442. Mai, L.Q., et al., *Mo doped vanadium oxide nanotubes: microstructure and electrochemistry.* Chemical Physics Letters, 2003. **382**(3-4): p. 307-312.
443. Bai, Z.C., et al., *Hierarchical MoS2@Carbon Microspheres as Advanced Anodes for Li-Ion Batteries.* Chemistry-a European Journal, 2015. **21**(50): p. 18187-18191.
444. M.StanleyWhittingham, *Chemistry of intercalation compounds: Metal guests in chalcogenide hosts.* Progress in Solid State Chemistry, 1978. **12**(1): p. 41-99.
445. Teng, Y.Q., et al., *MoS2 Nanosheets Vertically Grown on Graphene Sheets for Lithium-Ion Battery Anodes.* Acs Nano, 2016. **10**(9): p. 8526-8535.
446. Zhang, H.J., L.J. Gao, and Y.J. Gong, *Exfoliated MoO3 nanosheets for high-capacity lithium storage.* Electrochemistry Communications, 2015. **52**: p. 67-70.
447. Meduri, P., et al., *MoO3-x Nanowire Arrays As Stable and High-Capacity Anodes for Lithium Ion Batteries.* Nano Letters, 2012. **12**(4): p. 1784-1788.
448. Wang, H.Y., et al., *Few-layer MoS2 nanosheets incorporated into hierarchical porous carbon for lithium-ion batteries.* Chemical Engineering Journal, 2016. **288**: p. 179-184.
449. Guo, Z.Y., et al., *MoS2 nanosheet arrays supported on hierarchical porous carbon with enhanced lithium storage properties.* Chinese Chemical Letters, 2017. **28**(4): p. 743-747.
450. Yu-Guo Guo, J.-S.H., Li-Jun Wa, *Nanostructured Materials for Electrochemical Energy Conversion and Storage Devices.* Advanced Mateirals, 2008. **20**(23): p. 2878–2887.
451. Cao, X.H., et al., *Preparation of MoS2-Coated Three-Dimensional Graphene Networks for High-Performance Anode Material in Lithium-Ion Batteries.* Small, 2013. **9**(20): p. 3433-3438.
452. Sen, U.K. and S. Mitra, *High-Rate and High-Energy-Density Lithium-Ion Battery Anode Containing 2D MoS2 Nanowall and Cellulose Binder.* Acs Applied Materials & Interfaces, 2013. **5**(4): p. 1240-1247.
453. Hwang, H., H. Kim, and J. Cho, *MoS2 Nanoplates Consisting of Disordered Graphene-like Layers for High Rate Lithium Battery Anode Materials.* Nano Letters, 2011. **11**(11): p. 4826-4830.
454. Xue, X.Y., et al., *SnO2/alpha-MoO3 core-shell nanobelts and their extraordinarily high reversible capacity as lithium-ion battery anodes.* Chemical Communications, 2011. **47**(18): p. 5205-5207.
455. Chhowalla, M., et al., *The chemistry of two-dimensional layered transition metal dichalcogenide nanosheets.* Nature Chemistry, 2013. **5**(4): p. 263-275.
456. Lu, C.X., et al., *A binder-free CNT network-MoS2 composite as a high performance anode material in lithium ion batteries.* Chemical Communications, 2014. **50**(25): p. 3338-3340.
457. Eda, K., *Raman-Spectra of Hydrogen Molybdenum Bronze, H0.30moo3.* Journal of Solid State Chemistry, 1992. **98**(2): p. 350-357.
458. Mestl, G., et al., *Oxygen-Exchange Properties of Moo3 an in-Situ Raman-Spectroscopy Study.* Journal of Physical Chemistry, 1994. **98**(44): p. 11269-11275.
459. Li, Y.F., et al., *Flexible electrode for long-life rechargeable sodium-ion batteries: effect of oxygen vacancy in MoO3-x.* Journal of Materials Chemistry A, 2016. **4**(15): p. 5402-5405.
460. Tsumura, T. and M. Inagaki, *Lithium insertion/extraction reaction on crystalline MoO3.* Solid State Ionics, 1997. **104**(3-4): p. 183-189.
461. Sun, Y.M., et al., *Self-Assembled Hierarchical MoO2/Graphene Nanoarchitectures and Their Application as a High-Performance Anode Material for Lithium-Ion Batteries.* Acs Nano, 2011. **5**(9): p. 7100-7107.
462. Levi, M.D. and D. Aurbach, *The mechanism of lithium intercalation in graphite film electrodes in aprotic media .1. High resolution slow scan rate cyclic voltammetric studies and modeling.* Journal of Electroanalytical Chemistry, 1997. **421**(1-2): p. 79-88.
463. Park, M.S., et al., *Effects of low-temperature carbon encapsulation on the electrochemical performance of SnO2 nanopowders.* Carbon, 2008. **46**(1): p. 35-40.
464. Hashem, A.M., et al., *Electrochemical properties of nanofibers alpha-MoO3 as cathode materials for Li batteries.* Journal of Power Sources, 2012. **219**: p. 126-132.
465. Lee, S.H., et al., *Reversible Lithium-Ion Insertion in Molybdenum Oxide Nanoparticles.* Advanced Materials, 2008. **20**(19): p. 3627-+.

466. Gaberscek, M., et al., *The importance of interphase contacts in Li ion electrodes: The meaning of the high-frequency impedance arc.* Electrochemical and Solid State Letters, 2008. **11**(10): p. A170-A174.
467. El-Kady, M.F., et al., *Laser Scribing of High-Performance and Flexible Graphene-Based Electrochemical Capacitors.* Science, 2012. **335**(6074): p. 1326-1330.
468. Gershinsky, G., et al., *Electrochemical and Spectroscopic Analysis of Mg2+ Intercalation into Thin Film Electrodes of Layered Oxides: V2O5 and MoO3.* Langmuir, 2013. **29**(34): p. 10964-10972.
469. Riley, L.A., et al., *Conformal Surface Coatings to Enable High Volume Expansion Li-Ion Anode Materials.* Chemphyschem, 2010. **11**(10): p. 2124-2130.
470. Liu, Y.P., et al., *Liquid Phase Exfoliated MoS2 Nanosheets Percolated with Carbon Nanotubes for High Volumetric/Areal Capacity Sodium-Ion Batteries.* Acs Nano, 2016. **10**(9): p. 8821-8828.
471. Chernova, N.A., et al., *Layered vanadium and molybdenum oxides: batteries and electrochromics.* Journal of Materials Chemistry, 2009. **19**(17): p. 2526-2552.
472. Gorenstein, C.J.K.P.G., *Lithium intercalation in MoO3: A comparison between crystalline and disordered phases.* Solids And Materials, 1994. **59**(2): p. 173–178.
473. Jin, X., et al., *Efficient electron/hole transport in inorganic/organic hybrid solar cells by lithium ion and molybdenum trioxide codoping.* Journal of Power Sources, 2014. **268**: p. 874-881.
474. Zhang, X.J., et al., *MoO3/reduced graphene oxide composites as anode material for sodium ion batteries.* Ceramics International, 2017. **43**(4): p. 3769-3773.
475. Yu, X.Y., et al., *Porous MoO3 Film as a High-Performance Anode Material for Lithium-Ion Batteries.* Chemelectrochem, 2014. **1**(9): p. 1476-1479.
476. Fang, X.P., et al., *Lithium storage in commercial MoS2 in different potential ranges.* Electrochimica Acta, 2012. **81**: p. 155-160.
477. Xiao, J., et al., *Electrochemically Induced High Capacity Displacement Reaction of PEO/MoS2/Graphene Nanocomposites with Lithium.* Advanced Functional Materials, 2011. **21**(15): p. 2840-2846.
478. Xue, Q.F., et al., *Improving Film Formation and Photovoltage of Highly Efficient Inverted-Type Perovskite Solar Cells through the Incorporation of New Polymeric Hole Selective Layers.* Advanced Energy Materials, 2016. **6**(5).
479. Borchardt, L., M. Oschatz, and S. Kaskel, *Carbon Materials for Lithium Sulfur Batteries-Ten Critical Questions.* Chemistry-a European Journal, 2016. **22**(22): p. 7324-7351.
480. Shen, L.F., et al., *Hydrogenated Li4Ti5O12 Nanowire Arrays for High Rate Lithium Ion Batteries.* Advanced Materials, 2012. **24**(48): p. 6502-6506.
481. Doi, T., et al., *Electrochemical insertion and extraction of lithium ion at uniform nanosized Li4/3Ti5/3O4 particles prepared by a spray pyrolysis method.* Chemistry of Materials, 2005. **17**(6): p. 1580-1582.
482. Ye, L.Q., et al., *Synthesis of black ultrathin BiOCl nanosheets for efficient photocatalytic H-2 production under visible light irradiation.* Journal of Power Sources, 2015. **293**: p. 409-415.
483. Zhou, F., et al., *Carbon Nanofibers Decorated with Molybdenum Disulfide Nanosheets: Synergistic Lithium Storage and Enhanced Electrochemical Performance.* Angewandte Chemie-International Edition, 2014. **53**(43): p. 11552-11556.
484. Mukai, S.R., et al., *Reduction of irreversible capacities of amorphous carbon materials for lithium ion battery anodes by Li2CO3 addition.* Carbon, 2004. **42**(4): p. 837-842.
485. Andersson, A.M. and K. Edstrom, *Chemical composition and morphology of the elevated temperature SEI on graphite.* Journal of the Electrochemical Society, 2001. **148**(10): p. A1100-A1109.
486. Edstrom, K., et al., *Carbon electrode morphology and thermal stability of the passivation layer.* Journal of Power Sources, 2001. **97-8**: p. 87-91.
487. Hu, L.R., et al., *Fabrication of 3D Hierarchical MoS2/Polyaniline and MoS2/C Architectures for Lithium-Ion Battery Applications.* Acs Applied Materials & Interfaces, 2014. **6**(16): p. 14644-14652.
488. Li, Z.Y., et al., *Preparation of hierarchical C@MoS2@C sandwiched hollow spheres for lithium ion batteries.* Journal of Materials Chemistry A, 2017. **5**(8): p. 3987-3994.

489. Liu, H., et al., *Highly Ordered Mesoporous MoS2 with Expanded Spacing of the (002) Crystal Plane for Ultrafast Lithium Ion Storage.* Advanced Energy Materials, 2012. **2**(8): p. 970-975.
490. Mao, C.M., et al., *Carbon encapsulated nanosheet-assembled MoS2 nanospheres with highly reversible lithium storage.* Chemical Engineering Journal, 2016. **304**: p. 511-517.
491. Sun, Z., et al., *High rate lithium-ion batteries from hybrid hollow spheres with a few-layered MoS2-entrapped carbon sheath synthesized by a space-confined reaction.* Journal of Materials Chemistry A, 2016. **4**(27): p. 10425-10434.
492. Hong, Y.J. and Y.C. Kang, *General Formation of Tin Nanoparticles Encapsulated in Hollow Carbon Spheres for Enhanced Lithium Storage Capability.* Small, 2015. **11**(18): p. 2157-2163.
493. Cho, J.S., H.S. Ju, and Y.C. Kang, *Applying Nanoscale Kirkendall Diffusion for Template-Free, Kilogram-Scale Production of SnO2 Hollow Nanospheres via Spray Drying System.* Scientific Reports, 2016. **6**.
494. Li, Z.Y., et al., *A facile synthesis method and electrochemical studies of a hierarchical structured MoS2/C-nanocomposite.* Rsc Advances, 2016. **6**(79): p. 76084-76092.
495. Chang, K. and W.X. Chen, *In situ synthesis of MoS2/graphene nanosheet composites with extraordinarily high electrochemical performance for lithium ion batteries.* Chemical Communications, 2011. **47**(14): p. 4252-4254.
496. David, L., et al., *Polymer-Derived Ceramic Functionalized MoS2 Composite Paper as a Stable Lithium-Ion Battery Electrode.* Scientific Reports, 2015. **5**.
497. Pang, Q., et al., *Hybrid graphene@MoS2@TiO2 microspheres for use as a high performance negative electrode material for lithium ion batteries.* Journal of Materials Chemistry A, 2017. **5**(7): p. 3667-3674.
498. Nagao, M., A. Hayashi, and M. Tatsumisago, *All-solid-state lithium secondary batteries with high capacity using black phosphorus negative electrode.* Journal of Power Sources, 2011. **196**(16): p. 6902-6905.
499. Coleman, J.N., *Liquid Exfoliation of Defect-Free Graphene.* Accounts of Chemical Research, 2013. **46**(1): p. 14-22.
500. Xu, F., et al., *Scalable shear-exfoliation of high-quality phosphorene nanoflakes with reliable electrochemical cycleability in nano batteries.* 2d Materials, 2016. **3**(2).
501. Li, D., et al., *Black phosphorus polycarbonate polymer composite for pulsed fibre lasers.* Applied Materials Today, 2016. **4**: p. 17-23.
502. Sotor, J.S., G.; Macherzynski, W.; Paletko, P.; Abramski, K. M, *Black Phosphorus a New Saturable Absorber Material for Ultrashort Pulse Generation.* Appl. Phys. Lett. , 2015. **107**: p. 051108.
503. Li, W.F., et al., *Ultrafast and Directional Diffusion of Lithium in Phosphorene for High-Performance Lithium-Ion Battery.* Nano Letters, 2015. **15**(3): p. 1691-1697.
504. Aurbach, D., et al., *Failure and stabilization mechanisms of graphite electrodes.* Journal of Physical Chemistry B, 1997. **101**(12): p. 2195-2206.
505. McManus, D., et al., *Water-based and biocompatible 2D crystal inks for all-inkjet-printed heterostructures.* Nature Nanotechnology, 2017. **12**(4): p. 343-350.
506. Yau, H.C., et al., *Sonochemical degradation of N-methylpyrrolidone and its influence on single walled carbon nanotube dispersion.* Chemical Communications, 2015. **51**(93): p. 16621-16624.
507. Berrueco, C., et al., *Sample Contamination with NMP-oxidation Products and Byproduct-free NMP Removal from Sample Solutions.* Energy & Fuels, 2009. **23**(5-6): p. 3008-3015.
508. Nikolka, M., et al., *High operational and environmental stability of high-mobility conjugated polymer field-effect transistors through the use of molecular additives.* Nature Materials, 2017. **16**(3): p. 356-+.
509. Levi, M.D. and D. Aurbach, *The mechanism of lithium intercalation in graphite film electrodes in aprotic media. Part 1. High resolution slow scan rate cyclic voltammetric studies and modeling.* Journal of Electroanalytical Chemistry, 1997. **421**(1): p. 79-88.
510. Dubertret, B., T. Heine, and M. Terrones, *The Rise of Two-Dimensional Materials.* Accounts of Chemical Research, 2015. **48**(1): p. 1-2.

511. Mikhail D.; Aurbach, L.D., *The Mechanism of Lithium Intercalation in Graphite Film Electrodes in Aprotic Media. Part 1. High Resolution Slow Scan Rate Cyclic Voltammetric Studies and Modelling.* J. Electroanal. Chem. , 1997. **421**: p. 79-88.
512. Simon, P. and Y. Gogotsi, *Materials for electrochemical capacitors.* Nature Materials, 2008. **7**(11): p. 845-854.
513. Cai, X.Y., et al., *Graphene and graphene-based composites as Li-ion battery electrode materials and their application in full cells.* Journal of Materials Chemistry A, 2017. **5**(30): p. 15423-15446.
514. Wu, Z.S., et al., *Graphene/metal oxide composite electrode materials for energy storage.* Nano Energy, 2012. **1**(1): p. 107-131.
515. Parviz, D., et al., *Challenges in Liquid-Phase Exfoliation, Processing, and Assembly of Pristine Graphene.* Advanced Materials, 2016. **28**(40): p. 8796-8818.